

Robert A. Ploc¹

The Effect of Minor Alloying Elements on Oxidation and Hydrogen Pickup in Zr-2.5Nb

REFERENCE: Ploc, R. A., "The Effect of Minor Alloying Elements on Oxidation and Hydrogen Pickup in Zr-2.5Nb," *Zirconium in the Nuclear Industry: Thirteenth International Symposium, ASTM STP 1423*, G. D. Moan and P. Rudling, Eds., ASTM International, West Conshohocken, PA, 2002, pp. 297-312.

ABSTRACT: In CANDU[®] reactors, fuel and coolant are contained in horizontal pressure tubes made of Zr-2.5 wt% Nb alloy. In the past decade, the effect of more than 20 impurity elements, in various concentrations, on oxidation and deuterium pickup (at 300°C, $pD = 10.5$, Li_2O) have been investigated in over 70 Zr-2.5Nb alloys. The studies were performed using non-consumable arc melted alloy logs that were rolled and made into corrosion coupons and corroded in autoclaves. This study represents one of the largest collections of previously unpublished data on the effect of impurity elements on oxide film growth and deuterium pickup in a zirconium alloy. Elements such as Al, Ti, Mn, and Pt, to name but a few, were found to significantly accelerate the corrosion process. Some elements, such as tin, had a positive effect on oxidation (lowers the rate of oxide film development) and a negative effect on hydrogen pickup (increases pickup). Three parameters were important to the corrosion process, namely, microstructure, surface finish, and synergistic interactions between the impurity elements.

The above studies culminated in two response surface analyses (RSA). The first was conducted on the effect of C and Fe on oxygen and deuterium pickup in Zr-2.5Nb drop castings corroded at 325°C in CANDU[®] conditions. The second study was performed in autoclaves at 300°C on the effect of four impurity elements, C, Fe, Cr, and Si, in Zr-2.5Nb micro-tubes, which possess the same microstructure as full-size pressure tubes. The first RSA revealed a quadratic dependence of corrosion on C and Fe concentrations, with an optimum resistance at about 30 ppm (wt) C and 1100 ppm (wt) Fe. This has been partially confirmed by out-reactor corrosion of Zr-2.5Nb-Fe micro-pressure tubes. Trends in- and out-reactor were similar for oxidation but different in magnitude for deuterium pickup. There is no linear dependence on the Fe concentration in-reactor, implying that Fe and C form a complex. The second RSA showed no effect due to Si. Cr weakly influenced oxide film formation, at least for short-term exposures.

KEYWORDS: response surface analysis, impurities, Zr-2.5Nb, corrosion, hydrogen pickup, deuterium pickup, minor alloying additions

There is a paucity of literature dealing with the relationship between small concentrations of alloying elements and hydrogen pickup in zirconium alloys. Most publications deal with fabrication modifications or alloying additions to the Zircalloys in excess of 1% and discuss oxide film growth or nodular corrosion (see, for instance, Refs 1 to 4). A few publications have looked at the effect of trace elements such as in Ref 5 (Zircaloy-4); however, the primary emphasis has been on weight gain analysis that is due mainly to oxide film growth. Perforation of Zircaloy fuel cladding can be a concern if nodular corrosion occurs. With increased economic pressure for higher burnup, hydrogen ingress is receiving more attention

¹ Principal professional, Atomic Energy of Canada Limited, Chalk River Laboratories, Station 82, Chalk River, Ontario, K0J 1J0, Canada

In 1976 Cox reviewed the effect of alloying elements on zirconium corrosion [6], including the influence of minor elements (ppm range) in alloys other than the Zircalloys, for instance Zr-1%Nb. The referenced work originated from experiments performed in the 1950s, and not until recently have researchers begun to carry that work forward.

This publication deals with the corrosion of Zr-2.5Nb, the alloy used for CANDU® pressure tubes. Although this alloy has a low pickup rate, it does not possess an extensive precipitate population or suffer from nodular corrosion. However, it must be optimized to resist deuterium ingress because component lifetimes are approximately 30 years. Factors such as the presence of residual impurities in the alloy might influence deuterium pickup and therefore must be critically investigated. As late as the 1980s, there were no data to relate pickup to minor impurity concentrations.

Data generated from programs to determine the effect of low concentrations of impurities on deuterium ingress in CANDU materials and conditions (300°C, $pD = 10.5$) are reported here. The programs chronologically developed an increasing level of sophistication, from the testing of laboratory-produced non-consumable melted alloy buttons to a response surface analysis (RSA) of Zr-2.5Nb micro-pressure tubes. The order in which these corrosion programs were implemented was:

1. Non-consumable, arc-melted, Zr-2.5Nb alloy logs with various concentrations of added ternary elements (21 elements tested), usually in the range of 100 to 5000 ppm (wt), were hot-rolled into sheet form and corrosion tested [7,8].
2. Zr-2.5Nb/C drop castings [9].
3. Zr-2.5Nb drop castings with C and Fe concentrations determined from a statistical design of experiment (DOE) with the objective to determine the corrosion response over a limited range of Fe and C concentrations, i.e., an RSA [10].
4. RSA of micro-pressure tubes with various concentrations of C, Fe, Si, and Cr.

The references for Nos. 1 to 3 contain details of chemical compositions, fabrications routes, microstructures, and, in the case of No. 3, raw and detailed analysis data that permit an evaluation of the applicability, strength, and limitations of the RSA technique. Data in this manuscript have never been published, except Fig. 2, which appeared in a company publication [10], available upon request. Reference 10 was prepared to provide details of the RSA technique that otherwise, if included here, would have added unnecessary detail and confused the primary thrust of the manuscript, that is, to demonstrate the power and advantage of using statistical techniques to investigate complex phenomena such as corrosion.

The RSA is a method for designing a multi-control parameter experiment using the minimum number of tests that will generate a significant result over the complete range of the control variables. Synergistic interactions between variables can be revealed as well as a description of the response over the variable range, thus permitting the tailoring of an optimized product (i.e., determining an optimum response after considering trade-offs between the control variables).

In corrosion studies, it is often assumed that the effect of an alloying or impurity element is linear with its concentration. Even when non-linear responses are expected, it is rare that synergistic interactions with other elements have been considered. For instance, changing the concentration of Sn in a Zircaloy may have been investigated, but the data are relevant only to those alloys containing the same concentration of Fe, etc. What the RSA yields is not only how the concentration levels of Sn will affect the corrosion response, but also how the response changes for various combinations of all the other variables, i.e., such as the other alloying or impurity elements. By examining the fitting residuals, the RSA warns if a significant control variable has been overlooked. "What if" predictions are routine; for ex-

ample, what if the Sn concentration is one and a half times the current practice and the Fe concentration is double, or, if there is poor control of the Cr concentration, the RSA will predict the expected result.

Experimental Procedures

The preparation of non-consumable, arc-melted logs has been described in a previous publication [7]. For all the alloys, impurity elements were added to the same Zr-2.5Nb stock and arc-melted six times to form a 50 to 55 g log approximately 150 mm long and 15 mm in diameter. The logs were wrapped in zirconium foil, encapsulated in an evacuated quartz tube, and homogenized for seven days at 973 K (700°C), cooled, cleaned, heated to 1023 K (750°C) in air and hot rolled into strip, machined into 20 to 30 coupons (each about 15 × 7 × 1 mm), abraded to 600 grit, pickled, washed, dimensioned, and exposed to D₂O at 300°C. The compositional data listed in Table 1 were obtained using several analysis techniques, each of which often yielded different concentration values. Also, the apparent composition would, on occasion, vary from specimen to specimen. Therefore, the values in Table 1 should serve only as an approximation since they could be in error by as much as 30%. There was no attempt to control the coupon microstructure (see Ref 8) or measure variability in the impurity concentrations of the stock material.

Except for the alloys described above, Wah Chang, Albany, Oregon, U.S.A. fabricated all other materials. A small number of drop castings of Zr-2.5Nb with various concentrations of C were produced to test the corrosion response as a function of C concentration. These castings were manufactured from the same stock material and, therefore, maintained the same background impurity concentrations except for random amounts of tungsten originating from the arc-melting process. Drop castings were produced by non-consumable arc-melting (using a tungsten electrode) small quantities of Zr-2.5Nb with C fibers, then drop casting the melt to form a 2.5 × 2.5 × 9.5 cm button that was subsequently heated, cross-rolled, and finally, cold-rolled into 1.5 mm thick sheet (see Ref 10 for details). Corrosion coupons cut from the sheet were machine finished to RMS 40. A description of the drop castings and their chemical compositions can be found in Refs 9 and 10.

Whereas drop castings in which only C was varied were useful in answering some of the questions regarding corrosion response as a function of C concentration, it was not possible to determine whether synergistic interactions were present with other impurity elements. For example, the test data obtained for the fixed Fe (or any other element) concentration might be different if the Fe concentration was significantly changed. For this reason, an RSA experiment was designed with eleven unique, and five "repeat" drop castings [10] with various concentrations of C and Fe, generated by a commercially available software program, ECHIP [11], for a "continuous" quadratic response surface. These alloys were corroded in a test reactor and in an autoclave, in the same loop, for approximately 450 days. The corrosion response at 325°C was measured over the concentration range 150 to 3000 ppm (wt) for Fe and 30 to 300 ppm (wt) for C.

Although the Zr-2.5Nb-Fe/C RSA was instructive, it was performed on specimens (drop castings) that did not have a CANDU pressure tube microstructure. In Zr-2.5Nb pressure tubes, the α -Zr grains are elongated by the extrusion process and encased in a thin network of β -Zr (about 10% by volume when manufactured). This is very different from the almost equiaxed microstructure seen in drop castings, an example of which can be seen in Fig. 1 of Ref 10. Hence, a second DOE test matrix was produced for micro-pressure tubes having generally the same microstructure as full size tubes. Micro-pressure tubes were fabricated from forged alloy octagons with a nominal diameter of 5 cm and a length of 35 cm. A 12 to 13 cm length of the octagon was extruded into a 140 cm long micro-pressure tube with

TABLE 1—Corrosion data for non-consumable melted Zr-2.5Nb ternaries.

	Concentration in ppm (wt)	Days of Exposure	Oxygen, mg/dm ²	Deuterium, mg/dm ²	Control, Days	Control, mg/dm ²	Difference mg/dm ²	Performance Factor
Al	1000	3/60	32/S	0.786	60	0.265	0.52	3.0
Si	45	10	14	0.072	10	0.097	(0.02)	0.7
	300	10	13.7	0.103	10	0.097	0.01	1.1
	400	364	50	0.686	364	0.825	(0.14)	0.8
	515	364	149(s)	0.996	364	0.825	0.17	1.2
	2600	3/203	98/S	1.981	203	0.561	1.42	3.5
P	15	120/203	96(s)/S	0.946	203	0.561	0.38	1.7
	50	365	113	0.891	365	0.827	0.06	1.1
	375	80/120	44(s)/S	0.810	120	0.403	0.41	2.0
	592	203	161	0.773	203	0.561	0.21	1.4
Ti	475	1/10	89/S	0.858	10	0.097	0.76	8.9
	975	1/10	58/S	0.360	10	0.097	0.26	3.7
	2215	1/10	364/S	1.195	10	0.097	1.10	12.4
V	75	3	4 R	0.028	3	0.051	(0.02)	0.6
	110	301	70	0.722	301	0.727	(0.00)	1.0
	525	365	69(s)	1.158	365	0.827	0.33	1.4
	800	42/122	157/S	0.788	122	0.407	0.38	1.9
	900	300	144	0.866	300	0.725	0.14	1.2
	5400	120/200	254/S	1.551	200	0.556	1.00	2.8
Cr	410	360	56	0.731	360	0.819	(0.09)	0.9
	435	360	261	1.135	360	0.819	0.32	1.4
	890	120	165	0.667	120	0.403	0.26	1.7
	1010	120	148	0.865	120	0.403	0.46	2.1
	4550	300	107	0.984	300	0.725	0.26	1.4
	4965	120	729	1.646	120	0.403	1.24	4.1
Mn	260	364	124	0.924	364	0.825	0.10	1.1
	400	1/3	8/S	2.727	3	0.051	2.68	53.6
	1000*	3/40	19/S	0.332	40	0.209	0.12	1.6
	4020	120	215	0.702	120	0.403	0.30	1.7
Fe	150	202	51	0.255	202	0.560	(0.30)	0.5
	525	200	32	0.209	200	0.556	(0.35)	0.4
	640	202	56	0.609	202	0.560	0.05	1.1
	750	202	59	0.591	202	0.560	0.03	1.1
	4635	202	91	0.845	202	0.560	0.29	1.5
	4850	81	111	0.848	81	0.317	0.53	2.7
Ni	155	300	59(s)	0.543	300	0.725	(0.18)	0.7
	433	300	474(s)	4.203	300	0.725	3.48	5.8
	1000	120	600(s)	0.995	120	0.403	0.59	2.5
	1120	199	600	2.171	199	0.554	1.62	3.9
	5240	200	209(s)	46.871	200	0.556	46.32	84.3
Cu	470*	3	7	0.071	3	0.051	0.02	1.4
	1050*	3	8	0.695	3	0.051	0.64	13.7
	5300*	1	6	0.347	1	0.029	0.32	12.0
Ge	500a*	10/39	19/S	0.282	39	0.206	0.08	1.4
	500b*	60	50	0.705	60	0.265	0.44	2.7
	1100*	3	48	0.228	3	0.051	0.18	4.5

TABLE I—Continued

	Concentration in ppm (wt)	Days of Exposure	Oxygen, mg/dm ²	Deuterium, mg/dm ²	Control, Days	Control, mg/dm ²	Difference mg/dm ²	Performance Factor
Mo	585	60	195	0.432	60	0.265	0.17	1.6
	1090	40/121	45	1.199	121	0.405	0.79	3.0
	1200	199	39	0.512	199	0.554	(0.04)	0.9
	4600	1/39	27/S	0.630	39	0.206	0.42	3.1
Ag	350	3	S	4.317	3	0.051	4.27	84.8
	1000*	80/120	27(s)/S	0.658	120	0.403	0.26	1.6
In	1020	3/60	10/S	0.049	60	0.265	(0.22)	0.2
Sn	470	700	89	0.895	700	1.301	(0.41)	0.7
	1020	700	103	1.003	700	1.301	(0.30)	0.8
	5030	700	88	0.911	700	1.301	(0.39)	0.7
	9900	700	138	1.893	700	1.301	0.59	1.5
Ce	1150	4/40	55/S	0.654	40	0.209	0.44	3.1
	4600	10/40	58/S	0.370	40	0.209	0.16	1.8
Hf	860*	3	10	0.096	3	0.051	0.05	1.9
	1000*	3/10	32/S	0.206	10	0.097	0.11	2.1
	5000*	120	38	0.374	120	0.403	(0.03)	0.9
W	500 _a *	3	S	0.338	3	0.051	0.29	6.6
	500 _b *	40/61	94/S	0.418	61	0.267	0.15	1.6
	1100*	10/40	26/S	0.342	40	0.209	0.13	1.6
	5000*	120	49(s)	0.323	120	0.403	(0.08)	0.8
Re	430*	10	30	0.171	10	0.097	0.07	1.8
	880*	10	29	0.179	10	0.097	0.08	1.9
	4200*	10	30	0.146	10	0.077	0.05	1.5
	4600 _a *	10	22	0.071	10	0.097	(0.03)	0.7
	4600 _b *	3	21	0.144	3	0.051	0.09	2.8
Pt	440	10/40	37/S	0.289	40	0.209	0.08	1.4
	5000*	10/60	24/S	0.790	60	0.265	0.53	3.0
Au	570	1/10	S/S	0.271	10	0.097	0.17	2.8
	1000	60/120	25/S	0.455	120	0.403	0.05	1.1

* = indicates a questionable analysis

an outside diameter of 14 mm and wall thickness of 2.75 mm. Numerous 1.25 cm long sections were cut from the micro-tube for corrosion testing.

No attempt was made to investigate the role of microstructure in corrosion, only to maintain a consistent fabrication route for all of the alloys within a given experiment. If microstructural changes occurred as a result of changing the impurity concentrations, the effect was expected to be included within the corrosion responses and would require additional experimentation to deconvolute. If abrupt changes occurred, the response analysis would have indicated a "lack-of-fit." An identical argument applies to the role of surface finish (prior to corrosion), and, for this reason, surface finish has been held constant for all specimens. Reference 7 touches upon this subject in terms of the effect of cold-work, shot-peening, grinding, and electropolishing.

For the second DOE (micro-pressure tubes), it was decided to expand the number of alloying elements to include not only C and Fe, but also Si and Cr. It would have been desirable to expand the list to more than these four elements; however, the number of tests dramatically increases, as does the expense. This DOE required 20 alloy batches and 5 replicates for a total of 25 as compared to a total of 16 for the simpler Fe/C DOE. Figure 1 graphically displays the composition of the required alloys. Once the experimental parameters and their limits are defined, the required alloy compositions are extracted from standard textbook designs for a given experimental model (in this instance, quadratic). In fact, the number of alloys is slightly larger than the standard factorial designs so as to enhance the power to detect LOF results.

All corrosion tests were performed in reactor-grade D₂O (>99% purity). The deuterium concentration, measured by hot vacuum extraction mass spectroscopy (accuracy of 5%), was therefore a true measure of hydrogen absorbed during corrosion. Autoclaves were purged prior to use by bubbling high-purity argon through the D₂O for 45 min and then pulling a vacuum on the system until the temperature reached 40°C. The *pD* of 10.5 was measured at room temperature. Except for temperature, the autoclave tests associated with the in-reactor exposures (325°C) were performed in CANDU conditions (flux, deuterium over-pressure, and Lithium-ion concentration).

Results

Table I is a summary of the data generated from corrosion of the non-consumable arc-melted ternaries. Since these experiments were considered to be scoping in nature, only terminal (end of test) results are reported. In the Days of Exposure column are, on some occasions, listed two values separated by a "/". The first number refers to the first instance in which oxide spalling was observed and the second to the number of days the test was

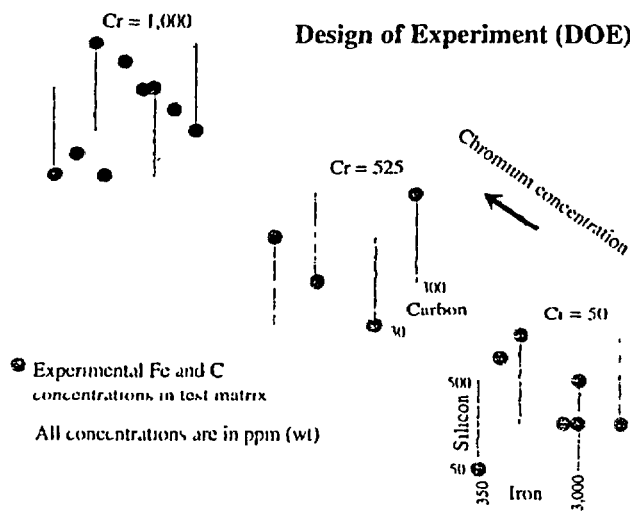


FIG 1—Zr-2.5Nb-Fe/C/Si/Cr alloys used to determine a quadratic response surface.

extended for purposes of determining deuterium pickup. In the Oxygen column, the weight gain refers to the first of the two exposure values, since spalling makes the accumulation of additional oxidation data meaningless. A lower case "(s)" indicates that spalling had been noted for some specimens with less exposure, and, hence, the weight gain due to oxidation is questionable but not necessarily in error. A capitalized "S" indicates that spalling has occurred. The "Control, mg/dm²" values (control being stock material that was processed in the identical manner as the ternary alloys but without an alloying addition) are for deuterium pickup and have been used to calculate the "Performance Factor" (ratio of the deuterium picked up in the specimen divided by the "Control" pickup). A performance factor of less than 1 indicates a reduction of deuterium pickup relative to the controls. Since most of the performance factors are greater than 1, it can be concluded that the addition of alloying elements to Zr-2.5Nb generally reduces the alloy's resistance to deuterium ingress.

The data describing corrosion of Zr-2.5Nb/C drop castings were reported in Ref 9. The results show that for the drop castings, which contained a constant impurity spectrum, deuterium pickup resistance decreased almost linearly with increasing C concentration. Oxidation was almost independent of C. When similar data were plotted for pressure tubes selected at random, the deuterium pickup resistance was almost constant from 50 to 90 ppm C; then, after a small increase in resistance at about 110 ppm C, it steeply decreased with increasing concentration. Because the pressure tubes were chosen at random (available data) their impurity spectra were different, most notably the Fe concentration. These data suggest that either the pressure tube microstructure was important or that there were synergistic interactions between C and Fe (or both).

The results from the RSA of Fe and C in Zr-2.5Nb drop castings can be seen in Fig. 2. These specimens were exposed in a test reactor that operated at 325°C using D₂O with a room temperature pD_{∞} of 10.2 to 10.3. The test loop also contained an autoclave (out-of-flux) for comparative studies; detailed information can be found in Ref 10. Information from longer exposures (450 days) has yet to be analyzed.

As mentioned, an RSA was performed for four elements, Fe, C, Si, and Cr, using micro-pressure tubes to ensure that the effect of the pressure tube microstructure was not being overlooked. These tests were performed in stand-alone autoclaves operating at 300°C rather than at 325°C as in the reactor loop. Although data are available for longer exposures, Fig. 3 is typical and shows the result from 150 days of exposure. The oxygen response surface has changed significantly for low Fe and C concentrations. Also, the deuterium response surface appears to display a reverse direction of curvature for high C and intermediate Fe. Whether the reverse curvature is due to the small Si influence, the lower temperature of 300°C, the change in the oxidation behavior, a curve-fitting artifact, or the pressure tube microstructure is unknown.

Table 2 indicates the statistically significant terms in the quadratic equation used to describe the shape of the response surfaces. Data are shown for both the two-parameter RSA drop castings and the four-parameter version for micro-pressure tubes. The asterisks are an indication of the statistical significance of the "quadratic term" shown on the left of the table. Three asterisks are more significant than two, which is more significant than one. The absence of an asterisk indicates that the corresponding term in the quadratic equation has little influence in determining the shape of the response surface.

Discussion

Because of errors in chemical characterization, inhomogeneous elemental distributions and variable microstructures, Table 1 should be used with caution. At best, it should be used as an indicator of how some impurity elements might affect oxidation and deuterium pickup in

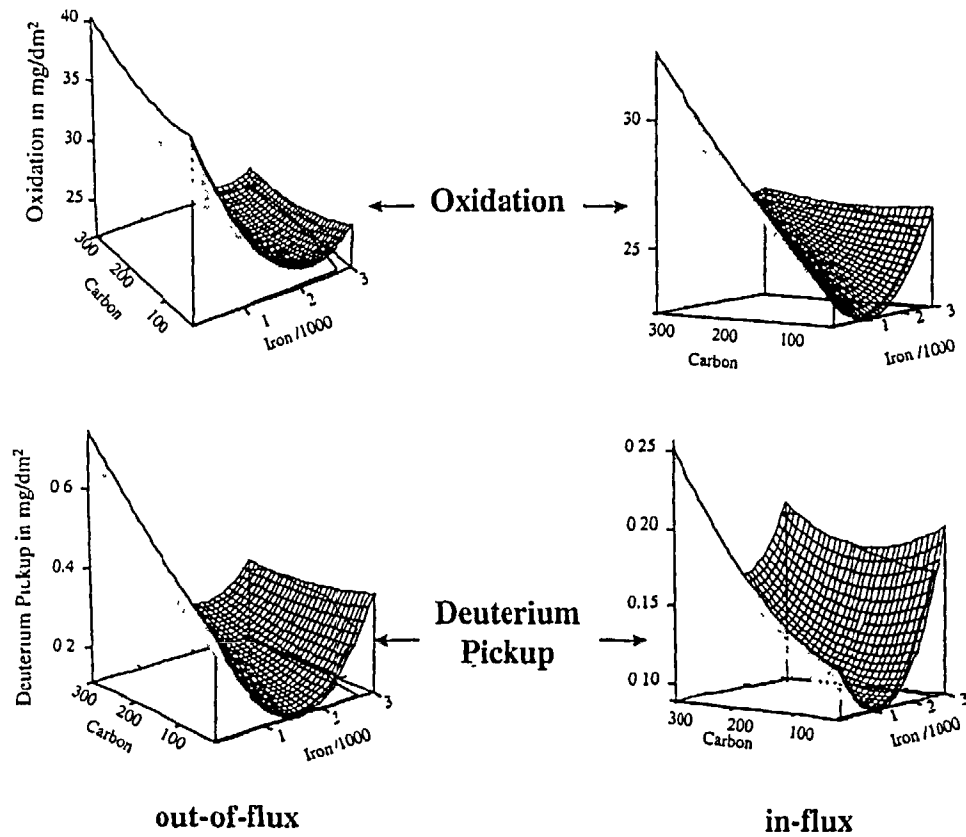


FIG 2—Response surfaces showing the quadratic effect of C and Fe on oxidation and deuterium pickup in Zr-2.5Nb drop-castings corroded for 208 days at 325°C in D₂O (pD = 10.5), both out-of-flux and in-flux

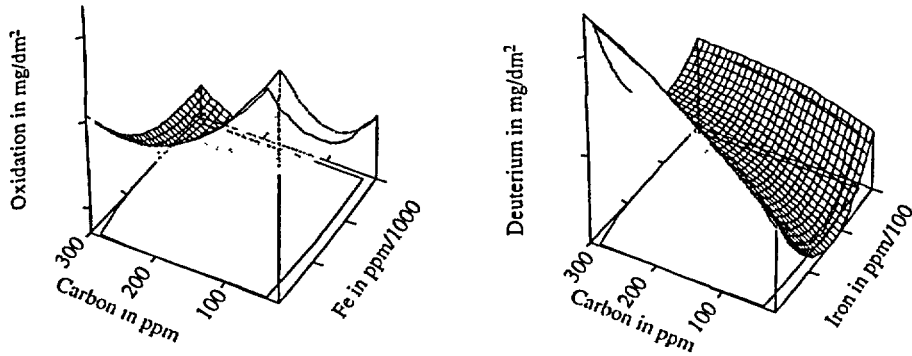


FIG. 3—Response surfaces showing quadratic effects of Fe and C (Cr and Si concentrations fixed) on corrosion for 150 days at 300°C in D₂O (pD = 10.5). Because Cr has very little effect and Si has no effect (see Table 2), response surfaces such as seen here are almost identical for all values of Cr and Si concentrations.

TABLE 2—The important quadratic equation parameters used in determining the shape of the various response surfaces seen in Figs. 2 and 3. Note that the corrosion of the micro-pressure tubes was at 300°C and the drop-castings were corroded at 325°C.

Quadratic Term	out-of-flux				in-flux		Fe/C/Si/Cr micro-tubes			
	Oxygen		Deuterium		Oxygen	Deuterium	Oxygen		Deuterium	
	208 d	450 d ¹¹	208 d	450 d	208 d	208 d	150 d	250 d	150 d	250 d ¹¹
Fe	***	***	***	***			***	***	***	***
C		**	***	***	**	***	***	***	***	***
Fe · C		***	***	***	**	**	*		**	*
Fe ²	*	***	***	***		**	*		**	***
C ²							**	**		*
Si										*
Cr							*	*		
Fe · Si										*
Fe · Cr								*		
C · Si									*	
C · Cr										
Si · C										
Si ²										
Cr ²										

*** quadratic term with most significance
 ** quadratic term with secondary significance
 * quadratic term with least significance
 no *'s quadratic term has no significance.
¹¹ indicates LOF (Lack-Of-Fit), requires further analysis.

Zr-2.5Nb. However, even with this limitation there are strong suggestions in the data that the effect of an element is non-linear with concentration. For instance, see the data for W, Cr, and Sn. Some elements, such as Al, Ti, Ni, Cu and the noble metals, are so deleterious from the point of view of deuterium pickup that they should always be kept at the lowest concentration that is economically feasible. Other elements are useful in limiting oxidation but not deuterium pickup and vice versa. Sn is an example in that it reduces oxidation but increases pickup. Examination of Table 1 "Performance Factors" also suggests that the effectiveness of an element can progressively increase with increasing exposure; for instance, see V and Sn.

Zr-2.5Nb-C drop castings were provided by Wah Chang (Albany, Oregon) to determine whether C had an impact on oxidation and deuterium ingress. As reported in Ref 9, C in the concentration range from 30 to 300 ppm (wt) had a weak influence on the oxidation rate (specimens contained about 185 ppm (wt) of Fe) but a strong influence on deuterium pickup. This would suggest that the mechanisms of oxidation and deuterium pickup are different. When the same data were plotted, but for random pressure tubes (all with different amounts of Fe and other elements) the results were slightly different. Although deuterium pickup once again showed a dependence on the C concentration, that dependence was weak until about 110 ppm C, then steeply increased with increasing concentration. Oxidation data also displayed a weak dependence but with a slight inflection around 130 ppm C. These two sets of data suggested that:

- deuterium pickup in Zr-2.5Nb is strongly dependent on C concentration
- oxidation is weakly dependent on C concentration
- alloy microstructure is important [9], especially in terms of deuterium pickup
- there may be a synergistic interaction between C and Fe.

For out-of-flux exposures at 325°C, the Zr-2.5Nb-Fe/C drop casting response surfaces shown in Fig 2 indicate that oxidation is weakly influenced by the C concentration (consistent with the observation above). The situation changes in-flux where the C concentration plays an important role, especially at low Fe concentrations and to a lesser effect at high Fe. For small amounts of C, there is a distinct minimum in the oxidation rate at about 1100 ppm Fe. For the in-flux results, the loci of minimum pickup follow a sloping line with respect to the C and Fe, so that at about 200 ppm C the minimum occurs for about 2000 ppm Fe. Table 2 shows why there is a difference between out and in-reactor behavior. For out-reactor, the dominant parameter is the Fe concentration, while, for in-reactor, there is an interaction between the C and Fe (i.e., the Fe-C quadratic term).

Figure 2 shows that, unlike oxidation, deuterium pickup is strongly dependent on C but only for low Fe concentrations. The reason for this behavior can be seen in Table 2; in the rig, there is no longer any dependence on the linear Fe concentration. The optimum concentration values for minimum deuterium pickup are 1510 ppm Fe/minimum C for out-reactor corrosion; in-reactor, the optimum becomes 1100 ppm Fe/minimum C. The effect of radiation is to decrease pickup by almost a factor of three; however, because of the steep curvature of the response surface, in-reactor values are more sensitive to small variations in the Fe concentration, especially for values higher than the optimum. Interestingly, the oxidation values are similar in- and out-reactor, which again emphasizes the observation, made from Table 1, that the mechanisms of oxidation and deuterium pickup are different.

The RSA generated for the micro-pressure tubes shows a somewhat different behavior for oxidation but a similar behavior for deuterium pickup. Reference to Table 2 indicates that the different oxidation behavior is likely due to the second order dependence on the C concentration. It seems clear from Table 2 that the alloy microstructure has an important

role in oxidation and to an unknown extent in determining the amount of deuterium ingress. In terms of oxidation, the optimum for maximum resistance for the micro-pressure tubes is about 2400 ppm Fe and 200 ppm C. Si appears to have a small effect and Cr no effect on deuterium pickup. Oxidation is not affected by Si but has a small Cr effect after 250 days of exposure at 300°C. Corrosion exposures and data analyses are continuing with special attention being paid to the LOF associated with one of the data sets.

When the above RSAs were performed, three independent Zr-2.5Nb/Fe micro-pressure tubes that had Fe and C concentrations within the RSA test ranges were already on test at 300°C ($pD = 10.5$, out-reactor), and, therefore, data from the tubes were ideal for checking the accuracy of the RSA predictions. The three tubes were made from stock material that contained approximately 45 ppm C and to which was added 50, 1000, and 2000 ppm Fe. Though it was not possible to make a precise comparison between the RSA predictions with the Fe-micro-tubes (because of the different corrosion conditions and experimental matrix), the closest comparison possible revealed good agreement. Pickup predictions for the Fe-micro-tubes using data generated from analysis of the Fe/C drop castings (which were corroded at 325°C and not 300°C) were that the micro-tube with 1000 ppm Fe should pick up less than half (40%) of the deuterium seen in the micro-tube with 50 ppm Fe. The same prediction, but using data generated by the four-element Fe/C/Si/Cr RSA (specimens corroded at 300°C), projected a relative pickup of 50% (the 1000 ppm Fe tube should absorb 50% of the amount of deuterium absorbed by the 50 ppm Fe micro-tube). The application of the existing RSA data to predict the Fe micro-tube behavior is slightly questionable because of the lack of comparable exposure times. However, the 1000 and 50 ppm Fe-micro-tubes did show a difference of 45% in the absorbed deuterium after 1100 days and 58% after 250 days. The four-element RSA predicted a deuterium pickup of 0.073 mg/dm² after 250 days, and the actual pickup for the same number of days in the autoclaves was 0.075 mg/dm². The agreement between prediction (based on the derived quadratic equations) and actual is within 5%.

RSA data are valid only within the boundary conditions of the experiment. It is possible to extrapolate outside those boundaries (such as concentration ranges or exposure times) but at considerable risk. To apply the RSA data to operating lifetimes of pressure tubes is therefore not recommended until considerably more exposure is achieved. Such experiments are now in progress.

As indicated in Table 2, there is a LOF for one of the data sets. To understand the possible origins of the LOF, the sensitivity of deuterium pickup to changes in the control parameters were determined from the partial differentials of the quadratic equations (208-day data), see Fig. 4. Both the C and Fe partial derivatives have been superimposed on the same axes in Fig. 4a; the line AB defines the C and Fe concentrations that produce the same change in the pickup resistance for small changes of either the Fe or C concentrations. Because the plane produced by the partial differential with respect to C is higher than that of Fe (for low Fe concentrations), C dominates the determination of the resistance to deuterium uptake. However, below the line AB (at high Fe and low C concentrations) the most effective means of influencing deuterium ingress is to change the Fe concentration. Figures 4b and 4c show how the planes produced by the partial differentials intersect the zero change plane (no change in the deuterium ingress rate). The intersection of the partial derivatives with the zero plane is a reflection of the fact that the response surfaces are curved and contain slope reversals; adding Fe or C can result in either an increase or decrease in pickup. A possible conclusion drawn from these observations is that the variability, which is often seen in many corrosion tests, may be linked to an inhomogeneous distribution of a dominant impurity (or alloying element) such as C that is in a synergistic relationship with another impurity, in this case Fe. For an accurate RSA, the chemical composition of each corrosion specimen

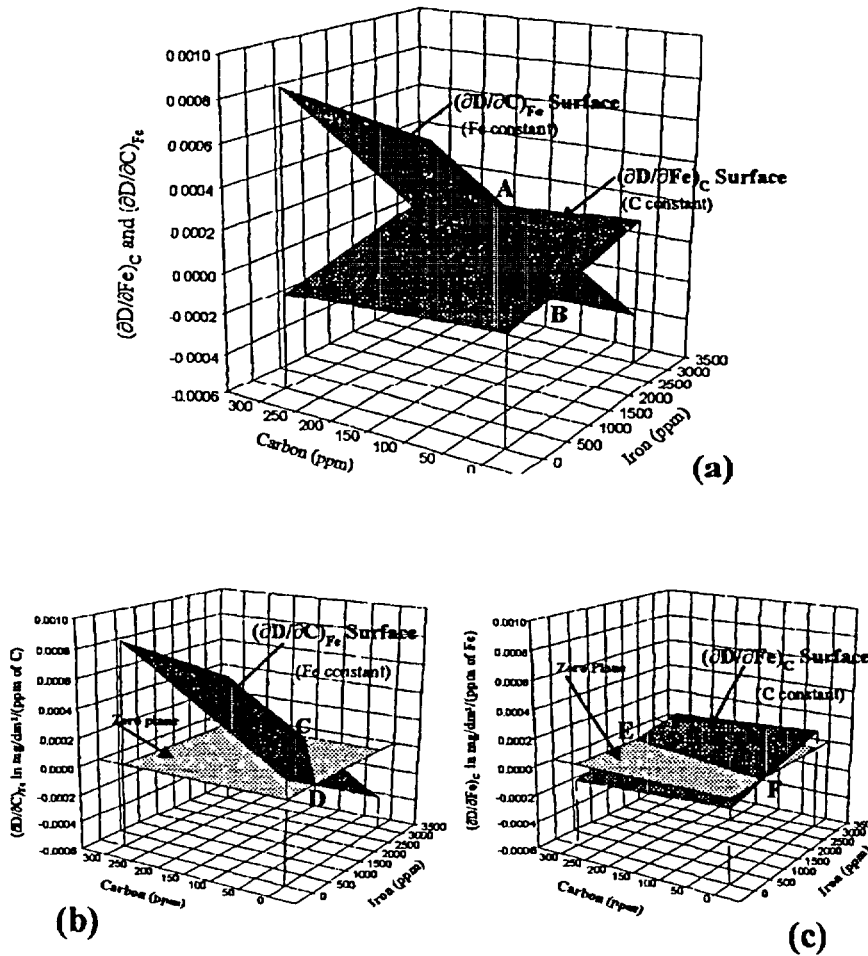


FIG 4—C and Fe partial differential surfaces taken from the quadratic equations describing deuterium pickup, plotted for the 208 day exposure of Zr-2.5Nb-Fe/C drop castings corroded at 325°C, in flux. (a) shows an upper and lower region where deuterium pickup can be most effectively modified by additions (or removal) of C or Fe respectively. In (a), the Fe and C partials have been plotted on the same axis, (b) and (c) show the lines produced by the partial differentials as they cross the zero change plane. Information via personal communication with G. A. McRae, Chalk River, ON, February 2001.

must be precisely determined and not left to the ingot analysis. Accurate C concentrations are notoriously difficult to obtain, however, as long as the same technique is used for all specimens, performed by the same operator, and on the same day the data should be internally consistent provided that any errors in the analysis technique are constant across the analyzed range. For example, an inherent variation of $\pm 5\%$ in the analysis for low C and $\pm 50\%$ for high C (or vice versa) would be unacceptable.

Conclusions

Corrosion scoping tests of laboratory produced Zr-2.5Nb ternary alloys using low concentrations of over 20 elements have suggested that the impact of an element may not be linear with concentration and that the effectiveness of the element may change with increasing exposure. Some elements have an accelerating effect on corrosion such as Al, Ti, Ni, Cu, and the noble elements. These should be minimized to ensure reduced oxidation and hydrogen pickup. Some elements, such as tin, tended to reduce oxidation but accelerate deuterium pickup.

Testing of Zr-2.5Nb/C drop castings revealed that C had little effect on oxidation but a dominant influence on hydrogen pickup. It was clear from these studies that the mechanisms of oxidation and hydrogen ingress were different. There were suggestions in the data of synergistic interactions between C and Fe.

An RSA was used to investigate oxidation and deuterium pickup in Zr-2.5Nb drop castings as a function of Fe and C additions, both in- and out-of-flux. Both the oxidation and deuterium pickup responses followed a quadratic dependence on the Fe and C concentrations. Out-of-flux oxidation of Zr-2.5Nb was found to be weakly influenced by the C concentration, but in-flux there was a strong dependence on C, primarily because of a synergistic interaction with Fe. Deuterium pickup was strongly dependent on C at low concentrations of Fe but less dependent on C at high values of Fe. The primary effect of radiation was to decrease the magnitude of the hydrogen pickup by almost a factor of three while the oxidation rate remained similar in- or out-of-flux. Again, the RSA clearly demonstrated that the mechanisms of oxidation and hydrogen pickup are different.

A second RSA was performed on Zr-2.5Nb micro-pressure tubes but expanding the number of alloying elements to four; Fe, C, Cr, and Si. Effects similar to those seen for the previously discussed Fe/C drop castings were observed. However, the tube microstructure appears to be important, particularly for oxidation. Cr had a small effect on oxidation and little or none on deuterium pickup. Si had no effect on oxidation and a small effect on hydrogen pickup.

Partial differentiation of the quadratic equations describing oxidation and hydrogen pickup was used to reveal the sensitivity of either of these phenomena to C and Fe. C was by far the most influential impurity in terms of hydrogen pickup. First derivative surfaces generated from the equations describing the corrosion response can be used to clarify many cases of what has been otherwise unknown reasons for specimen variability in corrosion tests. As well, regions of concentration can be defined that describe the most effective element to be used to modify the corrosion response.

Corrosion of Zr-2.5Nb can be adequately described by a quadratic dependence on the concentration levels of dominant impurities (such as C and Fe). The corrosion response to a specific impurity element can be confounded by synergistic interactions that suggest that a simple comparison of corrosion data between materials with uncontrolled impurity spectra will likely fail to reveal significant trends. For instance, C can increase or decrease corrosion depending on the Fe concentration.

Acknowledgments

Thanks and appreciation are extended to G. A. McRae for many useful discussions and for generating the data reproduced in Fig. 4. The suggestions of V. F. Urbanic are also appreciated.

References

- [1] Craig, M., Eucken, P. T., Finden, S. T.-P., and Weidinger, H. G., "Influence of Chemical Composition on Uniform Corrosion of Zirconium-base Alloys in Autoclave Tests," *Zirconium in the Nuclear Industry: Eighth International Symposium, ASTM STP 1023*, L. F. P. Van Swam and Craig M. Eucken, Eds., American Society for Testing and Materials, Philadelphia, 1988, pp. 113-127.
- [2] Graham, R. A., Tosdale, J. P., and Finden, P. T., "Influence of Chemical Composition and Manufacturing Variables on Autoclave Corrosion of Zircalloys," *Zirconium in the Nuclear Industry. Eighth International Symposium, ASTM STP 1023*, L. F. P. Van Swam and Craig M. Eucken, Eds., American Society for Testing and Materials, Philadelphia, 1988, pp. 334-345.
- [3] Graham, R. A. and Eucken, C. M., "Controlled Composition Zircaloy-2 Uniform Corrosion Resistance," *Zirconium in the Nuclear Industry: Ninth International Symposium, ASTM STP 1132*, C. M. Eucken and A. M. Garde, Eds., American Society for Testing and Materials, Philadelphia, 1991, pp. 279-301.
- [4] Harada, M., Kimpara, M., and Abe, K., "Effect of Alloying Elements on Uniform Corrosion Resistance of Zirconium-Based Alloys in 360°C Water and 400°C Steam," *Zirconium in the Nuclear Industry Ninth International Symposium, ASTM STP 1132*, C. M. Eucken and A. M. Garde, Eds., American Society for Testing and Materials, Philadelphia, 1991, pp. 368-390.
- [5] Peters, H. R. and Harlow, J. L., "The Effect of Trace Impurity Uranium on PWR Aqueous Corrosion of Zircaloy-4," *Zirconium in the Nuclear Industry: Eleventh International Symposium, ASTM STP 1132*, E. R. Bradley and G. P. Sabol, Eds., American Society for Testing and Materials, Philadelphia, 1996, pp. 295-316.
- [6] Cox, B., "Oxidation of Zirconium and Its Alloys," *Advances in Corrosion Science and Technology*, Vol. 5, M. G. Fontana and R. M. Staehle, Eds., Plenum Press, 1976, pp. 173-391.
- [7] Ploc, R. A., Amouzouvi, K. F., and Turner, C. W., "The Reduction of Corrosion and Deuterium Pickup in Zr-2.5Nb," *Microstructural Science*, Vol. 19, 1991, pp. 553-570.
- [8] Ploc, R. A., "The Influence of Impurities in Zr-2.5Nb on Oxygen and Deuterium Pickup at 573 K in D₂O," *Journal De Physique IV*, supplément au *Journal de Physique III*, Vol. 3, 1993, pp. 763-770.
- [9] Ploc, R. A., "Residual Carbon Impurities in Zr-2.5Nb and Their Effect on Deuterium Pickup," *Journal of Materials Science*, Vol. 279, 2000, pp. 344-350.
- [10] Ploc, R. A., "The Effect of Fe and C in Modifying Deuterium Pickup in Zr-2.5Nb: A Response Surface Analysis," Atomic Energy of Canada Report, AECL 12106, 2000 December.
- [11] ECHIP Incorporated, 724 Yorklyn Road, Hockessin, DE 19707-8733, U.S.A. Telephone (302) 239-5429.

DISCUSSION

A Strasser¹ (written discussion)—Please provide your opinion on the cause of the synergism between Fe and C and the reasons for the minima in oxidation and deuterium pickup at certain Fe-C composition combinations.

R. A. Ploc (author's response)—The simple answer to this question is that we don't know, although we would speculate along the following lines.

Fe and C are predominately in the β -phase, and in greater concentrations at the α/β boundaries. During corrosion, the oxide film develops channel porosity^{2,3} along some of the corroded α/β boundaries (from the free surface down to the oxide/metal interface) and, hence, the corrosion media can enter into the oxide film where it is in an environment rich in Fe, C, and Nb. C has a dominant, negative effect on pickup resistance, but Fe interacts with the C, thereby ameliorating its deleterious effect (hence, the negative FeC quadratic term in the Response Surface Analysis). At low Fe concentrations, pickup is almost totally dependent on the C concentration, since there is insufficient Fe to moderate its effect. At the other extreme, at high Fe concentrations, the FeC reaction is saturated and the excessive Fe determines the pickup resistance. This scenario leads to a steep dependence of pickup on C at low Fe concentrations, and a weak dependence at high concentrations.

Pickup for zero, or low C reveals the effect of Fe. Along the channel porosity, where Fe is concentrated, proton recombination is promoted, thereby forming molecular deuterium that selectively partitions to the water and, thereby, reducing the amount of deuterium absorbed by the alloy. As the Fe concentration increases, a second order effect begins to dominate. Fe is a β -stabilizer and causes α -grain refinement. An increase in the continuity of the β -phase along with grain refinement results in an increase in the amount of channel porosity. Therefore, on the high Fe side of the minimum, deuterium pickup begins to increase. The minimum, therefore, results from at least two competing mechanisms. The line describing the loci of minima is linear with increasing C, a result of the dominating effect of the C and the ameliorating role of the Fe (interaction of the C and Fe). The minima move to the high Fe side with increasing C, because increasing the Fe results in additional carbon being tied up and, hence, a decrease in absorption.

P. Barberis⁴ (written discussion)—You used Surface Response Analysis to model the global response to Fe and C. However, the range studied covers several domains of the phase diagram, and from a mechanistic point of view, I would not use RSA but rather variables linked to the phase diagram. Did you investigate the microstructure of the alloys, and particularly the presence of carbides and of Zr (Nb,Fe)₂ as a function of both C and Fe contents?

R. A. Ploc (author's response)—While it is true that the RSA assumes a continuous response, any significant perturbations from continuity would show up in the statistical measure of fit. In fact, the analysis would not produce a RS if there were a lack of fit, and the residuals would suggest that one had overlooked at least one important parameter (for instance, fabrication history). For the alloys and the fabrication history we used, the quadratic

¹ Aquarius Services Corp., U.S.A.

² Robert A. Ploc, "Mechanism of Deuterium Pickup in Zr-2.5Nb Alloy," *Materials at High Temperatures, Proceedings of the Fourth International Conference on the Microscopy of Oxidation*, Cambridge, U.K., September 1999, *Science Reviews*, 17 number 1/2 (2000) pp 29-34.

³ Robert A. Ploc and G. A. McRae, "Deuterium Absorption in CANDU Zr-2.5Nb Pressure Tubes," *Proceedings, 14th International Corrosion Congress*, September 2000, Cape Town, SA, paper #190.

⁴ CEZUS

fit was good. However, if the same alloys were given a different heat-treatment, it is possible that a different result might be obtained. The fabrication route for each alloy was constant but conceivably could be treated as a variable in a future analysis. Your desire to investigate the formation of precipitates as a function of C and Fe could then be met, however, there would be the practical problem of obtaining reproducible metallography and counting sufficient numbers of precipitates to provide meaningful statistics. Which technique(s) to use to reveal precipitate of different sizes would be an important and controversial decision.

In the Zr-2.5Nb system we know that precipitates can be found, but what is present in the alloy depends on the fabrication and processing history. In our case, we have yet to examine the specimens metallographically, but we know that most of the Fe and C are located in the β -phase. When the important quadratic terms in the equation of fit are examined, there is a suggestion that the Fe and C do interact (see response to question by Strasser and the ameliorating effect of Fe) and might be forming precipitates or some other complex.

A. Garde⁵ (written discussion)—Since in-reactor precipitation of β -Nb is one of the contributing factors for the improved corrosion resistance of Zr-2.5%Nb in CANDU reactors, could you comment on the impact of optimum combination of Fe, C concentrations on the β -Nb precipitation?

R. A. Ploc (author's response)—When you refer to corrosion resistance, you mean the rate of oxide film formation and not the deuterium ingress rate, which is the primary focus of this publication. The small precipitates which form in the α -Zr matrix, during the first two years of irradiation, are known to be β -Nb and responsible for a reduction in the oxidation rate (relative to other Zr alloys such as the Zircalloys). However, ingress and oxidation rates are often different, implying different mechanisms for each process. Table 2 also suggests a difference, i.e., the quadratic terms describing oxidation and ingress are different.

At this point, I doubt we have sufficient data to answer your question, however, the shape of the RSA curves may provide a clue. For instance, the out-of-flux oxidation rate is independent of the C concentration (see also Table 2) while in-flux, and at low Fe concentrations, the response surface shows a steep dependence on C. This suggests that irradiation-induced vacancies are important in the precipitation of β -Nb, i.e., apparently Fe ties up the vacancies reducing the likelihood of precipitation. As the Fe concentration increases (reducing the vacancy population), the oxidation rate begins to climb toward its out-of-flux value. One can conclude that C may also be performing a similar function, removing vacancies. As indicated in the response to one of the other questions, the out-of-flux Fe dependency may be related to grain refinement.

⁵ Westinghouse Electric Company

Glen M. McDougall¹ and Vincent F. Urbanic¹

The Influence of Material Variables on Corrosion and Deuterium Uptake of Zr-2.5Nb Alloy During Irradiation

REFERENCE: McDougall, G. M. and Urbanic, V. F., "The Influence of Material Variables on Corrosion and Deuterium Uptake of Zr-2.5Nb Alloy During Irradiation," *Zirconium in the Nuclear Industry: Thirteenth International Symposium, ASTM STP 1423*, G. D. Moan and P. Rudling, Eds., ASTM International, West Conshohocken, PA, 2002, pp 247-273

ABSTRACT: Current CANDU² reactors use Zr-2.5Nb pressure tubes that are extruded at 1088 K, cold-drawn 27%, and autoclaved at 673 K for 24 h. This results in a metastable, two-phase microstructure consisting of elongated α -Zr grains surrounded by a network of β -Zr filaments. To develop a mathematical model of corrosion and deuterium ingress in pressure tubes, we have considered the impact of variables including fast neutron flux, temperature, and the as-fabricated microstructure and its evolution during irradiation.

Small specimens of Zr-2.5Nb are being exposed under CANDU water chemistry conditions in the Halden Boiling Water Reactor³. The experiments involve fast neutron fluxes ($E \geq 1.05$ MeV) of 0, 1.7, and 4.5×10^{17} n · m⁻² · s⁻¹, and temperatures of 523 and 598 K. Specimens have been prepared from pressure tube materials representative of all current CANDU reactors, materials subject to thermal decomposition of the β -Zr phase, and tubes extruded over a range of conditions.

Results from the first three years of the Halden test program are summarized. At both 523 and 598 K, tubes made of β -quenched material exhibit lower oxidation rates than those made from non- β -quenched materials. In short-term out-of-flux exposures at 523 K, three non- β -quenched tubes appear to show linear oxidation kinetics. Similar behavior is not observed in tests conducted out-of-flux at 598 K, or in-flux at either temperature. At 598 K, β -quenched tubes exhibit significantly lower deuterium pickup rates than non- β -quenched tubes. When tested at 598 K, thermally aged specimens show declining oxidation and deuterium pickup rates with increasing β -Zr phase decomposition. At 523 K, the impact of thermal aging was less significant. Preliminary results from an "extrusion variable test" suggest that tubes fabricated according to the current CANDU specification show the best corrosion resistance.

KEYWORDS: corrosion, deuterium pickup, irradiation, temperature, Zr-2.5Nb, microstructure, β quenching, extrusion billet, soak time

In CANDU reactors, lithiated heavy water (D₂O) coolant reacts with the inside surfaces of Zr-2.5Nb pressure tubes to form a zirconium oxide (ZrO₂) film and deuterium. A fraction of the deuterium generated by the corrosion reaction finds its way into the pressure tube. Among the key variables influencing the corrosion and deuterium uptake of pressure tubes are fast neutron flux, temperature, and alloy microstructure [1,2]. Two aspects of tube mi-

¹ Scientist and branch manager, respectively, AECL—Chalk River Laboratories, Chalk River, Ontario K0J 1J0, Canada

² CANDU = CANada Deuterium Uranium. Registered trademark of Atomic Energy of Canada, Ltd.

³ Institutt for energiteknikk—OECD Halden Reactor Project, Halden, Norway

microstructure are important the as-fabricated microstructure and texture, and the evolution of microstructure under irradiation.

The fabrication route for modern CANDU pressure tubes has been detailed in an earlier paper [3]. After forging and machining, logs (or sometimes hollow billets) are "β quenched," i.e., heated into the β-phase region (1290 K), then quenched in water. This serves to homogenize the billet and refine the α-Zr grain structure. Prior to extrusion, the billet is preheated (or "soaked") at 1088 K, in the (α+β)-phase region. The tubes are then hot extruded at 1088 K and cold-drawn about 27% to achieve the final tube dimensions. At this point, the alloy has a two-phase microstructure (Fig. 1), consisting of elongated α-Zr grains surrounded by a network of metastable β-Zr. The α-phase grains are platelets with an aspect ratio of about 1:10-40 in the radial, transverse, and longitudinal directions, respectively. They contain approximately 0.6 to 1 wt% Nb in solution. The non-equilibrium β-phase separating the α-grains contains approximately 20 wt% Nb. As a final fabrication step, the pressure tubes are autoclaved for 24 h in 673 K light water steam. This promotes a partial decomposition of the β-phase, precipitating tiny particles of Nb-depleted ω-Zr in a matrix of Nb-enriched β-Zr (up to about 50 wt%).

During irradiation, three microstructural changes occur in CANDU pressure tubes that have an impact on corrosion and deuterium uptake: increased dislocation density in the α-Zr grains due to dislocation loop formation; a reduction in Nb in the supersaturated α-phase

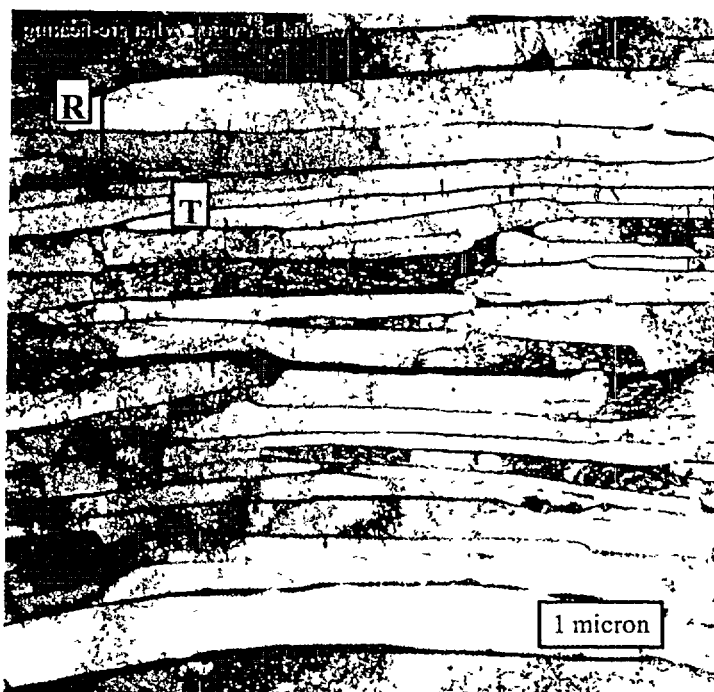


FIG 1—Typical grain structure of Zr-2.5Nb pressure tube looking down the axis of the tube. The light-colored α-Zr phase platelets are interspersed with dark-colored β-phase filaments. From Ref 2

due to irradiation-induced precipitation of β -Nb; and thermally induced decomposition of the β -Zr phase [2]. As the latter phenomenon proceeds, the volume fraction of β -phase decreases, with a corresponding increase in Nb concentration. Examination of removed pressure tube materials has demonstrated that the extent of β -phase decomposition is a function both of neutron flux and temperature. Given the flux/temperature profile for a CANDU fuel channel, β -phase decomposition is thought to have only a small impact on the corrosion and deuterium uptake of pressure tubes relative to α -phase effects. However, additional data are required from well-characterized materials irradiated under carefully controlled conditions.

The α/β -phase microstructure and texture of α -Zr grains in pressure tubes is largely determined by the hot extrusion process [4,5]. To minimize material variability and optimize the mechanical properties of Zr-2.5Nb pressure tubes, previous tests [3,6] have examined modifications to the billet pre-heating practice (15 min at 1088 K) currently used to produce CANDU pressure tubes. Varying the soak temperature over the range 1053 to 1123 K resulted in substantial differences in the tensile strength, ductility, and fracture toughness of finished tubes [3]. This was attributed to changes in the size and distribution of α -grains, and the degree of oxygen segregation into primary α -grains. Figures 2a and 2b are SEM micrographs of tubes extruded after extremes of pre-heat temperature and time, the figures depict a longitudinal-radial section through the respective tubes. Figure 2a (1053 K, 15 min) shows a uniform structure of fine, elongated α -grains (dark phase) with thin filaments of β -Zr at grain boundaries; in contrast, Fig. 2b (1123 K, 300 min) shows coarse, elongated primary α -grains (dark phase) separated by a Widmanstätten α -plate structure. On the basis of these tests, a reduction in extrusion temperature to 1053 K was advocated. However, the impact of changes in extrusion variables on subsequent corrosion and deuterium uptake must be considered.

To advance the development of a predictive model for corrosion and deuterium uptake in pressure tubes (both current and prototype designs), the impact of flux, temperature, and alloy microstructure must be evaluated. In an earlier paper [7], we summarized the neutron flux and temperature dependence of corrosion and uptake for pressure tube materials after 185 days exposure in a heavy water loop of the Halden Boiling Water Reactor. The current paper extends these results to a cumulative exposure of 553 days. As well, preliminary results are presented concerning the influence of β -Zr decomposition and extrusion-billet pre-heating on corrosion and deuterium uptake.

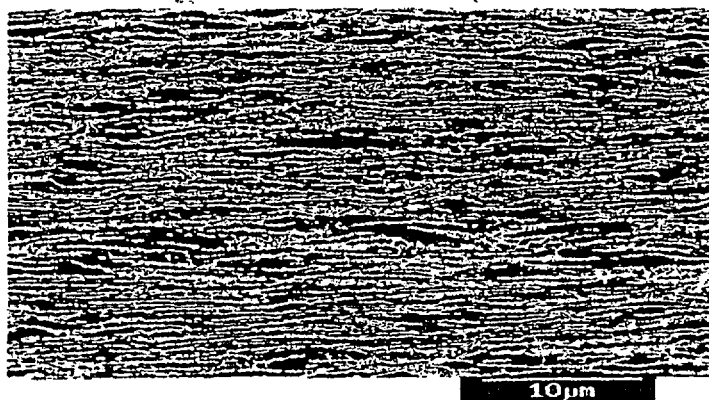


FIG 2a—Pressure tube microstructure as-extruded following a 15-min soak at 1053 K. From Ref. 3.

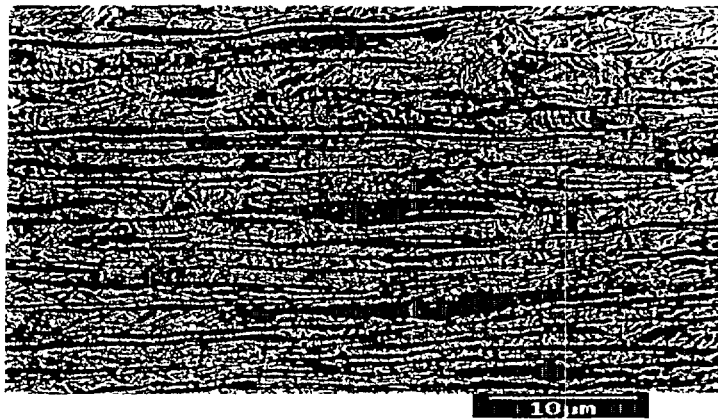


FIG 2b—Pressure tube microstructure as-extruded following a 300-min soak at 1123 K From Ref 3.

Experimental Procedure

Specimens were prepared to evaluate the dependence of corrosion and deuterium ingress on key variables:

- fast neutron flux and temperature,
- β quenching versus non- β quenching;
- thermal decomposition of the β -Zr phase; and,
- billet pre-heat time and temperature

All tests were performed with small specimens (30 by 10 by 1 mm) of Zr-2.5Nb pressure tube material. Table 1 summarizes the fabrication data for the tubes and Table 2 the ingot composition specifications.

Specimens for the flux-temperature test were prepared from tubes representative of all operating CANDU reactors. Some specimens were tested in the pickled condition; the balance was pre-oxidized for 24 h in 673 K light water steam. The material condition was that produced by the pressure tube fabrication process. Specimens for the thermal decomposition test were prepared as part of an earlier test program [2]. To bracket the extent of β -phase decomposition in as-fabricated CANDU pressure tubes (β -phase partially transformed during autoclaving), specimens were prepared from tube H026M, which had not been autoclaved. In this way, as-machined specimens could be used as controls. The remaining specimens were heated for 100 h at 673 to 723 K to induce varying levels of β -phase decomposition. Table 3 summarizes the thermal-aging treatments. Representative samples were analyzed by X-ray diffraction [7] to determine the Nb concentration in the β -phase. This result can be used as a measure of the degree of β -phase decomposition, the final (equilibrium) state is a matrix of α -Zr containing β -Nb precipitates (approximately 90 wt% Nb). All specimens were pickled prior to testing. For the extrusion variable test, specimens were machined from half-length pressure tubes extruded using a variety of billet pre-heat treatments [3]. Table 4

TABLE 1—Summary of fabrication data for Zr-2.5Nb pressure tubes.

Test Program	Tube Number	Alloy	Ingot Fabrication	
			Heat No	Beta Quenched
Flux-temperature	669	Zr-2.5Nb	377461	no
Flux-temperature	B1913	Zr-2.5Nb	390492R	no
Flux-temperature	B439	Zr-2.5Nb	396331	no
Flux-temperature	W061	Zr-2.5Nb	230871Q	yes
Flux-temperature	RX095	Zr-2.5Nb	233626Q	yes
Flux-temperature	Y321	Zr-2.5Nb	228391Q	yes
β -Zr decomposition	H026M	Zr-2.5Nb	210204Q	yes
Extrusion variable	RX080	Zr-2.5Nb	233074Q	yes
Extrusion variable	RX082	Zr-2.5Nb	233074Q	yes
Extrusion variable	RX083	Zr-2.5Nb	233074Q	yes
Extrusion variable	RX085	Zr-2.5Nb	233074Q	yes
Extrusion variable	RX086	Zr-2.5Nb	233074Q	yes
Extrusion variable	RX088	Zr-2.5Nb	233074Q	yes

summarizes the pre-heating temperatures (essentially the starting extrusion temperature⁴) and soak times employed. To ensure that the starting billet material for each tube had the same metallurgical history (including β quenching), all billets were taken from a single forged log. Following hot extrusion, the cold working and autoclaving of the tubes proceeded according to the standard fabrication practice.

All tests were performed in Loop 9 of the Halden reactor. The loop consists of parallel zirconium alloy in-flux assemblies (IFAs) connected to a stainless steel out-of-core loop system. The tests reported here were performed in two IFAs: one operated at a low neutron flux (peak = $1.7 \times 10^{17} \text{ n} \cdot \text{m}^{-2} \cdot \text{s}^{-1}$, $E \geq 1.05 \text{ MeV}$), the other at a higher flux (peak = $4.5 \times 10^{17} \text{ n} \cdot \text{m}^{-2} \cdot \text{s}^{-1}$, $E \geq 1.05 \text{ MeV}$). Inside each IFA, a cluster of fuel rods is arranged around a pair of vertical test channels operated at 523 and 598 K, respectively. The flow rate along each test channel results in an in-pile coolant residence time comparable to a CANDU fuel channel. To eliminate boiling along the high-temperature channels, coolant pressure is maintained at 15.5 MPa. In addition to the in-flux assemblies, loop coolant is also supplied to two out-of-flux autoclaves operated at 523 and 598 K.

In both the in- and out-of-flux test channels, specimens are arranged in groups on a holder extending the length of the channel. Each group consists of a stack of specimens separated by thin spacers; the stack is secured by a spring clip. All components in contact with the specimens (the holder, spacers, and spring clips) are of Zircaloy-4; the holder design carefully avoids creating narrow crevices with any specimens. In both the high- and low-flux IFAs, specimens are divided into two sets according to the relative flux to which they are exposed. "Constant flux" specimens experience a fast neutron flux from 85 to 100% of the peak value for that IFA; in contrast, "flux gradient" specimens experience values ranging from 10 to 50% of the peak flux. All data reported in this paper are from "constant flux" specimens.

⁴ At the end of the soak period, billets are transferred from the furnace to the extrusion press in less than a minute. As a result, a negligible temperature drop is expected before extrusion begins.

TABLE 2—Chemical analyses for Zr-2.5Nb ingots* used to prepare pressure tubes.

Pressure Tube No	669	B1913	B439	W061	RX095	Y321	H026M	RX080- RX088
TWCA Heat No	377461	390492R	396331	230871Q	233626Q	228391Q	210204Q	233074Q
Alloying								
Element	weight %							
Nb	2.7	2.7	2.6	2.6	2.6	2.6	2.5	2.6
O	0.12	0.12	0.11	0.11	0.11	0.11	0.11	0.12
Zr	balance	balance	balance	balance	balance	balance	balance	balance
Impurity								
Element	mg/kg							
Al	45	65	55	43	34	39	49	39
B	0.2	< 0.25	< 0.25	< 0.2	< 0.2	< 0.2	< 0.25	< 0.25
C	179	120	118	78	101	113	143	114
Cd	< 0.3	< 0.25	< 0.25	< 0.2	< 0.2	< 0.2	< 0.25	< 0.25
Cl	< 15							< 5
Co	< 5	< 10	< 10	< 10	< 10	< 10	< 10	< 10
Cr	133	82	< 80	< 100	< 100	< 100	< 80	< 100
Cu	28	< 25	< 25	< 25	< 25	< 25	< 25	< 25
Fe	1142	705	622	415	390	475	660	500
H	5	6	15	< 5	< 3	< 5	< 5	< 5
Hf	69	< 50	< 40	37	39	43	< 40	38
Mg	< 10	< 10	< 20	< 10		< 10	< 10	< 10
Mn	< 10	< 25	< 25	< 25	< 25	< 25	< 25	< 25
Mo	10	< 25	< 25	< 25	< 25	< 25	< 25	< 25
N	38	44	26	21	28	23	34	28
Ni	17	< 35	< 35	< 35	< 35	< 35	< 35	< 35
P				5	8			6
Pb	< 5	< 50	< 50	< 25	< 25	< 25	< 25	< 25
Si	72	87	62	27	25	29	< 60	27
Sn	23	< 25	50	< 25	< 25	< 25	< 25	< 25
Ta	< 200	< 200	< 200	< 100	< 100	48	< 200	< 100
Ti	< 50	< 25	25	31	< 25	< 25	< 25	
U	0.6	0.8	0.7	< 1	< 1	< 1	1.1	1.1
V	< 5	< 25	< 25	< 25	< 25	< 25	< 25	< 25
W	< 25	< 25	< 25	< 25	< 25	< 25	< 25	< 25

* Concentrations are ingot averages except for bold values, which are from samples of representative test specimens. Where no value is shown, the concentration was not reported.

TABLE 3—Zr-2 5Nb specimens prepared for thermal decomposition test

Pressure Tube	Treatment	Nb Concentration in β -Zr Phase, wt% [2]	Comment
H026M	Extruded + cold-worked	27	As-received material (no stress relief)
H026M	Extruded + 673 K/100 h	68	
H026M	Extruded + 723 K/100 h	85	

While the loop is designed to accommodate a wide range of water chemistries, the Halden tests are being performed under conditions typical of a CANDU reactor. A pH of 10.2 to 10.8⁵ is maintained by lithium additions (ion exchange resin in the deuteroxide form). The same water chemistry conditions are provided at the inlets to all test channels. Both inlet and outlet coolant streams from each channel are routinely analyzed, both by continuous on-line instrumentation and by periodic grab sampling. Dissolved deuterium and oxygen concentrations are monitored using on-line Orbisphere gas analyzers and maintained at 5 to 7 $\text{cm}^3 \cdot \text{kg}^{-1}$ and $<5 \mu\text{g} \cdot \text{kg}^{-1}$, respectively.

At the conclusion of each Halden reactor period (nominally 185 days), all specimens are ultrasonically cleaned and weighed. Selected specimens are removed for destructive examination; all data presented in this paper were obtained from these specimens. To date, examinations have been completed on specimens removed after the following exposure times: 553 days for the flux-temperature test; 200 days for the β -Zr decomposition test; and 195 days for the extrusion variable test.

Prior to post-irradiation examination, specimens were deoxidized in 50% (vol/vol) hydrochloric acid (HCl) at 333 K for 4 h. Oxide thickness was determined using weight gain measurements to the nearest 0.01 mg (all corrosion rates reported in this paper were calculated on this basis). To verify that these values were representative of the average thickness over the surface of each specimen, all were examined using Fourier transform infrared reflectance (FTIR) spectroscopy [8]. A mean oxide thickness for each specimen was calculated as the average of four measurements (two on each major surface). In the majority of cases,

TABLE 4—Billet pre-heat temperature and soak times used to fabricate Zr-2 5Nb tubes for "extrusion variable" test

Tube Number	Pre-Heat Temperature, K	Soak Time, min	Comment
RX080	1053	15	
RX082	1053	300	
RX083	1088	15	CANDU specification
RX085	1088	300	
RX086	1123	15	
RX088	1123	300	

⁵Hydrogen ion activities are reported as pH_{RT} , the apparent room temperature value, i.e., the value measured in a heavy water solution using a pH electrode calibrated in light water buffers at the same temperature.

oxide thickness results based on FTIR were within $\pm 10\%$ of the values based on O weight gains. Visual examination of the remaining coupons showed no indication of nodular corrosion or spalling. Both hydrogen and deuterium concentrations were determined by hot vacuum extraction mass spectrometry. With respect to the deuterium results reported in this paper, the measurement method is accurate to within 5% and has a precision (at 2σ) of $\pm 5\%$. The pickup rates calculated from these measurements have an uncertainty of $\pm 5\%$.

Results and Discussion

Effect of β Quenching

Of the Zr-2.5Nb pressure tubes used to prepare specimens for the flux-temperature test, three were made from billets water-quenched from the β -phase field prior to extrusion; this process is often referred to as " β quenching". For comparison, specimens were also prepared from three tubes of material which was β solution annealed at the same temperature, but subsequently air-cooled rather than quenched; billets treated in this manner are referred to as "non- β -quenched". While earlier CANDU reactors (for example Pickering A NGS) utilized tubes made of non- β -quenched material, newer units (for example, Wolsong 1) use exclusively tubes made from β -quenched material.

Figures 3, 4, and 5 depict oxidation kinetics for prefilmed specimens exposed for 553 days under three flux regimes. Each data point represents a single specimen. Figure 3 summarizes data for out-of-flux exposures in flow-through autoclaves. The results in Figs. 4 and 5 are for specimens exposed to fast neutron flux as follows: "low flux" = $1.25 - 2.06 \times 10^{17} \text{ n} \cdot \text{m}^{-2} \cdot \text{s}^{-1}$; and "high flux" = $3.96 - 4.88 \times 10^{17} \text{ n} \cdot \text{m}^{-2} \cdot \text{s}^{-1}$ (c.f., peak flux in a CANDU 6 fuel channel = $3.5 \times 10^{17} \text{ n} \cdot \text{m}^{-2} \cdot \text{s}^{-1}$). At both 523 and 598 K, specimens made from non- β -quenched materials oxidize faster than corresponding specimens made from β -quenched materials. At 523 K, out-of-flux β -quenched specimens and all in-flux coupons show a declining oxidation rate with time, with non- β -quenched materials developing a marginally thicker oxide after 553 days. However, after 295 days, out-of-flux specimens of non- β -quenched material oxidize at a constant rate; extrapolation to 553 days (fine dashed line) suggests a rate similar to that assumed by the same materials after 185 days exposure at 598 K. In contrast, at 598 K the separation in oxidation rate between β and non- β -quenched materials is most apparent under irradiation. In fact, after 553 days, it is evident that the difference in rates is greatest under high flux conditions.

Figures 6, 7, and 8 summarize the corresponding D pickup data for the same specimens. Each data point represents the average of two analyses of a single specimen. The figures illustrate several interesting points. First, in almost all cases, deuterium uptake is slightly higher for in-flux specimens compared to their out-of-flux counterparts. The only exception is specimens of non- β -quenched material tested at 598 K; out-flux and under low flux pickup rates for these specimens are comparable. However, higher rates are observed during exposures at high flux. Second, at 598 K and over the complete flux range studied, specimens of β -quenched material showed significantly lower D pick-up rates than non- β -quenched specimens tested under the corresponding flux. In contrast, at 523 K, pickup rates for the two sets of specimens were indistinguishable except under low flux conditions, where specimens of β -quenched material showed slightly better performance. With only three exceptions, specimens tested at 523 K exhibited low pickup rates that declined with time. However, Figs. 6 and 7 reveal an abrupt increase in D pickup for three specimens exposed for 553 days (data points indicated with arrows). The specimens are from two tubes (W061, made from β -quenched material, and 669, of non- β -quenched material). In terms of oxidation, no significant difference was observed between these specimens and identically prepared spec-

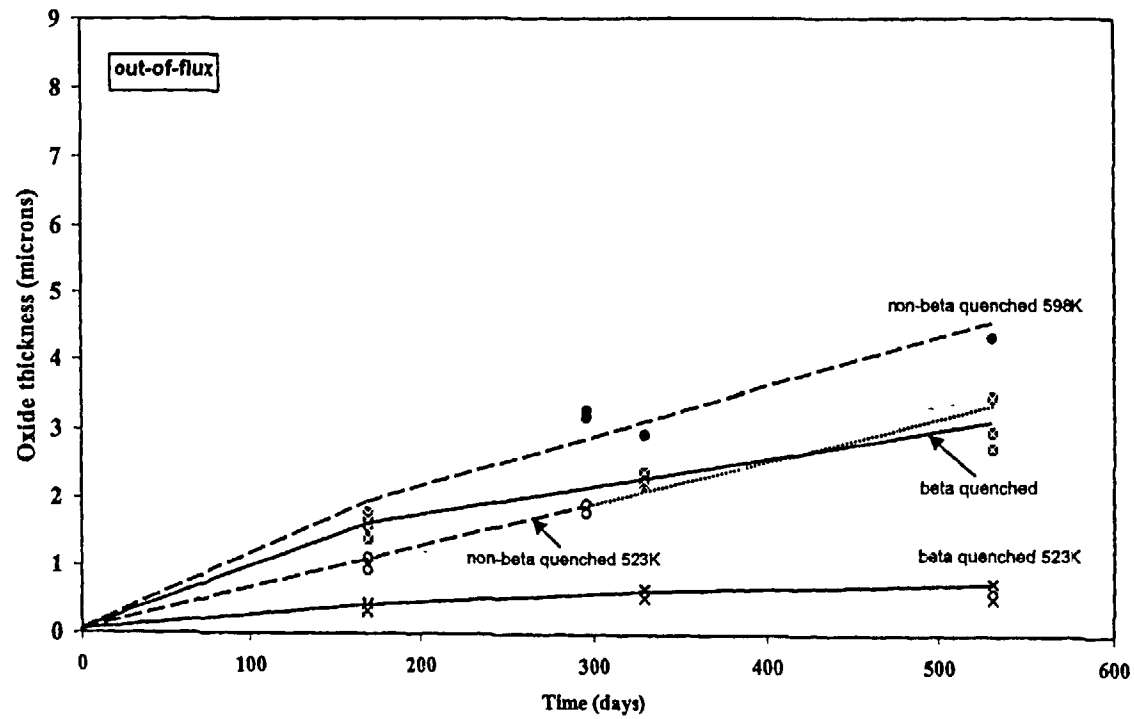


FIG 3—Oxidation of prefilmed Zr-2.5Nb pressure tube specimens in 523 and 598 K heavy water in Halden. Specimens exposed in flow-through, out-of-flux autoclave.

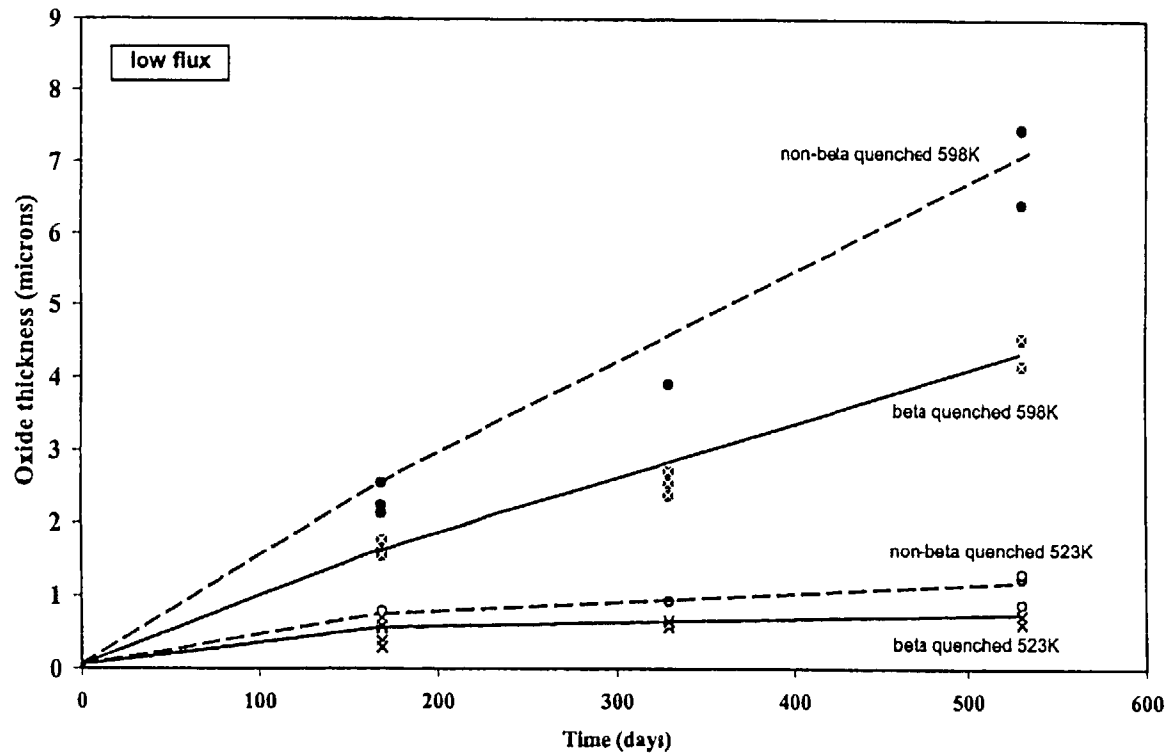


FIG 4—Oxidation of prefilmed Zr-2.5Nb pressure tube specimens in 523 and 598 K heavy water in Haloen. Specimens exposed under "low" flux, $1.25 - 2.08 \times 10^{17} \text{ n m}^{-2} \cdot \text{s}^{-1}$

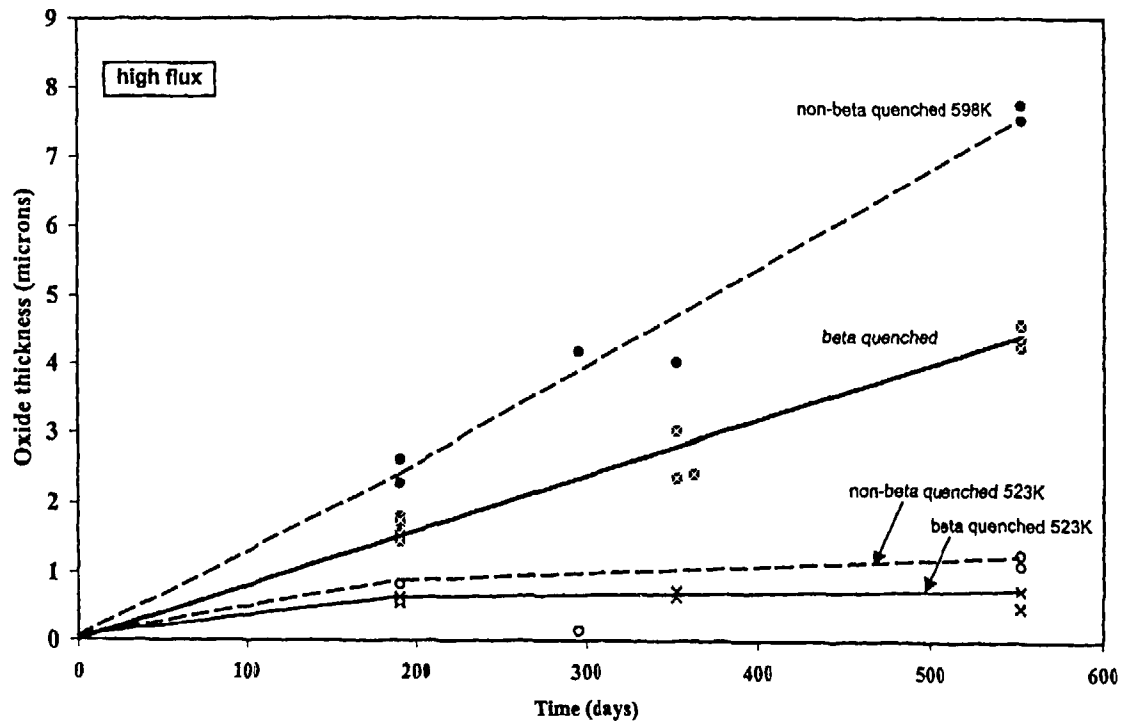


FIG. 5—Oxidation of prefined Zr-2.5Nb pressure tube specimens in 523 and 598 K heavy water in Halden. Specimens exposed under "high" flux $3.81 - 4.88 \times 10^{17} \text{ n} \cdot \text{m}^{-2} \cdot \text{s}^{-1}$.

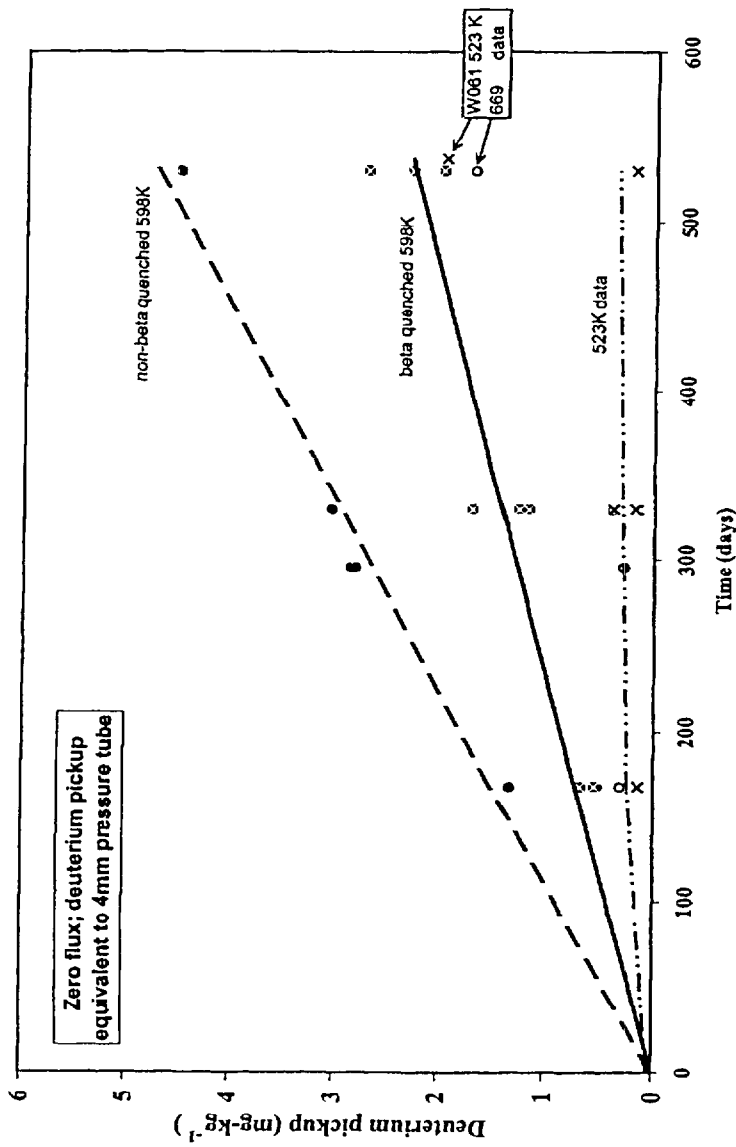


FIG 6—Deuterium pickup of prefilmed Zr-2.5Nb pressure tube specimens in 523 and 598 K heavy water in Halden. Specimens exposed out-of-flux, pickup expressed in terms of equivalent value for 4-mm thickness pressure tube corroded on one side

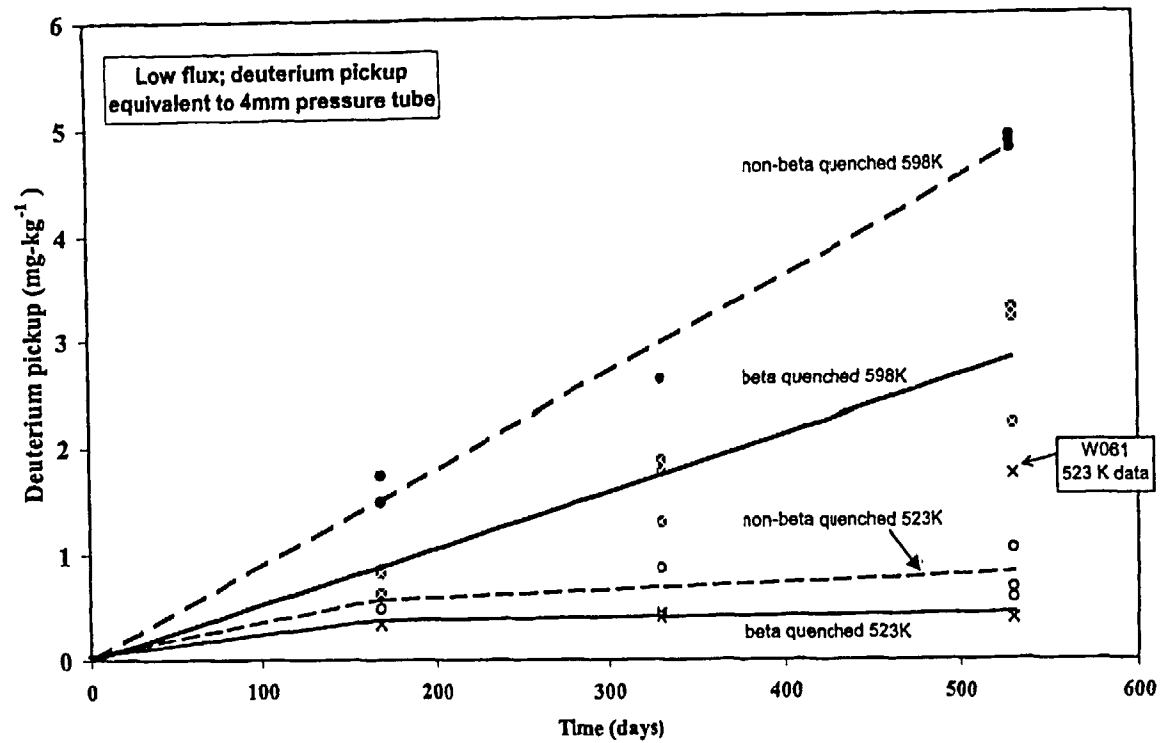


FIG 7—Deuterium pickup of prefilled Zr-2.5Nb pressure tube specimens in 523 and 598 K heavy water in Halden. Specimens exposed under "low" flux: $1.25 - 2.08 \times 10^{17} \text{ n} \cdot \text{m}^{-2} \cdot \text{s}^{-1}$. Pickup expressed in terms of equivalent value for 4-mm thickness pressure tube corroded on one side

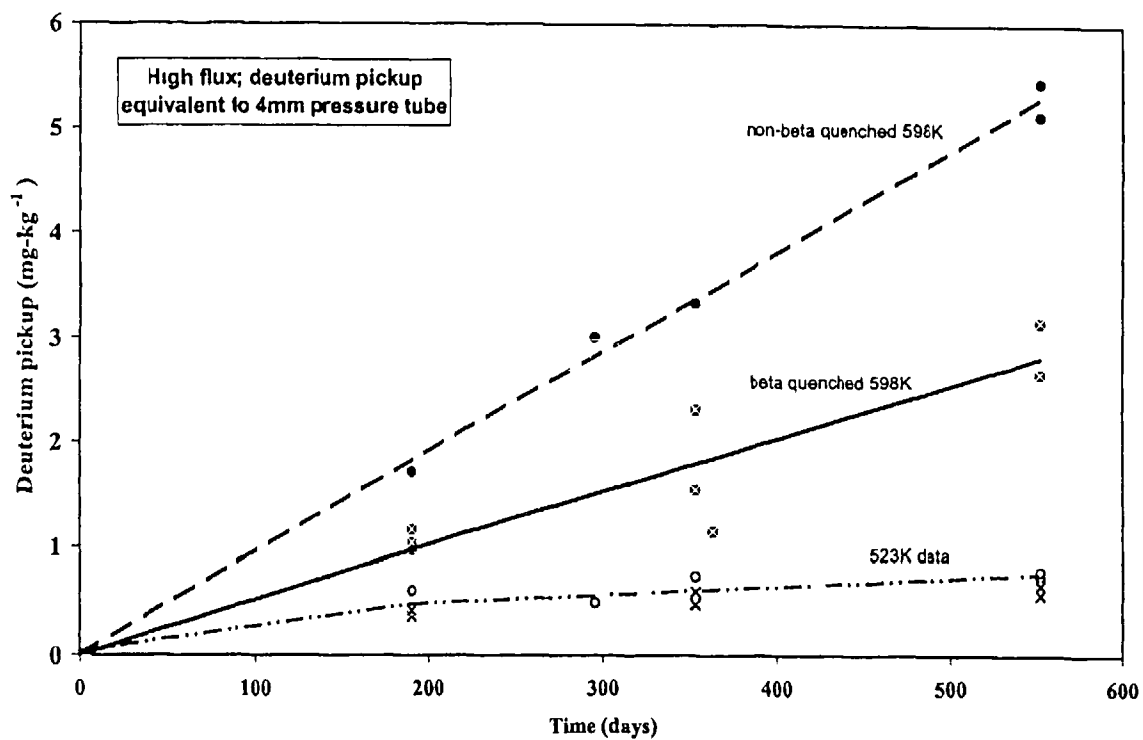


FIG 8—Deuterium pickup of prefilmed Zr-2.5Nb pressure tube specimens in 523 and 598 K heavy water in Halden. Specimens exposed under "high" flux, $3.81 - 4.88 \times 10^{17} \text{ n} \cdot \text{m}^{-2} \cdot \text{s}^{-1}$. Pickup expressed in terms of equivalent value for 4-mm thickness pressure tube corroded on one side.

imens tested under the same conditions. Additional data will be required to establish whether these tubes are in fact exhibiting a sudden change in pickup kinetics after approximately one hot year at 523 K.

Effect of Thermal Decomposition of the β -Zr Phase

Figures 9 and 10 summarize oxidation rates for pickled specimens from tube H026M as a function of the Nb content in the β -Zr phase of the as-prepared coupons. The Nb concentration can be used as a measure of the degree of β -phase decomposition; an increase occurs as decomposition progresses [7]. These preliminary data were collected after 200 days of a multi-year test. Each point represents the oxidation rate for a single specimen, normalized to the rate for an out-of-flux control (no β -phase decomposition). The absolute rates for as-received specimens exposed out-of-flux is reported in terms of oxide growth per year. Both figures show in-flux data obtained under two flux regimes: "low flux" = $1.43 - 1.47 \times 10^{17} \text{ n} \cdot \text{m}^{-2} \cdot \text{s}^{-1}$; and "high flux" = $3.45 - 3.52 \times 10^{17} \text{ n} \cdot \text{m}^{-2} \cdot \text{s}^{-1}$. For comparison, a vertical bar represents the range of β phase Nb concentrations measured in off cuts from a number of pressure tubes that were autoclaved during fabrication [7].

At 523 K, out-of-flux specimens show a dramatic decrease in oxidation rate with increasing decomposition of the β -phase. However, as-received materials (initially, 27% Nb in β -phase) irradiated at low or high flux exhibit essentially the same oxidation rate as thermally treated coupons exposed under the respective in-flux conditions or out-of-flux. Owing to the short duration of the test, the low oxidation rate of the as-received specimens cannot be attributed to increased β -phase decomposition. Over 200 days, low- and high-flux specimens would have experienced a fast fluence of 2.0 and $5.7 \times 10^{24} \text{ n} \cdot \text{m}^{-2}$, respectively. Measurements of pressure tube materials irradiated under comparable conditions of temperature and fluence [2] suggest that as-received specimens exposed under low and high flux would contain about 32 and 30% Nb in the β -phase, respectively. Clearly, such a small change in β -phase decomposition (Nb concentration increasing from 27 to 30 to 32%) cannot explain the observation of oxidation rates comparable to specimens with initial β -phase Nb levels of 68 and 85%. A more likely explanation would be the precipitation of β -Nb in the α -grains of the as-received specimens, which has been associated with a reduction in oxidation rate [2]. At 573 K, 2 to 5 nm Nb-rich precipitates are visible after a fluence of $1 \times 10^{24} \text{ n} \cdot \text{m}^{-2}$; while fewer precipitates are observed at 523 K for a comparable fluence [9], the density in the present samples may be sufficient to confer improved corrosion resistance. While all in-flux specimens would be expected to develop a similar density of β -Nb precipitates (and presumably experience a proportionate decrease in corrosion rate), it is possible that the behavior of the thermally treated specimens (i.e., initial β -phase Nb levels of 68 and 85%) is dominated by the high degree of β -phase decomposition.

At 598 K, out-of-flux specimens showed a steady decrease in oxidation rate with increasing β -phase decomposition. Under low and high flux conditions, while as-received specimens exhibited an enhanced oxidation rate, the remaining specimens showed a declining rate with increasing β -phase decomposition. Considering material with an initial β -phase Nb concentration of 85%, the out-of-flux specimen exhibited the lowest oxidation rate, with both in-flux specimens showing a higher rate. This is in contrast to the 523 K test, where oxidation rates for specimens thermally decomposed to the same extent approached a single value, irrespective of flux.

Figures 11 and 12 show the corresponding D pickup data. Each point represents the average of two analyses of a single specimen. The pickup rates are normalized as in the previous figures; the absolute rates for as-received specimens exposed out-of-flux is reported in terms of an "equivalent pressure tube" value, taking into account the surface area-to-mass

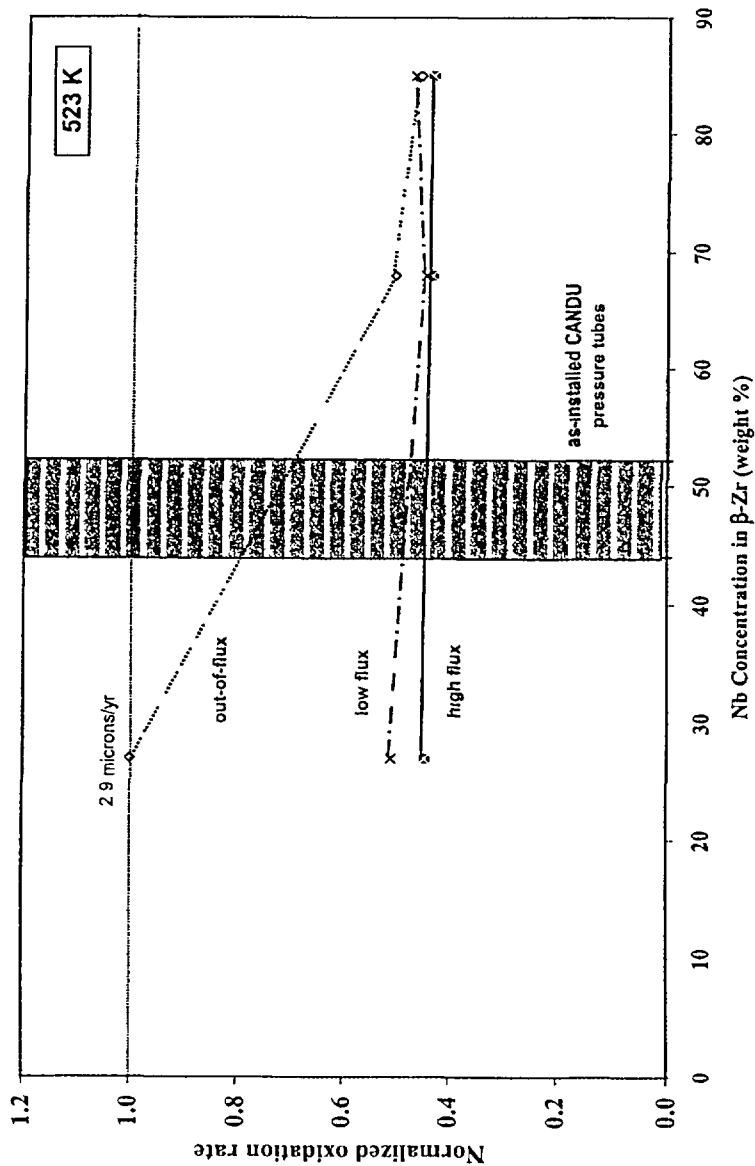


FIG 9—Oxidation of pickled Zr-2.5Nb pressure tube specimens in 523 K heavy water in Halden. Specimens thermally aged to induce varying Nb concentrations in β -Zr phase, then tested under the stated flux regime for 200 days. Oxidation data normalized to rate for as-received specimen exposed out-of-flux (2.9 $\mu\text{m}/\text{year}$)

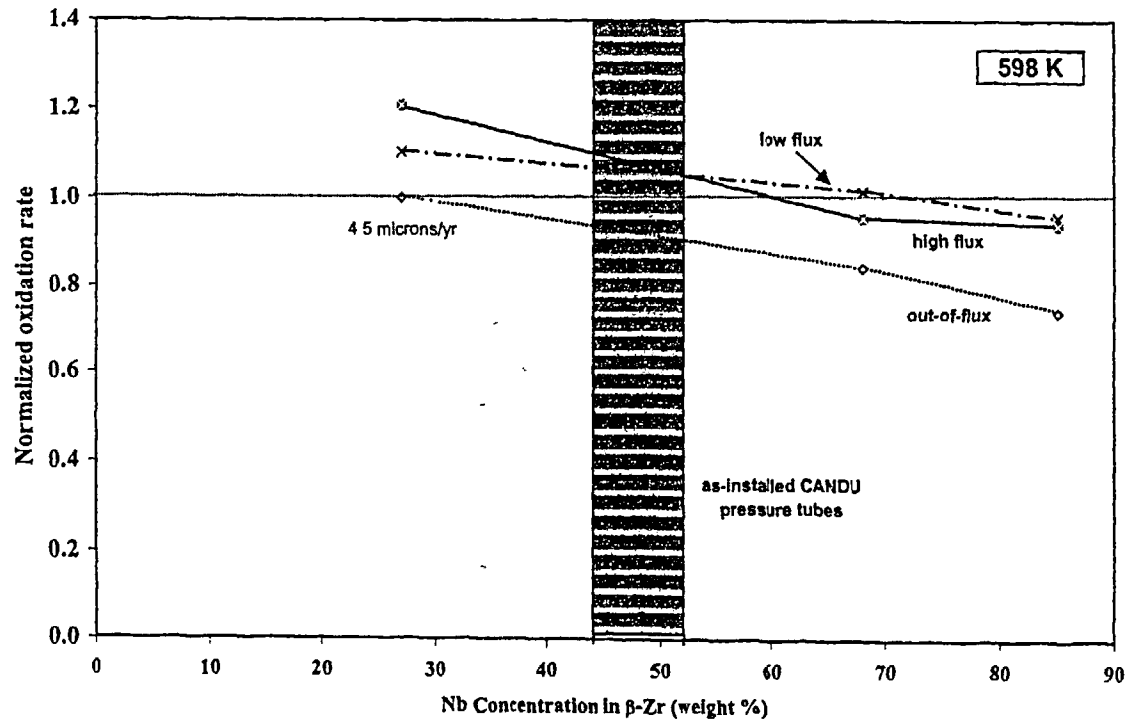


FIG 1C—Oxidation of pickled Zr-2.5Nb pressure tube specimens in 558 K heavy water in Halden. Specimens thermally aged to induce varying Nb concentrations in β -Zr phase, then tested under the stated flux regime for 200 days; Oxidation data normalized to rate for as-received specimen exposed out-of-flux (4.5 $\mu\text{m}/\text{year}$).

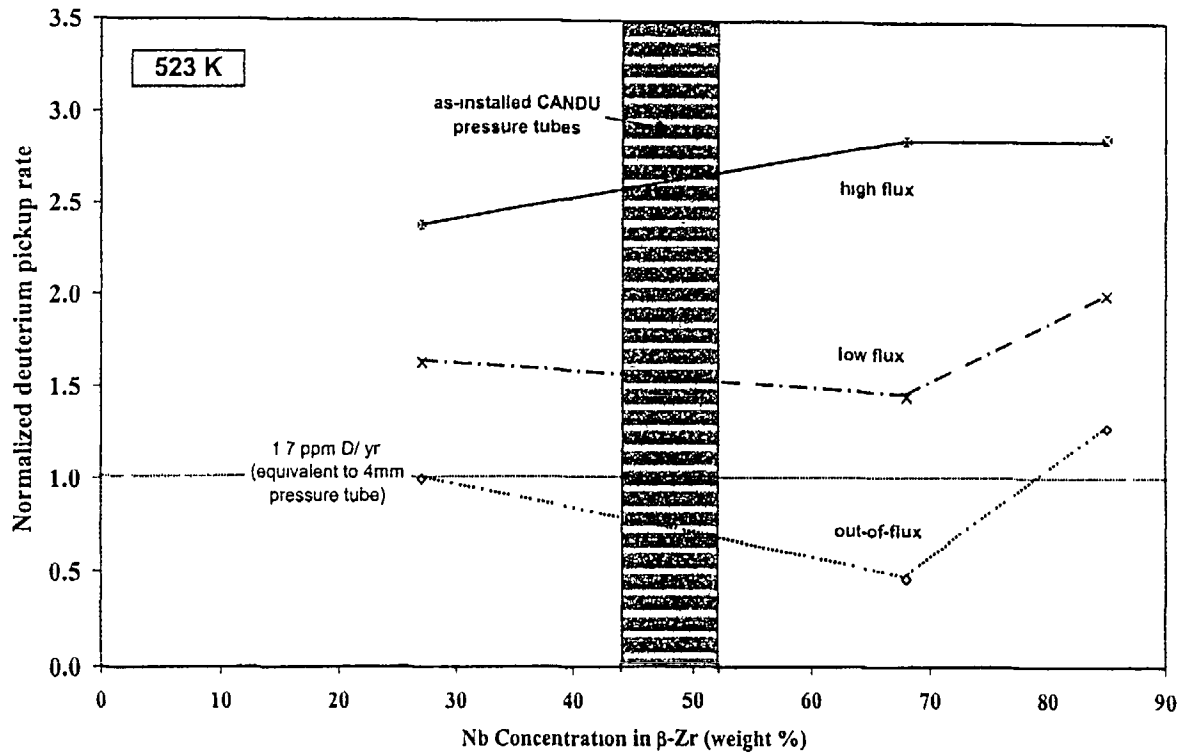


FIG 11—Deuterium pickup of pickled Zr-2.5Nb pressure tube specimens in 523 K heavy water in Halden. Specimens thermally aged to induce varying Nb concentrations in β -Zr phase then tested under the stated flux regime for 200 days. Pick-up data normalized to rate for as-received specimen exposed out-of-flux (1.7 ppm/year, equivalent rate for 4-mm pressure tube).

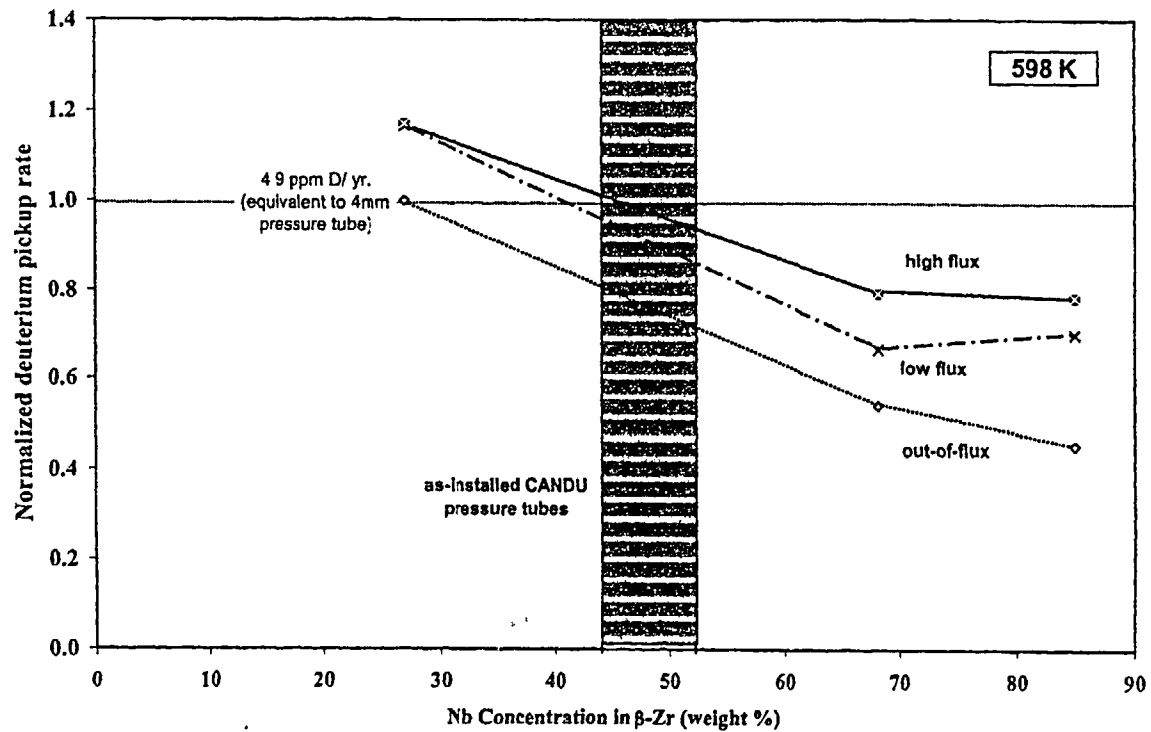


FIG. 12—Deuterium pickup of pickled Zr-2.5Nb pressure tube specimens in 598 K heavy water in Halden. Specimens thermally aged to induce varying Nb concentrations in β -Zr phase, then tested under the stated flux regime for 200 days. Pick-up data normalized to rate for as-received specimen exposed out-of-flux (4.9 ppm/year; equivalent rate for 4-mm pressure tube).

ratio of the specimens relative to pressure tubes. At both 523 and 598 K and across the range of β -phase decomposition studied, in-flux specimens experience higher pickup rates than the corresponding out-of-flux specimens. Specimens irradiated at 523 K show the greatest flux dependence of deuterium pickup. As well, the dependence of pickup rate on β -phase decomposition is significantly different at the two temperatures. At 523 K, pickup rates for out-of-flux and low-flux specimens decrease as the β -phase Nb concentration increases, thereafter, increasing rates are observed. At the same temperature, but under high flux conditions (approximating the peak in a CANDU 6 pressure tube), pickup rates initially increase with β -phase decomposition, then saturate at higher values. At 598 K, out-of-flux specimens exhibit a continuous decrease in D pickup rate with increasing β -phase decomposition. Initially, the same is true for specimens irradiated at low and high flux, however, rates tend to saturate at higher β -phase Nb concentrations. In all cases, the lack of data at intermediate Nb concentrations makes it difficult to determine the exact dependence on Nb concentration.

Effect of Billet Pre-heat Time and Temperature

Figures 13, 14, and 15 summarize oxidation rates for pickled specimens from a series of pressure tubes prepared from a single ingot. These preliminary data were collected after 195 days of a multi-year test. Each bar represents the oxidation rate for a single specimen, normalized to the rate for a specimen from tube RX083. Prior to extrusion, the corresponding billet was soaked for 15 min at 1088 K (current CANDU practice); in all figures, the absolute rate for RX083 specimens is reported in terms of oxide growth per year. The legend identifies the billet pre-heat time and temperature for each set of specimens, light-colored bars signify results for tubes prepared using a 15-min soak time, darker bars represent results for 300-min soak periods. In each figure, the data are grouped according to the test temperature. Figures 14 and 15 show in-flux data obtained under two flux regimes: "low flux" = $0.93 - 1.36 \times 10^{17} \text{ n} \cdot \text{m}^{-2} \cdot \text{s}^{-1}$, and "high flux" = $3.08 - 3.61 \times 10^{17} \text{ n} \cdot \text{m}^{-2} \cdot \text{s}^{-1}$.

Additional data (from longer exposures) will be required before any definitive conclusions can be reached. However, we can offer the following preliminary observations. First, out-of-flux and under low-flux conditions, changes in extrusion variables appear to have a greater impact on subsequent corrosion behavior at 523 K than at 598 K. At the latter temperature, oxidation rates for the various tube materials do not differ significantly. In contrast, when corrosion tests are conducted under high-flux conditions, significant variations in oxidation rate are observed among the various materials both at 523 and 598 K. Second, after 195 days exposure, only two sets of pre-extrusion conditions gave rise to tubes whose corrosion behavior surpassed tube RX083. When exposed at 523 K under high neutron flux, materials from billets soaked for 300 min at 1088 K and 300 min at 1123 K showed much lower oxidation rates. However, both materials showed a large temperature dependence of oxidation, exhibiting higher rates than RX083 when tested at 598 K. When one considers all flux-temperature conditions relevant to CANDU (i.e., those studied in the present test), tubes extruded according to the current specification gave, in general, the best corrosion performance.

Summary

An in-reactor program has been established to evaluate the influence of key variables on the corrosion of zirconium alloys. The program is ongoing and will continue to generate useful data in the future. On the basis of loop tests completed to date, the following observations can be made:

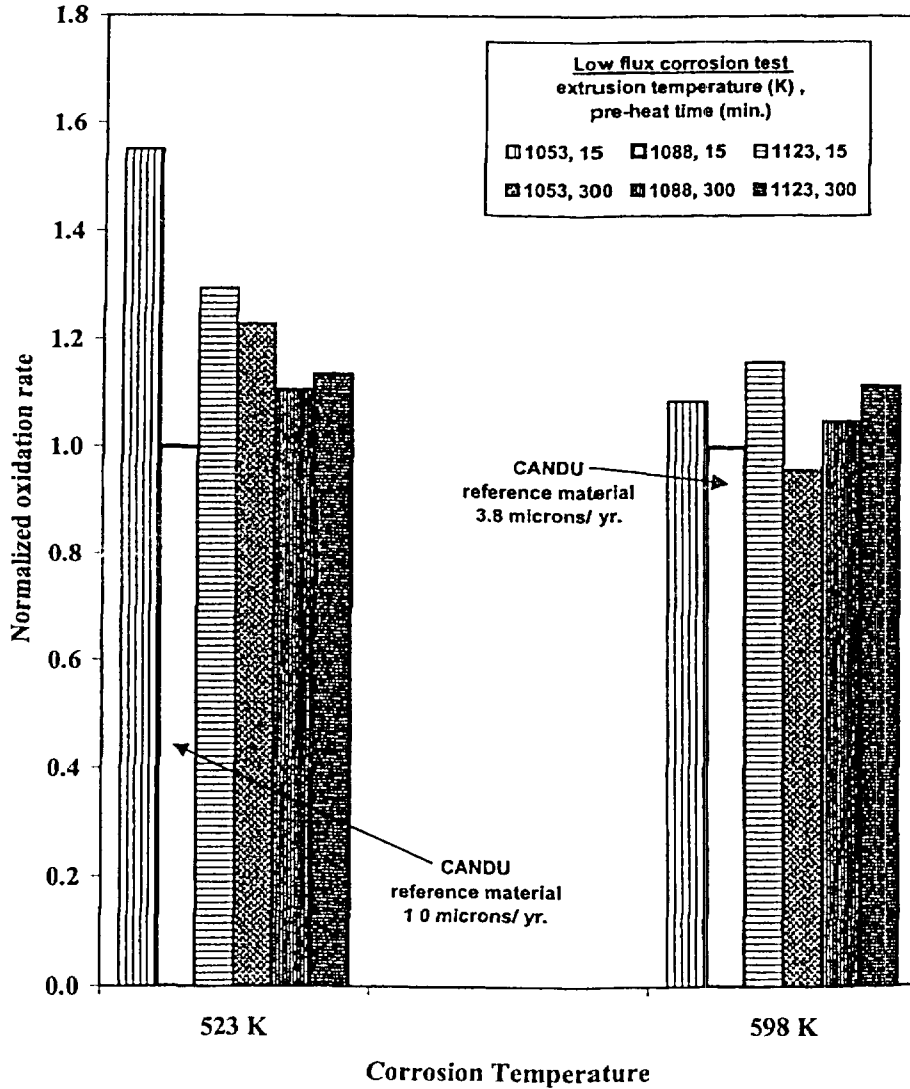


FIG 14—Oxidation of pickled 7r-2 5Nb pressure tube specimens in 523 and 598 K heavy water in Halden. Specimens machined from pressure tubes extruded under various conditions. Specimens exposed under "low" flux for 195 days. Oxidation data normalized to rate for pressure tube material fabricated according to current CANDU practice, then tested at stated temperature (523 K = 1.0 $\mu\text{m}/\text{year}$, 598 K = 3.8 $\mu\text{m}/\text{year}$)

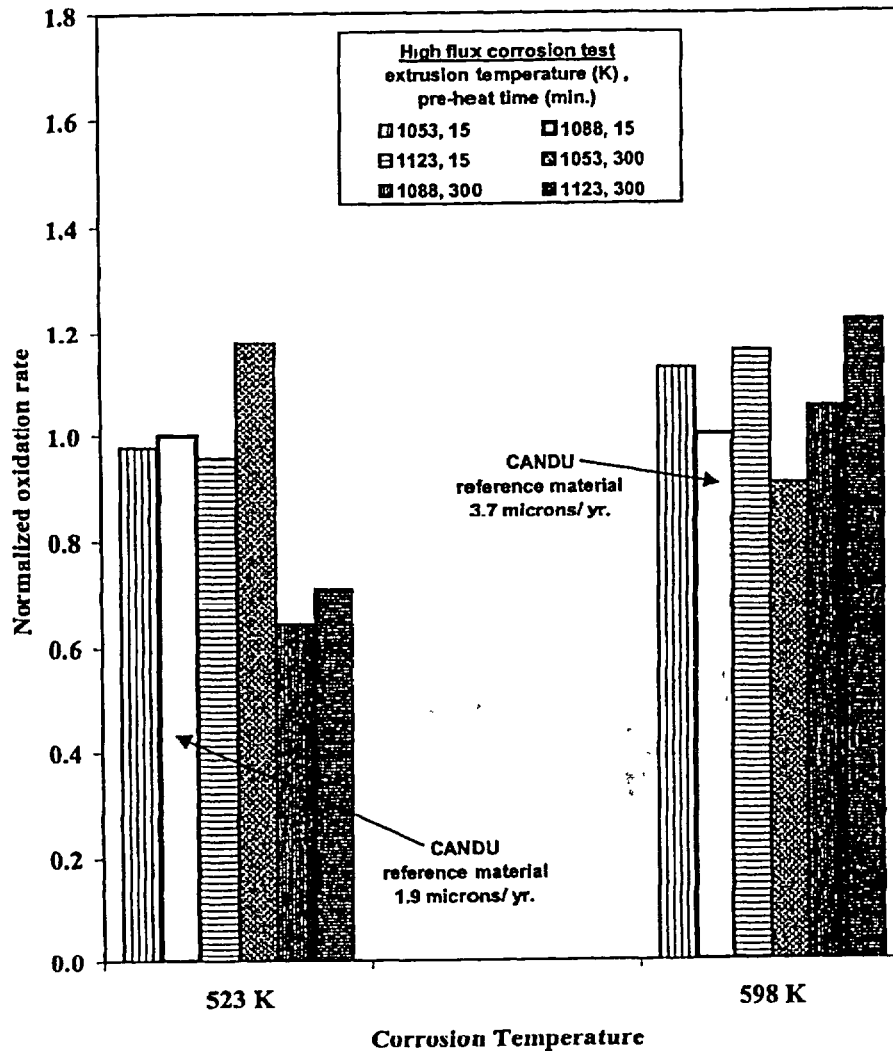


FIG. 15—Oxidation of pickled Zr-2.5Nb pressure tube specimens in 523 and 598 K heavy water in Halden. Specimens machined from pressure tubes extruded under various conditions. Specimens exposed under "high" flux for 195 days. Oxidation data normalized to rate for pressure tube material fabricated according to current CANDU practice, then tested at stated temperature (523 K = 1.9 $\mu\text{m}/\text{year}$, 598 K = 3.7 $\mu\text{m}/\text{year}$)

1. At both 523 and 598 K, prefilmed specimens from pressure tubes made of β -quenched material continue to show lower oxidation rates than tubes made from non- β -quenched material
2. At 598 K, prefilmed specimens from pressure tubes of β -quenched material exhibit significantly lower deuterium pickup rates than their non- β -quenched counterparts. Tests are underway to examine a number of factors that may contribute to the differing behavior of these two sets of pressure tubes (for example, impurity concentrations).
3. Evidence of linear oxidation rates (pressure tubes of non- β -quenched material, exposed out-of-flux) and accelerated deuterium pickup rates (pressure tubes of β -quenched and non- β -quenched material exposed to fast flux in the range 0 to $2.08 \times 10^{17} \text{ n} \cdot \text{m}^{-2} \cdot \text{s}^{-1}$) has been observed at 523 K. After 553 days, no examples of such behavior have been observed in any 598 K tests, nor under high flux conditions at 523 or 598 K.
4. In short-term tests at 598 K, increased levels of β -Zr decomposition lead to improved oxidation and deuterium pickup rates, both in- and out-of-flux. At 523 K, the impact of β -phase decomposition is significant out-of-flux, but less so in-flux.
5. Optimum corrosion performance is obtained from pressure tubes extruded according to the current CANDU specification.

These results will be invaluable in developing a predictive model of corrosion and deuterium ingress in CANDU pressure tubes

Acknowledgments

The authors gratefully acknowledge technical assistance from members of the Fuel Channels, the Health, Chemistry and Environment, and Nuclear Facility Operations Divisions within AECL, and staff of the OECD Halden Reactor Project in obtaining the data presented in this paper. In particular, the efforts of A. Audet, G. Rasewych, and A. Shaddick are much appreciated. Valuable discussions with Dr. A. A. Bahurmuz and Dr. R. Choubey are also acknowledged.

References

- [1] McDougall, G. M., Urbanic, V. F., and Aarrestad, O., "Studies of Zirconium Alloy Corrosion and Hydrogen Uptake During Irradiation," *Zirconium in the Nuclear Industry: Twelfth International Symposium, ASTM STP 1354*, G. P. Sabol and G. D. Moan, Eds., American Society for Testing and Materials, West Conshohocken, PA, 2000, pp. 756-772.
- [2] Urbanic, V. F. and Griffiths, M., "Microstructural Aspects of Corrosion and Hydrogen Ingress in Zr-2.5Nb," *Zirconium in the Nuclear Industry: Twelfth International Symposium, ASTM STP 1354*, G. P. Sabol and G. D. Moan, Eds., American Society for Testing and Materials, West Conshohocken, PA, 2000, pp. 641-657.
- [3] Choubey, R., Aldridge, S. A., Theaker, J. R., Cann, C. D., and Coleman, C. E., "Effects of Extrusion-Billet Preheating on the Microstructure and Properties of Zr-2.5Nb Pressure Tube Materials," *Zirconium in the Nuclear Industry: Eleventh International Symposium, ASTM STP 1295*, E. R. Bradley, and G. P. Sabol, Eds., American Society for Testing and Materials, West Conshohocken, PA, 1996, pp. 657-675.
- [4] Holt, R. A. and Aldridge, S. A., "Effect of Extrusion Variables on Crystallographic Texture of Zr-2.5 wt% Nb," *Journal of Nuclear Materials*, Vol. 135, 1985, pp. 246-259.
- [5] Fleck, R. G., Price, E. G., and Cheadle, B. A., "Pressure Tube Development for CANDU Reactors," *Zirconium in the Nuclear Industry: Sixth International Symposium, ASTM STP 824*, D. G. Franklin and R. B. Adamson, Eds., American Society for Testing and Materials, Philadelphia, 1984, pp. 88-105.

- [6] Theaker, J. R., Choubey, R., Moan, G. D., Aldridge, S. A., Davis, L., Graham, R. A. and Coleman, C. E., "Fabrication of Zr-2.5Nb Pressure Tubes to Minimize the Harmful Effects of Trace Elements," *Zirconium in the Nuclear Industry: Tenth International Symposium, ASTM STP 1245*, A. M. Gardc and E. R. Bradley, Eds., American Society for Testing and Materials, West Conshohocken, PA, 1994, pp. 221-242.
- [7] Griffiths, M., Mecke, J. F., and Winegar, J. E., "Evolution of Microstructure in Zirconium Alloys During Irradiation," *Zirconium in the Nuclear Industry: Eleventh International Symposium, ASTM STP 1295*, E. R. Bradley and G. P. Sabol, Eds., American Society for Testing and Materials, West Conshohocken, PA, 1996, pp. 580-602.
- [8] Ramasubramanian, N. and Ling, V. C., *Journal of Nuclear Materials*, Vol. 175, 1990, pp. 237-243.
- [9] Hosbons, R. R., Davies, P. H., Griffiths, M., Sagat, S., and Coleman, C. E., "Effect of Long-Term Irradiation on the Fracture Properties of Zr-2.5Nb Pressure Tubes," *Zirconium in the Nuclear Industry: Twelfth International Symposium, ASTM STP 1354*, G. P. Sabol and G. D. Moan, Eds., American Society for Testing and Materials, West Conshohocken, PA, 2000, pp. 122-138.

DISCUSSION

N. Ramasubramanian,¹ (written discussion)—For the as-extruded and non-autoclaved specimens, the β -Nb precipitation in low flux—is it in the α -Zr phase? For the same material, are the rates of deuterium pickup comparable, but initial pickup values different?

McDougall and Urbanic (authors' closure)—In the first question, reference is made to Fig. 9, which depicts the influence of initial β -Zr phase Nb concentration on the subsequent oxidation of coupons at 523 K under three flux levels. We see that after 200 days exposure under low or high flux conditions that oxidation rates for as-extruded material (β -phase Nb = 27 wt%) are remarkably similar to those for materials thermally aged to give 68 and 85 wt% Nb in the β -phase. Initially, we considered the possibility that the as-extruded material exhibited a low oxidation rate due to β -phase decomposition that occurred during irradiation testing. However, on the basis of data in Ref. 2, it can be inferred that, over a 200-day period, neither the low or high flux coupons could have experienced an increase in β -phase Nb concentration of more than a few percent. Thus we speculate that the low oxidation rate for coupons of as-extruded material is in fact due to radiation-induced precipitation of β -Nb in the α -Zr phase, previous work has correlated the appearance of such precipitates with flux suppression of corrosion in Zr-2.5Nb [2].

The corresponding deuterium pickup rates for these coupons are shown in Fig. 11. Since deuterium measurements were made only at the end of the test, the figure is based on average pickup rates; no initial pickup data are available. Figure 11 indicates that coupons of as-extruded material exhibit significant differences in pickup rate depending on the flux level. Comparing the in-flux results, coupons exposed under high flux conditions showed deuterium pickup rates ~1.6 times higher than under low flux, in contrast to the oxidation results (see Fig. 9).

P. H. Kreyns,² (written discussion)—Did you observe any effect of corrosion prefilm on the amount of deuterium pickup at low and high flux positions?

McDougall and Urbanic (authors' closure)—While this paper dealt primarily with coupons that were pickled and then prefilmed (average thickness = 0.5 to 1.5 μm), parallel tests were performed using pickled coupons from the same pressure tubes. In the majority of cases, deuterium pickup rates for pickled + prefilmed coupons were significantly lower than rates for corresponding coupons in the pickled condition. Under both low and high flux conditions, the difference was approximately 60% at 523 K and 23% at 598 K, based on average rate calculations. Long-term tests will allow us to compare instantaneous rates for pickled and pickled + prefilmed coupons, which may result in different values.

B. Kammenzind,³ (written discussion)—You showed a large difference between your autoclave corrosion rates and your low flux and high flux corrosion rates even after low fluence accumulation. You attribute the difference to precipitation of β -Nb in the α -grains. Could a second potential explanation be differences in the water chemistry between the autoclave and in-flux samples, such as oxygen content of the water?

McDougall and Urbanic (authors' closure)—In the Halden loop, both in- and out-of-flux samples were exposed to a single coolant stream containing a carefully controlled deuterium

¹ Ecatec, Inc.

² Bechtel Bettis

³ Bettis Laboratory

concentration. Reducing water chemistry was maintained at all times, resulting in dissolved oxygen levels of $\leq 5 \mu\text{g} \cdot \text{kg}^{-1}$, measured at the outlet of the test sections. To ensure that boiling did not occur along high-temperature channels (potentially allowing for stripping of dissolved deuterium into the gas phase), the loop pressure was maintained at 15.5 MPa. In this way, radiolysis was suppressed in the bulk coolant passing over the in-flux samples.

Pauline H. Davies,¹ Donald D. Himbeault,² Robert S.W. Shewfelt,³ and
Robert R. Hosbons⁴

Crack Growth Resistance of Irradiated Zr-2.5Nb Pressure Tube Material at Low Hydrogen Levels

Reference: Davies, P H , Himbeault, D. D , Shewfelt, R. S W , and Hosbons, R. R , "Crack Growth Resistance of Irradiated Zr-2.5Nb Pressure Tube Material at Low Hydrogen Levels," *Effects of Radiation on Materials- 20th International Symposium, ASTM STP 1405*, S T Rosinski, M L. Grossbeck, T R Allen, and A S Kumar, Eds , American Society for Testing and Materials, West Conshohocken, PA, 2001.

Abstract: The primary factors influencing the crack growth resistance of irradiated Zr-2.5Nb pressure tube material at low concentrations of hydrogen/deuterium are reviewed. These factors include the initial characteristics of the material, which have brought about improvements in the toughness, and the operating conditions in reactor. The paper presents an update on the current status of this work using J-R curves. Such curves are determined from curved compact and rising-pressure burst test specimens at 250°C, i.e., the lower end of the operating temperature range. Some of the challenges encountered in assessing the crack growth toughness of this high-strength, thin-walled material are discussed. The role of chlorine, known to be responsible for the presence of Zr-Cl-C particles and preferential decohesion and fissuring, is also highlighted. The results from the curved compact specimens suggest a limiting level of chlorine above which no further significant degradation in crack growth resistance occurs. This level of chlorine is about 3 wt ppm for material having a low concentration of zirconium phosphide ($P < 20$ wt ppm). Such results require confirmation using burst tests on material with intermediate levels of chlorine and low levels of zirconium phosphide.

Keywords: crack growth resistance (J-R) curve, fracture toughness, Zr-2.5Nb, pressure tube, irradiation, slant fracture

¹Senior research scientist, AECL, Chalk River Laboratories, Chalk River, Ontario K0J 1J0.

²Formerly research scientist, AECL, Whiteshell Laboratories, Pinawa, Manitoba R0E 1L0.

³Research scientist, AECL, Whiteshell Laboratories, Pinawa, Manitoba R0E 1L0.

⁴Formerly Head, Deformation Technology Branch, AECL, Chalk River Laboratories, Chalk River, Ontario K0J 1J0.

Introduction

The primary containment for the fuel in CANDU[®] reactors is provided by thin-walled pressure tubes of cold-worked Zr-2.5Nb. These tubes typically have a length of 6.3 m, an inside diameter of 103 mm, and a wall thickness of 4.2 mm. During service heavy water flows through the tubes to cool the fuel. The tubes operate at an internal pressure of between 10 and 11 MPa at temperatures varying from 250-265°C (inlet ends) to 290-315°C (outlet ends) depending upon the reactor unit. Considerable progress has been made recently in understanding the primary factors influencing the crack growth resistance and failure mechanism of the material. This includes the effects of irradiation, deuterium pickup and the role of pre-existing particles. The paper presents an update on the current status of this work for irradiated material having low concentrations of hydrogen/deuterium. The results presented are from crack growth resistance curves obtained from curved compact and burst test specimens tested at 250°C, i.e. the lower end of the operating temperature range.

Material

CANDU reactor pressure tubes are manufactured from extruded and cold-worked (about 26%) Zr-2.5Nb. The results reported here are for material manufactured to the earlier specification shown in Table 1.

Table 1 - Chemical specification for Zr-2.5Nb pressure tubes for CANDU[®] reactors.

Element	Specification (up to 1987)	Current
Niobium	2.4-2.8 wt%	2.5-2.8 wt%
Oxygen	900-1300 ^a	1000-1300
Carbon	< 270	≤ 125
Chlorine	-----	≤ 0.5
Chromium	≤ 200	≤ 100
Hydrogen	≤ 25 ^b	≤ 5
Iron	≤ 1500	≤ 650
Nickel	≤ 70	≤ 35
Nitrogen	≤ 65	≤ 65
Phosphorus	-----	≤ 10
Silicon	≤ 120	≤ 100
Tantalum	≤ 200	≤ 100
Zirconium and Other Impurities	Balance	Balance

^a Concentration of remaining elements given in ppm by weight.

^b 20 ppm hydrogen for ingot, 25 ppm hydrogen for final tube

The final microstructure of the material is dual-phase with a network of elongated α -phase (hexagonal-close-packed), containing about 1 wt% Nb in solution, surrounded by a thin film of β -phase (body-centered-cubic), with about 20 wt% Nb [1].

Pauline H. Davies,¹ Donald D. Himbeault,² Robert S.W. Shewfelt,³ and
Robert R. Hosbons⁴

Crack Growth Resistance of Irradiated Zr-2.5Nb Pressure Tube Material at Low Hydrogen Levels

Reference: Davies, P. H., Himbeault, D. D., Shewfelt, R. S. W., and Hosbons, R. R., "Crack Growth Resistance of Irradiated Zr-2.5Nb Pressure Tube Material at Low Hydrogen Levels," *Effects of Radiation on Materials: 20th International Symposium, ASTM STP 1403*, S. T. Rosinski, M. L. Grossbeck, T. R. Allen, and A. S. Kumar, Eds., American Society for Testing and Materials, West Conshohocken, PA, 2001

Abstract: The primary factors influencing the crack growth resistance of irradiated Zr-2.5Nb pressure tube material at low concentrations of hydrogen/deuterium are reviewed. These factors include the initial characteristics of the material, which have brought about improvements in the toughness, and the operating conditions in reactor. The paper presents an update on the current status of this work using J-R curves. Such curves are determined from curved compact and rising-pressure burst test specimens at 250°C, i.e., the lower end of the operating temperature range. Some of the challenges encountered in assessing the crack growth toughness of this high-strength, thin-walled material are discussed. The role of chlorine, known to be responsible for the presence of Zr-Cl-C particles and preferential decohesion and fissuring, is also highlighted. The results from the curved compact specimens suggest a limiting level of chlorine above which no further significant degradation in crack growth resistance occurs. This level of chlorine is about 3 wt ppm for material having a low concentration of zirconium phosphide ($P < 20$ wt ppm). Such results require confirmation using burst tests on material with intermediate levels of chlorine and low levels of zirconium phosphide.

Keywords: crack growth resistance (J-R) curve, fracture toughness, Zr-2.5Nb, pressure tube, irradiation, slant fracture

¹Senior research scientist, AECL, Chalk River Laboratories, Chalk River, Ontario K0J 1J0.

²Formerly research scientist, AECL, Whiteshell Laboratories, Pinawa, Manitoba R0E 1L0

³Research scientist, AECL, Whiteshell Laboratories, Pinawa, Manitoba R0E 1L0.

⁴Formerly Head, Deformation Technology Branch, AECL, Chalk River Laboratories, Chalk River, Ontario K0J 1J0.

Introduction

The primary containment for the fuel in CANDU[®] reactors is provided by thin-walled pressure tubes of cold-worked Zr-2.5Nb. These tubes typically have a length of 6.3 m, an inside diameter of 103 mm, and a wall thickness of 4.2 mm. During service heavy water flows through the tubes to cool the fuel. The tubes operate at an internal pressure of between 10 and 11 MPa at temperatures varying from 250-265°C (inlet ends) to 290-315°C (outlet ends) depending upon the reactor unit. Considerable progress has been made recently in understanding the primary factors influencing the crack growth resistance and failure mechanism of the material. This includes the effects of irradiation, deuterium pickup and the role of pre-existing particles. The paper presents an update on the current status of this work for irradiated material having low concentrations of hydrogen/deuterium. The results presented are from crack growth resistance curves obtained from curved compact and burst test specimens tested at 250°C, i.e. the lower end of the operating temperature range.

Material

CANDU reactor pressure tubes are manufactured from extruded and cold-worked (about 26%) Zr-2.5Nb. The results reported here are for material manufactured to the earlier specification shown in Table 1.

Table 1 - Chemical specification for Zr-2.5Nb pressure tubes for CANDU[®] reactors

Element	Specification (up to 1987)	Current
Niobium	2.4-2.8 wt%	2.5-2.8 wt%
Oxygen	900-1300 ^a	1000-1300
Carbon	< 270	≤ 125
Chlorine	-----	≤ 0.5
Chromium	≤ 200	≤ 100
Hydrogen	≤ 25 ^b	≤ 5
Iron	≤ 1500	≤ 650
Nickel	≤ 70	≤ 35
Nitrogen	≤ 65	≤ 65
Phosphorus	-----	≤ 10
Silicon	≤ 120	≤ 100
Tantalum	≤ 200	≤ 100
Zirconium and Other Impurities	Balance	Balance

^a Concentration of remaining elements given in ppm by weight.

^b 20 ppm hydrogen for ingot, 25 ppm hydrogen for final tube

The final microstructure of the material is dual-phase with a network of elongated α -phase (hexagonal-close-packed), containing about 1 wt% Nb in solution, surrounded by a thin film of β -phase (body-centered-cubic), with about 20 wt% Nb [1].

Degradation occurs during service as a result of irradiation damage as well as deuterium pickup from the pressurised heavy water. Periodically surveillance tubes are removed from reactor and the mechanical properties assessed to ensure that the tubes remain "fit for service". Although some small specimen studies have been conducted on pre-selected material irradiated in test reactors, the majority of information on the crack growth resistance of irradiated Zr-2.5Nb pressure tube material is from surveillance tubes.

Mechanical test results have been obtained to date on irradiated Zr-2.5Nb pressure tube material sampled from tubes removed from Pickering Nuclear Generating Station (NGS) A Units 3 and 4, Bruce NGS A Units 1 to 4 and Wolsong Nuclear Power Plant (NPP) Unit 1. The tubes sampled operated for up to 18 years in service at a fast neutron flux of between 2.5 and $4 \times 10^{17} \text{ n m}^{-2} \cdot \text{s}^{-1}$ to give a maximum fast neutron fluence of $18 \times 10^{25} \text{ n m}^{-2}$ ($E > 1 \text{ MeV}$). (All neutron fluences in this paper are for $E > 1 \text{ MeV}$.) All the material was fabricated in the late 1960s and 1970s by early production techniques, e.g. from double-vacuum, arc-melted ingots. The majority of mechanical test results have been obtained at a test temperature of 250°C . This temperature corresponds to the lowest (inlet) irradiation temperature of the surveillance material and was selected to avoid removal of any irradiation damage by annealing. In addition, the maximum total equivalent hydrogen concentration (hydrogen + 0.5 deuterium concentration by weight) of this material is $< 30 \text{ wt ppm}$, so that the hydrogen isotopes would all be in solution at test temperatures $\geq 250^\circ\text{C}$. (The terminal solid solubility for hydride dissolution at 250°C is about 29 wt ppm .)

Unirradiated archive material from the surveillance tubes is also available for testing. The material comes from rings of material that are removed from the front and back ends of a tube before installation. The front end refers to the end that emerged first in the extrusion operation.

Experimental Techniques

Two different techniques are used to assess the crack growth resistance of irradiated pressure tube material. The first is a small-scale specimen method using 17-mm wide curved compact specimens machined directly from the tube material [2-4] (see Figure 1). The second is a large-scale specimen method for rising-pressure burst tests using 500-mm long sections with a 55-mm long, axial through-wall starter crack [5-7] (see Figure 2). In each case specimens are oriented for crack growth in the axial direction on the radial-axial plane. After fatigue pre-cracking of the starter notch, specimens are loaded at a rate corresponding to an initial rate of increase of stress intensity factor of about $1 \text{ MPa}\sqrt{\text{m}} \text{ s}^{-1}$. Any stable crack growth is monitored using the direct-current potential drop method. The positions of the constant current and voltage leads are selected to ensure that the relationship between the voltage and crack length for a planar crack front is approximately linear.

Curved compact specimens are loaded in displacement control to produce about 3 to 4 mm of crack growth and the load, load point displacement and potential drop signal are all monitored. After unloading, the crack extension area is marked by heat tinting, and the measured (average) crack extension matched to the change in potential drop voltage during the test. This allows direct calibration of the potential drop method for each

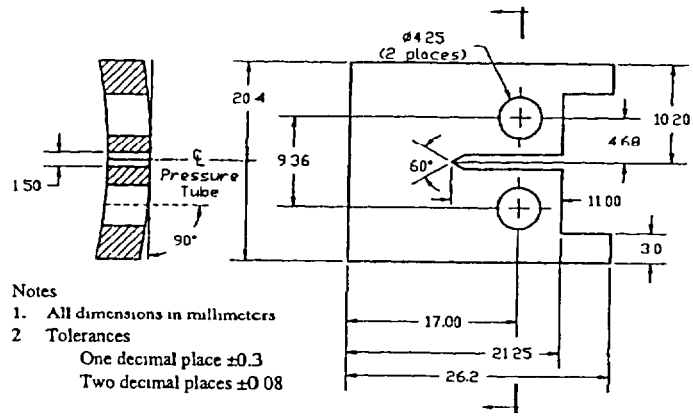


Figure 1 - Standard (17-mm wide) curved compact specimen configuration

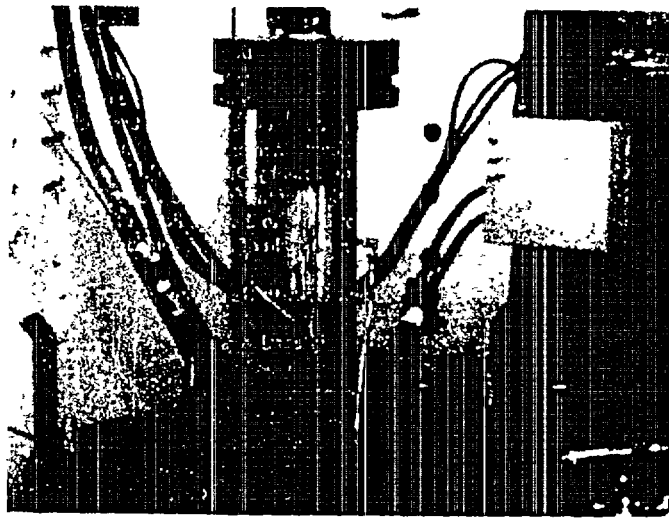


Figure 2 - Burst test specimen with mechanical end caps and potential drop leads

specimen on an individual basis. Problems occasionally arise when testing irradiated specimens from tubes of higher toughness. Such material may exhibit a load drop after about 1.5 to 2 mm crack growth which is associated with secondary crack initiation from the back face at about 45° to the radial-axial plane. No correction method for such secondary cracking has been found. Current practice is to use the calibration factor from a specimen of similar toughness (i.e. load, displacement and voltage characteristics before the load drop) which did not exhibit "back-face cracking." The origin of such crack growth behavior is under investigation.

Burst test specimens are internally pressurized to failure with argon gas and the pressure and potential drop voltage monitored. In this case calibration of the potential drop method on an individual basis is not possible, since crack instability occurs just beyond maximum pressure. Studies of burst test specimens interrupted before achieving crack instability at 250°C suggest the potential drop method provides conservative assessments of crack extension during the early stages of crack growth. This is because of contributions to the voltage change from through-thickness yielding. However, given the mixed-mode nature of the fractures observed for both the small- and large-scale specimen geometry (see next section) the true bias of the results is unknown.

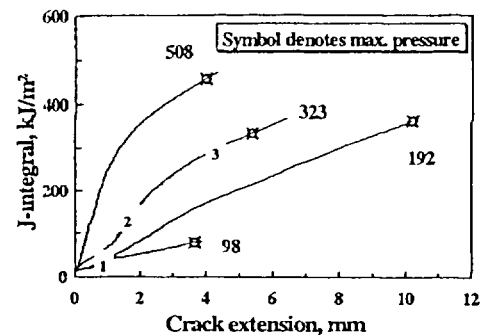
The J-integral parameter used for characterizing the crack growth resistance of Zr-2.5Nb pressure tube material may be considered the elastic-plastic equivalent of the linear elastic strain energy release rate, G . This is especially true for the rising-pressure burst test [5-7], where J is calculated using a strip yield equation for an axial through-wall crack in a thin shell [8], i.e. an elastic equation with a small-scale plasticity correction factor.

In comparison, for curved compact specimens the standard ASTM equation for J for a flat compact specimen is used [2-4]. This equation is based on the original non-linear elastic interpretation and analysis of Rice for the deformation J-integral [9], but the validity of this approach is questionable after crack initiation, e.g. work by Turner [10]. In fact, different values for J are obtained if alternative analyses are used, e.g. the modified J-integral [11], the dissipation J-integral [12]. Such differences can be significant when crack front tunneling occurs, see recent paper on Zr-2.5Nb pressure tube material by Davies [13]. However, for the purposes of surveillance testing, the limitations of the standard ASTM equation based on the deformation J-integral are accepted due to the simplicity of the approach and its current widespread acceptance within the field of elastic-plastic fracture mechanics.

Crack Growth Resistance (J-R) Curves and Fracture Modes

A J-integral versus crack extension (crack growth resistance or J-R) curve may be considered a measure of the elastic-plastic energy expended during crack growth, with the shape reflecting the macroscopic crack growth process in the material. For irradiated Zr-2.5Nb pressure tube material a large range of different shape J-R curves are observed depending upon the characteristics of the individual pressure tube, the irradiation and test conditions as well as the specimen geometry. For example, Figure 3 shows the range of J-R curves obtained from burst tests at 250°C for the original tubes removed from Pickering NGS A Units 3 and 4 [6].

Figure 3 - Range of crack growth resistance (J - R) curves from rising-pressure burst tests on surveillance tubes removed from Pickering NGS A Units 3 and 4 at 250°C



Such curves show evidence of the three stage crack growth behavior observed earlier for small specimens [14]. These three stages can be classified as indicated below

- 1) Stage 1 (plateau) due to a low energy-absorbing, flat fracture mode developing in the region of highest constraint at the mid-thickness
- 2) Stage 2 (increasing slope of J - R curve) due to a high energy-absorbing, transition fracture mode developing in the region of intermediate constraint between the mid-thickness and surface
- 3) Stage 3 (decreasing slope of J - R curve) due to a low energy-absorbing slant fracture mode developing from the region of lowest constraint at the surface

Thus individual irradiated Zr-2.5Nb pressure tubes may be characterized as being of low, intermediate or high toughness depending upon the relative contributions of these different fracture modes.

- 1) Low toughness: dominated by flat and slant fracture modes, i.e. stage 1 and 3.
- 2) Intermediate toughness: flat, transition and slant fracture modes all significant, i.e. stage 1, 2 and 3.
- 3) High toughness: dominated by transition and slant fracture, i.e. stage 2 and 3.

An example of a fractograph for a high toughness specimen showing the three different fracture modes is shown in Figure 4

The relative contributions of the different stages depends upon the relative proportions and energy-absorbing capacities of the different fracture modes, which is determined by the ease of void nucleation, void growth and coalescence ahead of the crack tip. Therefore, the relative proportions and energy-absorbing capacities of the three different fracture modes depends on the following factors

- 1) The size, shape and distribution of the particles present since this influences the probability of nucleating voids [15]
- 2) The deformation characteristics of the matrix which influences the local crack-tip stress for void nucleation, growth and coalescence (ligament failure) [15-17]
- 3) The specimen geometry which influences the crack-tip stress and the probability of achieving the stress level required for void nucleation, growth and coalescence [18,19]

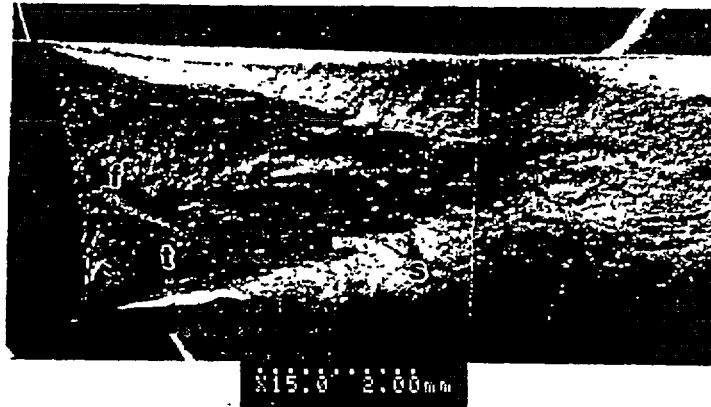


Figure 4 - Scanning electron fractograph of burst test specimen from a tube of high toughness tested at 250°C showing narrow flat fracture zone at mid-section (*f*), wide cup-shaped transition zone (*t*), and slant fracture developing at surfaces (*s*) (Tilt angle view at 45°.)

For irradiated Zr-2.5Nb pressure tube material the factors in 1) and 2) are strongly influenced by the initial properties of the as-installed tubes (e.g. ingot material, fabrication variables) as well as the operating conditions of the tubes in a given reactor (e.g. fast neutron fluence and irradiation temperature). Therefore, some discussion of the influence of these variables on the J-R curves is warranted. The majority of this work is based on the results from small curved compact specimens. The effects of specimen geometry, and confirmation of the influence of such variables on the J-R curves from rising-pressure burst tests, is presented afterwards.

Factors Influencing J-R Curves from Small Specimens (Parametric Studies)

Void-Nucleating Particles

Void-nucleating particles may be considered as primary or secondary depending upon whether they are responsible for initial void nucleation ahead of the crack tip at relatively low stress levels or at higher stress levels contributing to ligament failure between the primary voids. The majority of work on Zr-2.5Nb pressure tube material to date has focused on the study (and elimination) of particles responsible for primary void nucleation. In addition to the well known effects of zirconium hydride [20], such particles include a Zr-Cl-C (complex carbide), responsible for preferential decohesion and fissuring [21,22], zirconium phosphide and carbide [21-23]. Quantitative

relationships between crack growth toughness and fissure spacing and length (an indirect measure of the density of Zr-Cl-C particles) are given elsewhere for the unirradiated [21] and irradiated material [22]. Relationships between toughness and density of zirconium phosphide and carbide particles are provided in reference [23].

In addition, it has been shown that tubes fabricated from ingots made-up from 100% recycled material (i.e. passed through the production process twice and equivalent to quadruple vacuum-arc-melted material) exhibit the highest toughness [21-24]. This is because of the low concentration of chlorine and an absence of Zr-Cl-C particles [21-23]. The influence of these pre-existing particles have now been eliminated by careful control of the ingot chemistry, including the use of selected raw materials and quadruple vacuum-arc-melting [24].

The effect of chlorine on the crack growth resistance of irradiated Zr-2.5Nb pressure tube material at 250°C is demonstrated in Figures 5 and 6 using the results from small specimens sampled from surveillance tubes. Figure 5 shows the initial crack growth toughness (dJ/da), which is a measure of the "toughening rate" of the material during the early stages of crack growth, and is calculated as the linear regression slope of the J - R curve between the 0.15 and 1.5 mm offset lines. For comparison, the J value based on maximum load-bearing capacity or load, (J_m) is given in Figure 6. The chlorine concentration was determined from unirradiated archive material from the different surveillance tubes using Glow Discharge Mass Spectroscopy (GDMS). For clarity, only results from tubes having a low concentration of zirconium phosphide have been included, i.e. $P < 20$ wt ppm, since previous work has shown that such particles have little effect below this level [23]. Both sets of results demonstrate a sharp reduction in toughness with increasing Cl at concentrations < 3 wt ppm with little further change at higher Cl levels. The results also show that the Cl concentration of the Zr-2.5Nb pressure tube material fabricated in the late 1960s and 1970s from 100% recycled material was < 1 wt ppm. This compares with a level of Cl < 0.2 wt ppm which is now achievable with careful material selection and ingot melting practice.

Figure 5 - Initial crack growth toughness (dJ/da) from curved compact specimens of irradiated material tested at 250°C versus Cl. Results sorted according to source of ingot material. Results selected from material with $P < 20$ wt ppm. Fast neutron fluence of 4 to 18×10^{25} $n \cdot m^{-2}$ and irradiation temperature of 254 to 295°C

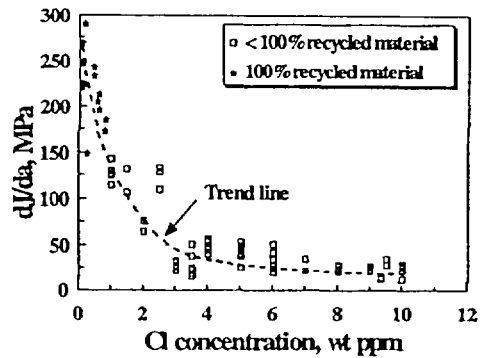
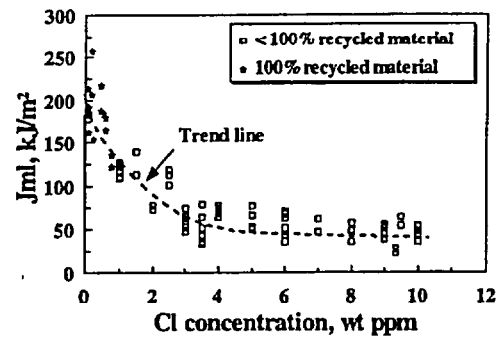


Figure 6 - J at maximum load (J_{ml}) from curved compact specimens of irradiated material tested at 250°C versus Cl. Results sorted according to source of ingot material. Results selected from material with $P < 20$ wt ppm. Fast neutron fluence of 4 to $18 \times 10^{25} \text{ n m}^{-2}$ and irradiation temperature of 254 to 295°C.



Deformation Characteristics of Matrix

The deformation characteristics of irradiated Zr-2.5Nb pressure tube material are determined by the propensity for slip, dislocation channeling and twinning at a given test temperature, i.e. by the yield stress and the twinning stress [14,25,26]. Such factors influence the tendency for void nucleation and also for void growth and coalescence once the voids are formed, and are sensitive to the operating conditions of a given pressure tube, i.e. the fast neutron fluence and irradiation temperature.

For example, at low fluences ($< 3 \times 10^{24} \text{ n m}^{-2}$) irradiation at a temperature of about 250°C increases the transverse yield stress and ultimate tensile strength under static loading conditions at 240°C by about 200 and 180 MPa, respectively, [27]. At higher fluences only a small further increase in strength is observed, e.g. about 5 MPa per increase in fluence of $1 \times 10^{25} \text{ n m}^{-2}$ [27]. Such results show little difference between the yield stress and ultimate tensile strength after irradiation, a characteristic of a low work-hardening material before the onset of strain localization (work-softening) by twinning and/or dislocation channeling [14,25,26]. These changes are primarily associated with an increase in the (a-type) dislocation density [27,28].

Therefore the main effect of irradiation on crack growth resistance is expected to occur early in the life of a reactor pressure tube, within the first year. This is demonstrated in Figures 7 and 8 which show the initial crack growth toughness (dJ/da) and maximum load toughness (J_{ml}) versus fluence for material from tubes having a lower (< 0.2 wt ppm) and higher (< 4 wt ppm) chlorine concentration. The sharp decrease in toughness at low fluences ($< 3 \times 10^{24} \text{ n m}^{-2}$) is associated with an increased susceptibility of the material to void nucleation resulting from irradiation hardening [22,27]. At higher fluences there is little evidence of further degradation, behavior consistent with the toughness being governed mainly by the presence of pre-existing particles in addition to the near saturation in the hardening response. However, both sets of results exhibit considerable scatter, the source of which is discussed below.

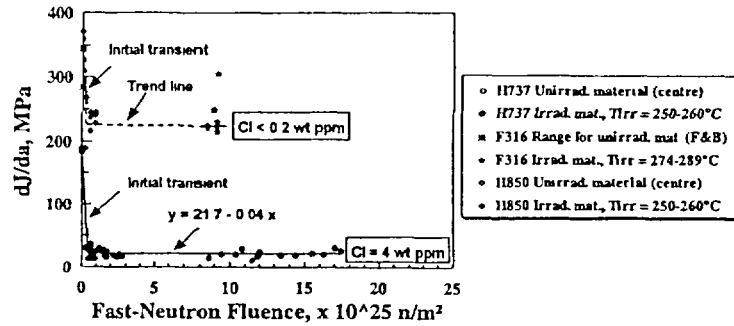


Figure 7 - Initial crack growth toughness (dJ/da) from curved compact specimens of irradiated material tested at 240/250°C versus fast neutron fluence. Note that tube H737 and H850 were irradiated in test reactors compared with results obtained from the surveillance tube F316. T_{irr} is the irradiation temperature in °C. All material with $P < 10$ wt ppm. F & B refer to unirradiated material obtained from archive rings removed from front and back ends of tube before installation.

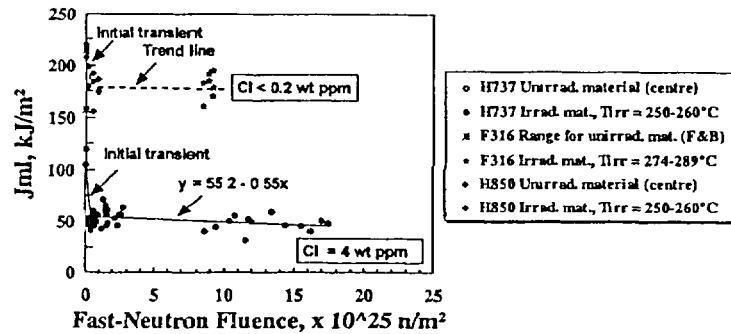
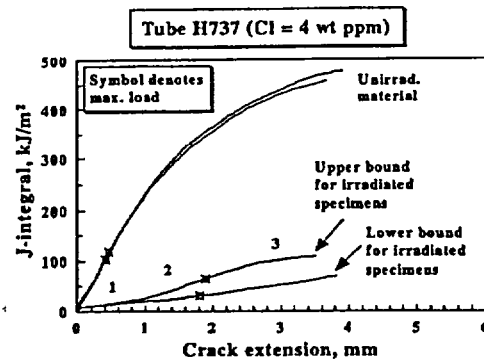


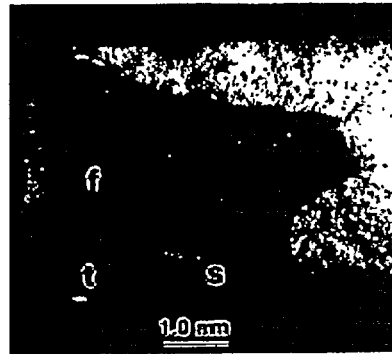
Figure 8 - J at maximum load (J_m) from curved compact specimens of irradiated material tested at 240/250°C versus fast neutron fluence. Note that tube H737 and H850 were irradiated in test reactors compared with results obtained from the surveillance tube F316. T_{irr} is the irradiation temperature in °C. All material with $P < 10$ wt ppm. F & B refer to unirradiated material obtained from archive rings removed from front and back ends of tube before installation.

Figure 9 - Range of J-R curves at 240°C from curved compact specimens of tube H737 (Cl = 4 wt ppm) before and after irradiation in the OSIRIS test reactor, Saclay, France. Fast neutron fluence of 0.4 to $17.4 \times 10^{23} \text{ n}\cdot\text{m}^{-2}$ and irradiation temperature about 250°C.



The effect of irradiation fluence on the J-R curves obtained for the material of lower toughness (Cl = 4 wt ppm) tested at 240°C is shown in Figure 9. Here the sharp reduction in the initial slope and formation of stage 1 plateau is associated with the development of a wide tunnel-shape flat fracture zone at the mid-section, as shown in Figure 10.

Figure 10 - Optical fractograph showing stable crack growth region of irradiated specimen from tube H737 (Cl = 4 wt ppm) irradiated in OSIRIS test reactor. Features include tunnel-shape, flat fracture zone at mid-section (f), narrow cup-shaped transition zone (t), and wide slant fracture developing at surface (s) (Normal view)

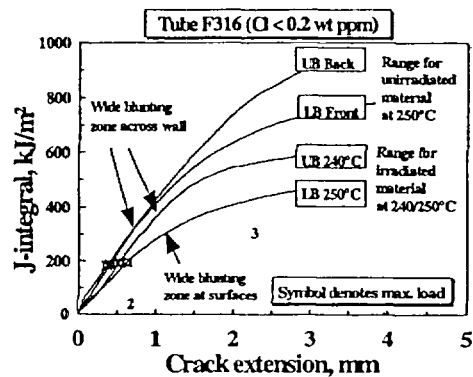


Such flat fracture zones are associated with preferential void nucleation and growth at Zr-Cl-C (complex carbide), aligned in the axial or extrusion direction of the tube [21,22]. This is manifested by fissures on the radial-axial fracture plane. The large variation in the J-R curves at longer crack extensions for the irradiated material (stage 2 and 3) is related to a tendency of such material to develop slant fracture. The latter may occur preferentially at one or other surface as the crack front tunnels forward at the mid-wall to relieve the high crack-tip constraint, as indicated in Figure 10. Thus

specimens with lower J-R curves exhibit not only wider flat fracture zones, but also an increased tendency to develop slant fracture, i.e. a reduction in the width of the transition zones between the regions of flat and slant fracture. In this regard the maximum load toughness (J_m) is a more reliable indicator of such behavior than the initial crack growth toughness (dJ/da), since the latter is a measure of the initial J-R curve slope and does not reflect the crack growth behavior at larger crack extensions.

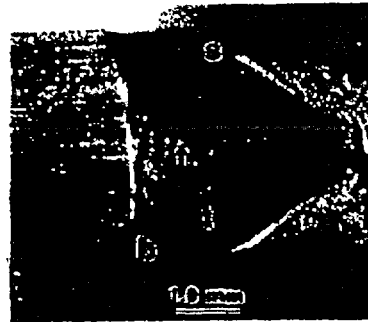
In comparison, Figure 11 shows the effect of fluence on the J-R curves obtained for a material of higher toughness (Cl = 0.2 wt ppm) tested at 240°C and 250°C.

Figure 11 - Range of J-R curves at 240/250°C from curved compact specimens of surveillance tube F316 (Cl < 0.2 wt ppm). Fast neutron fluence of $9.2 \times 10^{23} \text{ n m}^{-2}$ and irradiation temperature of 286 to 289°C. Results for unirradiated material obtained from archive rings removed from front and back ends of tube before installation. UB and LB refer to upper and lower bound curve results, respectively.



In this case the reduction in initial J-R slope after irradiation is not as large as for the material with 4 wt ppm Cl, and there is no evidence of stage 1 crack growth. This is believed to be due to the absence of significant void nucleation sites. The variation in the J-R curves arises mainly from differences in the initial slope which result from variations in size of the crack-tip blunting zone. For example, specimens sampled from unirradiated material exhibit full through-thickness yielding and a wide crack-tip blunting zone extending fully across the wall about 1 mm ahead of the fatigue crack. However, after irradiation the blunting zone does not always extend fully through the thickness, as shown in Figure 12 by the fracture surface for an irradiated specimen tested at 250°C. Here, the blunting zone is narrow at the mid-wall, where the crack-tip stress state (constraint) is high, but extends from the mid-wall as two triangular-shape regions, up to 1 mm ahead of the fatigue crack to the surface where the constraint is low. Therefore, for material of higher toughness, the initial crack growth toughness (dJ/da) does not necessarily reflect a true measure of crack extension, e.g. by microvoid coalescence. In the current case dJ/da reflects a combination of both blunting and crack extension which are difficult to separate.

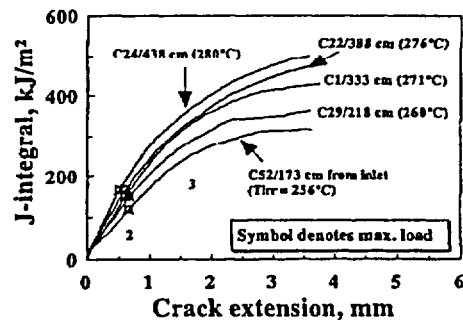
Figure 12 - Optical fractograph showing stable crack growth region of irradiated specimen from surveillance tube F316 ($Cl < 0.2$ wt ppm). Features include wide blunting zones at surface (b), tunnel-shape, flat fracture zone at mid-section (f), wide cup-shaped transition zone (t), and narrow slant fracture developing at surface (s). (Normal view.)



An increase in the irradiation temperature is known to produce a reduction in the α -type dislocation density and the hardening [29]. Thus at the same test temperature, increasing the irradiation temperature is expected to increase the crack growth resistance curve due to the reduction in local crack-tip stress.

Limited results on small specimen tests at 250°C suggest that the J-R curves from material of lower toughness are less sensitive to irradiation temperature than those from higher toughness material [7]. An example of the sensitivity of material from a surveillance tube of higher toughness ($Cl \leq 0.2$ wt ppm, $P \leq 57$ wt ppm) is shown in Figure 13 [7].

Figure 13 - Comparison of J-R curves at 250°C from curved compact specimens sampled from different axial locations of surveillance tube 508 ($Cl \leq 0.2$ wt ppm, $P \leq 57$ wt ppm) Fast neutron fluence of 9 to 11×10^{25} n. m⁻². T_{irr} is the irradiation temperature in °C



In Figure 13 the J-R curves are from small specimens machined from different axial locations along the main section of the tube where the fast neutron flux was relatively constant, varying from only 9 to 11×10^{25} n. m⁻². In all cases the specimens were machined from the same circumferential location, i.e. the 9 o'clock position where the 6 o'clock and 12 o'clock positions refer to the bottom and top of the tube, respectively, viewing from the inlet end. Such results clearly show the increase in crack growth

resistance (stage 2 and 3) with increasing axial distance from the inlet end of the tube [7].

Figures 14 and 15 show plots of the initial crack growth toughness (dJ/da) and maximum load toughness (J_{ml}), respectively, versus irradiation temperature for the same series of tests. The figures show duplicate small specimen test results from each location, as well as the corresponding values of transverse UTS, and provide confirmation of the inverse relationship between crack growth resistance and transverse strength.

Figure 14 - Variation in initial crack growth toughness (dJ/da) and transverse UTS at 250°C with irradiation temperature for curved compact specimens sampled from different axial locations of surveillance tube 508 (Cl ≤ 0.2 wt ppm, P ≤ 57 wt ppm) Fast neutron fluence of 9 to 11 × 10²⁵ n m⁻²

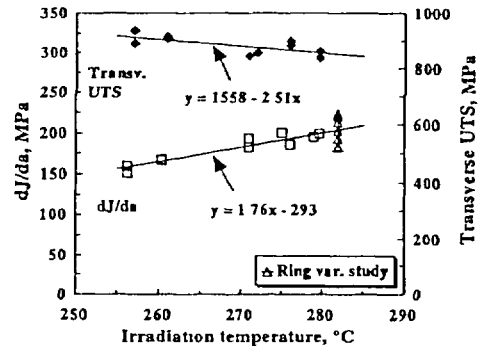
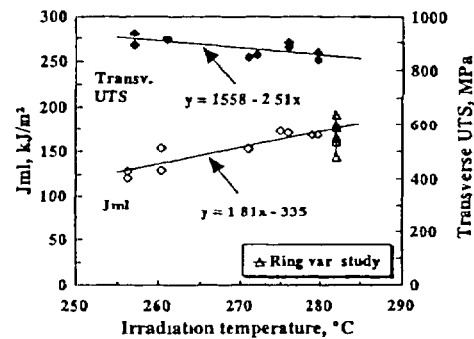


Figure 15 - Variation in J at maximum load (J_{ml}) and transverse UTS at 250°C with irradiation temperature for curved compact specimens sampled from different axial locations of surveillance tube 503 (Cl ≤ 0.2 wt ppm, P ≤ 57 wt ppm) Fast neutron fluence of 9 to 11 × 10²⁵ n m⁻²



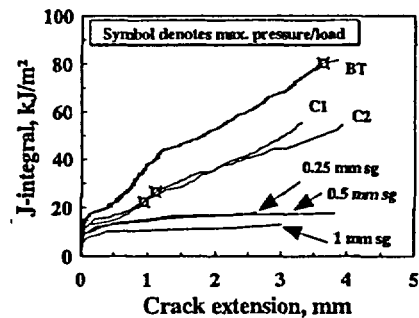
For comparison, Figure 14 and 15 include results from a variability study on a ring of material sampled 463 cm from the inlet. For the latter, the lowest and highest toughness results were obtained for locations closest to the top (12 o'clock) and bottom (6 o'clock) positions, respectively, consistent with the lower local temperature towards the top of the tube as a result of more coolant flowing above the fuel. The range in

results from the ring variability study are generally in agreement with expected behavior based on those obtained from the different axial locations. In particular, the results imply a temperature difference between the top and bottom of the tube of about 20°C, in good agreement with the predicted behavior of CANDU reactor tubes based on modeling studies [30].

Geometry (Constraint) Effects

The previous section has shown the influence of primary variables (particles, deformation characteristics of the matrix) on the J-R curves of irradiated Zr-2.5Nb pressure tube material based on the results of curved compact specimens. However, the majority of J-R curves from small specimens generally lie well below those from burst tests as a result of the higher crack-tip stress (constraint) associated with the former compared with the latter [5,6]. This is demonstrated in Figure 16, which compares the J-R curves from a matched set of small- and large-scale specimens for a surveillance tube of lower toughness. Results from both plane and side-grooved curved compact specimens are shown. The shape of the different J-R curves are consistent with a higher proportion of flat fracture (stage 1) and a lower proportion of transition fracture (stage 2) being observed for the higher constraint, bend-type specimen compared with the burst test specimen.

Figure 16 - Comparison of J-R curves at 250°C from standard burst test and plane and side-grooved curved compact specimens from surveillance tube 98 (Cl = 8 to 10 wt ppm, P = 12 to 15 wt ppm). "sg" refers to depth of side-groove machined on each surface.



At higher levels of toughness the agreement between the J-R curves from small- and large-scale specimens generally improves due to the dominance of the high-energy absorbing transition fracture mode (stage 2) [6]. This is shown in Figure 17, where the use of side-grooves is now less effective in suppressing through-thickness yielding in the curved compact specimens.

However, at all levels of toughness care must be taken in applying the results from small specimens to the actual tube geometry. This is because crack instability in a burst test occurs predominantly by slant fracture (stage 3). Such a fracture mode develops from the two surfaces after the crack-tip stress state is relieved by crack-front tunneling at the mid-section. However, in small specimen testing, such slant fracture may only

Figure 17 - Comparison of J-R curves at 250°C from standard burst test and plane and side-grooved curved compact specimens from surveillance tube 508 (Cl ≤ 0.2 wt ppm, P ≤ 57 wt ppm)

just be in evidence close to the specimen surfaces at the termination of the test. In addition, the out-of-plane bending or bulging associated with a rising-pressure burst test also promotes slant

fracture, especially at higher levels of toughness corresponding to wider crack openings. This effect is responsible for the material dependence of crack-size-effects observed recently for material of higher toughness, i.e. a decrease in crack growth resistance for burst tests with long starter cracks (i.e. > 65 mm) such that the J-R curves lie below those of the matching small specimens (see Figure 18) [7]

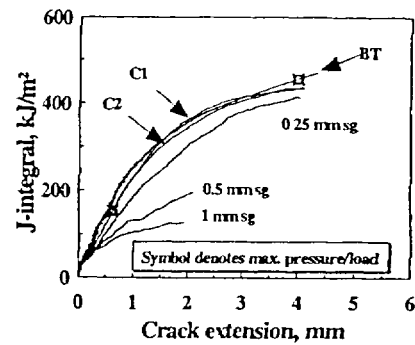
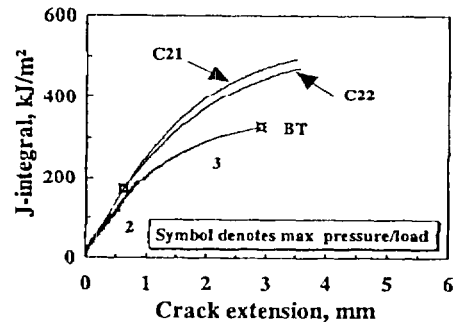


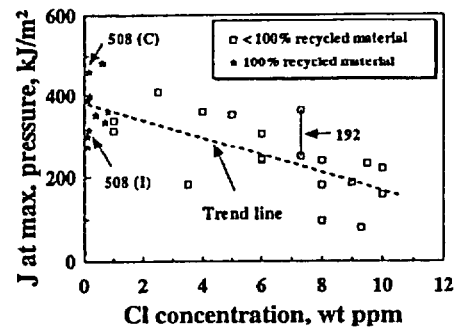
Figure 18 - Comparison of J-R curves at 250°C from burst test with long initial crack size of 71 mm and curved compact specimens from surveillance tube 508 (Cl ≤ 0.2 wt ppm, P ≤ 57 wt ppm).



Factors Influencing J-R Curves from Rising-Pressure Burst Tests

The foregoing has demonstrated the importance of confirming the effect of variables on the J-R curves of the irradiated material by means of large-scale tests, such as rising-pressure burst tests, before applying such results to the in-reactor situation

Figure 19 - J at maximum pressure toughness based on instantaneous crack size (J_{mpi}) from standard burst tests on surveillance tubes versus Cl. Results sorted according to source of ingot material. P of 6 to 60 wt ppm, fast neutron fluence of 7 to $17 \times 10^{25} \text{ n}\cdot\text{m}^{-2}$ and irradiation temperature of 256 to 287°C .



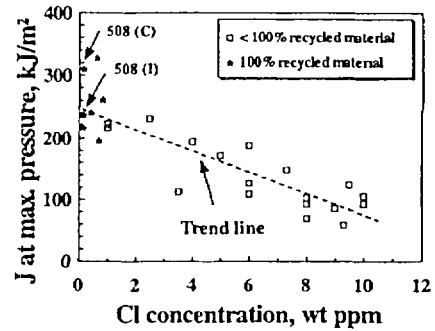
An example is shown in Figure 19 using the results from standard rising-pressure burst tests on surveillance tubes conducted at 250°C . Here the maximum pressure toughness has been calculated based on the instantaneous crack size (J_{mpi}) and plotted versus the chlorine concentration measured from unirradiated archive material. In each case the starter crack was located at the 3 o'clock position to minimize any variations in toughness arising from circumferential variations in irradiation temperature. With the exception of the results for tube 508 (see below), each data point corresponds to the crack instability (maximum pressure) position on the J-R curve for a different tube. The results confirm the influence of bulk chlorine on toughness, with tubes fabricated from 100% recycled material (chlorine concentration < 1 wt ppm) having the highest toughness. However, compared with the small specimen results of J_{mi} versus chlorine in Figure 6, there is considerably more scatter in Figure 19 and insufficient data to determine the true shape of the relationship between J_{mpi} and chlorine concentration. This is in part due to uncertainties in the definition of the instability point, e.g., for tube 192 which exhibited an extended plateau in the pressure versus crack extension curve [6.7]. Such uncertainty (and scatter) in the data can be reduced by using a J value based upon the hoop stress at failure and initial crack size (J_{mpo}), as shown in Figure 20.

The remaining scatter in Figure 19 arises mainly from variability in the following factors.

- 1) Experimental error including uncertainties in the local Cl concentration of the burst test specimen.
- 2) Size and distribution of zirconium phosphide and carbide particles.
- 3) Irradiation hardening due to variations in fluence and irradiation temperature.
- 4) Initial deformation characteristics of the individual tube.

For material with Cl < 1 wt ppm (100% recycled material), variations in the Cl concentration are relatively small, i.e. ≤ 0.1 wt ppm. However, for material with Cl > 1 wt ppm ($< 100\%$ recycled material), variations in Cl ≤ 1 wt ppm have been observed in the GDMS results from duplicate samples, as well as from material sampled from the front and back end of the tube. The largest variation in Cl is observed for tubes

Figure 20 - J at maximum pressure toughness based on initial crack size (J_{mpo}) from standard burst tests on surveillance tubes versus chlorine concentration. Results sorted according to source of ingot material. P of 6 to 60 wt ppm, fast neutron fluence of 7 to $17 \times 10^{25} \text{ n m}^{-2}$ and irradiation temperature of 256 to 287°C .



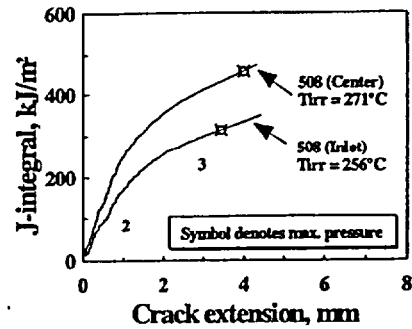
fabricated from billets sampled from the top of an ingot, i.e. the final solidification zone. Such tubes also tend to have a lower average Cl concentration compared with their "sisters" (tubes from the same ingot) due to the reduction in volatile trace elements towards the top of the ingot.

Zirconium phosphide and carbide particles up to several microns in diameter have been observed on many of the fracture surfaces of the burst test specimens [6,7]. This is because the majority of burst tests have been conducted on the original tubes removed from Pickering NGS A Unit 3 and 4 for which the concentration of phosphorus and carbon was generally high, i.e. up to about 80 wt ppm and 180 wt ppm, respectively [22,23]. This is well above the level at which zirconium phosphides and carbides have been identified on fractures, i.e. ≥ 8 wt ppm and 125 wt ppm, respectively [22,23]. However, in comparison to the small specimen results in Figure 6, there are too few burst test results to limit the database, e.g. to tubes with $P < 20$ wt ppm.

The role of irradiation hardening in reducing the J-R curves obtained from burst tests has been confirmed by tests on two sections of tube 508. This tube was fabricated from 100% recycled material and had a phosphorus concentration up to 57 wt ppm. The J-R curve results are shown in Figure 21 for the two sections taken from the center and inlet regions of the pressure tube [7]. The fast neutron fluence and irradiation temperature are $11.1 \times 10^{25} \text{ n m}^{-2}$ and 271°C for the former and $9.3 \times 10^{25} \text{ n m}^{-2}$ and 256°C for the latter. For these tests the difference in fast neutron fluence is small and the reduction in crack growth resistance in Figure 21 arises mainly from the variation in transverse strength. The latter was measured after each burst test at the 9 o'clock position (i.e. diametrically opposite the starter flaw), giving values of 852 and 913 MPa for the center and inlet/center test sections, respectively. The relative magnitude of this effect of irradiation hardening on the maximum pressure toughness parameters, J_{mp} and J_{mpo} , is indicated in Figures 19 and 20, respectively. Such results are very similar to the previous results obtained from the corresponding small specimens (see Figures 13 to 15).

Early attempts to rationalize all the burst test specimen results from the original Pickering 3 and 4 tubes solely on the basis of chlorine concentration and transverse

Figure 21 - Comparison of J-R curves at 250°C from standard burst tests sampled from two different axial locations of surveillance tube 508 (CI ≤ 0.2 wt ppm, P ≤ 57 wt ppm). T_{irr} is the irradiation temperature in °C. The difference in fast neutron fluence is relatively small and varied from 9 to 11×10^{25} n·m⁻² for material sampled from the center and the inlet end of the pressure tube, respectively.



strength proved reasonably successful (see Figure 16 in reference 7). However, as results from tubes installed in later reactors have become available, it is now clear that such relationships are sensitive to the initial deformation characteristics of the individual tube, e.g. initial yield stress and twinning stress. For example, variability in yield stress can arise from variations in the oxygen and niobium concentrations [31] as well as the initial dislocation density [31], grain structure and texture [32]. Such variations can result from minor changes in ingot chemistry, fabrication route and extrusion variables [33-35].

The sensitivity of the crack growth resistance of irradiated Zr-2.5Nb pressure tube material to the initial deformation properties of the tube at 250°C is due to the similarity of the yield and twinning stresses in the operating temperature regime after irradiation [26]. These parameters determine not only the local crack-tip stress for void nucleation, but also the propensity for deformation by dislocation channeling and/or twinning compared with slip, i.e., for strain localization. Such strain localization contributes to the failure of ligaments between neighboring voids (stage 1 and 2 crack growth) and controls the onset of slant fracture at the surface (stage 3). Therefore, removal of void nucleation sites is particularly beneficial. This is because it increases the effective wall thickness for local ligament failure, and also reduces the extents of stable crack growth and tunneling which orient the crack front for easy development of the "sliding-off" mechanism.

Work is now underway to extend the database of burst test results and to determine the quantitative relationship between crack growth resistance and CI using material with intermediate levels of CI and low levels of zirconium phosphide. The initial deformation characteristics of the burst test material are also being studied with the aim of elucidating the microstructural factors responsible for the variability in results in Figures 19 and 20. This should allow further rationalization of the results obtained from different reactor units as well as the potential for producing further improvements in crack growth resistance.

Summary

The key factors controlling the crack growth resistance of irradiated Zr-2.5Nb pressure tube material at 250°C at low levels of hydrogen/deuterium have been reviewed using the current database of small- and large-scale specimen results from different CANDU reactor pressure tubes. The review highlights the role of the following factors.

- 1) The mixed-mode nature of the crack growth process in the irradiated, thin-walled material, i.e. flat, transition and slant fracture modes
- 2) The relative proportions and energy-absorbing capacities of the different fracture modes, which is determined by the ease of void nucleation, growth and coalescence ahead of the crack tip
- 3) The role of primary void nucleating particles, e.g. Zr-Cl-C (complex carbide), zirconium phosphide and carbide, the beneficial effects of eliminating them. For example, the removal of chlorine and Zr-Cl-C particles by quadruple vacuum-arc-melting.
- 4) The deformation characteristics of the matrix, e.g. yield stress and twinning stress, which control the tendency for void nucleation, growth, coalescence and strain localization (work-softening)
- 5) The specimen geometry, e.g. crack size, geometry and material effects in influencing the relationship between the J-R curves obtained from different specimens.

The current results from curved compact specimens, having a low concentration of zirconium phosphide ($P < 20$ wt ppm), suggest a limiting level of Cl (about 3 wt ppm) above which no further significant degradation in the crack growth resistance occurs. Such results require confirmation using rising-pressure burst tests on material with intermediate levels of Cl and low levels of zirconium phosphide.

The influence of minor variations in tube fabrication on the deformation behavior of Zr-2.5Nb pressure tube material (item 4 above) also requires study. This should allow further rationalization of the results obtained from different reactor units as well as the potential for producing further improvements in crack growth resistance.

Acknowledgments

Many individuals contributed to the production of the results reported in this work over a number of years. In particular, thanks are due to R. Behnke, G. R. Brady, G. R. Kasprick, G. C. Longhurst, A. R. Reich, J. M. Smeltzer, A. K. West, as well as the hot cell staff at the Whiteshell and Chalk River Laboratories for their technical assistance. Special thanks go to R. R. Bawden and J. C. Owens at Chalk River for retrieval and shipment of surveillance material for testing and to G. D. Moan for supplying unirradiated archive material for testing. Funding of this work by the CANDU Owners Group (COG) under Work Packages 3192, 3305, 6506 and 6536 and contract COG-0013613 is gratefully acknowledged.

References

- [1] Cheadle, B. A., Coleman, C. E., and Licht, H., *Nuclear Technology*, Vol. 57, 1982, pp. 413-425.
- [2] Chow, C. K. and Simpson, L. A., *Fracture Mechanics: Eighteenth Symposium, ASTM STP 945*, D. T. Read, R. P. Read, Eds., American Society for Testing and Materials, West Conshohocken, PA, 1988, pp. 419-439.
- [3] Simpson, L. A.; Chow, C. K., and Davies, P. H., CANDU Owners Group Report No. COG-89-110-I, AECL, September 1989.
- [4] Himbeault, D. D., and Davies, P. H., CANDU Owners Group Report No. COG-98-161-I, AECL, January 1999.
- [5] Davies, P. H. Shewfelt, R. S. W. and Järvinen, A. K., *Constraint Effects in Fracture: Theory and Applications, ASTM STP 1244*, M. Kirk and A. Bakker, Eds., American Society for Testing and Materials, West Conshohocken, PA, 1995, pp. 392-424.
- [6] Davies, P. H. and Shewfelt, R. S. W., *Zirconium in the Nuclear Industry: Eleventh International Symposium, ASTM STP 1295*, E. R. Bradley and G. P. Sabol, Eds., American Society for Testing and Materials, West Conshohocken, PA, 1996, pp. 492-517.
- [7] Davies, P. H. and Shewfelt, R. S. W., *Zirconium in the Nuclear Industry: Twelfth International Symposium, ASTM STP 1354*, G. P. Sabol and G. D. Moan, Eds., American Society for Testing and Materials, West Conshohocken, PA, 2000, pp. 356-376.
- [8] Kiefner, J. F., Maxey, W. A., Eiber, R. J. and Duffy, A. R., *Progress in Flaw Growth and Fracture Toughness Testing, ASTM STP 536*, American Society for Testing and Materials, West Conshohocken, PA, 1973, pp. 461-481.
- [9] Rice, J. R., *Journal of Applied Mechanics, Transactions of ASME*, Vol. 35, 1968, pp. 379-386.
- [10] Turner, C. E., *Size Effects*, Mechanical Engineering Publications, London, 1986, pp. 25-31.
- [11] Ernst, H. A., *Elastic-Plastic Fracture. Second Symposium, Volume I, ASTM STP 803*, C. F. Shih and J. P. Gudas, Eds., American Society for Testing and Materials, 1983, pp. 1191-1213.
- [12] Turner, C. E., *Fracture Mechanics: Twenty Second Symposium (Volume I), ASTM STP 1131*, H. A. Ernst, A. Saxena and D. L. McDowell, Eds., American Society for Testing and Materials, 1992, pp. 71-92.
- [13] Davies, P. H., *Fatigue and Fracture Mechanics: Twenty Eighth Volume, ASTM STP 1321*, J. H. Underwood, B. D. MacDonald and M. R. Mitchell, Eds., American Society for Testing and Materials, West Conshohocken, PA, 1997, pp. 535-561.
- [14] Chow, C. K. and Simpson, L. A., *Fracture Mechanics: Nonlinear Fracture Mechanics- Volume II-Elastic-Plastic Fracture, ASTM STP 995*, J. D. Landes, A. Saxena and J. G. Merkle, Eds., American Society for Testing and Materials, West Conshohocken, PA, 1989, pp. 537-562.

- [15] Thomason, P. F , *Ductile Fracture of Metals*, Pergamon Press, Oxford, Ch 1 to 4, 1990, pp 1-114
- [16] Ritchie, R. O , Server, W. L , and Wullaert, R A , *Metallurgical Transactions A*, Vol 10A, 1979, pp. 1557-1570.
- [17] Hutchinson, J. W., and Tvergaard, V , *Fracture Mechanics, Perspectives and Directions (Twentieth Symposium)*, ASTM STP 1020, R P. Wei and R P Gangloff, Eds , American Society for Testing and Materials, 1989, pp 61-83.
- [18] Shih, C. F , *Journal of Mechanics and Physics of Solids*, Vol. 29, 1981, pp. 305-326
- [19] Dodds, R H , Shih, C. F , and Anderson, T , *International Journal of Fracture*, Vol 64, 1993, pp 101-133.
- [20] Wallace, A. C , Shek, G K , and Lepik, O E , *Zirconium in the Nuclear Industry: Eighth International Symposium, ASTM STP 1023*, L F . Van Swam and C. M Eucken, Eds , American Society for Testing and Materials, 1989, pp. 66-88
- [21] Aitchison, I. and Davies, P H., *Journal of Nuclear Materials*, Vol 203, 1993, pp 206-220
- [22] Davies, P. H , Hosbons, R. R , Griffiths, M and Chow, C K , *Zirconium in the Nuclear Industry Tenth International Symposium, ASTM STP 1245*, A M. Garde and E. R Bradley, Eds , American Society for Testing and Materials West Conshohocken, PA, 1994, pp 135-167
- [23] Davies, P H , Aitchison, I , Himbeault, D D , Jarvine, A K. and Watters, J F., *Fatigue and Fracture of Engineering Materials and Structures*. Vol 18. 1995, pp 789-800
- [24] Theaker, J. R., Choubey, R , Moan, G D , Aldridge, S. A., Davies, L., Graham, R. A. and Coleman, C E , *Zirconium in the Nuclear Industry: Tenth International Symposium, ASTM STP 1245*, A. M. Garde and E. R. Bradley, Eds , American Society for Testing and Materials West Conshohocken, PA, 1994, pp. 221-242
- [25] Dutton, R.. AECL Report No. 9930, 1989 April
- [26] Himbeault, D D , Chow, C. K. and Puls, M P , *Metallurgical and Materials Transactions A*, Vol 25A, 1994, pp 135-145
- [27] Hosbons, R. R , Davies, P H Griffiths, M Sagat, S and Coleman, C. E , *Zirconium in the Nuclear Industry: Twelfth International Symposium, ASTM STP 1354*, G. P. Sabol and G. D. Moan, Eds., American Society for Testing and Materials, West Conshohocken, PA, 2000, pp 122-138.
- [28] Chow, C. K., Coleman, C. E , Hosbons, R. R , Davies, P. H , Griffiths, M , and Choubey, R , *Zirconium in the Nuclear Industry. Ninth International Symposium, ASTM STP 1132*, C. M Eucken and A. M Grade, Eds , American Society for Testing and Materials, West Conshohocken, PA, 1992, pp. 246-275
- [29] Sagat, S , Coleman, C. E , Griffiths, M , and Wilkins, B. J S., *Zirconium in the Nuclear Industry Tenth International Symposium, ASTM STP 1245*, A M. Garde and E. R Bradley, Eds , American Society for Testing and Materials, West Conshohocken, PA, 1994, pp 35-61

- [30] Tabatabai, M. and Byrne, T , Ontario Hydro Report No A-NFC-94-34-K, 1994 April.
- [31] Winton, J., Murgatroyd, R. A., Watkins, B., and Nichols, R. W., *Transactions of the Japanese Institute of Metals*, Volume 9 Supplement, 1968, pp. 630-636
- [32] Cheadle, B., and Ells, C. E., *Transactions of the Metallurgical Society of AIME*, Vol 233, 1965, pp. 1044-1052
- [33] Cheadle, B , *Zirconium in the Nuclear Industry, ASTM STP 633*, A. L. Lowe, Jr., G. W. Parry, Eds , American Society for Testing and Materials West Conshohocken, PA, 1977, pp. 457-485.
- [34] Holt, R A and Aldridge, S. A , *Journal of Nuclear Materials*, Vol 135, 1985, pp. 246-259
- [35] Choubey, R., Aldridge, S. A , Theaker, J. R., Cann, C. D., and Coleman, C. E., *Zirconium in the Nuclear Industry: Eleventh International Symposium, ASTM STP 1295*, E R. Bradley and G. P. Sabol, Eds , American Society for Testing and Materials West Conshohocken, PA, 1996, pp. 657-675.

Experiences in Examining and Dispositioning Flaws In Zr-2.5Nb Pressure Retaining CANDU Reactor Components

Andrew Celovsky
AECL – Chalk River Laboratories
Chalk River, Ontario, KOJ 1P0, Canada

John Slade
NB Power
Point Lepreau, New Brunswick, E0G 2H0, Canada

ABSTRACT

CANDU¹ reactors use Zr-2.5Nb alloy pressure tubes, as the primary pressure boundary within the reactor core. These components are subject to periodic inspection and material surveillance programs. Occasionally, the inspection program uncovers a flaw, whereupon the flaw is assessed as to whether it compromises the integrity of the pressure-retaining component. In 1998, such a flaw was observed in one pressure tube of a reactor. Non-destructive techniques and analysis were used to form a basis to disposition the flaw, and the component was fit for a limited service life. This component was eventually removed from service, whereupon the destructive examinations were used to validate the disposition assumptions used. Such a process of validation provides credibility to the disposition process. This paper reviews the original flaw and its subsequent destructive evaluation.

NOMENCLATURE

[H] _{eq}	hydrogen equivalent concentration in wt. ppm. Given that CANDU reactor use heavy water (D ₂ O) as the primary coolant, the convention for CANDU reactors is to consider hydrogen as the protium isotope only, to distinguish it from the deuterium isotope. Then, $[H]_{eq} = [H] + \frac{1}{2}[D]$ where [H] and [D] are the protium and deuterium isotope concentrations in wt. ppm, respectively.
R	gas constant, 8.314 J/K
T	temperature in Kelvin
Zr	Zirconium
Nb	Niobium
TSSD	Terminal Solid Solubility of hydrogen in Zr-2.5Nb material upon Dissolution
A ₁ , A ₂	Constants

INTRODUCTION

There are currently 32 CANDU nuclear reactors operating or under construction worldwide. A key feature of the CANDU reactor is the 380 to 480 horizontal Zr-2.5Nb pressure tubes, containing the fuel bundles, through which the primary heavy water coolant flows. These Zr-2.5Nb pressure tubes are a primary pressure-retaining component, and during service are subjected to operational temperature of 249 to 313°C, coolant pressures of 9.6 to 11.2 MPa, and neutron flux up to 3.7×10^{17} n/m²/s. Occasionally, routine inspection of the pressure tubes will uncover a service related flaw, which must be assessed to insure that safe operation of the reactor is not compromised. This paper describes the assessment of one such flaw, and the verification of the assessment parameters during its destructive examination after removal from service. This type of assessment and verification are used to ensure that the Zr-2.5Nb pressure tubes continue to perform their function of containing the primary heavy water coolant under operational conditions.

The flaw was discovered during a routine inspection of a fuel channel in June 1998. The flaw was likely the result of foreign material, which entered the primary heat transport system during a major reactor service outage in 1995. Once in the primary heat transport system, the foreign material scored the inside surface of the pressure tube, most likely during a re-fuelling operation for that channel (Table 1). After discovery of the flaw, an assessment of the flaw was conducted and the flaw was not considered detrimental to the safety of the reactor. The pressure tube containing the flaw continued in-service, until the pressure tube could be replaced during a convenient planned outage. The flaw was destructively examined to verify the parameters of the flaw assessment. Such information can be used to assess similar flaws in other reactor units.

¹ Registered trademark of Atomic Energy of Canada Limited

Table 1: Significant Dates Relating to Flaw

ACTIVITY	DATE	SIGNIFICANCE
Reactor Re-Start after Service Outage	Dec 1995	Outage when foreign material inadvertently introduced into the Primary Heat Transport Circuit
Re-Fueling Dates for given Location	Dec. 1995 Nov 1996 May 1997	Movement of fuel bundles after inadvertent introduction of foreign material into Primary Heat Transport Circuit
Inspection of Pressure Tube	Jan. 1998	Initial discovery of the flaw, at 13.0 Full Power Years of operation.
Removal of Pressure Tube Containing the Flaw	June 1998	At 13.3 Full Power Years of operation

ASSESSMENT OF THE FLAW

The major concern regarding flaws in CANDU reactor pressure tubes is the potential of the flaw to initiate and propagate a crack by Delayed Hydride Cracking (DHC). This is a mechanism whereby hydrogen, dissolved in the pressure tube, preferentially precipitates at the high stress region produced at the flaw tip, exacerbated by reactor cool-downs. With each successive reactor cool-down, more hydrogen, as a brittle hydride platelet, precipitates at the flaw tip. Furthermore the hydride platelets precipitate perpendicular to the tensile hoop stress. When a critical condition exists, such as the hydride platelets reaching a certain size, the brittle hydride platelets can no longer support the tensile hoop stress and a crack initiates. With further thermal cycles from reactor start-up and shut-downs, and subsequent hydride precipitation, the crack front can propagate.

During a periodic in-service inspection a flaw was discovered in one pressure tube, on the inside surface at the 6 o'clock orientation. At the time of discovery, the pressure tube had seen 13.0 Full Power Years (FPY) of operation. The flaw was conservatively assessed and found to be acceptable for at least 4 additional thermal cycles and a further 1.6 FPY of operation, for a total of 14.6 FPY of operation [1]. The process to assessing a flaw involved: first, defining the existing flaw condition, second, determining the operating conditions that the flaw is to experience over the assessment period, and third, determining the condition of the flaw at the end of the assessment period.

In terms of defining the existing flaw, the principle parameters are length, width, depth, and whether the flaw tip is blunt or sharp. Such information is obtained from non-destructive inspection data. Second, the expected operating conditions for the period of assessment are established, including the expected number of thermal cycles, the total operating time, and the operating and any residual stresses. Third, the expected operating conditions are applied to the flaw, thereby establishing the flaw condition at the end of the assessment period.

Two significant operating condition details were assessed for the flaw under consideration. First, the flaw was located in the inlet rolled joint region where residual stresses are known to exist in the pressure

tube as a result of forming the rolled joint, which connects the pressure tube to the end fitting. Second, the manner by which the flaw was formed could induce additional residual stresses. The latter condition was a new consideration for a flaw in a CANDU reactor pressure tube.

The length of the assessment period of this flaw provided sufficient time for a planned and orderly removal of the pressure tube, with minimal disruption to station operation. The pressure tube containing the flaw was ultimately removed after 13.3 FPY including one additional thermal cycle, well within the assessment period of 14.6 FPY and 4 additional thermal cycles. Once removed, the flaw in the pressure tube was destructively examined, and compared to the assessment values (Table 2).

Table 2: Comparison of Various Assessment Parameters with Measured Values

PARAMETER	ASSESSMENT VALUE AT 14.6 FPY	MEASURED VALUE AT 13.3 FPY	COMMENT
Local Operating Temperature at Flaw	267°C	267°C	At inlet end of the pressure tube
Maximum Flaw Depth	0.32 mm	0.29 mm	Assessment values conservative
Hydrogen (protium) Conc'n	7 ¹ ppm	11 ppm	
Deuterium Conc'n	54 ¹ ppm	54 ppm	
Hydrogen Equivalent, Conc'n	34 ppm	38 ppm	TSSD at Normal Operating Conditions of 267°C is 38 ppm
Maximum Tensile Residual Stress due to Flaw (Hoop direction)	400 MPa	74 MPa	Assessment values conservative
Flaw Type	Short sharp & long blunt portions	Short sharp & long blunt portions	
As-rolled Residual Stress	100 MPa ²	79 MPa ³	Assessment Values Conservative

1. Estimated value based on samples from a similar tube under similar conditions, including estimated deuterium pick-up to the end of the assessment period.
2. Estimated in the as-rolled condition, which would be expected to relax to -26.5 MPa due to operation.
3. Calculated based on the measured rolled joint profile.

A critical component of the flaw assessment, and one of the most difficult parts of the assessment to quantify, was the stresses immediately under the flaw itself. The flaw was produced by foreign material in a ploughing, rather than a cutting action, along the bottom of the pressure tube, 6 o'clock. It would be expected that a flaw produced in such a manner would result in high residual stresses immediately under the flaw, as the foreign material distorts the pressure tube material.

As identified previously, hydride platelets will tend to selectively precipitate perpendicular to the local tensile stresses. The introduction of a flaw resulted in two items to be considered. First, the flaw would act as a stress riser to concentrate the hoop stresses from both normal operation and from any remaining residual manufacturing stresses. Second, the flaw formation process itself could result in stresses near the flaw. Previous experiences with flaws in CANDU reactors were concerned with the combination of the operating and residual stresses at a flaw tip. This flaw introduced a third stress component: stress from the flaw formation process.

At the operating temperature of 267°C, the yield stress of the pressure tube material is approximately 800 MPa [2]. Also, the upper limit of the combined service and residual stresses at the flaw location was estimated at 400 MPa. Thus, the conservative maximum residual stress due to the flaw formation, without yielding of the material would be 400 MPa (i.e. 800 - 400 MPa). Based on this conservative assumption, the flaw was found to satisfy the acceptance criteria for minimum safety margins for 4 additional thermal cycles and a further 1.6 FPY of operation [3].

An equally important consideration in the assessment was the hydride concentration in the flaw region. Hydride ratcheting is the process of hydride growth and partial dissolution during cooling and heating, respectively [4]. For hydride ratcheting to occur, the local hydrogen concentration must exceed the Terminal Solid Solubility (TSS) limit as given by Equation 1 [5].

$$[H]_{eq} = A_1 \exp \{-A_2 / (RT)\} \quad (1)$$

At the flaw location near the inlet end of the pressure tube, the local operating temperature is 267°C, which corresponds to a TSS limit of 38 ppm. Thus, at or below 38 ppm, hydride concentration through ratcheting is not expected to occur. Thus, DHC initiation and propagation is also not expected. Also, the shutdown, or cool-down, cycle of the reactor in terms of decreasing the temperatures and pressures (operating stress) is structured to avoid hydride ratcheting.

DESTRUCTIVE ANALYSIS

To confirm the analytical assessment of the flaw, there were two key parameters to measure. First were the stresses due to the flaw formation process. Second was the local hydride concentrations and evidence of hydride accumulation at the flaw tip. The general features of the flaw are shown in Figure 1.

Measurement of the Residual Stresses due to the Flaw Formation Process

The flaw region was isolated into a single piece of material approximately 165 mm in the axial direction x 35.4 mm in the circumferential direction and 4.2 mm thick. The sectioning process relieves any residual hoop stresses, thereby leaving only the stresses due to the flaw formation process. A neutron diffraction technique was used to measure the stresses under the flaw at six depths through the wall thickness at the deepest region of the flaw [6]. The residual stresses were measured in a sample volume of 0.3 mm x 0.3 mm x 2 mm.

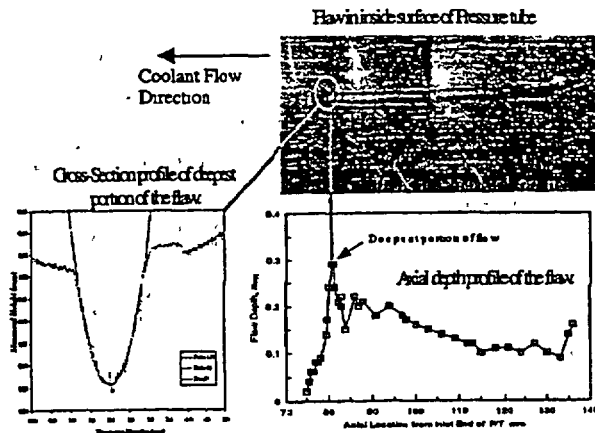


Figure 1: a) Plan view of in-service flaw
 b) Axial depth profile of flaw
 c) Cross-Section of deepest portion of flaw with root radii

The through-wall residual hoop stress profile under the flaw was compressive immediately under the flaw on the inside surface, becoming tensile at a depth of about 1 mm, then tending towards zero at the outside surface (Figure 2). The maximum measured hoop stress was 74 MPa, which was significantly lower than the conservative estimate of 400 MPa. However, the measured value of 74 MPa would be expected to be somewhat lower than the as fabricated value due to relaxation from its time at operating temperature. This was a significant result, insofar as establishing the magnitude of the residual stresses associated with the formation of this type of flaw.

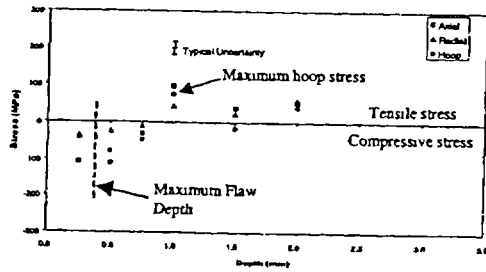


Figure 2: Through-wall residual stress profile in the vicinity of the deepest portion of the flaw.

Measurement of the Hydrogen Concentration

Small pellets were obtained from the pressure tube material, and subsequently analysed for their hydrogen and deuterium concentrations [7]. The axial profile of the hydrogen equivalent concentration is presented in Figure 3, and shows the steep concentration gradient typical for the inlet region of a pressure tube. At the deepest region of the flaw, the hydrogen equivalent concentration was determined to be 38 ppm. This value did not exceed the TSS limit at the inlet operating temperature of 267°C, so hydride accumulation through ratcheting is not expected to occur.

The lack of any hydride accumulation was confirmed in a metallographic cross-section through the deepest regions of the flaw (Figure 4a), which showed no evidence of hydride accumulation at the flaw tip. A comparison with a previous laboratory test specimens (Figure 4b) illustrates the appearance of the accumulation of hydrides at a flaw tip.

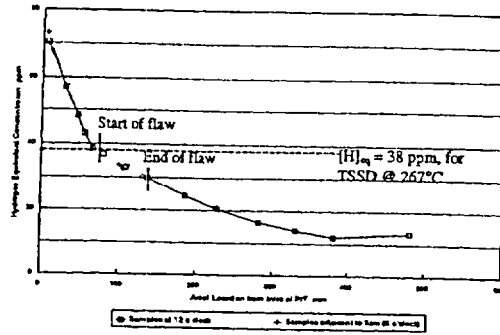


Figure 3: Hydrogen equivalent concentration, both adjacent to the flaw at 6 o'clock and at 180 degrees from the flaw at 12 o'clock.

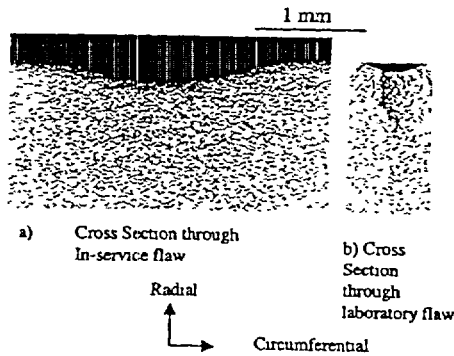


Figure 4: Metallographic cross-section of flaw
a) Through in-service flaw, without any evidence of hydride accumulation, near maximum flaw depth location
b) Through flaw from a laboratory test specimen with clear evidence of hydride accumulation at the flaw tip.

CONCLUSIONS

A flaw was discovered during a routine inspection of a fuel channel in a pressure tube. Conservative assessments of the flaw indicated the flaw was not detrimental to the safety of the reactor for the specified operating period. Before the end of the assessment period, the pressure tube containing the flaw was removed from service and destructively examined. This allowed direct measurement of various parameters, which were then compared to the values estimated for the assessment. In general, the assessment parameters were conservative and the flaw was not detrimental to the safety of the reactor. Measurements of the various parameters can be used to develop more representative estimates of the bounding conditions in assessing similar types of flaws in future assessments.

REFERENCES

1. Wong, H., et al., "The Role of Leak-Before-Break in Assessments of Flaws Detected in CANDU Pressure Tubes," *J. Press. Vess. Piping* 1990, Vol. 43, pp. 23-37.
2. Hosbons, R.R., Davies, P.H., Griffiths, M., Sagat, S., and Coleman, C.E., "Effect of Long-Term Irradiation on the Fracture Properties of Zr-2.5Nb Pressure Tubes," *ASTM 12th Int. Symp. On Zirconium in the Nuclear Industry*, ASTM STP 1354, American Society for Testing and Materials, 2000, pp. 122-138.
3. Sagat, S., Shi, S. Q., and Puls, M.P., "Crack Initiation Criterion at Notches in Zr-2.5Nb Alloys," *Materials Science and Engineering*, A176, 1994, pp. 237-247.
4. Eache, R.L., D.R. Metzger, D.R., and Leger, M., "The Thermal Ratcheting of Hydrogen in Zirconium-Niobium - An Illustration Using Finite Element Modelling," *Scripta Metallurgica et Materialia* Vol. 29, 1993, pp. 335-340.
5. Kearns, J.J., "Terminal Solubility and Partitioning of Hydrogen in the Alpha Phase of Zirconium, Zircaloy-2 and Zircaloy-4," *Journal of Nuclear Materials*, Vol. 22, 1967, pp. 292-303.
6. Rogge, R.B., Holden, T.M., and Root, J.H., "Standard Diffractometer Set-Up Procedure for Applied Neutron Diffraction for Industry Experiments," 1996, AECL Report RC-1652.
7. Green, L.W., Bickel, G.A., Leeson, P.K., James, M.W.D., Lamarche, T.G., Michel, H., "A Hot Vacuum Extraction Mass Spectrometric System for Determination of H and D in Zirconium," 1996, AECL Report AECL-11342.

**CRACK INITIATION BEHAVIOUR IN SMALL ROOT RADIUS Zr-2.5Nb
PRESSURE TUBE SPECIMENS UNDER MONOTONIC AND CYCLIC
LOADING CONDITIONS AT AMBIENT TEMPERATURE**

Edward T.C. Ho
Kinectrics Inc.
800 Kipling Avenue
Toronto, Ontario
M8Z 6C4, Canada

Rameshwar Choubey
Atomic Energy of Canada Ltd.
Chalk River Laboratories
Chalk River, Ontario
K0J 1J0, Canada

Gordon K. Shek
Kinectrics Inc.
800 Kipling Avenue
Toronto, Ontario
M8Z 6C4, Canada

Stefan Sagat
Atomic Energy of Canada Ltd.
Chalk River Laboratories
Chalk River, Ontario
K0J 1J0, Canada

Douglas A. Scarth
Kinectrics Inc.
800 Kipling Avenue
Toronto, Ontario
M8Z 6C4, Canada

ABSTRACT

To evaluate crack initiation from small radius flaws in Zr-2.5Nb pressure tubes in operating CANDU¹ reactors, a number of crack initiation tests under both monotonic and cyclic loading in notched tension specimens have been carried out at ambient temperature. Test specimens were machined with the tensile axis parallel to the circumferential or transverse direction in both as-fabricated and ex-service pressure tube materials. The test specimens were first pre-conditioned by subjecting them to a notch-tip creep stress relaxation cycle, and a subsequent hydride formation cycle whereby notch-tip hydrides are produced. Some specimens with no notch-tip hydride were also tested. Test specimens were instrumented with acoustic emission (AE) and DC potential drop (PD) monitoring systems for detection of crack initiation and growth. Test results indicated the following trends: (a) the existence of notch-tip hydride lowers the crack initiation stress, with the hydride effect being much stronger under monotonic loading than under cyclic loading; (b) the greater the hydrogen concentration, the lower the notch-tip hydride crack initiation stress under monotonic loading; (c) for a given alternating elastic peak stress, the smaller the root radius the greater the resistance to crack initiation, (d) as expected, the number of cycles to crack initiation is a strong function of the alternating elastic peak stress, for a given specimen geometry. An analysis of the test results and their impact on flaw evaluation methodology for Zr-2.5Nb pressure tubes is described.

INTRODUCTION

The CANDU (CANada Deuterium Uranium) power reactor is a pressurized heavy water reactor that uses natural uranium dioxide fuel. Depending on the particular design, the reactor core consists of a lattice of 380, 390 or 480 horizontal pressure tubes which are fabricated from a cold worked and stress-relieved Zr-2.5Nb alloy. These pressure tubes contain fuel bundles. The pressure tubes are approximately 6 m long with a 103 mm inside diameter and a 4 mm wall thickness. These tubes are susceptible to a phenomenon known as Delayed Hydride Cracking (DHC). The highly textured material is susceptible to DHC when there is diffusion of hydrogen atoms to a service-induced flaw under a stress gradient, precipitation of hydride platelets on favourable habit planes in the zirconium alloy matrix material, and development of a hydrided region at the flaw tip. The hydrided region can fracture under a sufficient stress to the extent that a crack forms and DHC is said to have initiated. This crack can then grow by the DHC mechanism. The process of DHC is described by Dutton *et al* [1] and by Cheadle *et al* [2]. Hydrogen is present in the manufactured pressure tube as an impurity element, while during operation, pressure tubes can absorb a fraction of the deuterium generated from the corrosion reaction of zirconium with the heavy water coolant, thus increasing the equivalent hydrogen concentration ($H_{eq} = H + \frac{1}{2} D$) in the tube with time.

The types of service-induced flaws found during in-service inspection of Zr-2.5Nb alloy pressure tubes include fuel bundle scratches, crevice corrosion marks, fuel bundle bearing pad fretting flaws and debris fretting flaws. To date, experience with fretting flaws has been favourable, and crack growth from an in-service fretting flaw has not been detected. The fretting flaws are evaluated for crack initiation by DHC and fatigue. It has to be demonstrated

¹ CANada Deuterium Uranium

that crack initiation of the flaw tip hydrided region will not occur by an overload or a fatigue mechanism. Overload is defined as loading of the hydrided region above the hydride formation stress.

The current test program was undertaken with the objective of providing an experimental database for very small radius (VSR) flaws to evaluate fatigue initiation and overload on a flaw tip hydrided region. A review of the existing fatigue data [3] for Zr-2.5Nb pressure tube material indicated that only very blunt (root radii of 0.12 mm and 0.50 mm) flaws with low hydrogen concentrations (about 12 wt. ppm) have been investigated to date. Therefore, the test program was planned to supply information suitable for use in the analysis of in-service produced flaws in operating pressure tubes that reflects our current understanding of flaw geometry, including very small radii, and the effects of cyclic loading and overloads on flaws with notch-tip hydrides. Consequently, the test program was designed to obtain the following information:

- (a) behaviour of flaws in pressure tube material with bulk equivalent hydrogen concentrations in the main body of tube of up to 45 ppm;
- (b) new crack initiation data due to overloads and cyclic loading for VSR flaws;
- (c) the effects of hydrogen concentration, creep relaxation and hydride formation history, including load reduction, on the formation and morphology of notch-tip hydrides.

EXPERIMENTAL

Material

Two types of Zr-2.5Nb pressure tube material were used to machine test specimens in the present study. Material from an as-fabricated production-grade Zr-2.5Nb pressure tube was used for the unirradiated specimens. Material from an ex-service pressure tube with a fast neutron fluence of $0.58 \times 10^{26} \text{ n/cm}^2$ ($E > 1 \text{ MeV}$) was used to machine the pre-irradiated specimens. The available materials properties data for these two pressure tubes are listed in Table 1 [4,5].

Table 1: Summary of Materials Properties Data for Unirradiated and Pre-irradiated Pressure Tube Materials

Materials Property	Unirradiated Material	Pre-irradiated Material
0.2% Yield Strength (RT)	785 MPa	1043 MPa
Ultimate Tensile Strength (RT)	805 MPa	N/A*
0.2% Yield Strength (250°C)	559 MPa	791 MPa
Ultimate Tensile Strength (250°C)	609 MPa	798 MPa

* N/A – Not Available

Test Facilities

Monotonic and cyclic tests were conducted on unirradiated pressure tube material using a standard MTS servohydraulic Materials Test System. This system consists of a MTS 250 kN capacity series 810 load frame with a MTS model 442 control package. A 25 kN capacity load cell calibrated over all four ranges (10%, 20%, 50% and 100%) was used for monitoring specimen loading. Calibrated type-K

thermocouples were used for ambient and specimen temperature monitoring. The data acquisition system consists of a HP model 3852A capable of monitoring and recording microvolt signals from the DC potential drop (PD) leads, millivolt signals from the type-K thermocouples and voltage signals from the 25 kN load cell. The crack initiation and growth in the notched specimens was monitored by a DC PD technique. An acoustic emission (AE) monitoring system was added to complement the PD monitoring system, especially for the monotonic loading tests.

Monotonic and cyclic tests were conducted on pre-irradiated pressure tube material using two MTS servohydraulic Materials Test Systems set up in two hot cells at Chalk River Laboratories. Each system is equipped with a 20 kN load cell with a calibrated 10 kN load cell cartridge for tension and compression. The load cycle pattern is generated by a program through a model 458 20 Micro Profiler. An IBM PC with a Data Translation data acquisition board stores data from channels carrying potential drop and reference potential drop signals, load, stroke, time, data point number and cycle number during a given test. Calibrated type-K thermocouples are used for ambient and specimen temperature monitoring. The data is collected through the MTS Testlink system.

Specimen Preparation

The specimen design chosen for the present study is a transverse 'dogbone' design, as shown in Figure 1. Specimen blanks were prepared from a chord section of a pressure tube. For unirradiated pressure tube material, the specimen blanks were fabricated from a tube section using an electrical discharge machining (EDM) method. For pre-irradiated material, the specimen blanks were machined individually using a milling machine set up in a hot cell.

To simulate the equivalent hydrogen concentration in a pressure tube that had been subjected to many years of service, appropriate lengths of the unirradiated and the pre-irradiated pressure tubes were hydrided to a target hydrogen concentration of 45 ± 3 ppm, using an electrolytic hydriding technique.

The 45° V-notches or flaws, 0.400 and 0.800 mm deep with a root radius of 10, 15 and 100 μm , were machined on the ID side of the specimen blanks, as shown in Figure 1. This precision machining was carried out using a micro-broaching procedure developed at Kinectrics.

Test Procedures

Notch-tip Hydride Pre-conditioning. Prior to testing, the test specimens were subjected to a specified pre-conditioning procedure. This test specification required subjecting the specimens to a creep hold for 24 h at 300°C at a specified nominal stress corresponding to a specified stress intensity factor (K_I), assuming the notch to be a sharp crack. This was followed by a cooling cycle which simulated a specific reactor shut down cooling cycle.

To obtain the required hydrogen concentration in solution specified for the test specimens, the pre-conditioning cycle illustrated in Figure 2 combined creep-relaxation and hydride formation cycles. All the hydrogen (nominal 45 ppm) in the specimens are dissolved

during the creep cycle at 300°C and then are re-precipitated under reduced loading during the cooling cycle. In cases where the specified hydrogen concentration in solution was lower than 45 ppm, the specimens were first subjected to a creep relaxation cycle at 300°C for 24 h at a nominal stress of 98, 101 or 162 MPa, depending on the particular specimen geometry. Then they were cooled under a relatively low nominal stress of about 10 MPa to ambient temperature. Next, the specimens were heated under full load to a specified re-solution temperature (261°C for 35 ppm and 266°C for 37 ppm) for 2 h and then cooled to precipitate notch-tip hydrides under reduced loading following the specified cooling cycle in terms of cooling rate.

In the experimental setup for unirradiated specimen pre-conditioning, three (3) specimens were loaded in series in a 'daisy-chain' to increase the rate of specimen preparation prior to testing. The pre-irradiated specimens were thermal cycled individually [6]. After thermal cycling, each pre-irradiated specimen was lightly polished and etched on edge and metallographically examined for notch-tip hydride.

For the 100 µm root radius specimens, the above-mentioned hydride reorientation cycle was modified by adding one to two repeat cycles to increase notch-tip hydride precipitation in these blunter flaws

Monotonic Loading Tests. For monotonic testing of unirradiated material, the test specimen was instrumented with AE, notch PD and reference PD (RPD) monitoring probes, as shown in Figure 3. The data acquisition system was initiated just prior to turning on the DC power supply for the current leads. The specimen and load train assembly was allowed to stabilize for 15-20 minutes prior to testing. The test specimen was then subjected to constant actuator ram displacement rate while monitoring the load cell signal, the DC potential drop signals, the AE signal and the specimen temperature at discrete time increments. The specimen was quickly unloaded when a suitable size jump in the AE signal was observed. The appropriate size of this jump in the AE signal was determined in some preliminary tests where the AE system sensitivity was optimized for the specific experimental setup being used. For monotonic testing of pre-irradiated specimens, a similar procedure to the above was modified appropriately for use in the hot cell environment. Pin-loading was also used for pre-irradiated specimens [6].

Cyclic Loading Tests. For cyclic testing of unirradiated material, the test specimen was also instrumented with AE, PD and RPD monitoring probes. Cyclic testing was performed under a load-control mode. The data acquisition system was initiated just prior to turning on the DC power supply for the current leads. The specimen and load train assembly was then allowed to stabilize for 15-20 minutes prior to testing. The function generator was initiated and the specified upper and lower load limits were achieved by manually adjusting the set point and span for the load channel. This operation was usually accomplished in a time frame of 20 to 30 seconds. For cyclic testing of pre-irradiated specimens, a similar procedure to the above was modified accordingly for use in the hot cell environment.

RESULTS AND DISCUSSION

Notch-tip Hydride Pre-conditioning

The pre-conditioning cycles described earlier were effective in producing notch-tip hydrides. Examples of notch-tip hydrides observed in unirradiated 15 µm and 100 µm root radius specimens are shown in Figures 4 and 5, respectively. Similar observations were made in the pre-irradiated specimens, with the exception that the notch-tip hydrides tended to be longer. Also, more than one hydride straight below and inclined at an angle to the notch front was observed. It should also be noted here that the notch-tip hydrides were sub-surface, with a few exceptions in the pre-irradiated specimens where the hydrides were much closer to the notch. This formation of sub-surface hydrides was the result of stress relaxation during the 24 hour creep cycle at 300°C, and the 20% unloading during hydride formation at about 250°C.

Examination of a number of unirradiated specimens following either monotonic or cyclic testing indicated that there is a significant specimen-to-specimen variability in the notch-tip hydrides. This is evident in the size, morphology and distribution of the notch-tip hydrides along the notch front, especially in the 15 µm root radius unirradiated specimens with a hydrogen concentration in solution of 37 ppm. The specimen-to-specimen variability observed in the notch-tip hydrides, likely resulted from a number of factors, which include the following:

- (a) the alignment of the particular specimen within the daisy-chain load train assembly;
- (b) small variability in the nominal dimensions of the three specimens in a given daisy-chain of three specimens;
- (c) the inherent variability in the notch-tip hydride formation process which is a complex process involving diffusion of hydrogen to the notch tip, and the nucleation and growth of hydride platelets at the notch tip;
- (d) the variability in the microstructure within a given pressure tube material;
- (e) possible variations in the hydrogen concentration from specimen to specimen.

As will be presented later, the size, morphology and location of the notch-tip hydrides along the notch front have a great influence on the magnitude of the monotonic loads needed to crack these sub-surface hydrides.

Monotonic Loading Tests

Figure 6 presents a representative variation of the AE signal and the nominal stress on the specimen with test time for an unirradiated specimen under constant ram displacement loading. The AE signal clearly shows a significant jump at some stage during the monotonic loading. For the unirradiated material monotonic loading tests, the determination of the nominal notch-tip hydride crack initiation stress was based on an AE jump criterion, such as that presented in Figure 6. This significant burst or jump in the AE emission results from the cracking of the sub-surface notch-tip hydrides. In the majority of the cases examined, this indication of notch-tip hydride cracking was confirmed by metallographic or fractographic examination of the specimen notch-tip region.

A similar behaviour was observed with the pre-irradiated specimens under monotonic loading. However, for the pre-irradiated specimens, the notch-tip hydride crack initiation stress was based on a criterion involving a combination of AE activity and notch PD voltage increase. For the pre-irradiated specimens, the notch-tip hydride crack initiation stress was determined from both strip-chart and computer recorded data using a 2 μV increase in PD criterion [6]. This method gave a more conservative value of crack initiation stress compared to that from the jump in AE signal which usually occurred after the 2 μV increase in PD was reached. Also, the AE signal was not fully reliable because of noise and spurious indications.

The micrograph in Figure 7 shows the presence of some thumbnail-shaped cracked notch-tip hydrides on the fracture surface of an unirradiated specimen following monotonic loading. These thumbnail cracks have been marked by loading the specimen to a nominal stress of about 40 MPa and heat tinting for about 12 h at 300°C. In this particular case, the nominal stress causing the notch-tip hydrides to crack, indicated by a significant jump in the AE signal, is 186 MPa. The monotonic loading was terminated at a maximum nominal stress of 189 MPa.

The results obtained from the monotonic tests of unirradiated and pre-irradiated specimens are summarized in Table 2. The data in Table 2 show that, compared to the pre-irradiated material, there is a considerable variability in the notch-tip hydride crack initiation stress for the unirradiated specimens, especially the 15 μm root radius specimens with a hydrogen concentration in solution of 37 ppm. This significant variability is attributed mainly to the variability in the notch-tip hydride formation observed in the individual specimens. It should also be noted here that the observed notch-tip hydride crack initiation stresses are significantly higher than the hydride formation stress of 78 and 80 MPa for the 15 and 100 μm root radius specimens, respectively, and 120 MPa for the 10 μm root radius specimens.

Table 2: Summary of Monotonic Notch-tip Hydride Crack Initiation Stress

Material Type	No. of Tests	[H]* (ppm)	Notch Depth (mm)	Notch Root Radius (μm)	Nominal Notch-tip Hydride Crack Initiation Stress (MPa)
Unirradiated	8	45	0.800	15	105 - 161
Unirradiated	12	37	0.800	15	177 - 395
Unirradiated	6	45	0.800	100	436 - 459
Unirradiated	3	37	0.800	100	436 - 495
Pre-irradiated	3	37	0.400	10	149 - 180
Pre-irradiated	3	37	0.800	15	116 - 127

* [H] - nominal hydrogen concentration in solution

Three-dimensional finite element stress analyses of the dogbone specimen design were performed for the three notch geometries investigated under the pin loading conditions used in the present monotonic and cyclic tests [7]. The analysis showed that for a

nominal stress of 100 MPa, the elastic notch-tip peak stress in the 10, 15 and 100 μm root radius specimens were 1760, 2405 and 988 MPa, respectively. Therefore, for the above-mentioned notch geometries, the elastic notch-tip peak stress, σ_p , for a given nominal stress, σ_n , is given by the linear relationships.

$$\sigma_{p,10} = 1760(\sigma_n/100) \text{ (MPa)} \quad (1)$$

$$\sigma_{p,15} = 2405(\sigma_n/100) \text{ (MPa)} \quad (2)$$

$$\sigma_{p,100} = 988(\sigma_n/100) \text{ (MPa)} \quad (3)$$

Similarly, the alternating elastic von Mises peak stress, $\Delta\sigma_p^e$, is given by the relationship

$$\Delta\sigma_p^e = 0.436(\sigma_{p,max} - \sigma_{p,min}) \text{ (MPa)} \quad (4)$$

where, the factor 0.436 was derived from the expression $0.5[1 - \nu + \nu^2]^{1/2}$, ν is the Poisson's ratio for the Zr-2.5Nb pressure tube material and is taken to be 0.4 in the above calculation, and $\sigma_{p,max}$ and $\sigma_{p,min}$ are the maximum and minimum elastic peak stresses in the fatigue cycle.

The above equations were used to convert the nominal stresses into peak or alternating elastic von Mises stresses for the three types of specimens examined.

Cyclic Loading Tests

Figure 8 presents a representative variation of the AE, PD and RPD voltage signals in a cyclic loading test carried out under a load-control mode. In the majority of the cases, the AE signal did not exhibit any large jumps like those observed in the monotonic tests. With continued cyclic loading, the notch PD signal showed a very gradual rise. A similar behaviour was observed with the pre-irradiated specimens.

The micrograph in Figure 9 shows the presence of a fatigue crack which has been marked by heat tinting an unirradiated 15 μm root radius specimen using the same procedure as that described earlier for the monotonic loaded specimen. In this particular case, the maximum nominal stress causing the crack initiation and growth at the notch tip during the 4500 cycles of testing was 112.3 MPa.

A summary of all the cyclic results obtained from both unirradiated and pre-irradiated specimens, together with previous data reported by Hosbons and Wotton [3], is presented in Figure 10. In the Figure 10 legend, the number in parenthesis following each specimen type is the root radius of the notch in the specimen in mm.

From previous experience on fatigue testing of specimens with the present dogbone design [8], it was found that the notch PD signal could be used for monitoring crack initiation and growth. It was observed that the notch PD signal was at an approximate steady-state condition after the DC constant current power supply was turned on for about 10-12 minutes. In view of this observation, a statistical

analysis of the PD signal during this near steady-state period was carried out. The results obtained indicated that the PD and RPD signals were generally within $\pm 0.5 \mu\text{V}$ of the mean value for each [8]. For an applied constant current of 2 amperes, the notch PD signal was generally in the range of 400-500 μV , depending on the particular spacing of the PD leads on the specimen. Subsequently, it was found that by subtracting this mean value from the measured PD signal, starting from the time immediately preceding the first cycle, the reprocessed delta potential drop (DPD) signal can be examined in greater clarity.

In the present analysis, by performing a series of cyclic tests and subsequent fractographic and/or metallographic examinations, it was observed that crack initiation occurred after a DPD increase of about 2 μV . On the basis of the above observations, a DPD value of 2 μV was selected as the criterion for crack initiation under cyclic loading conditions.

To eliminate any bias and variability in the analysis of the DPD data, the DPD data was fitted using a second order polynomial utilizing the Trend Line function available in Microsoft Excel. The fitted quadratic equation was solved analytically to obtain the two roots. In most cases, it became obvious which root corresponds to the 2 μV DPD criterion for crack initiation. In some pre-irradiated material tests, the curve fitting was improved by applying it to a limited section of the DPD versus cycle (or load) plot (around the DPD of 2 μV) rather than to the whole range of data.

Detailed analysis of the present cyclic data indicated the following trends:

- (a) for a given alternating elastic peak stress, notches with smaller, sharper root radii have a greater resistance to crack initiation than the blunter notches, indicating that there is a significant root radius effect on crack initiation;
- (b) there appears to be an adverse effect of irradiation on the crack initiation behaviour, however, this observation is based on a very small data set for the pre-irradiated specimens where the range in the cycles to crack initiation was very large;
- (c) as expected, the number of cycles to crack initiation is a strong function of the alternating elastic von Mises peak stress for a given specimen geometry;
- (d) based on a limited number of tests carried out on unirradiated specimens without notch-tip hydrides, the presence of sub-surface notch-tip hydrides does not seem to have a large effect on the crack initiation behaviour in this material in the unirradiated condition;
- (e) the specimen-to-specimen variability in the cycles to crack initiation in the unirradiated material generally seems to be consistent, with the range in cycles to crack initiation lying within a factor of about 4 for a given alternating elastic von Mises peak stress.

GENERAL DISCUSSION

Factors Affecting the Formation of Hydrided Regions at Flaw Tips

Results obtained from the present study indicate that the formation of zirconium hydrides at the flaw tips is influenced by such

factors as, the hydrogen concentration in solution in the zirconium alloy matrix, the depth and root radius of the flaw, and the temperature and stress history of the flaw. This complex set of variables affecting the formation of notch-tip hydrides has resulted in producing a large variability in the size, morphology and distribution of sub-surface notch-tip hydrides in the present dogbone specimens.

Effect of Root Radius on Crack Initiation at Flaw Tips under Cyclic Loading Conditions

The effect of flaw tip root radius on crack initiation under cyclic loading conditions is illustrated by the data presented in Figure 11. This plot shows clearly that under the same alternating elastic von Mises peak stress, the 100 μm root radius specimens are more susceptible to crack initiation than the 15 μm root radius specimens. This observation is consistent with observations on the effect of flaw root radius in DHC experiments under constant loading conditions reported by Lee and Sagat [5]. This observation is also consistent with the process-zone model [9,10,11], which predicts that the threshold peak flaw-tip stress for DHC initiation depends on $(1/\rho)^2$, where ρ is the root radius of the flaw.

Effect of Notch-Tip Hydrides on Crack Initiation at Flaw Tips under Cyclic Loading Conditions

The effect of notch-tip hydrides on crack initiation in unirradiated material under cyclic loading conditions is illustrated by the data presented in Figure 12. This plot shows that the cycles to crack initiation in specimens containing no notch-tip hydrides is within the range of values observed for specimens containing notch-tip hydrides. Although the amount of data from the non notch-tip hydride specimens is rather limited, the results to date indicate that the role played by the notch-tip hydride on crack initiation is minimal. This observation is consistent with the fact that for the specimens tested to date; the notch-tip hydrides are sub-surface and exist as discrete thumbnail-shaped hydrided regions distributed along the notch front. In addition, the elastic von Mises peak stresses used in the fatigue tests are well below the notch-tip hydride fracture stress measured under monotonic loading conditions. However, this observation of no discernible effect of notch-tip hydrides on crack initiation behaviour in unirradiated material needs to be confirmed by additional tests.

Examination of the very limited data presented by Hosbons and Wotton [3] showed that, in the case of pre-irradiated material, the presence of notch-tip hydrides may lower the crack initiation resistance. However, because the number of data points is very limited, the lower cycles observed for the specimens containing notch-tip hydrides may in fact be within the range of values for non notch-tip hydride specimens, if more tests of the two types of specimens were to be carried out.

Effect of Irradiation on Crack Initiation at Flaw Tips under Cyclic Loading Conditions

The effect of irradiation on crack initiation under cyclic loading conditions is illustrated by the data presented in Figure 13. This plot shows that, except at the lowest alternating stress level examined, the range in cycles to initiation in the pre-irradiated pressure material, for the 15 μm root radius specimens, overlaps the two separate ranges of

values observed for the 15 and 100 μm root radius unirradiated specimens at alternating elastic von Mises peak stresses of about 680 and 840 MPa. This large range in the cycles to initiation in the pre-irradiated specimens makes it very difficult to make a more quantitative determination of the effect of irradiation on crack initiation behaviour in the small root radius specimens. The only clear observation from the data is that some of the pre-irradiated data points lie at the low end in the range of values determined experimentally. In view of this observation, it is apparent that more tests of pre-irradiated material need to be carried out to determine if there is an effect of irradiation on crack initiation behaviour.

Implementation of the Monotonic and Cyclic Test Results on Flaw Evaluation Methodology for Zr-2.5Nb Pressure Tubes

Inspection results from various CANDU units have indicated that debris fretting flaws in some operating Zr-2.5Nb pressure tubes have a wide range of root radii. In addition, as the pressure tubes age equivalent hydrogen concentrations are also increasing. In recognition of these issues, an improved methodology is required to assess these flaws in terms of fatigue. Work is underway to fit the present fatigue crack initiation data to develop an engineering fatigue evaluation curve for flaws with hydrides. The engineering fatigue evaluation curve may be implemented into a methodology to assess fatigue initiation from in-service flaws in the proposed CSA Standard N285.8 [12] for pressure tube fitness for service.

CONCLUSIONS

Based on the monotonic and cyclic loading tests carried out in the present study, the following conclusions can be stated.

- (1) The specified test specimen pre-conditioning procedure was effective in producing notch-tip hydrides, although a significant specimen-to-specimen variability in the morphology, size and distribution along the notch front, of the notch-tip hydrides was observed.
- (2) A large variability was observed in the notch-tip hydride crack initiation stress under monotonic loading in unirradiated specimens, especially those with a hydrogen concentration in solution of 37 ppm. This large variability can be attributed to the large variability in the notch-tip hydride formation process in these specimens.
- (3) Even though the number of monotonic loading data for pre-irradiated material is limited, the scatter in pre-irradiated material data is much less than that in unirradiated material data. Also, the average crack initiation stress under monotonic loading for pre-irradiated material is generally less than that for unirradiated material.
- (4) For the same alternating elastic peak stress, notches with small root radii have a greater resistance to crack initiation than blunter notches, indicating that there is a significant root radius effect on crack initiation. This observation is consistent with results on DHC crack initiation behaviour under constant loading conditions and is also consistent with a process-zone model.
- (5) Based on limited data available on unirradiated specimens containing no notch-tip hydrides, the effect of notch-tip hydrides on crack initiation behaviour under the cyclic loading conditions examined in the present study appears to be non-discernible.
- (6) Irradiation appears to lower the crack initiation resistance under cyclic loading. However, the limited data available exhibits a large variability and additional tests need to be conducted to determine the effect of irradiation on crack initiation behaviour more precisely.
- (7) The monotonic and cyclic data obtained from this study can be used to develop an engineering fatigue evaluation curve that is suitable for analysis of crack initiation in service-induced flaws in CANDU reactor pressure tubes.

ACKNOWLEDGEMENTS

Funding for the work reported here was provided by contracts with the CANDU Owners Group to AECL and Kinectrics under Fuel Channel Projects 10202 and 10203, respectively, and by a contract with Ontario Power Generation Inc and Bruce Power under Kinectrics Project 9107. Messrs. G.W. Newman, N. Azer and D.H.B. Mok of Ontario Power Generation Inc. provided valuable inputs to the formulation of the test program. Mr. D.M. Kawa of Kedward, Kawa and Assoc. Ltd. carried out the finite element stress analyses for the pin loaded dogbone specimens used in the present study. Messrs. K.F. McCarthy and J.M. Smeltzer of AECL-Chalk River Laboratories and Messrs. H. Seahra and M.J. McGraw provided valuable technical support in carrying out the specimen pre-conditioning to form notch-tip hydrides and the monotonic and cyclic loading tests on both unirradiated and pre-irradiated pressure tube specimens.

REFERENCES

- 1 Dutton, R., Nuttall, K., Puls, M.P. and Simpson, L.A., October 1977, "Mechanisms of Hydrogen Induced Delayed Cracking in Hydride Forming Materials," *Metallurgical Transactions*, Vol. 8A, pp. 1553-1562.
- 2 Cheadle, B.A., Coleman, C.E. and Ambler, J.F.R., 1987, "Prevention of Delayed Hydride Cracking in Zirconium Alloys," in *Zirconium in the Nuclear Industry. Seventh International Symposium, ASTM STP 939*, pp. 224-240.
- 3 Hosbons, R.R. and B.L. Wotton, B.L., January 1987, Atomic Energy of Canada Ltd., Chalk River Laboratories, unpublished work.
- 4 Ho, E.T.C. and McGraw, M.J., January 1997, "Creep, Stress Relaxation and Tensile Testing of Zr-2.5Nb Pressure Tube R912 Material", Ontario Hydro Technologies, unpublished work.
- 5 Lee, W.K. and Sagat, S., January 1996, "Interim Report on the Effect of Material Variability on DHC Initiation in Blunt Notches", Ontario Hydro Technologies, unpublished work.
- 6 Choubey, R., McCarthy, K.F., Smeltzer, J.M. and Sagat, S., September 2001, Atomic Energy of Canada Ltd., Chalk River Laboratories, unpublished work.
- 7 Kawa, D.M., May 2001, Kedward, Kawa and Assoc. Ltd., unpublished work.
- 8 Ho, E.T.C. and McGraw, M.J., December 2001, "Preliminary Results on Monotonic and Cyclic Loading on Crack Initiation

- Behaviour in Small Root Radius Specimens", Kinectrics Inc., unpublished work
9. Scarth, D.A. and Smith, E., 1999, "Developments in Flaw Evaluation for CANDU Reactor Zr-Nb Pressure Tubes," *Proceedings of the 1999 ASME Pressure Vessels and Piping Conference*, Boston, MA, August 1-5, PVP-Vol. 391, pp. 35-45, also published in the *ASME Journal of Pressure Vessel Technology*, Volume 123, February 2001, pp. 41-48.
 10. Scarth, D.A. and Smith, E., 2000, "The Use of Failure Assessment Diagrams to Describe DHC Initiation at a Blunt Flaw," *Proceedings of the 2000 ASME Pressure Vessels and Piping Conference*, Seattle, WA, July 23-27, PVP-Vol. 412, pp. 63-73.
 11. Scarth, D.A., 2002, "A New Procedure For Evaluating Flaws in CANDU Nuclear Reactor Pressure Tubes For the Initiation of Delayed Hydride Cracking," draft Ph.D. thesis to be submitted to University of Manchester, Manchester, U.K.
 12. "CSA-N285.8-M200X: Technical Requirements for In-service Evaluation of Zirconium Alloy Pressure Tubes in CANDU Reactors," October 2001, draft proposed CSA-N285.8-M200X, prepared by the CSA Subcommittee on N285.8, Canadian Standards Association

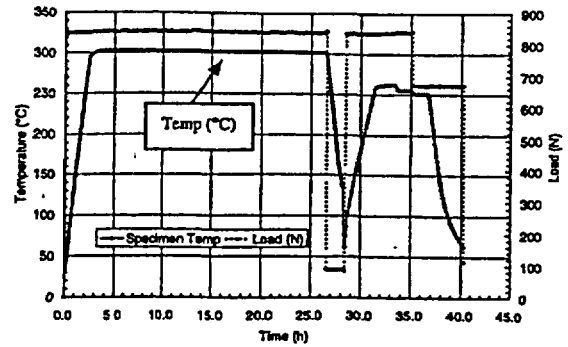


Figure 2: Principal Pre-conditioning Cycle for Monotonic and Cyclic Test Specimens with 15 μm Root Radius and 37 ppm Hydrogen Concentration in Solution

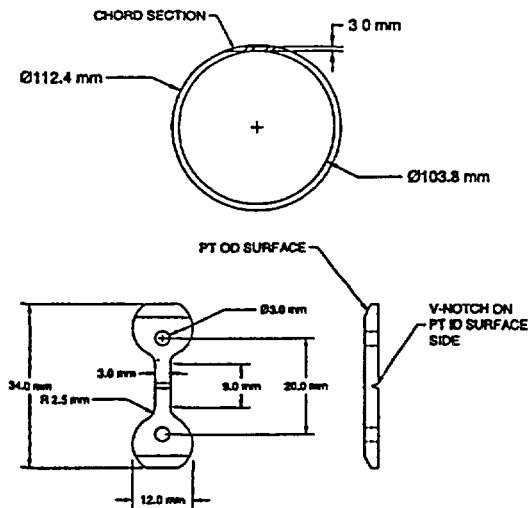


Figure 1: Transverse 'Dogbone' Specimen Design for Monotonic and Cyclic Loading Tests

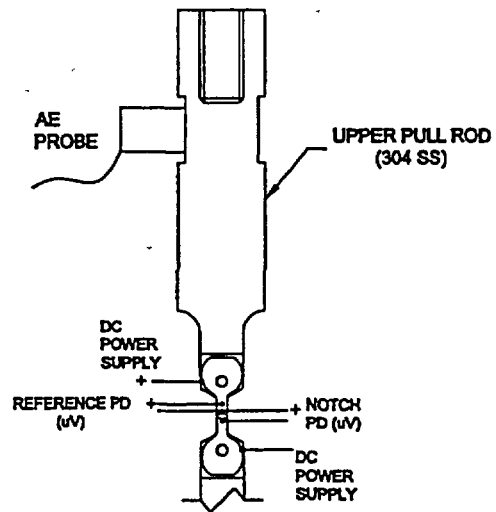


Figure 3: Schematic Diagram Illustrating the Placement of AE and PD Probes in the Experimental Setup using Pin Loading for Unirradiated Specimens

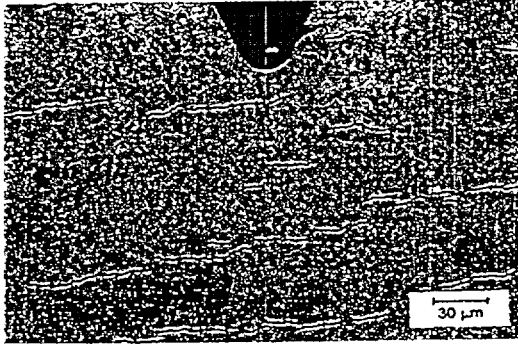


Figure 4: Nature of Sub-surface Notch-tip Hydrides In 15 μm Root Radius Specimens

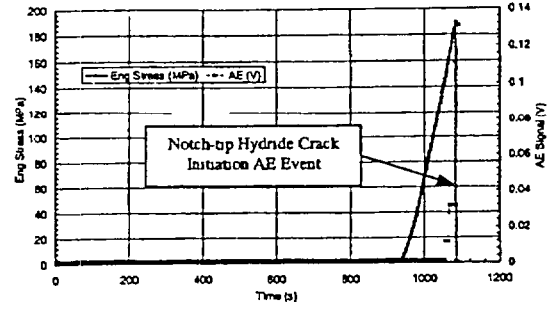


Figure 6: Variation of AE Signal and Nominal Stress with Monotonic Loading to Notch-tip Hydride Crack Initiation in 15 μm Root Radius Specimen 927

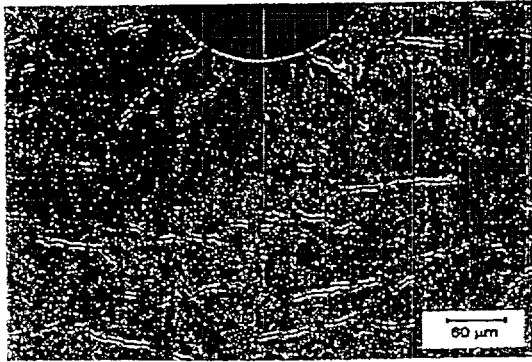


Figure 5: Nature of Sub-surface Notch-tip Hydrides In 100 μm Root Radius Specimens

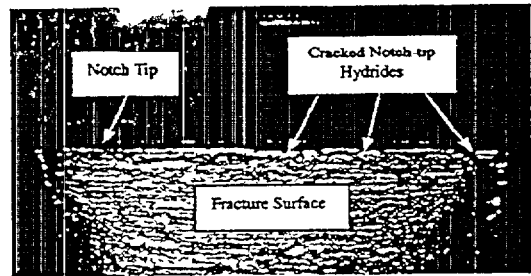


Figure 7: Examples of Cracked Thumbnail-shaped Notch-tip Hydrides in Unirradiated Specimen 927 after Monotonic Loading to Crack Initiation and Subsequent Heat Tinting under Load

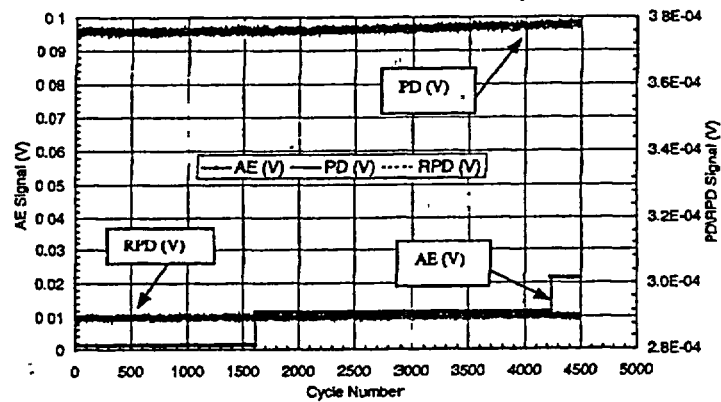


Figure 8: Variation of AE, PD and RPD Voltage Signals with Cyclic Loading to Crack Initiation in 15 μm Root Radius Specimen 921

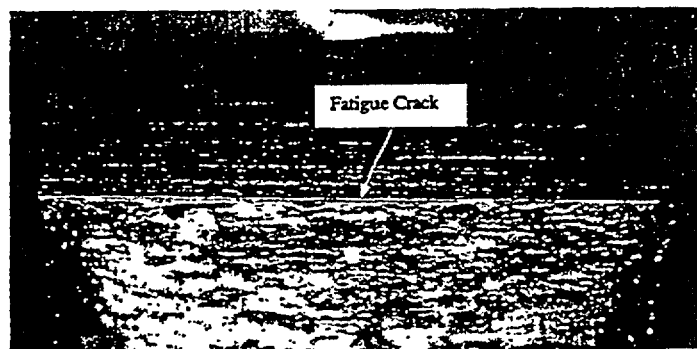


Figure 9: Example of a Fatigue Crack Initiated and Grown from the Notch Front in Unirradiated Specimen 921 after 4500 Cycles and Subsequent Heat Tinting

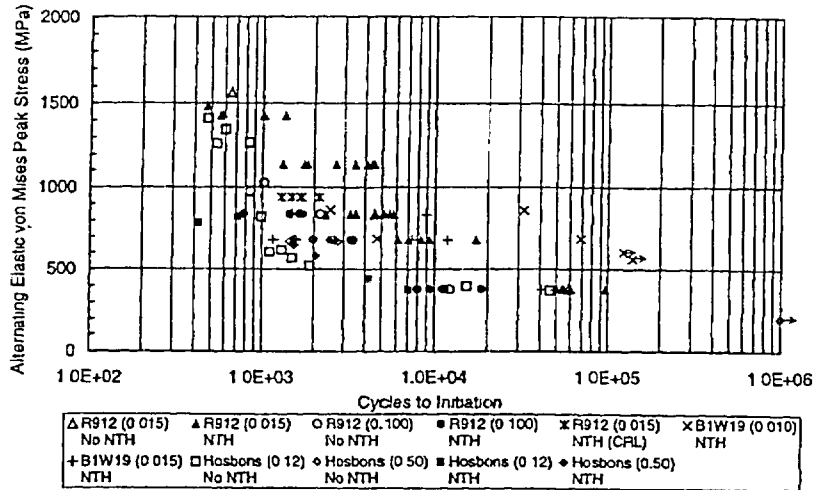


Figure 10: Plot Illustrating the Present Cyclic Data together with Previous Data reported by Hosbons and Wotton [3] (number in parenthesis is the specimen notch root radius in mm, NTH – Notch-tip Hydride)

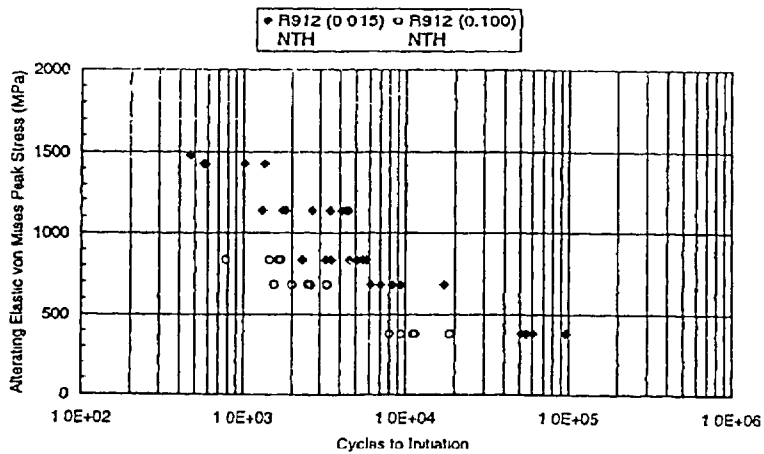


Figure 11: Plot Illustrating the Effect of Notch Root Radius on Crack Initiation Behaviour at Flaw Tips in Zr-2.5Nb Pressure Tube Material (NTH – Notch-tip Hydride)

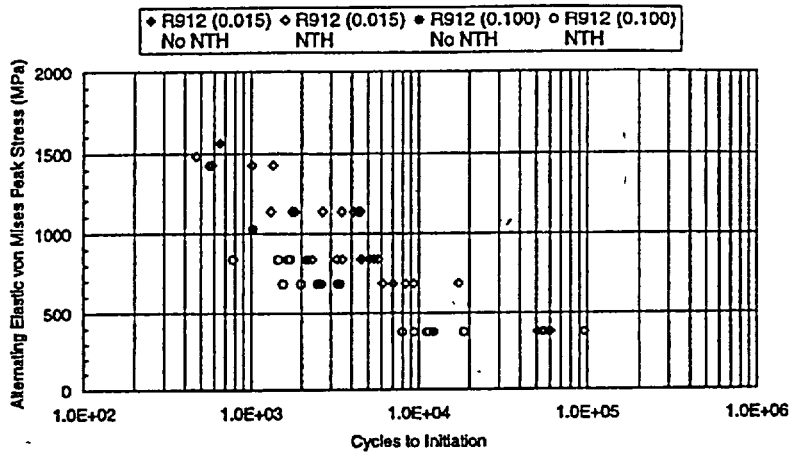


Figure 12: Plot Illustrating the Effect of Notch-tip Hydrides on Crack Initiation Behaviour at Flaw Tips in Zr-2.5Nb Pressure Tube Material (NTH – Notch-tip Hydride)

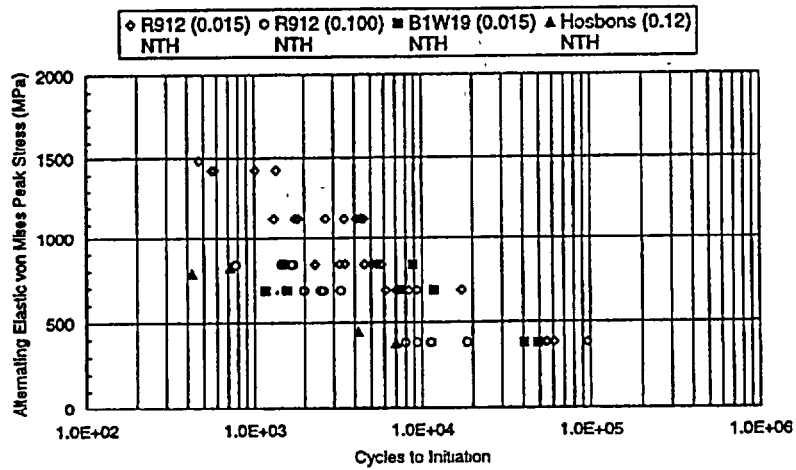


Figure 13: Plot Illustrating the Effect of Irradiation on Crack Initiation Behaviour at Flaw Tips in Zr-2.5Nb Pressure Tube Material (NTH – Notch-tip Hydride)

Crack initiation criterion at notches in Zr-2.5Nb alloys

S. Sagat

Materials and Mechanics Branch, AECL Research, Chalk River Laboratories, Chalk River, Ont K0J 1J0 (Canada)

S. Q. Shi and M. P. Puls

Materials and Mechanics Branch, AECL Research, Whiteshell Laboratories, Pinawa, Man. R0E 1L0 (Canada)

Abstract

This work investigates the experimental conditions necessary for initiation of delayed hydride cracking in Zr-2.5Nb alloys. The experiments were performed on 240 notched cantilever beam specimens loaded in pure bending to a wide range of stresses. The test temperature was 250 °C with weekly cycles between 60 and 295 °C. The results are interpreted in the light of a recently proposed fracture criterion for hydrides at cracks and notch tips. This criterion is based on the premise that crack initiation occurs if the local tensile stress at the hydride exceeds that for hydride fracture. The local stress at the hydride is expressed as the sum of the peak stress at the notch and the stress in the hydride arising from the hydride formation process. The fracture stress of the hydride is obtained experimentally. An approximate analytical method, based on a modified Neuber's rule, was used to calculate the plastic zone size needed to estimate the peak stress at the notch. These approximate calculations show that the threshold notch tip stress for cracking is between 675 and 750 MPa.

1. Introduction

Zirconium alloys are largely used in the nuclear industry because of their low neutron capture cross-section and excellent corrosion and mechanical properties. The solubility of hydrogen decreases rapidly with decreasing temperature, and the excess hydrogen precipitates as a zirconium hydride phase. The hydride phase is brittle, and consequently under some conditions has a deleterious effect on mechanical properties, such as fracture toughness and ductility, particularly at temperatures below 150 °C. Zirconium alloy components can also fail by a time dependent process called delayed hydride cracking (DHC) which does not require a large amount of hydrides present in the bulk to be effective. It is this process that is responsible for crack initiation and propagation in zirconium alloy components [1]. Over the years significant advances in the understanding of DHC in zirconium alloys have been made. The process consists of the following steps [2]:

- (a) diffusion of hydrogen to a high tensile stress region, usually the tip of a flaw;
- (b) nucleation and growth of hydrides in this region;
- (c) fracture of the hydride;
- (d) repetition of the above events which leads to crack growth.

Of these steps, the diffusion of hydrogen and the repeated propagation process have been studied the most and are consequently fairly well understood [3-5]. The crack initiation step is the most important part of the DHC process but it is still the least understood. Since most flaws in real components are blunt and shallow, the concept of the stress intensity factor, defined by the linear elastic fracture mechanics, cannot be used. An experimental programme was set up to study crack initiation from blunt flaws and to determine criteria for crack initiation from such flaws.

2. Experimental details

A section of Zr-2.5Nb pressure tube, designated G1175, with a 103.4 mm inside diameter and a 4.1 mm wall thickness, was used for specimen preparation. The tube had an initial hydrogen concentration of 0.11 at.%. Deuterium was added gaseously to this section at 400 °C followed by a homogenizing treatment at 400 °C for 3 days. Hydrogen-deuterium analysis using a vacuum extraction method gave the total hydrogen isotope concentration of 1.2 ± 0.18 at.%.

240 cantilever beam specimens, with different notch depths and root radii, were machined from this tube, Fig. 1. A test matrix was designed to include a suf-

efficient range of outer fibre stresses (OFS) so that failure rates from zero to 100% were covered, Table 1. Since crack initiation is a highly variable process, ten specimens for each test condition were used to obtain better statistics of the results. Strict quality control was implemented to ensure that the variability in specimen dimensions, in each group of ten, was minimal. It was the intention in this work to study the crack initiation process strictly as a function of the notch geometry and the applied stress and to keep other variables constant. The high hydrogen concentration in the specimens ensured that there was always sufficient hydrogen available for cracking.

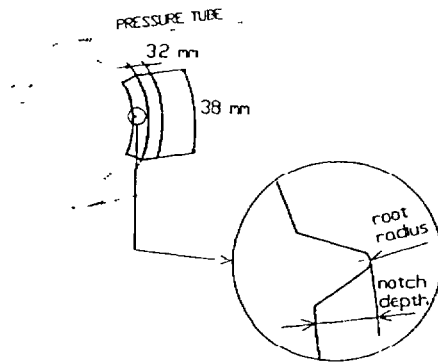


Fig. 1. Dimensions of cantilever beam specimens prepared from Zr-2.5Nb pressure tubes.

The specimens were loaded in pure bending using a set of grips of which one was fixed and the other was used to hang a dead weight calculated according to the required OFS, Fig. 2. The specimens were loaded into six large furnaces each holding up to 40 specimens. The specimens were tested at 250 °C with weekly temperature cycles between 60 and 295 °C, Fig. 3. The specimens were temperature cycled to achieve the optimum conditions for crack initiation. It was shown previously [4, 6] that temperature cycling, and approaching the test temperature by cooling, enhanced DHC because of the hysteresis in the terminal solid solubility (TSS) of hydrogen in zirconium alloys [7]. The fact that the reactors are subjected to temperature cycling during operation and shut-downs added another incentive for studying the crack initiation under temperature cycling conditions.

A failure detection system based on electrical studies indicated failures and at the same time started a timer that was then used to determine the exact time of failure. The time to failure consisted of the incubation time (the time from the beginning of the test until cracking started) and the time to grow the initiated crack to failure.

Experiments were also performed on a test apparatus equipped with acoustic emission to detect cracking. The method using the acoustic emission for monitoring hydride cracking has been described elsewhere [8]. In this experiment, a notched specimen was temperature cycled under load and the acoustic emission was used

TABLE 1. Experimental parameters
Constant root radius, notch root radius 0.05 mm

Number of specimens	Notch depth (mm)	OFS (MPa)						
		100	150	185	200	300	400	500
20	1.0	10/6.1			10/12.1			
50	0.8	10/5.2	10/7.8	10/9.6	10/10.4	10/15.6		
40	0.4	10/3.5			10/7.0	10/10.4	10/13.9	
40	0.2				10/4.8	10/7.2	10/9.7	10/12.1
40	0.1				10/3.4	10/5.1	10/6.8	10/8.5
30	0.05					10/3.6	10/4.8	10/6.0

Different root radius notch depth 1 mm

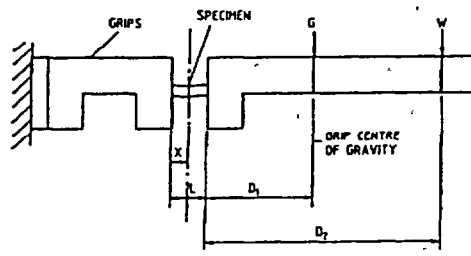
Number of specimens	Root radius (mm)	OFS = 250 MPa
10	0.05	10/15
10	0.18	10/15
10	0.3	10/15
10	0.64	10/15

Entries are given as number of specimens/ K_1 (MPa m^{1/2})
OFS outer fibre stress

to detect when, during the temperature cycle, the cracking started

3. Peak stress concept

Notches in specimens used in this work ranged from sharp (0.05 mm root radius) to blunt 0.64 mm). Characterization of the stress state at notches requires a different treatment than that at sharp cracks. Using the stress intensity factor K_I for notches would over-



- L - SPECIMEN GAUGE LENGTH
- X - POINT OF STRESS
- D₁ - DISTANCE FROM END OF GRIP TO CENTRE OF GRAVITY
- D₂ - DISTANCE FROM END OF GRIP TO POINT OF LOAD
- G - WEIGHT OF GRIP
- W - APPLIED LOAD

Fig 2. Schematic diagram of testing apparatus

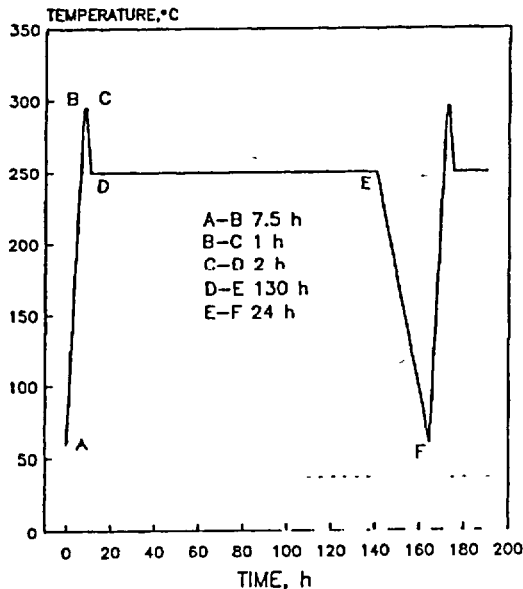


Fig 3 Temperature cycle used in crack initiation tests

estimate the stress, particularly on shallow notches with large root radii. Conversely, using the applied far-field stress would underestimate the stress level. In this paper we propose to use the peak stress ahead of the notch to characterize the stress state. Figure 4 shows schematically the geometry of a shallow notch with a hydride having a thickness t and a length L . A far-field tensile stress σ^a is applied in the y direction. If the depth of the notch c is small compared with the depth of the specimen in the x direction, the stress ahead of the notch can be obtained from the theory of linear elasticity [9]. The maximum elastic tensile stress σ_{ct}^{max} occurs at the tip of the crack ($r=0, \theta=0$) and is given by the expression

$$\sigma_{ct}^{max} = \sigma^a \left[1 + 2 \left(\frac{c}{\rho} \right)^{1/2} \right] \tag{1}$$

where the critical applied stress σ_c^a is limited by the yield stress σ_y :

$$\sigma_c^a = \frac{\sigma_y}{1 + 2(c/\rho)^{1/2}} \tag{2}$$

Local yielding around the notch tip will occur when the far-field applied stress σ^a is higher than the critical stress σ_c^a , resulting in the formation of a plastic zone which increases in size r_{pz} with increasing applied stress. From the slip-line theory [10], the plastic zone size r_β corresponding to the maximum possible value of the normal stress ahead of the notch is given by

$$r_\beta = \rho [\exp(\pi/2 - \omega) - 1] \tag{3}$$

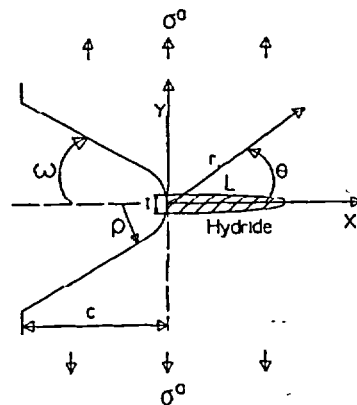


Fig 4 Schematic diagram depicting notch and notch-tip hydride geometries, and the direction of applied stress

where ω is the flank angle of the notch. When $r_{pz} < r_\beta$, the maximum normal stress σ_{yy}^{max} is given by (Fig. 5(a))

$$\sigma_{yy}^{max} = \sigma_y \left[1 + \ln \left(1 + \frac{r_{pz}}{\rho} \right) \right] \quad (r_{pz} < r_\beta) \quad (4)$$

When $r_{pz} = r_\beta$, σ_{yy}^{max} reaches its maximum possible value:

$$(\sigma_{yy}^{max})^{max} = \sigma_y \left(1 + \frac{\pi}{2} - \omega \right) \quad (r_{pz} \geq r_\beta) \quad (5)$$

which is independent of root radius. A further increase in the applied stress causes r_{pz} to increase but produces no further increase in σ_{yy}^{max} , as shown in Fig. 5(b).

To be able to determine σ_{yy}^{max} , the plastic zone size r_{pz} has to be estimated and compared with r_β . An approximate analytical method, utilizing a modified Neuber's rule, was used to calculate the plastic zone size needed to estimate the maximum notch tip normal stress [11]. After the plastic zone size was calculated, eqns. (4) and (5) were used to determine σ_{yy}^{max} .

The objective of these experiments was to determine the number of cycles and the time to failure as a function of the peak stress ahead of the notch. Of particular interest is the peak stress below which no cracking occurs, *i.e.* the threshold peak stress. Also of interest is the process of hydride development at the notch and the conditions that cause the hydride to fracture and thus initiate DHC.

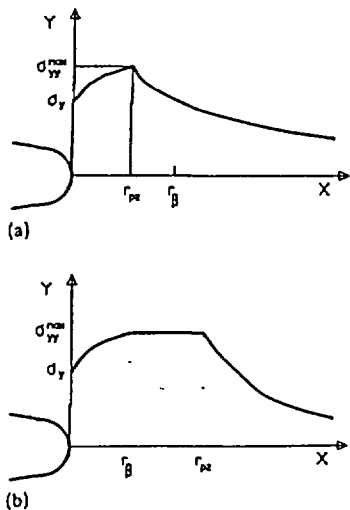


Fig. 5. Stress ahead of a notch (a) for $r_{pz} < r_\beta$, (b) for $r_{pz} \geq r_\beta$.

4. Experimental results

The tests were performed over a period of about 4 years. Most failures occurred within 3 years from the start of the experiment. No failures occurred during the last year, which indicates that threshold conditions for cracking have been approached. At the time of shut down, 123 specimens had failed. Table 2 and Fig. 6 give the fraction of failed specimens in each group of ten specimens as a function of the peak stress σ_{yy}^{max} . Figures 7 and 8 show the number of cycles and the total time to failure as a function of σ_{yy}^{max} . The results show a large variability in the times to failure and the number of temperature cycles to failure (Table 3), confirming that crack initiation is a highly variable process. With respect to the temperature profile used in these tests, most failures occurred about 30 h after the end of the temperature cycle, whereas very few failures occurred during the remainder of the isothermal hold, Fig. 9. This information shows the importance of temperature cycling for DHC initiation. These results indicate that the crack initiated during the temperature cycle, and grew to failure during the isothermal hold at 250 °C. The threshold stress for cracking, in terms of the peak stress σ_{yy}^{max} , was found to be between 675 and 750 MPa. To find out when exactly during the temperature cycle the cracking started, acoustic emission was used in some tests. To accelerate testing, the hold time at 250 °C was shortened from 130 h to 3 h. The results from these tests show that cracking started after cool-down from the peak temperature to test temperature and continued growing during subsequent cool-down, but stopped during heating, Fig. 10. The absence of cracking on approaching the test temperature by heating was previously observed by Ambler [6].

Tests on specimens with different notch root radii showed that for the same notch depth and applied stress, the number of failures decreased with increasing root radius (Table 2).

Fractographic examination of specimens showed that fracture of the specimens occurred in four stages, Fig. 11:

- (a) growth of the hydride to a critical length;
- (b) fracture of the crack tip hydride;
- (c) DHC growth;
- (d) ductile fracture.

In the first two stages, the crack tip hydride that had developed over a number of temperature cycles reached critical size and fractured. The fracture of this hydride produced a sharp crack that was susceptible to a time dependent DHC process. The crack grew by DHC (for about 30 h) until the remaining cross-section of the specimen was not able to sustain the applied load and failed by ductile fracture.

TABLE 2. Experimental results
Constant root radius, notch root radius 0.05 mm

Number of specimens	Notch depth (mm)	OFS (MPa)						
		100	150	185	200	300	400	500
20	1.0	0/710 cracks			1/1026			
50	0.8	0/674 cracks	0/836 cracks	0.8/935 cracks	1/974	1/1176		
40	0.4	0/585			0.3/830	1/1028	1/1176	
40	0.2				0/712 cracks	0.4/885	0.8/1029	1/1150
40	0.1				0/623	0.3/767	0.7/895	0.7/1006
30	0.05					0/674	0.3/785	0.5/885

Different root radius, notch depth 1 mm		
Number of specimens	Root radius (mm)	OFS = 250 MPa
10	0.05	0.9/1147
10	0.18	0.5/862
10	0.3	0.1/772
10	0.64	0/665

Entrées are given as fraction of failed specimens/ σ_{yy}^{max} (MPa)
OFS outer fibre stress

TABLE 3. Time and number of temperature cycles to failure for different σ_{yy}^{max}

σ_{yy}^{max} (MPa)	Applied stress (MPa)	Notch depth (mm)	Total test time (h)	Number of temperature cycles
767	300	0.1	2100-18900	18-111
785	400	0.05	1800-16700	16-89
830	200	0.4	13400-14500	80-101
885	300	0.2	12000-20800	59-152
885	500	0.05	580-16900	7-90
895	400	0.1	200-28000	3-83
935	185	0.8	1990-4600	12-31
974	200	0.8	421-21100	5-153
1006	500	0.1	1300-22100	10-163
1026	200	1.0	41-20482	2-151
1028	300	0.4	420-20900	5-152
1029	400	0.2	300-14200	4-56
1150	500	0.2	170-2400	2-9
1176	300	0.8	13-244	1-6
1176	400	0.4	15-520	1-5

Total test time is the time at 250 °C.

Metallographic examination of specimens revealed a local reorientation of the hydrides from the original orientation in the radial-transverse plane, with respect to the pressure tube orientation, into a plane normal to the applied stress, that is the radial-axial plane. In specimens with shallow notches tested at high applied stresses, the reorientation occurred in the upper half of the specimen where the stress was tensile but the

hydride(s) at the notch tip were predominant, Fig. 12(a). In specimens with deeper notches, tested at low applied stresses, the reorientation was more localized around the notch, Fig. 12(b). Examination of the notch tip hydrides at different positions through the cross-section of the specimen revealed that the hydrides were continuous and varied in length by about 35%. For example, a specimen with a 0.05 mm deep notch,

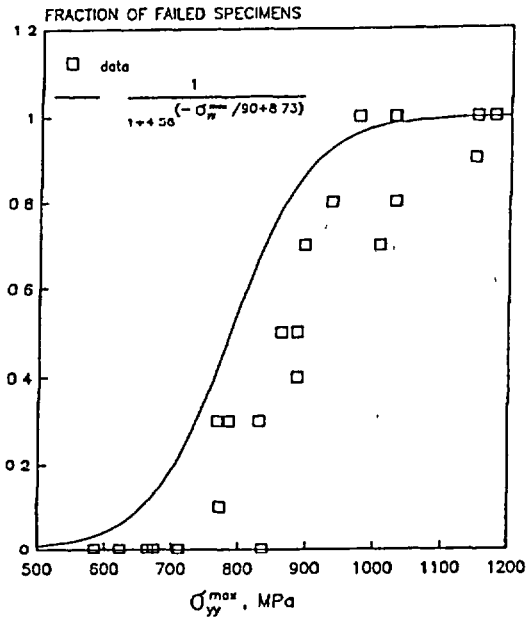


Fig. 6. The relationship between the probability of failure and σ_{yy}^{max} . The probability density function, derived from the best fit to the data, represents the upper bound of the data.

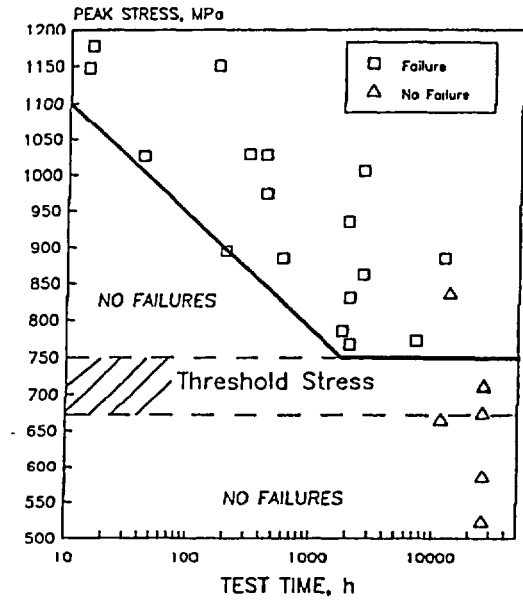


Fig. 8. Minimum total test time to failure (excluding time for temperature cycles) as a function of σ_{yy}^{max} .

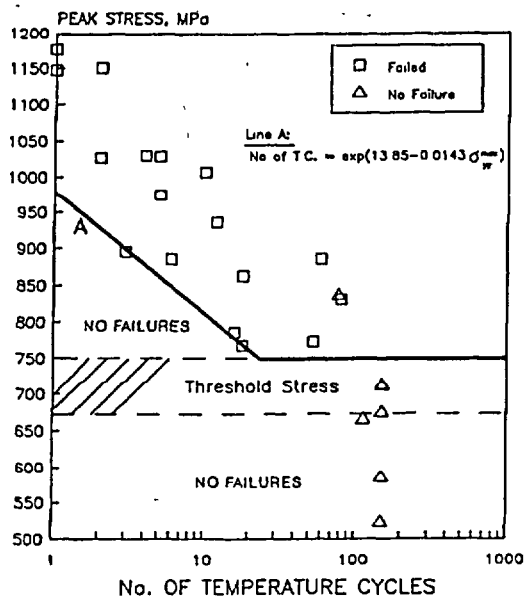


Fig. 7. Minimum number of temperature cycles to failure as a function of σ_{yy}^{max} .

tested at 500 MPa, had the following hydride lengths through its width:

Position (mm)	Surface	0.9	1.8	2.7
Hydride length (μm)	185	165	120	170

The length and thickness of the notch-tip hydrides were measured in each specimen which had not failed during the test. The thickness of the hydride was measured at the base of the notch where the thickness was greatest. In cases where there was a cluster of hydrides at the notch root, the total thickness of the cluster and the length of the longest hydride were measured. The results showed that the length and thickness of the notch tip hydrides generally increased with increasing σ_{yy}^{max} , whereas the length to thickness ratio remained constant at an average value of 6.3, Fig. 13. Further examination revealed that in some specimens the notch tip hydrides were cracked (Table 2). Since, in principle, the specimens with cracks could be considered to have failed, and thus alter the value of the threshold stress derived from the data, it was important to find out when these cracks had occurred. To estimate when these cracks had occurred, the oxide thickness on the fracture surface of the cracks was analysed by a Fourier transform IR reflection spectrometer (FTIR) [12]. The analysis showed that the oxide thicknesses on all the cracks were below the detection limit of the instrument which is about $0.7 \mu\text{m}$. To

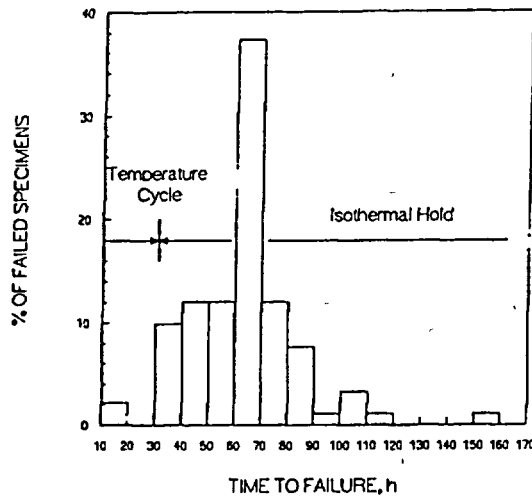


Fig 9. Distribution of failure times with respect to the weekly temperature profile.

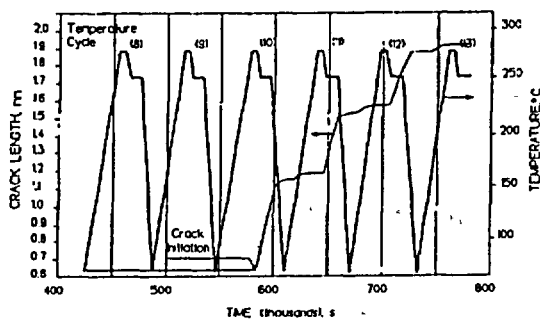


Fig 10. The relationship between the different segments of the temperature cycle and crack growth

determine the time corresponding to an oxide thickness less than or equal to $0.2 \mu\text{m}$, the oxidation kinetics of Zr-2.5Nb material in dry air at 250°C with temperature cycles to 295°C , was required. The oxide thickness was measured by FTIR on the surfaces of specimens that had failed at different times during the test. Figure 14 shows the oxide growth kinetics in relation to the total test time, with the best fit line to the data. The results show that to grow an oxide thickness of $0.2 \mu\text{m}$, the total time required would be about 100 h. Based on these results, it is concluded that the cracks in some specimens occurred shortly before the tests were terminated, and possibly in others during removal from the furnaces.

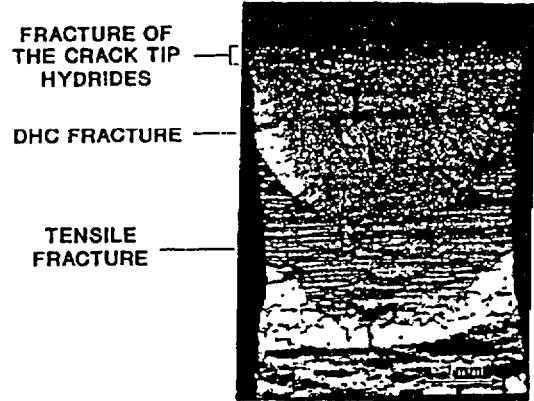


Fig 11. Fracture surface of a specimen after failure.

5. Discussion

The results can be summarized as follows. Repeated temperature cycling of the specimens under stress caused hydrides to form at an increased rate at the notch tip. After reaching a critical size, the hydrides fractured and the resulting crack grew by DHC. The cracking started during a temperature cycle and most of the failures occurred shortly after the temperature cycle. Cracking continued until the remaining cross-sectional area of the specimen was no longer able to sustain the applied stress, and failure was by ductile fracture. After 4 years of testing, the threshold stress for cracking, in terms of the peak stress σ_{yy}^{max} , was found to be between 675 and 750 MPa. With increasing peak stress, the probability of failure increased and at the peak stresses above 1000 MPa, the failure rate approached 100%. In the following, the results are assessed in relation to these observations.

5.1. Threshold stress for DHC

The threshold stress is by definition the minimum stress required for the initiation of DHC. A traditional approach to determine the threshold stress experimentally has involved loading a number of specimens to different stresses and, after a period of time, determining the stress below which no cracking has occurred. This method immediately identifies the time as an important factor in determining the threshold stress value. The longer the time, the smaller will be the threshold value until the true threshold stress is attained. Figs. 7 and 8. In the absence of a theoretical treatment of the threshold stress, it is difficult to judge when the true threshold stress conditions are attained in an experiment. The usual indicator is the time in-

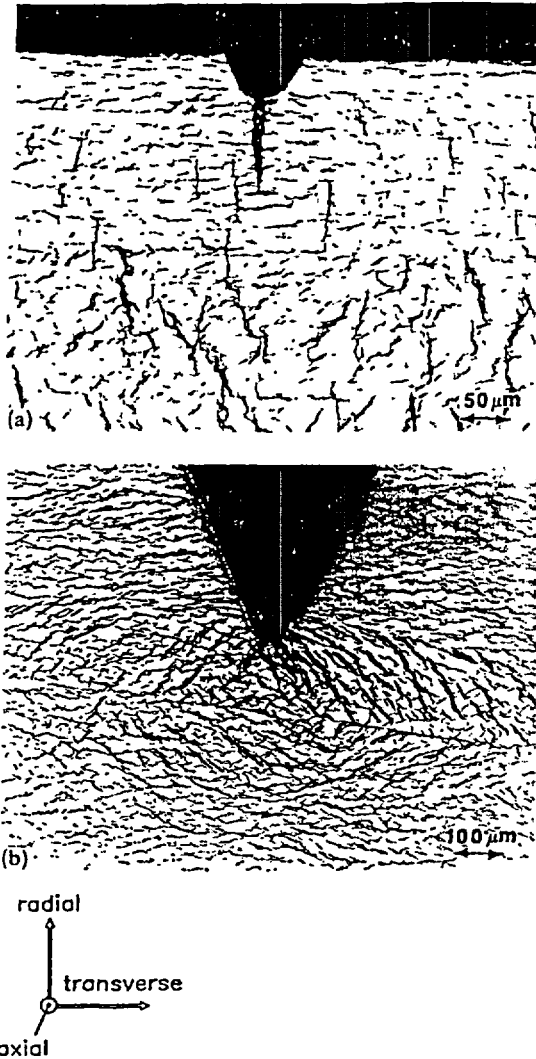


Fig. 12. Hydride development ahead of a notch in two extreme cases in the test matrix. (a) specimen with a 0.05 mm deep notch tested at an applied stress of 500 MPa ($\sigma_{yy}^{max} = 885$ MPa); (b) specimen with a 1 mm deep notch tested at an applied stress of 100 MPa ($\sigma_{yy}^{max} = 710$ MPa).

terval between failures. The time interval is very short at the beginning of the experiment and gradually increases. Eventually no failures occur for a long period of time, which indicates that the specimens that have not failed are stressed below the true threshold stress. This concept was used in this experiment in which, after having no failures for a period of about 1

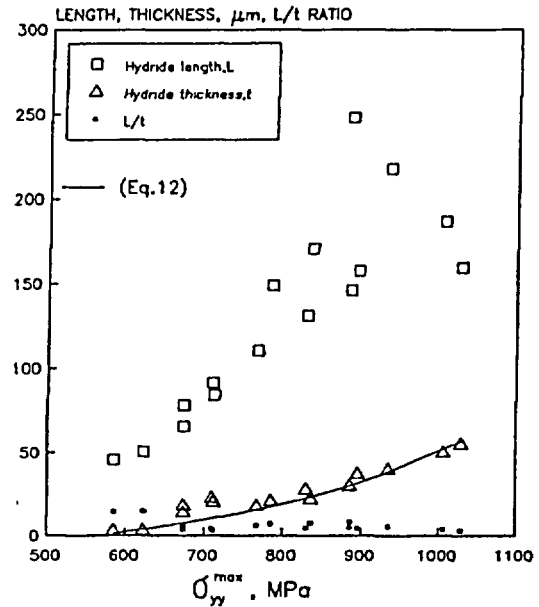


Fig. 13. Length L , thickness t , and L/t in notch tip hydrides in specimens that have not failed, as a function of σ_{yy}^{max} .

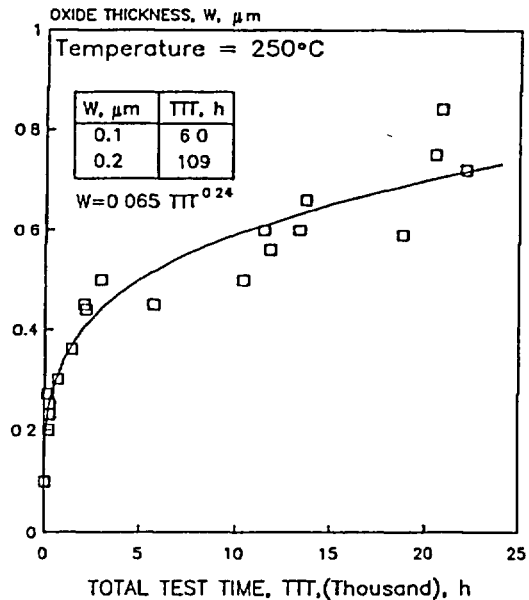


Fig. 14. Oxidation kinetics of Zr-2.5Nb material in dry air at 250°C, with weekly cycles between 290 and 60°C. The line is the best fit to the data

year, it was assumed that the threshold stress conditions were well defined and a further waiting period would not change the results very much. The results in Table 2 show that the maximum peak stress which did not cause a single failure or result in hydride cracking was 674 MPa and the minimum peak stress that caused specimen failure was 767 MPa, hence the threshold peak stress should be between these two values. Figure 6 shows the expected (upper bound) fraction of failures if the peak stress is increased above the threshold value.

5.2 Fracture criteria

The experimental results clearly show that, prior to crack initiation, a hydride or group of hydrides formed at the notch tip. The observed variability in time and number of cycles to failure is probably related to the morphology of hydrides at the notch tip. This morphology is controlled by the variability in microstructure and crystallographic texture and possibly other inhomogeneities in the material that are possible at the notch tip. The notch tip hydride growth is accelerated by the mechanism of "thermal ratcheting" by which the hydride grows during cooling but does not dissolve during heating [13]. At some point the hydride at the notch tip fractures and DHC is initiated. These experiments show that large hydrides can develop at the notch tip without fracturing, which means that the presence of a hydride or hydrides at flaws does not automatically indicate that cracking is imminent. However, the cracking of the notch tip hydrides in some specimens indicates that these hydrides may be susceptible to fracture under handling. In the absence of this type of loading the hydride would grow to a certain size (usually called the critical hydride size) and then fracture. Presently, there is a lack of theoretical understanding of the criterion that causes such a hydride to fracture. Shi *et al.* have recently developed a conceptual fracture criterion for hydrides at shallow notches in zirconium alloys [14]. The model assumes that a hydride having a thickness t and a length L in a far-field stress σ^a acting along the y direction (Fig. 4) will fracture if the local tensile stress at the hydride exceeds the hydride fracture stress σ_f^h . It is assumed that it is sufficient for the stress to exceed the fracture stress at any point within the hydride to initiate an unstable crack that will propagate the entire length of the hydride. This assumption may not be true if the stress field is sharply peaked over a short distance. This is not the case for the stress field in front of a blunt notch. Mathematically, the concept of a critical stress exceeding a threshold stress for hydride fracture may be written as

$$\sigma_{cr}^a + \sigma^h \geq \sigma_f^h \quad (6)$$

where σ_{cr}^a is the effective applied stress on the hydride and σ^h is the stress in the hydride created by the hydride formation process (negative for compression). It is also assumed that these two stresses can be combined linearly and that in front of a blunt notch,

$$\sigma_{cr}^a = \sigma_{cr}^a \quad (7)$$

It has been shown [14] that for an elliptically shaped hydride, σ^h may be given by

$$\sigma^h = -\frac{\alpha}{2} \frac{E \varepsilon_1 t}{(1-\nu^2)} \frac{t}{L} \quad (8)$$

where E is Young's modulus, ν Poisson's ratio in the zirconium matrix, ε_1 the stress-free strain of the hydride in the y direction, and

$$\alpha = \left(\frac{8}{15} - \frac{\pi}{4} \right) \frac{t}{L} + \frac{\pi}{4} \quad (9)$$

Combining eqns. (6), (7) and (8), an expression relating the peak stress ahead of a notch with the internal stress in the hydride and its fracture stress can be written as

$$\sigma_{cr}^a + \frac{\alpha}{2} \frac{E \varepsilon_1 t}{(1-\nu^2)} \frac{t}{L} \geq \sigma_f^h \quad (10)$$

From eqn. (10), the critical hydride length L_c is

$$L_c = \frac{\alpha E \varepsilon_1 t}{2(1-\nu^2)(\sigma_{cr}^a - \sigma_f^h)} \quad (11)$$

An important parameter in eqn. (11) is the hydride thickness t . If multilayered hydrides are formed at the notch tip, then t is the total thickness of the hydrides at the notch root (subtracting the matrix between the hydride layers). It is assumed that t and L_c are controlled by different mechanisms [14]. A theoretical approximation was made [14] to calculate the total hydride thickness, t_e

$$t_e = \frac{15(1-\nu^2) \sigma_{cr}^a r_{pz}}{4E \varepsilon_1} \quad (12)$$

where $E = 81,550$ MPa, $\varepsilon_1 = 0.054$, $\nu = 0.329$ for Zr-2.5Nb at 250 °C and r_{pz} is the plastic zone size in the x direction (see Fig. 4). Both σ_{cr}^a and r_{pz} may be estimated using a simple method described in ref. 11. One condition for using eqn. (12) is that the total hydride thickness t (or t_e) should be smaller than the plastic zone size in the y direction (see Fig. 4). Since we have no means of estimating the plastic zone size in the y direction, we assume, in the following discussion, that the plastic zone sizes in both directions are similar.

Comparing t_e , calculated from eqn. (12), with the average value t measured from the specimens that have

not failed (Table 4), one can see that the overall agreement is good (Fig. 13) except for four cases, marked by "+". However, examining these four cases, we can see that $r_{pz} \approx t$, or even $r_{pz} < t$. This means that eqn. (12) is not valid for these four cases. It was found that if the total thickness of the hydrides within the plastic zone boundary is measured, then eqn. (12) gives better predictions. The above model predicts whether DHC will occur and also predicts the critical hydride length for DHC initiation. It is obvious from eqn. (11) that if $\sigma_{yy}^{max} < \sigma_f^h$, DHC is impossible. L_c in Table 4 is calculated using the theoretical hydride thickness from eqn. (12). For a temperature of 250°C, a yield stress of 540 MPa, a hydrogen concentration of 1.19 at.%, and a hydride fracture stress $\sigma_f^h = 600$ MPa, the model predicts correctly whether DHC initiation will occur or

not, Table 4. For some notch geometries and applied stresses, DHC is impossible because $\sigma_{yy}^{max} < \sigma_f^h$. In other cases the hydride may never be able to grow to the critical length if the hydrostatic stress gradient for hydrogen diffusion vanishes at a distance from the notch tip region where $\sigma_{yy}(L) = \sigma^a$.

Experimentally, it proved to be difficult to measure the critical hydride length on failed specimens. Consequently, the hydride length and thickness were only measured on those specimens that had not failed. Obviously, in these specimens the hydrides would not be expected to have reached the critical value, but in some cases, particularly those in which cracks were observed, or those from groups for which most specimens had failed, they may have approached their critical values closely (see the data marked ** in Table

TABLE 4. Measured and theoretical critical hydride size for DHC initiation at notches

c (mm)	ρ (mm)	σ^a (MPa)	σ_{yy}^{max} (MPa)	Plastic zone		Measured hydride size		Theoretical critical length (eqn. (11)) L_c (μm) (use t_h)	Experimental results: initiation? (probability of failure)	Prediction by this model of DHC initiation	Reasons
				r_{pz} (μm)	t_h (μm)	t (μm)	L (μm)				
0.05	0.05	300	674	14.1	7.2*	14.2	78	186	No	No	$\sigma(L_c) = \sigma^a$
0.05	0.05	400	785	28.1	14.1	21.1	149	174	Yes(0.3)	Yes	
0.05	0.05	500	885	44.7	30.0	30.3	248	194	Yes(0.5)	Yes	
0.1	0.05	200	623	8.3	3.9	3.3	57	333	No	No	$\sigma(L_c) = \sigma^a$
0.1	0.05	300	767	26.1	15.2	18.2	110	172	Yes(0.3)	Yes	
0.1	0.05	400	895	46.4	31.5	37.3	158	197	Yes(0.7)	Yes	
0.1	0.05	500	1006	68.5	52.3	50.0	187	232	Yes(0.7)	Yes	
0.2	0.05	200	712	18.8	10.2*	20.5	64	172	Yes(0.0)*	Yes	
0.2	0.05	300	885	44.7	30.0	30.0	146	194	Yes(0.4)	Yes	
0.2	0.05	400	1029	73.6	57.5	55.0	160	240	Yes(0.8)	Yes	
0.2	0.05	500	1150	105					Yes(1.0)	Yes	
0.4	0.05	100	585	4.3	1.9	3.1	46		No	No	$\sigma_{yy}^{max} < \sigma_f^h$
0.4	0.05	200	830	35.5	22.4	28.0	131	181	Yes(0.3)	Yes	
0.4	0.05	300	1028	73.4					Yes(1.0)	Yes	
0.4	0.05	400	1176	115					Yes(1.0)	Yes	
0.8	0.05	100	674	14.1	7.2*	18.3	65	186	Yes(0.0)*	Yes	$\sigma(L_c) = \sigma^a$
0.8	0.05	150	836	36.5	23.2	22.3	171	183	Yes(0.0)**	Yes	
0.8	0.05	185	935	53.9	38.3	40.0	218	209	Yes(0.8)**	Yes	
0.8	0.05	200	974	61.7					Yes(1.0)	Yes	
0.8	0.05	300	1176	118					Yes(1.0)	Yes	
1.0	0.05	100	710	18.5	10.0*	22.9	91	173	Yes(0.0)*	Yes	$\sigma(L_c) = \sigma^a$ for $t = 60 \mu\text{m}$
1.0	0.05	200	1026	72.9					Yes(1.0)	Yes	
1.0	0.05	250	1147	104					Yes(0.9)	Yes	
1.0	0.18	250	862	147					Yes(0.5)	Yes	
1.0	0.3	250	772	161					Yes(0.1)	Yes	
1.0	0.64	250	665	166					No	No	

*Cracks are observed in a few unfailed specimens

**Cracks are observed in most unfailed specimens

* $t \geq t_{pz}$

4) For other cases, the predicted critical hydride lengths are larger than measured hydride lengths as expected. Considering the uncertainty of some of the input parameters, in particular the hydride fracture stress, the prediction is quite good.

6. Limitation of the data

The experiments in this work were performed on one material with a high hydrogen concentration, subjected to a specific temperature cycle. Since the effects of factors such as the material variability, hydrogen concentration and temperature cycling, in particular the peak temperature and the cooling rate during the cycle, are not yet well established, both the experimental results and the model predictions have limitations if applied outside the range of parameters of this test matrix.

7. Conclusions

- (1) Repeated temperature cycling helps hydrides to form at the notch tip.
- (2) The notch tip hydrides increase in length and thickness with increasing peak stress ahead of the notch, but the length to thickness ratio remains constant.
- (3) DHC initiation occurs after cooling from a peak temperature to the test temperature and most of the failures occur shortly after the temperature cycle.
- (4) The hydride fractures if the local tensile stress at the hydride exceeds the hydride fracture stress $\sigma_{yy}^{max} + \sigma^h \geq \sigma_f^h$.
- (5) The threshold stress for cracking, in terms of the peak stress σ_{yy}^{max} , was found to be between 675 and 750 MPa.
- (6) With increasing peak stress the probability of failure increases and at peak stresses of about 1000 MPa, the failure rate approaches 100%.

Acknowledgments

We would like to thank D. E. Foote, K. D. Weisenberg, H. D. Herrington for assisting with experiments at Chalk River Laboratories and H. VanDam at General Electric Canada Inc., and V. C. Ling and M. A. Maguire for the FTIR analysis. Collaboration and discussion with the following people is greatly appre-

ciated: Dr. C. E. Coleman, Professor E. Smith, W. K. Lee, and D. A. Scarth. The work was funded by the Candu Owners Group (COG) through WPIR 2-31-3124.

References

- 1 E. G. Price, B. A. Cheadle, G. R. Evans and M. W. Hardie, Update of operating experience with cold-worked Zr-2.5Nb pressure tubes in CANDU reactors, *IAEA Technical Committee Meet on Exchange of Operational Safety Experience of Pressurized Heavy Water Reactors, Cordoba, Argentina, April 3-5, 1991, and Atomic Energy of Canada Rep. COG-91-65, 1991*
- 2 L. A. Simpson and K. Nuttall, Factors controlling hydrogen assisted subcritical crack growth in Zr-2.5Nb alloys, *Zirconium in the Nuclear Industry, ASTM STP 633, 1977* (ASTM, Philadelphia, PA), pp 608-629.
- 3 R. Dutton and M. P. Puls, A theoretical model for hydrogen induced sub-critical crack growth, *Conf on Effect of Hydrogen on Behaviour of Materials*, American Institute of Mining, Metallurgical, and Petroleum Engineers, 1975, pp 428-439.
- 4 L. A. Simpson and M. P. Puls, The effect of stress, temperature and hydrogen content on hydride-induced crack growth in Zr-2.5Nb, *Metall Trans A*, 10(1979) 1093-1105.
- 5 M. P. Puls, Elastic and plastic accommodation effects on metal-hydride solubility, *Acta Metall*, 21 (8) (1984) 1759-1769.
- 6 J. F. R. Ambler, Effect of direction of approach to temperature on the delayed hydrogen cracking behaviour of cold-worked Zr-2.5Nb, *Zirconium in the Nuclear Industry, ASTM STP 874, 1984* (ASTM Philadelphia PA) pp 653-674.
- 7 M. P. Puls, On the consequences of hydrogen supersaturation effects in Zr alloys to hydrogen ingress and delayed hydride cracking, *J Nucl Mater*, 165(1989) 128-141.
- 8 S. Sagat, J. F. R. Ambler and C. E. Coleman, Application of acoustic emission to hydride cracking, *29th Acoustic Emission Working Group Meet Royal Military College of Canada, Kingston, 1986, and Atomic Energy of Canada Rep., AECL-9258, 1986*.
- 9 I. N. Sneddon, *Proc. R. Soc London, Ser A*, 187(1946) 229.
- 10 A. S. Tetelman and A. J. McEvily, Jr., *Fracture of Structure Materials*, Wiley, New York, 1967, p 47.
- 11 S. Q. Shi and M. P. Puls, A simple method of estimating maximum normal stress and plastic zone size at a shallow notch under plane strain, submitted to *Int J Pressure Vessels Piping*.
- 12 N. Ramasubramanian and V. C. Ling, Fourier transform infrared reflection (FTIR) spectroscopy of corrosion films on irradiated zirconium alloys, *Atomic Energy of Canada Rep., AECL 10310, 1990*.
- 13 R. L. Eadie, D. Metzger and M. Leger, The thermal ratcheting of hydrogen in solution in zirconium-niobium in theory and as demonstrated by finite element modelling, *Scripta Metall*, 29(1993) 335-340.
- 14 S. Q. Shi and M. P. Puls, Criteria of fracture initiation at hydrides in zirconium alloys I, sharp cracks, *J. Nucl Mater.*, in press.
- 15 S. Q. Shi, S. Sagat and M. P. Puls, Criteria of fracture initiation at hydrides in zirconium alloys II, shallow notch, *J. Nucl Mater.*, in press.

M. Griffiths,¹ W. G. Davies,¹ A. R. Causey,¹ G. D. Moan,²
R. A. Holt,³ and S. A. Aldridge⁴

Variability of In-Reactor Diametral Deformation for Zr-2.5Nb Pressure Tubing

REFERENCE: Griffiths, M., Davies, W. G., Causey, A. R., Moan, G. D., Holt, R. A., and Aldridge, S. A., "Variability of In-Reactor Diametral Deformation for Zr-2.5Nb Pressure Tubing," *Zirconium in the Nuclear Industry: Thirteenth International Symposium, ASTM STP 1423*, G. D. Moan and P. Rudling, Eds., ASTM International, West Conshohocken, PA, 2002, pp. 796-810.

ABSTRACT: The diametral expansion of pressure tubes in CANDU™ reactors due to irradiation creep and growth is an important property that may limit the useful life of the tubes. Measurements accumulated over many years have shown that there is considerable variability in diametral strain rates between tubes. There is also considerable variability in the creep and growth response as a function of axial location, which is due to axial variations in operating temperature and flux, and to a gradual change in grain structure and crystallographic texture from one end of the tube to the other. The net effect is that pressure tubes tend to deform at a faster rate when the back end of the tube (i.e., the end leaving the extrusion press last) is installed at the fuel-channel outlet. The primary cause of the difference in microstructure along a given tube is the temperature change during the extrusion process. This end to end variation itself varies from tube to tube, due to variations in extrusion conditions from one extrusion run to the next, and also due to variations in ingot chemistry and billet processing.

A semiempirical predictive model has been developed previously to represent the irradiation creep and growth behavior of a generic pressure tube, with a standardized microstructure, as a function of temperature and neutron flux. The diametral strain data from one hundred and twenty-five Zr-2.5Nb pressure tubes have been compared with the model. Deviations from predicted behavior have been correlated with the available microstructure, chemistry, and manufacturing data. Apart from obvious microstructural dependencies of diametral strain, such as the relationship with texture, grain structure is also a significant parameter that varies considerably from tube to tube and correlates strongly with diametral strain. The textures and grain structures, themselves, are related to manufacturing conditions (billet processing, extrusion pressures, temperatures, and soak times) and also, to some extent, on the impurity content of the material (due to the modifying effects on the Zr-Nb phase diagram).

KEYWORDS: Zr-2.5Nb, pressure tubes, zirconium alloys, nuclear reactor materials, neutron irradiation, deformation, creep, growth, flux, temperature, X-ray diffraction, microstructure, texture, grain size, oxygen, chemical analysis, statistical analysis, predictive models, rate theory

Introduction

Zr-2.5Nb pressure tubes for CANDU reactors are manufactured by extrusion of hollow β -forged billets at a temperature of about 1090–1120°K, i.e., in the (α + β)-phase field. Cur-

¹ Senior Researcher, AECL, Chalk River Laboratories, Chalk River, Ontario, Canada K0J 1J0

² Manager, Reactor Engineering Services, AECL, Sheridan Park, Mississauga, Ontario, Canada L5K 1B2.

³ Division Director, AECL, Chalk River Laboratories, Chalk River, Ontario, Canada K0J 1J0

⁴ President, Nu-Tech Precision Metals Inc., 460 McCartney St., Arnprior, Ontario, Canada K7S 3H2.

™ CANada Deuterium Uranium

rently, all billets are β -quenched into water from 1288°K; however, this was not always the case, and operating reactors contain a mixture of pressure tubes: some made from β -quenched billets and some not. Following extrusion, the tubes are cold-drawn about 27% to give a final tube thickness of about 4.2 mm, an inside diameter of about 104 mm, and a length of 6.3 m. The grain structure resulting from extrusion consists of thin, platelet-like, hexagonal close-packed (hcp) α -zirconium grains (containing <1 wt% Nb) interspersed with a network of metastable body-centered-cubic (bcc) β -zirconium (containing about 20 wt% Nb) corresponding with the composition at the monotectoid point of the Zr-Nb phase diagram. The metastable β -phase filaments subsequently decompose partially during the final stress-relief treatment for 24 h at 400°C to give a mixture of Nb-depleted (hcp) ω -phase embedded in the remaining Nb-enriched (bcc) β -phase.

The α -grains are mostly oriented with $\{11\bar{2}0\}$ prism planes perpendicular to the radial direction, $\{10\bar{1}0\}$ prism planes perpendicular to the longitudinal direction, and (0001) basal planes perpendicular to the transverse direction, although there are a range of basal-pole orientations spreading from the transverse to the radial direction in the radial-transverse plane. Most of the α -grains with basal poles oriented towards the transverse direction are nearly parallel with the tube surface, and have an aspect-ratio of about 1:(5–10):(20–40) in the radial, transverse, and longitudinal directions, respectively. Others that have basal poles oriented towards the radial direction are either kinked platelets or have a different aspect ratio (1:(1–2) (5–10)) so that they appear almost equiaxed when viewed along the axis of the tube.

The final cold-draw introduces a high density of dislocations. The dislocation structure of the α -grains consists of a mixture of a- and c-component dislocations with densities of about 4×10^{14} and $1 \times 10^{14} \text{ m}^{-2}$, respectively [1].

During operation of a CANDU reactor, the cold-worked Zr-2.5Nb pressure tubes are expected to operate to high fluences at temperatures of about 520–585°K and pressures of about 10 MPa in a fast neutron flux of about $4 \times 10^{17} \text{ n} \cdot \text{m}^{-2} \cdot \text{s}^{-1}$. The tubes elongate and expand diametrically during service due to irradiation creep and growth. The irradiation deformation of the tubes varies along their length and from tube to tube.

A semiempirical model has been developed that predicts the in-reactor deformation for an average tube based on the operating conditions [2]. The model can take into account texture variations by allowing for modification of the creep anisotropy factors. However, empirical factors that are introduced into the model to account for end-to-end differences in irradiation creep and growth rates are fixed, and are, therefore, a source of error when these factors vary due to changes in microstructure. Apart from texture, the only other microstructural feature known to vary significantly from the front-to-back end of pressure tubes is grain size. In the model [2], the effect of grain size is factored into the axially dependent growth term ($K_6(x)$) based on a theoretical assessment of the dependency of irradiation growth on grain size [3]. There is currently no grain size (or other) dependency that is applied to the axially dependent creep term ($K_4(x)$). Because of this, the model cannot capture adequately the effects of grain size variations that occur along the lengths of tubes and from tube to tube.

Experimental

Diametral Strain Measurements

Diametral strain measurements were obtained in-reactor by use of a gaging tool as described in [2].

Manufacturing and Mechanical Test Data

Information about the ingot chemistry and thermo-mechanical treatments, up to and including extrusion, has been compiled in a database for all tubes for which there was diametral strain data. Mechanical test data for these tubes, obtained as part of their acceptance tests, were also compiled. In addition, where possible, chemical analyses of the archive materials were obtained, as these are more representative of the tube chemistry than values estimated from the ingot data.

Microstructure Data From Offcuts of In-Service Pressure Tubes

X-ray Diffraction (XRD) specimens (about 100 mm² area × 0.5-mm thick) were prepared by cutting slices from archive material from the tubes with normals corresponding to each of the three principal tube axes, i.e., perpendicular to the radial (R), longitudinal (L), and transverse (T) directions of the tubes. Each specimen was then chemically polished using a solution of 5% HF, 45% HNO₃, and 50% H₂O to remove at least 0.025 mm—the depth of damage from the low speed diamond wheel used to cut the specimen. Dislocation densities and lattice parameters were determined from line-broadening analysis of X-ray diffraction peaks obtained using a Rigaku diffractometer with a 12 kW (rotating anode) generator with Ni-filtered, CuK_α radiation, and for high diffraction angles, a Siemens diffractometer and a 1 kW X-ray generator with Ni-filtered, CuK_α radiation. Measurements on the broadening of the (3030) prism-plane diffraction lines of the hcp α-phase gives information about a-component dislocation densities, and measurements of the broadening of the (0004) basal-plane diffraction lines give information about c-component dislocation densities [1].

Basal-pole textures were measured following standard procedures and were compiled in the form of Kearns texture parameters [4].

Transmission electron microscopy (TEM) specimens were prepared by punching 3-mm-diameter discs out of 0.1-mm-thick slices with surfaces perpendicular to the longitudinal direction of the tube. Foils were then made by electropolishing with a solution of 10% perchloric acid in methanol at about -40°C with a current density of about 0.01 A mm⁻² using a Materials Science Northwest twin-jet apparatus. Carbon replicas for grain size analysis were prepared from the XRD specimens by means of a two-stage replica technique. Grain size and orientation distributions were obtained from TEM micrographs by measuring the minimum grain thickness at 1 μm intervals, looking down the long axis of the pressure tube. TEM analyses were performed using a Philips CM 30 (300 kV) electron microscope.

Results

The diametral strain profiles as a function of axial location of typical pressure tubes are illustrated in Fig. 1. The solid circles represent a pressure tube installed with back end at the outlet, and the open circles represent a tube installed with its back end at the inlet. The variation in diametral strain behavior from tube to tube is illustrated in Fig. 2. The measured strain values are compared with those predicted for an average pressure tube for a given set of operating conditions and a given axial location. Examination of the various microstructural and chemistry variables indicates that the main parameters that correlate with measured/predicted diametral strain are texture, grain size, and oxygen content.

Microstructure

Measurements of 81 Zr-2.5Nb pressure tubes in the diametral strain database show that there is a general trend for increasing F_r and decreasing F_l from front to back of the tubes

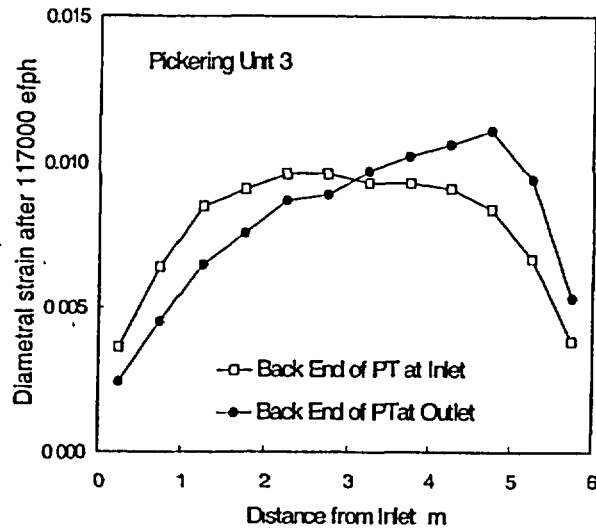


FIG. 1—Typical diametral strain profiles for Zr-2.5Nb pressure tubes installed in a CANDU reactor after 117000 effective full power hours (efph) of operation. Asymmetry occurs when the back end is installed at the outlet.

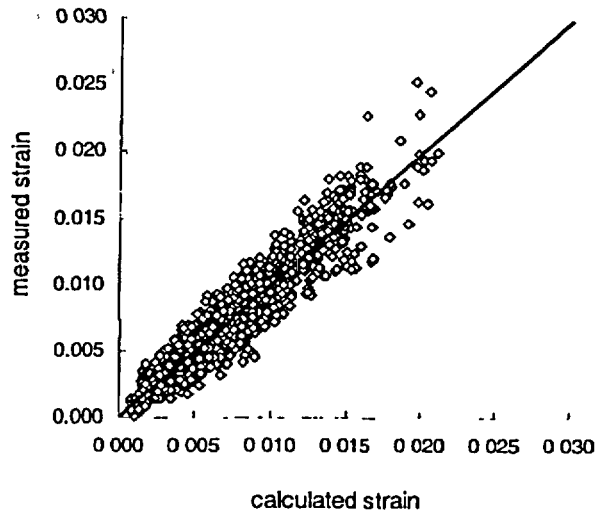


FIG. 2—Measured against predicted [2] diametral strains for Zr-2.5Nb pressure tubes installed in a typical CANDU reactor illustrating the degree of variability in behavior.

TABLE 1 Mean and standard deviation (SD) of basal texture parameters for 81 pressure tubes in the variability database.

	Front End				Back End			
	F_r	F_t	F_l	F_t-F_r	F_r	F_t	F_l	F_t-F_r
Mean	0.298	0.642	0.057	0.344	0.350	0.605	0.051	0.255
SD	0.025	0.031	0.017	0.054	0.029	0.032	0.050	0.059

(Table 1). The diametral strain rate has a negative slope with respect to F_t-F_r [5], generally decreases from front to back, and can account for some, but not all, of the increased diametral strain rates at the back ends.

Likewise, average grain size (minimum thickness) tends to decrease from the front to the back ends of Zr-2.5Nb pressure tubes (Table 2).

In the latter case, many thousands of grains have to be measured for each tube to obtain a meaningful representation of the true grain structure. Unfortunately, there are few sets of data collected in a consistent manner, and therefore, in this case, data are presented corresponding to front-end measurements from 11 tubes and back-end measurements for 26 tubes only. Although these trends from front-to-back ends are generally true for all tubes, there are large variations in textures and grain structures from tube to tube. Figure 3 illustrates distinct differences in grain structures for two tubes, and Fig. 4 illustrates the distribution of texture parameters for many tubes. The effects of the variation in grain structure and texture as related to the peak back end diametral strain are illustrated in Figs. 5 and 6. In the case of grain structure, average back end grain thicknesses are plotted against measured/predicted diametral strain ratio corresponding with the peak strain for a given tube; the trend line is a best-fit polynomial curve (see discussion). For the texture data, the trend is assumed to be linear [5]. In addition to texture and grain structure, the other main variable relating to diametral strain is oxygen content, measured/predicted peak diametral strain ratio decreasing with increasing oxygen content, Fig. 7.

Statistical Analysis

In order to establish that there is a statistically significant trend between measured/predicted diametral strain and each of the statistically significant microstructure parameters (texture, grain size, and oxygen content), a simple linear regression analysis was applied to each set of data illustrated in Figs. 5, 6, and 7. The analysis showed that the most statistically significant trend was for grain size, the probability that a fitted linear slope (-2.42) occurred by chance being 3×10^{-4} . Likewise, for oxygen and texture the probability that the fitted

TABLE 2—Mean and standard deviation (SD) of grain thickness (μm) for 11 front ends and 26 back ends of pressure tubes in the variability database.

	Front End	Back End
Mean	0.45	0.34
SD	0.08	0.06



FIG. 3—Micrographs illustrating differences in grain structures for two different pressure tubes viewed looking down the longitudinal axis: Top—tube FF (front end), bottom—tube A (front end).

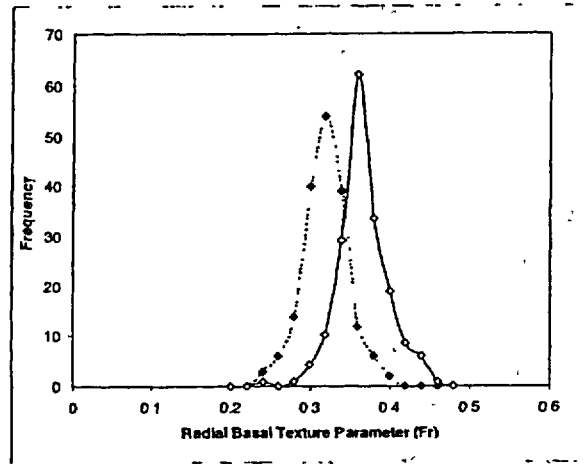


FIG 4—Histograms illustrating distribution of radial basal pole textures for many tubes in various CANDU reactors: dotted line—front ends, full line—back ends

slopes (-2.64×10^{-4} and -0.48 respectively) occurred by chance was 1.17×10^{-2} and 0.1, respectively. Although the variation in tube-to-tube texture exceeds the average axial variations in texture (see Fig. 4), and these axial variations have a significant effect on diametral strain, texture (in a single parameter fit) is the least significant parameter in this case. This can be explained by the fact that textures are taken from a single 10×10 mm section from a tube with a circumference of 176 mm, and preliminary analysis shows that texture parameters can, in some cases, vary by as much as 10–20% around the circumference.

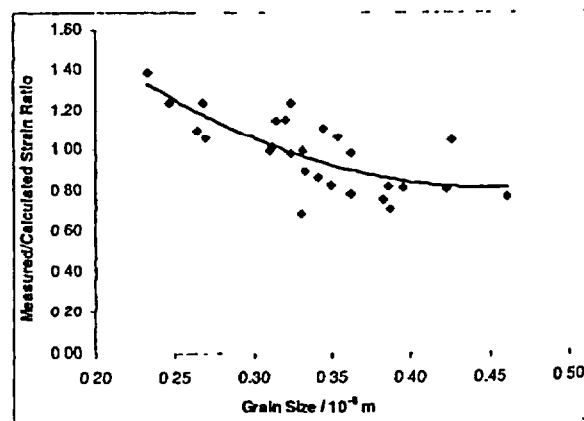


FIG. 5—Relationship between grain thickness and measured/predicted peak diametral strain ratio for back ends of various Zr-2 Nb pressure tubes

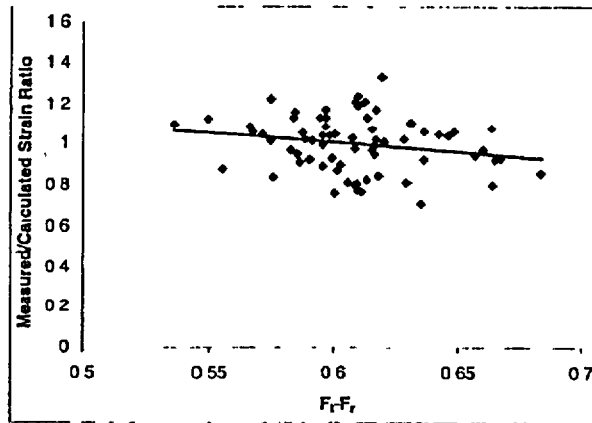


FIG 6—Relationship between texture parameters and measured/predicted peak diametral strain ratio for back ends of various Zr-2.5Nb pressure tubes

For this reason, a single texture sample may not be representative of the tube as a whole, and this additional variability will weaken the apparent correlation between texture variations and variations in diametral strain.

Discussion

Statistical analyses have shown that diametral-strain rates for Zr-2.5Nb pressure tubes are strongly correlated with grain structure, texture, and oxygen content. In order to give a probabilistic assessment of tubes likely to exhibit high diametral strain, better statistical

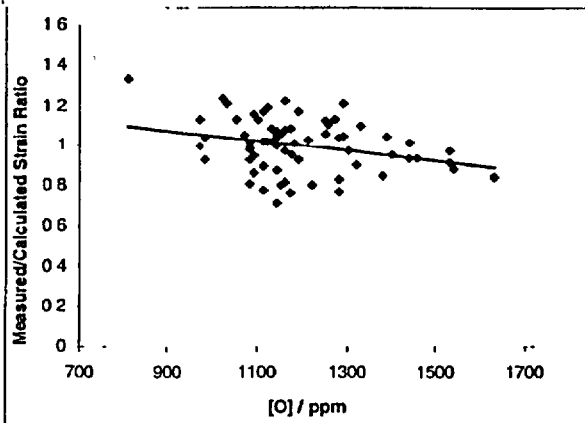


FIG. 7—Relationship between oxygen content and measured/predicted peak diametral strain ratio for back ends of various Zr-2.5Nb pressure tubes.

assessments of the main microstructure variables, texture, and grain thickness, are required. The former is being pursued by taking additional measurements at four clock positions for all tubes that are in the database. The latter is being pursued by shifting to an alternate method of grain-size measurement that involves semiautomated image analysis from SFM micrographs.

Apart from the correlations with the main physical parameters (texture, grain size, and oxygen content) described in this paper, empirical relationships exist between the recorded manufacturing variables and the measured/predicted diametral strain ratio. These relationships are related to the microstructural parameters that ultimately control the deformation behavior. There is a positive correlation between β -quenching of the billet prior to extrusion and diametral strain that is probably related to the effect of β -quenching on the final α -grain size in the as-extruded tube [6].

The two main recorded extrusion variables are soak time prior to extrusion and extrusion pressure. Unfortunately, soak temperatures are not available and, therefore, must be inferred to some extent from the extrusion pressures [7]. In general, diametral strain increases with increasing back-end extrusion pressure. This is primarily because this manufacturing variable has a significant relationship with texture and grain structure [7]. Higher extrusion pressures are consistent with a higher volume fraction of α -phase and could translate into a higher radial-basal texture parameter [8] and smaller average α -grain size when extrusion temperature is the controlling factor [6]. The volume fraction of the α -phase (and therefore extrusion pressure) is primarily dependent on temperature, but is also dependent on oxygen (an α -phase stabilizer) and iron (a β -phase stabilizer) to a lesser extent.

There is negative correlation between soak times and extrusion pressures that has been related to changes in the partitioning of oxygen between the α - and β -phases [7], but there is no statistically significant trend relating soak times to diametral strain. The correlation between total oxygen content and diametral strain ratio is itself complex, because an increase in the total oxygen content increases the volume fraction of α -phase and, therefore, extrusion pressure, and this correlates with a higher diametral strain ratio. The negative correlation between oxygen content and diametral strain ratio (Fig. 7) is then either (a) due to the effect of oxygen on point defect behavior and irradiation deformation directly, or (b) because increased oxygen both increases the volume fraction and coarsens the prior α -phase, resulting in a larger average α -grain size after extrusion.

Even though lower extrusion pressures due to higher temperatures are indicative of a lower α -phase volume fraction but coarser α -grain size, the final grain size distribution can contain a large number of very small grains. These finer, nonaligned (Widmanstätten) grains form due to undercooling of the beta-phase, and this structure is often more prevalent at the front end of the extrusion, Fig. 8. The trend for larger average grain sizes for increasing extrusion temperature can then reverse when the Widmanstätten structure is produced [7]. Cooling rates are therefore important, and can result in either a very coarse structure due to growth of existing alpha-grains or a mixed coarse/fine structure due to undercooling. It has also been suggested that the larger separation of the coarser prior-alpha grains may be significant with respect to the production of a finer Widmanstätten grain structure in some tubes [7].

Although there is a sound theoretical basis for relating differences in diametral strain with differences in texture [2,5], there is little theoretical or experimental support for the effect of grain size and oxygen. It could be argued that the negative trend with oxygen is reasonable, based on the known effect of oxygen vis-à-vis strain aging [9]. Likewise, the grain size dependency is implicitly illustrated by front-to-back-end differences in diametral strain. In addition, previous theoretical and experimental work on irradiation growth has shown a grain-size effect that would be consistent with high diametral strains [3].

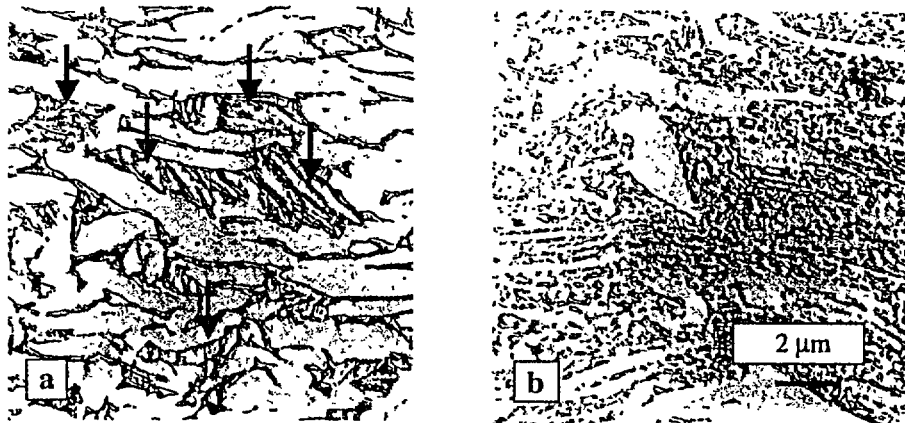


FIG. 8—Micrographs of carbon replicas illustrating differences in grain structures for a typical pressure tube viewed looking down the longitudinal axis: (a) front end, (b) back end. Nonaligned (Widmanstätten) grains formed during cooling of the beta-phase after extrusion are more prevalent at the front end (arrowed in (a)).

The possibility of enhanced creep and growth with smaller grain sizes has been investigated further, using conventional rate-theory models. Adopting a similar model to that used for calculating irradiation growth [3], with the addition of a creep term [10], the calculations indeed show the appropriate grain size and temperature dependencies for irradiation growth [3,11], and these are illustrated in Figs. 9 and 10. In this case, the net strains for a polycrystalline aggregate are calculated assuming no grain interactions and Kearns texture pa-

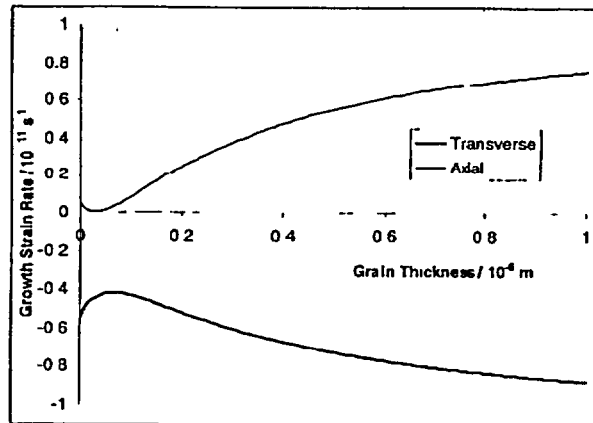


FIG. 9—Calculated grain size dependence of transverse irradiation growth for polycrystalline Zr-2.5Nb pressure tubing at 565 K (a -network dislocation density = $4 \times 10^{14} \text{ m}^{-2}$, c -network dislocation density = $1 \times 10^{14} \text{ m}^{-2}$, $F_N = 0.4$, $F_T = 0.6$, and $F_I = 0$)

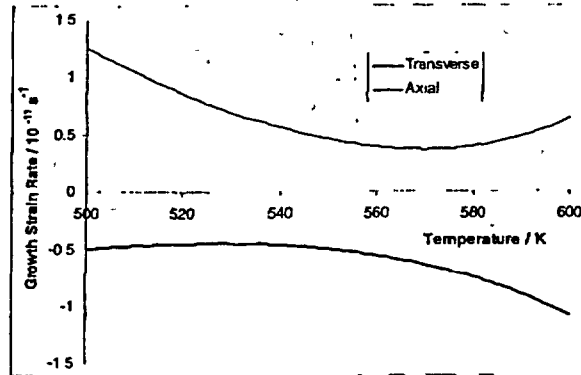


FIG 10—Calculated temperature dependence of irradiation growth for polycrystalline Zr-2.5Nb pressure tubing with an average grain size of 0.3 μm (*a*-network dislocation density = $4 \times 10^{14} \text{ m}^{-2}$, *c*-network dislocation density = $1 \times 10^{14} \text{ m}^{-2}$, $F_R = 0.4$, $F_T = 0.6$, and $F_L = 0$).

parameters [4] of $F_R = 0.4$, $F_T = 0.6$, and $F_L = 0$. With the inclusion of an elastodiffusion term [10], the total transverse deformation rate (irradiation creep and growth) exhibits the correct grain size and temperature dependence consistent with the data [5] (Figs. 11 and 12). In this case, only single-crystal strains are calculated for a typical grain, with a thickness of 0.3 μm and an aspect-ratio of about 1:10:40 in the radial, transverse, and longitudinal directions, respectively, for the biaxial stress state that exists in an in-service pressure tube [5]. For all calculations, it has to be assumed that interstitial bias parameters that are dependent on crystallographic direction increase with increasing temperature.

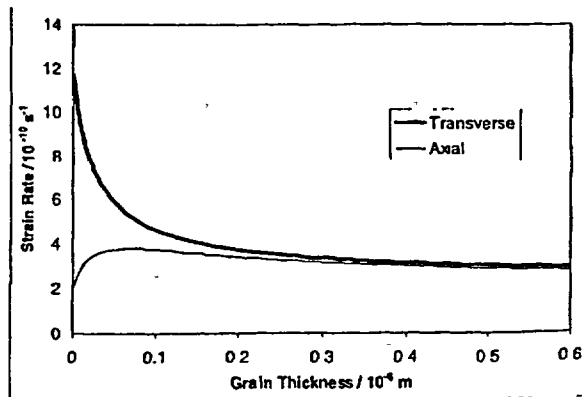


FIG. 11—Calculated diametral strain rates for a single grain in a Zr-2.5Nb pressurized tube as a function of grain thickness for a grain aspect-ratio of 1:10:40 in the radial, transverse, and longitudinal directions, respectively, at 565 K (*a*-network dislocation density = $4 \times 10^{14} \text{ m}^{-2}$, *c*-network dislocation density = $1 \times 10^{14} \text{ m}^{-2}$).

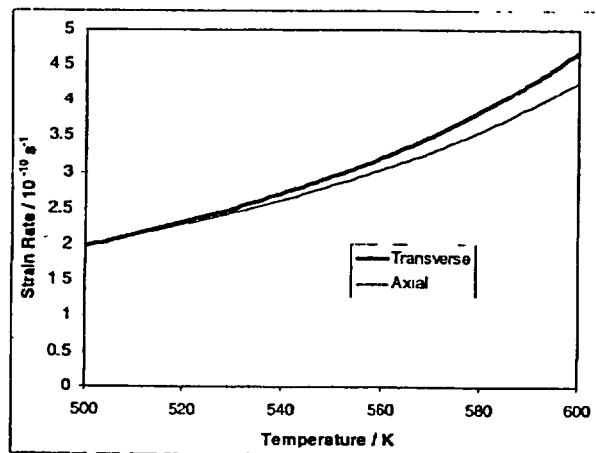


FIG. 12—Calculated diametral strain rates for a single grain in a Zr-2.5Nb pressurized tube as a function of temperature for a grain thickness of $0.3 \mu\text{m}$ and an aspect-ratio of 1:10:40 in the radial, transverse, and longitudinal directions, respectively (α -network dislocation density = $4 \times 10^{14} \text{ m}^{-2}$, ϵ -network dislocation density = $1 \times 10^{14} \text{ m}^{-2}$).

Conclusions

The variation in diametral strain rates in Zr-2.5Nb pressure tubes can be largely accounted for based on variations in texture, oxygen content, and grain structure. Of these parameters, grain size is the most significant. Oxygen affects diametral strain directly, probably by having a direct effect on point defect behavior. Oxygen also modifies the extrusion conditions by affecting the volume fraction of α -phase and therefore, together with iron, has a secondary role in affecting the two main parameters (texture and grain structure) that account for variations in diametral strain. These two microstructural parameters are largely controlled by the manufacturing process (billet quenching, extrusion preheat times, and extrusion temperatures). Further work is underway, making use of nonlinear multiple regression analysis, in an attempt to understand the relationship between diametral strain, manufacturing conditions, grain size, texture, and oxygen and iron content. In addition, improved sampling will be employed at numerous circumferential locations to obtain better representative microstructural data (texture, grain structure, dislocation densities, and offcut chemistry).

Acknowledgments

The authors would like to thank D. Sage and J. C. Owens for assistance in collecting the X-ray diffraction data, and D. Gallindo, R. E. Mayville, and O. T. Woo for assistance in grain structure determinations. The authors would also like to thank S. J. Bushby for useful discussions and comments on the manuscript. The work was funded by the CANDU Owners Group.

References

- [1] Griffiths, M., Mecke, J. F., and Winegar, J. E., "Evolution of Microstructure in Zirconium Alloys During Irradiation," *Zirconium in the Nuclear Industry: Eleventh International Symposium, ASTM*

- STP 1295, E. R. Bradley and G. P. Sabol, Eds., ASTM International, West Conshohocken, PA, 1996, pp 580-602.
- [2] Christodoulou, N., Causey, A. R., Holt, R. A., Tome, C. N., Badie, N., Klassen, R. J., Sauve, R., and Woo, C. H., "Modeling In-Reactoer Deformation of Zr-2.5Nb Pressure Tubes in CANDU Power Reactors," *Zirconium in the Nuclear Industry: Eleventh International Symposium, ASTM STP 1295*, E. R. Bradley and G. P. Sabol, Eds., ASTM International, West Conshohocken, PA, 1996, pp 518-537.
- [3] Holt, R. A., "Irradiation Growth in Zr-Alloy," *Journal of Nuclear Materials*, Vol. 159, 1988, pp. 310-338.
- [4] Kearns, J. J., "Thermal Expansion and Preferred Orientation in Zircaloy," WAPD-TM-472, Report of Westinghouse Electric Corporation, Bettis Atomic Power Laboratory, Pittsburgh, PA, 1965
- [5] Christodoulou, N., Causey, A. R., Woo, C. H., Tome, C. N., Klassen, R. J., and Holt, R. A., "Modelling the Effect of Texture and Dislocation Density on Irradiation Creep of Zirconium Alloys," *Effects of Radiation on Materials: 16th International Symposium, ASTM STP 1175*, A. S. Kumar, D. S. Gelles, R. K. Nanstad, and E. A. Little, Eds., ASTM International, West Conshohocken, PA, 1993, pp. 1111-1128.
- [6] Cheadle, B. A., "Fabrication of Zirconium Alloys into Components for Nuclear Reactors," *Zirconium in the Nuclear Industry: Third International Symposium, ASTM STP 633*, A. L. Howe and G. W. Parry, Eds., ASTM International, West Conshohocken, PA, 1977, pp 457-485
- [7] Choubey, R., Aldridge, S. A., Theaker, J. R., Cann, C. D., and Coleman, C. E., "Effects of Extrusion-Billet Preheating on the Microstructure and Properties of Zr-2.5Nb Pressure Tube Materials," *Zirconium in the Nuclear Industry: Eleventh International Symposium, ASTM STP 1295*, E. R. Bradley and G. P. Sabol, Eds., ASTM International, West Conshohocken, PA, 1996, pp 657-675
- [8] Holt, R. A. and Aldridge, S., "Effect of Extrusion Variables on Crystallographic Texture of Zr-2.5Nb," *Journal of Nuclear Materials*, Vol 135, 1985, pp. 246-259.
- [9] Kelly, P. M. and Smith, D. P., "Strain-Aging in Zirconium-Oxygen Alloys," *Journal of Nuclear Materials*, Vol 46, 1973, pp. 23-34.
- [10] Woo, C. H., "Irradiation Creep Due to Elastodiffusion," *Journal of Nuclear Materials*, Vol 120, 1984, p 55.
- [11] Holt, R. A. and Fleck, R. G., "The Contribution of Irradiation Growth to Pressure Tube Deformation," *Zirconium in the Nuclear Industry: Ninth International Symposium, ASTM STP 1132*, C. M. Focken and A. M. Garde, Eds., ASTM International, West Conshohocken, PA, 1990, pp 218-227.

DISCUSSION

G. D. Moan (written discussion)—The microstructure shown in the figures for Tubes FF and A (?) were those in two tubes made 30 years ago, one from US material and the other from European material. The microstructure of later tubes is more uniform.

Griffiths et al. (authors' closure)—Yes, the two Tubes FF and A were from two different, nonstandard sources (USA and France respectively). Tube FF had a high Fe content and Tube A had a low Fe content. These examples illustrate extremes of variability from tube to tube. I agree, later tubes have a more uniform microstructure.

Young Suk Kim¹ (written discussion)—

- (1) What is the critical neutron fluence to initiate the nonlinear growth of CANDU Zr-2.5Nb tube which is subjected to annealing at 400°C for 24 h for prefilming?
- (2) The reason for raising this question is that we have observed no change in the C-type dislocation density with the neutron fluence up to about 9×10^{25} n/m² in the Wolsong-1 tube. Please comment on the nonlinear growth pattern of CANDU 6-type pressure tubes.

Griffiths et al. (authors' closure)—

- (1) In the case of cold-worked materials, there is no critical fluence necessary for the onset of nonlinear growth. This is because c-component dislocation loops nucleate on existing c-component network dislocations that have a significant screw character. We believe that one of the reasons for having a delay before the onset of "breakaway" growth in annealed Zr-alloy is the incubation period necessary for the nucleation of c-component loops. The nucleation barrier appears to be small or insignificant when nucleation occurs on existing dislocations (see Griffiths et al. JNM 225 (1995) p. 245 and Holt et al. STP 1354 (2000) p. 86).
- (2) The evolution of the c-component dislocation structure is difficult to establish in such a complex system as exists in Zr-2.5Nb pressure tubing, especially if one is taking measurements from many tubes irradiated to different fluences, because of the large degree of variability that exists. Using a combination of XRD line-broadening and TEM analysis, a statistically significant trend is observed for data from ex-service pressure tubes that extends to fluences $> 10 \times 10^{25}$ n · m⁻² and is particularly apparent for grains oriented with their c-axes parallel with the radial direction of the tube. The trend is much clearer when dealing with a single source material (see Hosbons et al. STP 1354 (2000) p. 122).

R. K. Srivastava² (written discussion)—What was the production route followed for the tubes you studied? Most of the problems you referred to can be solved if tubes are pilgered. Extrusion followed by two-stage cold pilgering, and then autoclaving, results in uniform microstructure along the length

Griffiths et al. (authors' closure)—The tubes were fabricated according to a standard production process for CANDU reactor pressure tubes (see Choubey et al. STP 1295 (1996) p.

¹ KAERI.

² Nuclear Fuel Complex, Hyderabad, India.

657). Much of the variability that is reported in this paper comes from "historic" tubes, i.e., tubes manufactured in the 1960s and 1970s. Tubes fabricated currently do not exhibit the same degree of variability, either axially or from tube to tube. The variability in the older tubes was due to the extrusion conditions, not the cold drawing, and would not be corrected by pilgering. There would be an interest in the properties and operating behavior of pilgered tubes if such data were presented at future Zr Symposia.

Stefan Sagat,¹ Christopher E. Coleman,² Malcolm Griffiths,³ and
Brian J. S. Wilkins⁴

The Effect of Fluence and Irradiation Temperature on Delayed Hydride Cracking in Zr-2.5Nb

REFERENCE: Sagat, S., Coleman, C. E., Griffiths, M., and Wilkins, B. J. S., "The Effect of Fluence and Irradiation Temperature on Delayed Hydride Cracking in Zr-2.5Nb," *Zirconium in the Nuclear Industry: Tenth International Symposium, ASTM STP 1245*, A. M. Garde and E. R. Bradley, Eds., American Society for Testing and Materials, Philadelphia, 1994, pp. 35-61.

ABSTRACT: Zirconium alloys are susceptible to a stable cracking process called delayed hydride cracking (DHC). DHC has two stages: (a) crack initiation that requires a minimum crack driving force (the threshold stress intensity factor, K_{IH}) and (b) stable crack growth that is weakly dependent on K_I . The value of K_{IH} is an important element in determining the tolerance of components to sharp flaws. The rate of cracking is used in estimating the action time for detecting propagating cracks before they become unstable. Hence, it is important for reactor operators to know how these properties change during service in reactors where the components are exposed to neutron irradiation at elevated temperatures. DHC properties were measured on a number of components, made from the two-phase alloy Zr-2.5Nb, irradiated at temperatures in the range of 250 to 290°C in fast neutron fluxes ($E \geq 1$ MeV) between 1.6×10^{17} and 1.8×10^{18} n/m² · s to fluences between 0.01×10^{23} and 9.8×10^{23} n/m². The neutron irradiation reduced K_{IH} by about 20% and increased the velocity of cracking by a factor of about five. The increase in crack velocity was greatest with the lowest irradiation temperature. These changes in the crack velocity by neutron irradiation are explained in terms of the combined effects of irradiation hardening associated with increased $\langle a \rangle$ -type dislocation density, and β -phase decomposition. While the former process increases crack velocity, the latter process decreases it. The combined contribution is controlled by the irradiation temperature. X-ray diffraction analyses showed that the degree of β -phase decomposition was highest with an irradiation temperature of 290°C while $\langle a \rangle$ -type dislocation densities were highest with an irradiation temperature of 250°C.

KEY WORDS: delayed hydride cracking, crack velocity, threshold stress intensity factor, irradiation fluence, irradiation temperature, zirconium, zirconium alloys, nuclear materials, nuclear applications, radiation effects

¹Research Metallurgist, AECL Research, Materials and Mechanics Branch, Chalk River Laboratories, Chalk River, Ontario K0J 1J0, Canada.

²Branch manager, AECL Research, Fuel Channel Components Branch, Chalk River Laboratories, Chalk River, Ontario K0J 1J0, Canada.

³Research metallurgist, AECL Research, Reactor Materials Research Branch, Chalk River Laboratories, Chalk River, Ontario K0J 1J0, Canada.

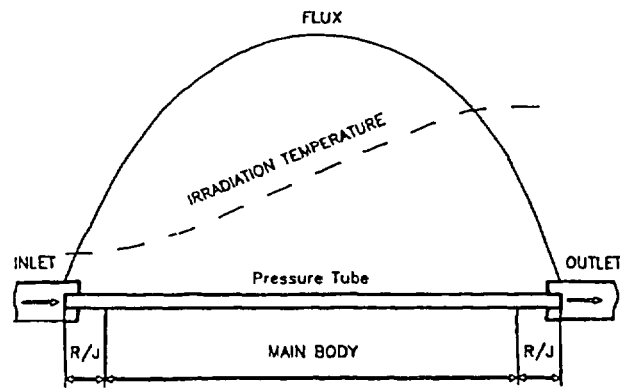
⁴Senior research metallurgist, AECL Research, Materials and Mechanics Branch, Whiteshell Laboratories, Pinawa, Manitoba R0E 1L0, Canada.

Delayed hydride cracking (DHC) is a stable crack growth mechanism in zirconium alloys. Hydrogen accumulates at a stress raiser. If sufficient hydrogen is present, hydrides form and, if the stress is high enough, the hydrides fracture and the crack advances. The process is then repeated until the crack becomes unstable. The two main characteristic parameters of DHC are the crack velocity, V , and the threshold loading below which cracks do not grow; with sharp cracks at moderate loads, linear elastic fracture mechanics is used, and the threshold stress intensity factor is called K_{IH} . Neutron irradiation at some temperatures increases V and reduces K_{IH} [1,2]. At least two methods exist to evaluate the effect of irradiation on DHC: (1) prepare appropriate specimens, then irradiate them in a reactor, or (2) machine specimens from components removed from reactors for surveillance. In this paper, we describe the results of experiments using both methods. Many cold-worked Zr-2.5Nb pressure tubes were removed from CANDU power reactors as part of a planned large-scale retubing program and thus a comprehensive evaluation program was possible. The objectives were to measure the effects of irradiation fluence and irradiation temperature on V and K_{IH} and to relate the results to the microstructural changes produced by irradiation.

Experimental Procedure

Material

Pressure tubes in CANDU reactors are made from Zr-2.5Nb alloy by hot extrusion of hollow billets followed by 25% cold work. The extrusion process results in a crystallographic texture with the following resolved basal pole fractions: 0.32 (radial), 0.61 (transverse), and 0.07 (axial). The pressure tubes are about 6 m long and have an inside diameter of 103 mm and a wall thickness 4.1 mm. They are joined to stainless steel end fittings by internal rolling. The material used in these experiments came from 45 pressure tubes that were removed from power reactors and from offcuts. The offcuts are small pieces of archived material cut off from each end of a pressure tube prior to operation. The tubes were removed from different lattice positions and sampled at different axial positions along the tube to provide a range of irradiation fluences and temperatures. A schematic diagram of a pressure tube and related terminology used throughout this paper are shown in Fig. 1. The rolled joint (R/J) regions are



SCHEMATIC

FIG. 1—A schematic diagram of a fuel channel in CANDU reactor.

defined as the pieces that are within about 200 mm from each end of the tube, and the remainder of the tube is referred as the main body.

Zr-2.5Nb material was also irradiated in a high flux reactor (OSIRIS) at Centre d'Etudes Nucleaires de Saclay. The purpose of this irradiation was to achieve end-of-life fluences substantially ahead of the life of the tubes in the reactors. Two materials were used for this irradiation: standard, cold-worked Zr-2.5Nb (tube H737) and Zr-2.5Nb material produced by a modified route, TG3R1 (Task Group 3 Route 1 material developed at Ontario Hydro). The TG3R1 pressure tubes were produced using a lower extrusion ratio and higher percent cold-work than standard pressure tubes, and had an extra stress relieve at 500°C for 6 h after cold drawing. Details about production routes for the fabrication of cold-worked Zr-2.5Nb tubes are given in Ref 3. About 1 atomic percent of hydrogen was added gaseously to these materials prior to irradiation. To achieve a uniform distribution of hydrogen, the materials were homogenized at 400°C for 72 h. The irradiation of H737 material was called ERABLE and the irradiation of TG3R1 material was called TRILLIUM. Both irradiations have been carried out at a temperature of 250°C.

Specimens

Two types of specimens were prepared from the tubes: (1) cantilever beam (CB) and (2) curved compact toughness (CCT) specimens, Fig. 2. The CB specimens were used for measuring

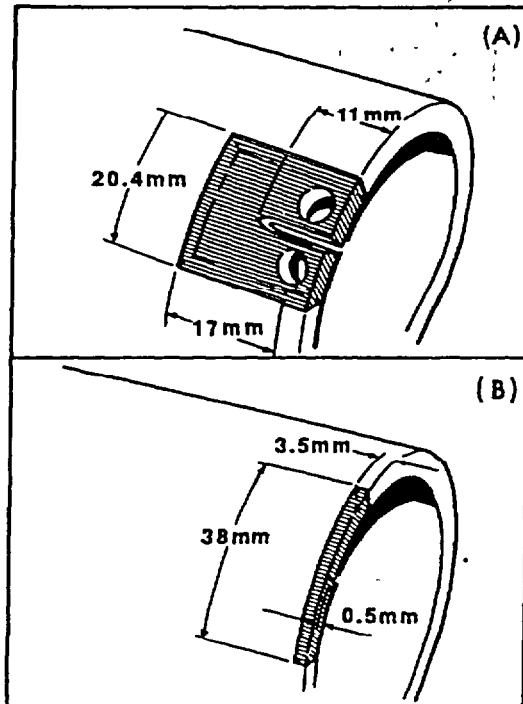


FIG. 2—Curved compact toughness (A) and cantilever beam (B) specimens used in DHC tests.

V and K_{IH} in the radial direction, and the CCT specimens for measuring V in the axial direction. Cracks were started in CB specimens from 0.5-mm-deep notches machined on the inside surface. The CCT specimens were fatigue pre-cracked. Because the initial hydrogen concentration in the specimens was low, hydrogen was added to some specimens electrolytically to allow testing up to 290°C. In this technique a layer of solid zirconium hydride is deposited on the surface of the specimen. The specimen is then homogenized at a solvus temperature corresponding to the required hydrogen concentration. This treatment results in uniform distribution of fine hydrides through the bulk of the specimen.

Experimental Techniques

Crack velocity of DHC is sensitive to the temperature history; the maximum value of V is attained by cooling (without undercooling) to the test temperature from above the solvus temperature of hydrogen in zirconium [4]. Thus, a standard procedure for measuring V was developed as shown in Fig. 3. To minimize annealing of irradiation damage, the maximum peak test temperature in irradiated material should not be greater than the irradiation temperature plus 10°C. The load can be applied either at the end of the high temperature soak, or after attaining the test temperature. The latter avoids premature cracking during cooling and allows an accurate evaluation of the time to crack initiation. The loads applied should be within ASTM criteria for linear elastic fracture mechanics, that is, ASTM Test Method for Plane-Strain Fracture Toughness of Metallic Materials (E 399-90). CB specimens were loaded in

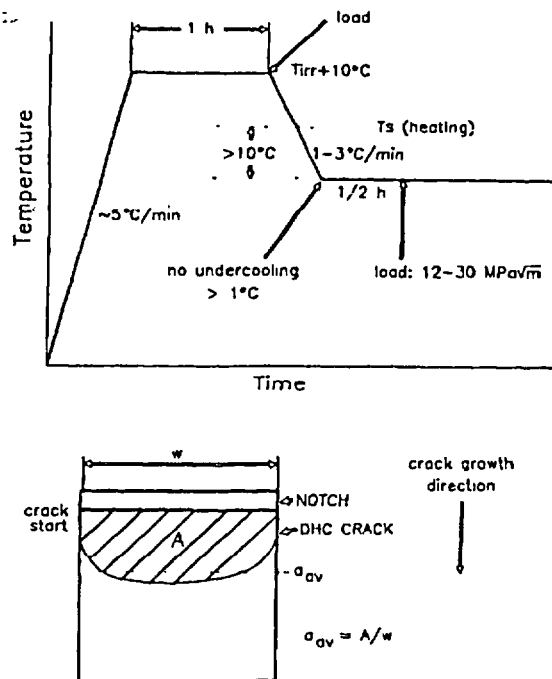


FIG 3—Standard temperature and loading history for DHC testing.

bending and cracking was detected by acoustic emission [5]. CCT specimens were dead weight loaded in tension in a creep frame and cracking was monitored by a d-c potential drop method [6]. The cracks were grown from about 0.5 to 2.0 mm. Crack velocity was derived from the average crack depth divided by the time over which steady cracking occurred. Crack depth was defined as the area of DHC, delineated by heat-tinting, divided by the specimen thickness.

In the literature, two methods of determining K_{IH} , have been described as follows:

1. A number of specimens are loaded to different K_I and incubation times for cracking are measured; K_{IH} is estimated by a projection to infinite time [7]. Measuring K_{IH} using this technique takes several years, but provides realistic values.
2. One specimen only is used and K_{IH} is measured over a relatively short period of time by either increasing the load until cracking starts or decreasing the load until cracking ceases [5,8].

The method we have standardized on for quick comparisons is based on decreasing the load. After the standard temperature cycle, the specimen is loaded to $17 \text{ MPa}\sqrt{\text{m}}$. Once cracking is initiated, the K_I is reduced 2% per $5 \mu\text{m}$ of crack growth, derived from the calibration of the acoustic emission through an automatic feedback system [5]. The load is reduced until acoustic emission stopped and no further indications are obtained for at least 24 h. K_{IH} is derived from this final load and the average crack depth.

Experimental Errors

The main sources of errors in the measurement of DHC velocity are:

1. uncertainty in the determination of the time for steady cracking, and
2. uncertainty in the determination of the crack depth.

It takes a certain amount of time, called incubation time, before cracking starts. Before steady crack growth is attained, the cracking may go through a transient period, during which the cracking may be erratic or intermittent. Neither the incubation time nor the transient time should be included in the crack velocity calculation. The uncertainty in determining the time of steady cracking depends on the sensitivity of the acoustic emission or potential drop techniques and on estimating the onset of steady cracking, which is not always clear-cut.

Crack propagation is not always uniform across the specimen section; hence, the average crack depth, derived by dividing the cracked area by the specimen thickness, is sensitive to the crack shape. Crack velocity in nonuniform cracks and cracks that tunnel excessively, may be different from those in uniform cracks, even if crack areas are the same.

The errors arising from temperature and load measurements are small in comparison with the errors in determining crack depth and time of cracking.

Based on data, we estimate that the error in measurement of DHC velocity is $\pm 25\%$ and $\pm 50\%$ from the mean, in unirradiated and irradiated material, respectively.

The error in the measurement of K_{IH} , using the standard load reducing method, depends on the following:

1. uniformity of DHC crack,
2. accuracy of acoustic emission equipment,
3. accuracy of load measurement, and
4. the required "wait time" of no cracking.

As far as the crack shape is concerned, similar arguments apply to K_{IH} tests as those discussed for crack velocity tests. In a K_{IH} test, it is absolutely mandatory that the acoustic emission equipment is not noisy, because each time false counts are recorded, the load is reduced and this leads to underestimating K_{IH} .

An accurate load measurement is important because the loads are very small when K_{IH} is approached.

We estimate the error in measuring K_{IH} , using the load reducing method, to be $\pm 1 \text{ MPa}\sqrt{\text{m}}$ ($\pm 15\%$).

Microstructural Examinations

The microstructure of cold-worked Zr-2.5Nb consists of flat, α -zirconium grains surrounded by thin layers of continuous β -zirconium, Fig. 4. To study the evolution of the microstructure, notably the decomposition of the β -phase during the irradiation, and the evolution of the dislocation substructure, X-ray diffraction (XRD) was used; transmission electron microscopy was not able to resolve the changes occurring in the β -phase or evaluate the dislocation substructure quantitatively. Specimens for analysis by XRD were prepared by cutting thin slices from the tube perpendicular to each of the three principal tube axes, that is, longitudinal normal (LN), transverse normal (TN), radial normal (RN). The LN(10 $\bar{1}$ 0) α , TN(0002) α , LN(110) β , and RN(200) β diffraction lines were measured using a Rigaku rotating anode diffractometer with CuK_α radiation. The RN(11 $\bar{2}$ 0) α diffraction lines were measured using a Siemens diffractometer also operating with CuK_α radiation. The line shapes of the X-ray profiles for the α -phase were analyzed using the Fourier method and these were interpreted in terms of dislocation density for $\langle a \rangle$ -type and $\langle c \rangle$ -component dislocations [9,10].

Results

The factors that affect DHC were expected to be irradiation fluence, irradiation temperature, test temperature, and direction of testing on the plane normal to the transverse direction.

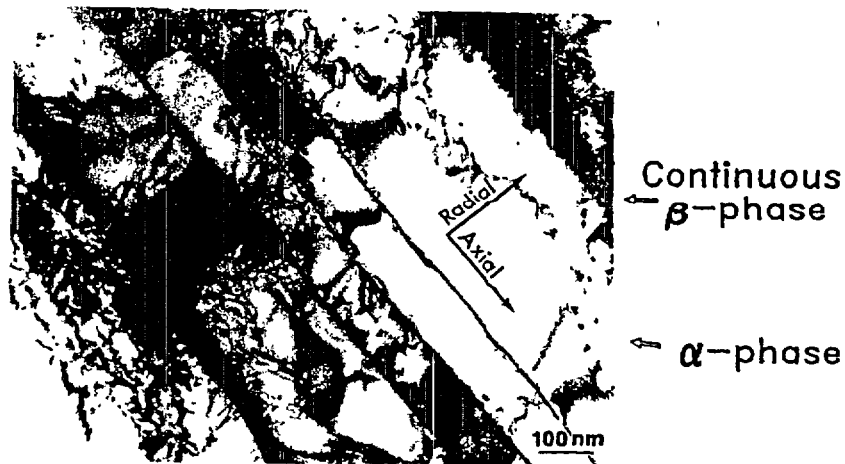


FIG. 4—Microstructure of cold-worked Zr-2.5Nb pressure tube

Effect of Irradiation Fluence

The effect of irradiation fluence was studied on specimens prepared from the R/J and main body regions of pressure tubes removed from power reactors, and on specimens from the end-of-life irradiations in France. DHC velocities in both the radial and axial directions were determined as a function of fluence. Tensile properties in the transverse direction were determined as a function of fluence.

In the R/J region, the crack velocity increased rapidly with fluence, Figs 5 and 6. The results from the end-of-life irradiations (TRILLIUM and ERABLE) showed a weak dependence of the crack velocity on fluence, Fig. 6. In specimens from the main bodies of pressure tubes, the crack velocity was three to five times higher than that of unirradiated material and was found to be independent of fluence, Figs. 5 and 6. These observations suggest that the effect of irradiation saturates at about 1×10^{25} n/m². The yield stress follows a similar behavior, Fig. 7 [11], it saturates at about 0.3×10^{25} n/m².

Effect of Irradiation Temperature

In CANDU reactors, the temperature along the channel increases from about 250°C at the inlet end to about 290 to 300°C at the outlet end. As shown in Figs. 5 and 6, the crack velocities are higher at the inlet end than at the outlet end. Figures 8 and 9 show the crack velocity as a function of position along the fuel channel. The velocity drops off sharply towards the R/Js and decreases gently from the inlet end towards the outlet end. These results are obtained on 45 pressure tubes and the scatter includes tube-to-tube variability.

Direction of Testing

Shapes of cracks in early Pickering and Bruce reactors indicated that the rate of crack growth in the axial direction of the tube is about twice that in the radial direction. This

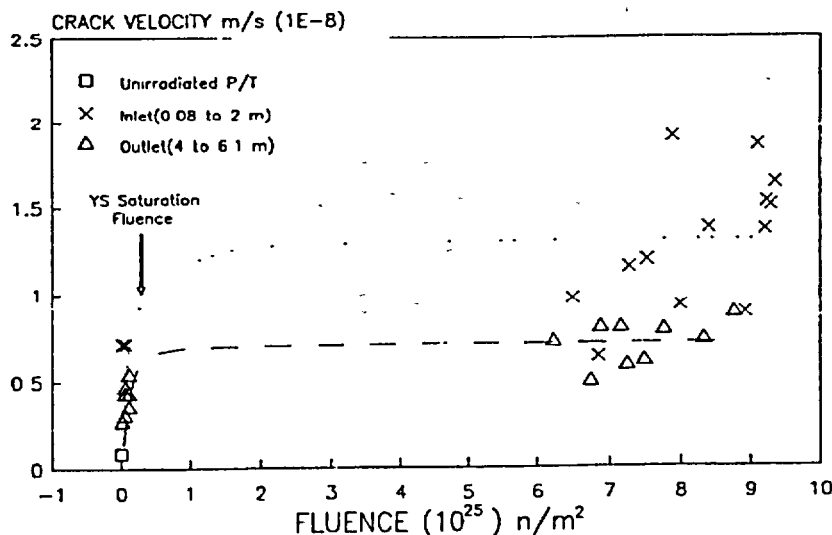


FIG. 5—Dependence of axial DHC velocity on irradiation fluence (test temperature, 130°C).

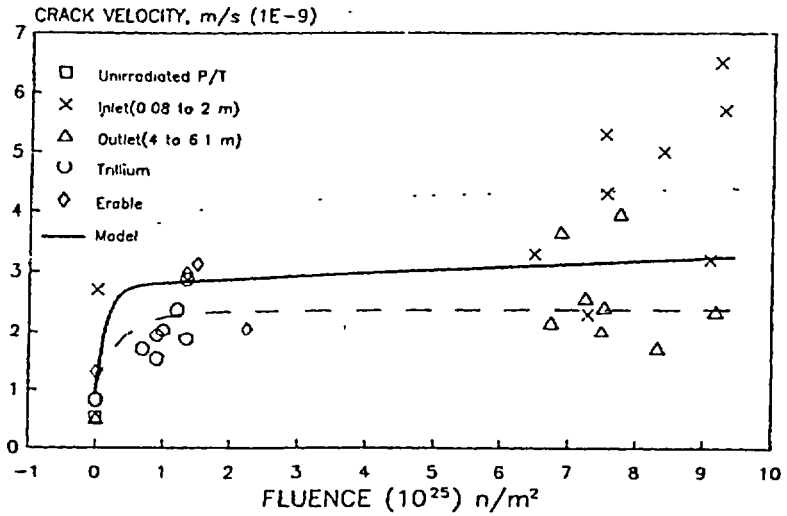


FIG. 6—Dependence of radial DHC velocity on irradiation fluence (test temperature: 130°C).

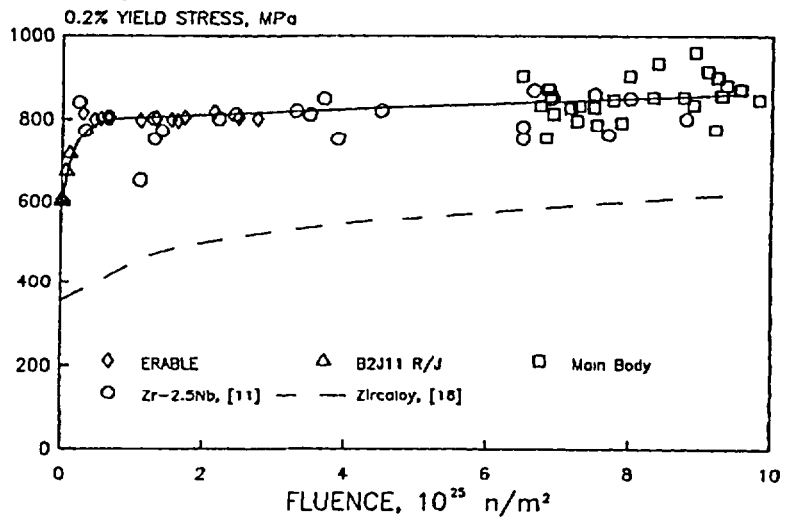


FIG. 7—Dependence of yield stress on irradiation fluence (test temperature: 250°C).

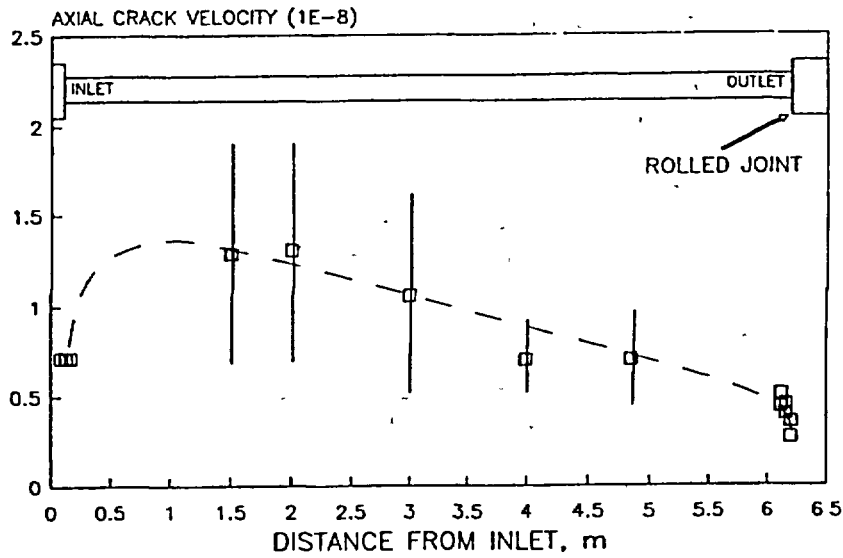


FIG. 8—Variation of axial DHC velocity along pressure tube (test temperature: 130°C).

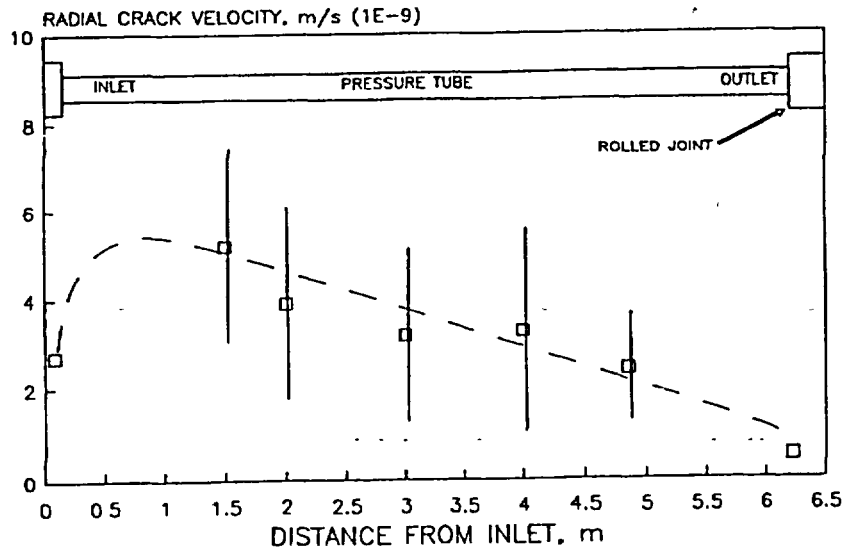


FIG. 9—Variation of radial DHC velocity along pressure tube (test temperature: 130°C)

observation was confirmed in a round-robin test performed at Chalk River Laboratories (CRL), Whiteshell Laboratories (WL), and Ontario Hydro Research Division (OHRD). Standard, unirradiated Zr-2.5Nb pressure tube material with two hydrogen concentrations, 0.36 and 0.50 atomic percent, was used in this round robin. WL and OHR used CCT specimens and measured crack velocity in the axial direction of the pressure tube, and CRL used CB specimens and measured crack velocity in both the radial and axial directions. The objective of this round robin was to determine the variability in crack velocity between CCT and CB specimens and to determine the effect of crack growth direction on DHC velocity. In general, there was good agreement between all three laboratories in the axial crack velocity measurements, which confirmed that the specimen type was not a factor in crack velocity determination. The experimental uncertainty in the results from all three laboratories was less than 25% of the mean at a given hydrogen concentration and crack growth direction. The crack velocity in the axial direction was found to be 1.7 to 1.9 times higher than that in the radial direction, Table 1.

Crack velocities were also measured, in both the radial and axial directions, on the 45 pressure tubes removed from different lattice positions in four power reactors. The majority of the tubes from the power reactors had low hydrogen isotope concentrations (0.05 to 0.1 atomic percent) and had to be tested at temperatures between 120 and 140°C. Some tubes had high hydrogen isotope concentrations at the outlet end, and some specimens were hydrided electrolytically to allow testing up to 300°C.

To measure the radial velocity, cantilever beam specimens were prepared from different axial positions of these tubes. The temperature dependence of the crack velocity followed an Arrhenius relationship as shown in Fig. 10. A least-squares regression produced the following expression for V in m/s

$$V_r = 0.0863 \exp(-58/RT) \quad (1)$$

where

$$R = 8.314 \times 10^{-3} \text{ kJ/mol,}$$

T = the absolute temperature, and 95% confidence limits are a factor of ± 2.6 from the mean.

Crack velocities, measured on the offcut material from two tubes, are grouped around the lower bound line of the irradiated material, Fig. 10. In these tests, many specimens were prepared from sections near the inlet and outlet ends of pressure tubes. Comparing crack velocities in these sections, it was observed that those coming from the inlet sections had consistently higher crack velocities than those from the outlet sections, as shown in Fig. 11. The average crack velocity at the inlet end is about twice that at the outlet end. The least-square regression analysis gave the following expression for the mean V_i in m/s, for inlet and outlet, respectively

TABLE 1—Comparison of axial (V_A) and Radial (V_R) velocities determined at CRL.

H concentration, atomic %	Test Temperature, °C	Axial V_i , m/s	Radial V_i , m/s	V_A/V_R
0.5	250	$11.8 \times 10^{-4} \pm 3.1$	$6.1 \times 10^{-4} \pm 1.3$	1.9
0.5	200	$2.3 \times 10^{-4} \pm 0.15$	$1.2 \times 10^{-4} \pm 0.16$	1.9
0.36	250	$5.9 \times 10^{-4} \pm 0.87$	$3.5 \times 10^{-4} \pm 0.46$	1.7
0.36	200	$2.2 \times 10^{-4} \pm 0.23$	$1.3 \times 10^{-4} \pm 0.17$	1.7

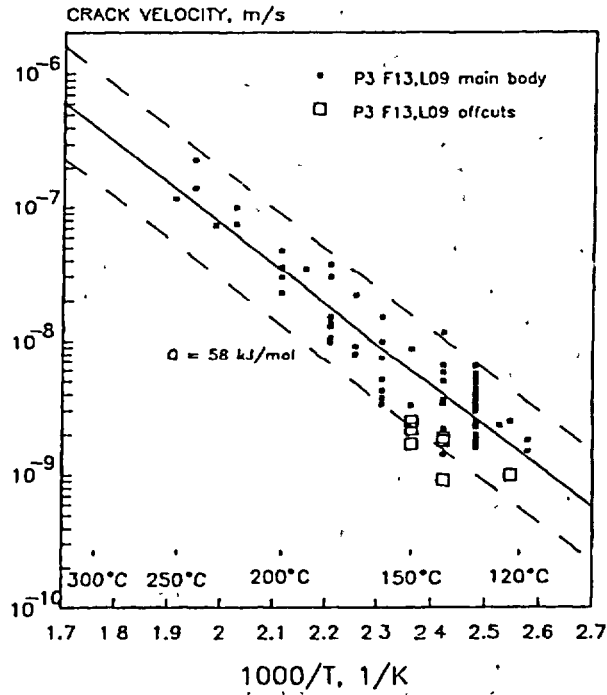


FIG. 10—Temperature dependency of radial DHC velocity

$$V_{rad} = 0.169 \exp(-59/RT) \tag{2}$$

with 95% confidence limits equal to a factor of ± 1.7 from the mean, and

$$V_{out} = 0.068 \exp(-58/RT) \tag{3}$$

with 95% confidence limits equal to a factor of ± 2.1 from the mean.

Figure 12 shows the temperature dependence of the axial crack velocity. The least-square analysis gave the following expression for the mean V , in m/s

$$V_A = 4.02 \times 10^{-3} \exp(-43/RT) \tag{4}$$

with 95% confidence limits equal to a factor of ± 2.3 from the mean.

These results show that the temperature dependency of V in the axial direction is smaller than that in the radial direction, Fig 13. At low temperature, $V_A > V_{rad}$, but at 300°C, both velocities have about the same value.

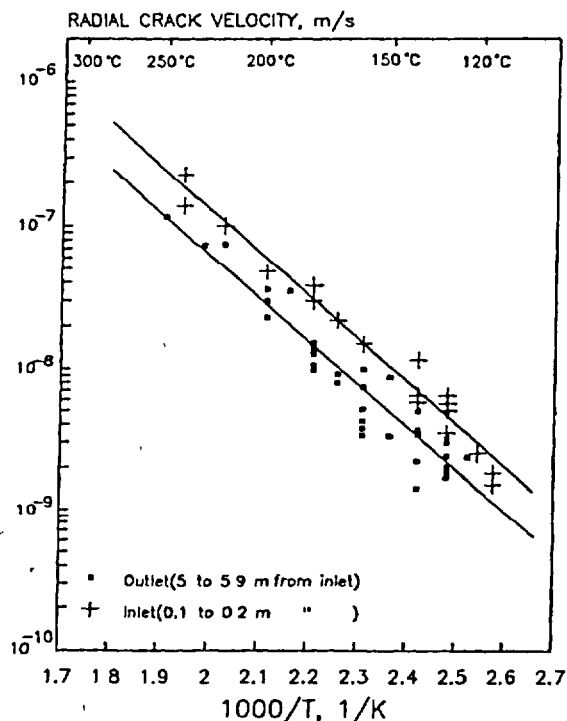


FIG. 11—Difference between radial DHC velocity at the outlet and inlet ends of pressure tube.

Threshold Stress Intensity Factor

The threshold stress intensity factor, K_{IH} , was measured using the load-reducing method on several tubes removed from reactors and on their offcuts. The results showed a small decrease in K_{IH} as the fluence increased to about 1×10^{25} n/m², but no decrease in K_{IH} was observed with further increase in fluence, Fig. 14. The average K_{IH} in the offcuts was 7.5 ± 1.3 MPa \sqrt{m} and, in the irradiated material, it was 6.2 ± 0.9 MPa \sqrt{m} at the 95% confidence level. Within the temperature range of 140 to 250°C, K_{IH} remained constant, Fig. 15.

Microstructural Examinations

XRD analysis shows that enrichment of the β -phase by niobium occurs during service and increases significantly from the inlet toward the outlet, Fig. 16. The enrichment is the result of a gradual decomposition of metastable 20 to 40 atomic percent niobium-enriched β -Zr towards a stable β -Nb phase about 88 atomic percent niobium at 300°C. X-ray diffraction indicates a variation in $\langle a \rangle$ -type dislocation density along the length of the tubes, being highest at the inlet end and decreasing by about 20% toward the outlet end, Fig. 17. The data from samples taken from within 0.5 m of the centers of the tubes show that the $\langle a \rangle$ -type dislocation density has saturated by fluences of about 2×10^{25} n/m², Fig. 18.

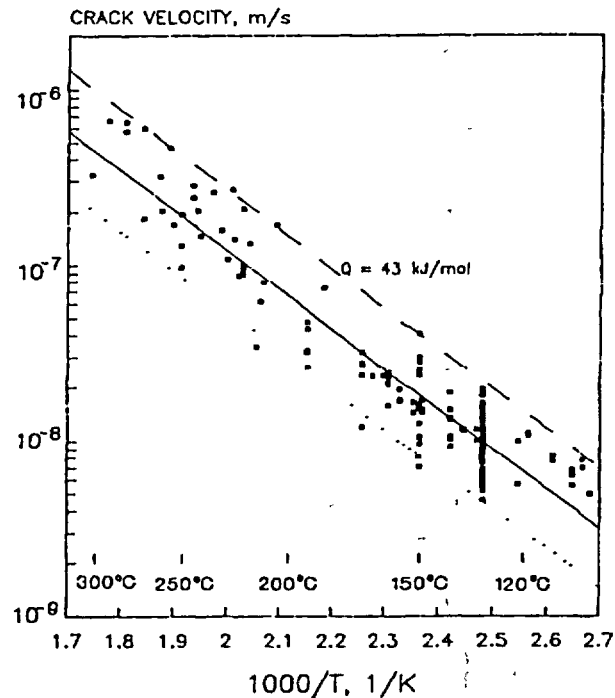


FIG 12—Temperature dependency of axial DHC velocity

Discussion

The results are summarized as follows. The crack velocity, V , of DHC in cold-worked Zr-2.5Nb is increased by a factor of up to five times, and K_{IH} is slightly reduced by neutron irradiation. The effects saturate after about $1 \times 10^{25} \text{ n/m}^2$. V decreases with increase in irradiation temperature. In unirradiated material, V in the axial direction is twice that in the radial direction, but in irradiated material, the dependence of V on direction changes with testing temperature. Neutron irradiation produces damage in the crystal lattice of Zr-2.5Nb in the form of predominantly type- $\langle a \rangle$ dislocation loops that harden the material. The irradiation hardening saturates at a fluence of about $2 \times 10^{25} \text{ n/m}^2$ and so does the yield stress. The β -phase decomposition is controlled by the irradiation temperature—the higher the temperature, the greater is the decomposition. Both the yield stress and the state of the β -phase decomposition have been shown to affect DHC velocity [12,13]. The results will be discussed in the context of these observations.

Effect of Irradiation Fluence

The effect of irradiation fluence on DHC can be explained by the theory of delayed hydride cracking developed by Dutton and Puls [14], and later improved by Puls [8,15] and Ambler [16]. According to this theory, when there is a hydride present at the crack tip, its rate of growth is determined by the rate of diffusion of hydrogen into the crack-tip region. The driving

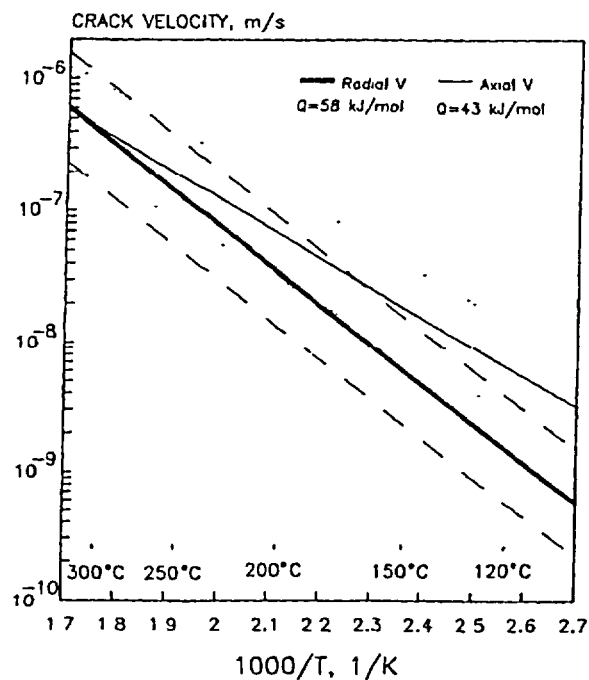


FIG. 13—Comparison between radial and axial DHC velocity.

forces for diffusion are: hydrogen concentration gradient, stress gradient, and thermal gradient. The theory assumes that the crack velocity is equal to the rate of growth of the hydride at the crack tip. The rate of diffusion of hydrogen atoms, dN/dt , into the cylinder of unit length and radius, r , is

$$\frac{dN}{dt} = -2\pi r J_H \quad (5)$$

where J_H is the hydrogen flux ($\text{atoms} \cdot \text{m}^{-2} \cdot \text{s}^{-1}$).

Assuming that the crack velocity is equal to the rate of growth of the hydride at the crack tip, the crack velocity, da/dt , can be written as

$$\frac{da}{dt} = \frac{-2\pi r J_H}{\alpha \alpha_c N_H} \quad (6)$$

where

α = the thickness to length ratio of the hydride,
 $\alpha \alpha_c$ = the thickness of the hydride at fracture, and
 N_H = the atomic density of the hydride.

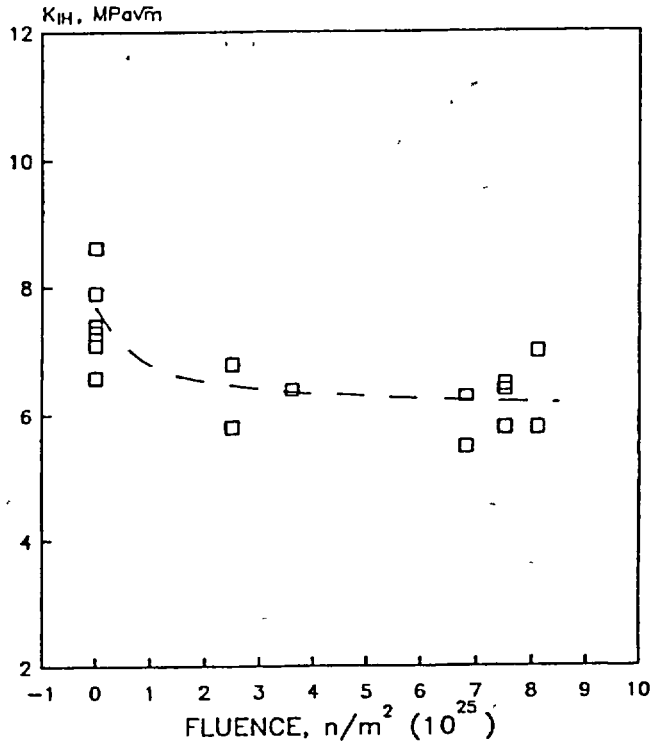


FIG. 14—Dependence of K_{IH} on irradiation fluence.

Substituting for hydrogen flux

$$J_H = \frac{D_0 C_0}{r \Omega_z \phi} (E_L - E_I) \tag{7}$$

the crack velocity, da/dt , can be written as

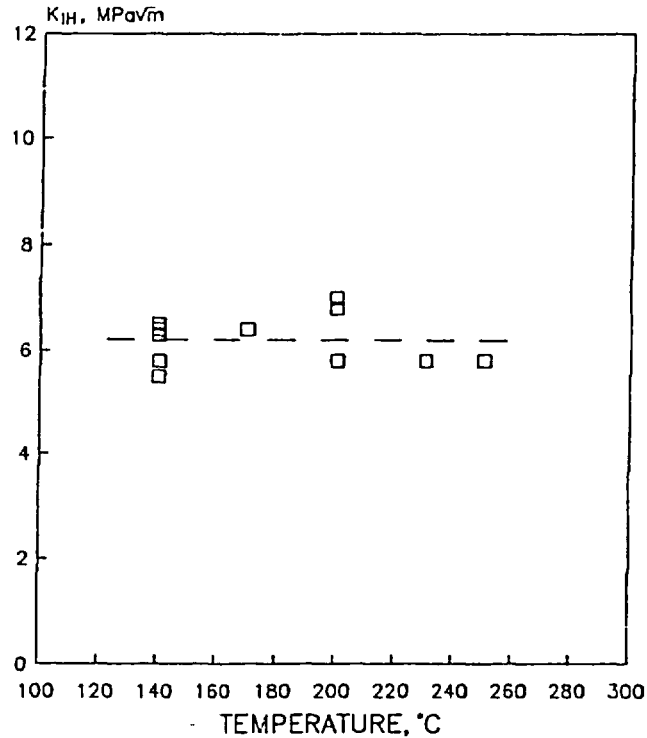
$$\frac{da}{dt} = \frac{2\pi D_0 C_0}{\Omega_z \alpha a_c N_H \phi} (E_L - E_I) \tag{8}$$

where

$$E_{L1} = \exp\left\{\frac{(w_r^{inc})_{L1} + (w_r^e)_{L1}}{xR(T)_{L1}}\right\} \tag{9}$$

$$\phi = \int_1^t \frac{1}{r} \exp\left\{\frac{(F - w_H^e + Q_D)}{RT}\right\} dr \tag{10}$$

The remaining parameters in Eqs 5 to 10 are given in Appendix I.

FIG. 15—Temperature dependency of K_{IH} .

In this model, the effect of irradiation fluence can be accounted for through the value of the yield stress of the material as shown by Puls [15]. There are two terms that are sensitive to yield stress: the position of the maximum stress, a_c , and the interaction energy of the crack-tip hydride with the locally applied stress, $(w_f)_1$. a_c is related to the plastic zone size at the crack tip that depends on the yield stress. $(w_f)_1 = -6.66\sigma_y$, for δ -hydrides. Using the average yield stress from Fig. 7, the model predicts an increase in the mean DHC velocity due to the irradiation hardening to be a factor of about 3, Fig. 19. The current model does not account for either the direction of the crack growth or for the decomposition of the β -phase. However, as diffusion data become available for the anisotropic microstructures of pressure tubes, the model can be expanded to include the crack growth in two-phase material in both the radial and axial directions.

Crack velocity in unirradiated cold-worked Zircaloy-2 is much lower than that in Zr-2.5Nb [2,17]. Results of experiments show that irradiation to a fluence of 7.7×10^{25} n/m² increases the crack velocity in Zircaloy-2 by a factor of 50, making it similar to that of irradiated Zr-2.5Nb, Fig. 19 (for Harvey tubes in Ref 2 that had a similar texture to that of standard Zr-2.5Nb pressure tubes). Using an increase in yield stress from 350 to 600 MPa from irradiation [18], and the diffusion coefficient for α -Zr, the preceding model predicts an increase in the crack velocity, but only by an order of magnitude. Clearly, the increase in yield stress alone cannot fully account for the observed behavior in Zircaloy-2.

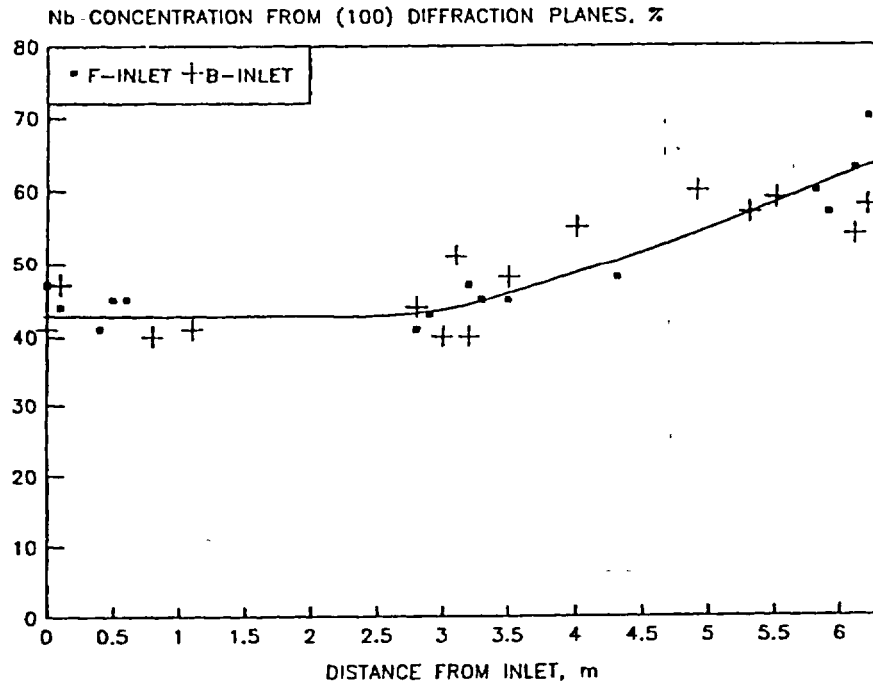


FIG. 16—Percentage of niobium in the β -phase of Zr-2.5Nb pressure tubes as a function of position relative to the inlet, for back (B) and front (F) ends relative to the extrusion process.

A conceptual model for K_{IH} was recently developed [19]. The theoretical expression for K_{IH} is given in terms of the elastic constants, the yield stress of the material, the hydride fracture stress (σ_f^h), and the thickness of the crack-tip hydride (t) as follows

$$(K_{IH})^2 = \frac{E \cdot t}{1 - \nu^2} \left\{ \frac{0.043E \cdot \epsilon_H}{(1 - \nu^2) \left[\frac{1}{1 - 2\nu} - \frac{\sigma_f^h}{\sigma_y} \right]} - \gamma \cdot \sigma_y \right\} \quad (11)$$

where

σ_y = the yield stress of the material, and
 γ = a constant (~ 0.025).

Other parameters in this equation are defined in Appendix I. The values of K_{IH} calculated by this model are smaller than those measured experimentally, Table 2. The model assumes that the crack-tip hydride covers the entire fracture surface. The higher values measured in experi-

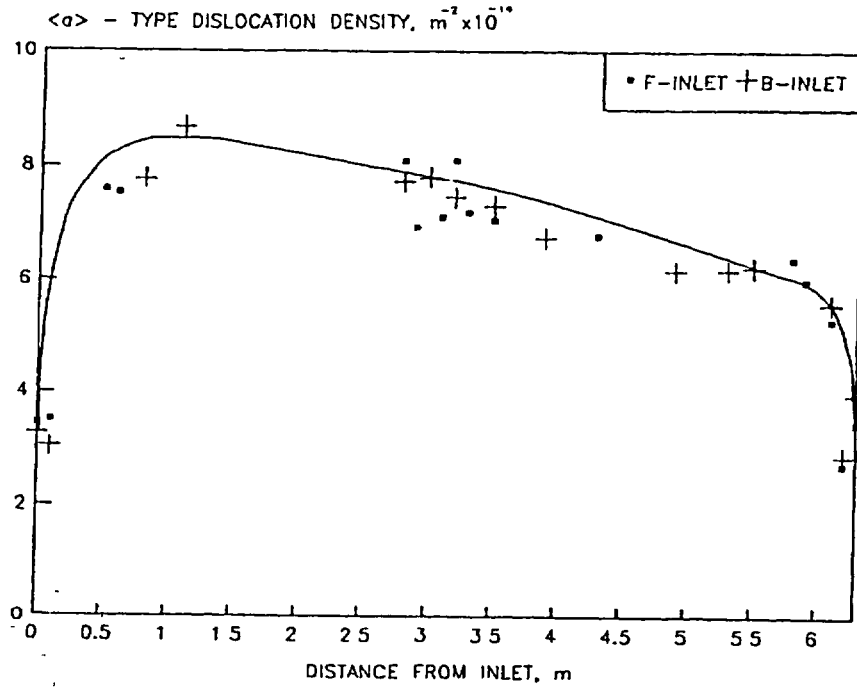


FIG. 17— $\langle a \rangle$ -type dislocation density in Zr-2.5Nb pressure tubes as a function of position relative to the inlet, for back (B) and front (F) ends relative to the extrusion process.

ments were assumed to be caused by the fact that the hydrides may not cover the whole front of the crack and the experimental K_{IH}^{exp} was related to the theoretical K_{IH} as follows

$$K_{IH}^{exp} = fK_{IH} + (1 - f)K_i \quad (12)$$

where

f = the fraction of hydride coverage at the crack tip, and

K_i = the initiation fracture toughness of the matrix (zirconium alloy) material.

Substituting $K_{IH} = 3.7 \text{ MPa}\sqrt{\text{m}}$, $K_{IH}^{exp} = 6.2 \text{ MPa}\sqrt{\text{m}}$, and $K_i = 30 \text{ MPa}\sqrt{\text{m}}$ into Eq 12, f is 0.9, that is, hydrides should cover nearly all of the area ahead of the crack tip. Our preliminary results based on metallographic examinations of hydrides at crack tips show that, at low values of K_i (near K_{IH}), the hydrides are well developed and continuous. However, further examinations need to be done to quantify the state of the crack-tip hydrides more accurately.

The model predicts a slight reduction in K_{IH} with irradiation that agrees with experimental results. This reduction is mainly due to an increased yield stress by neutron irradiation in the irradiated material. Our preliminary results on unirradiated Zr-2.5Nb indicate that a material with a lower yield stress has a higher value of K_{IH} , but most of such material also has a

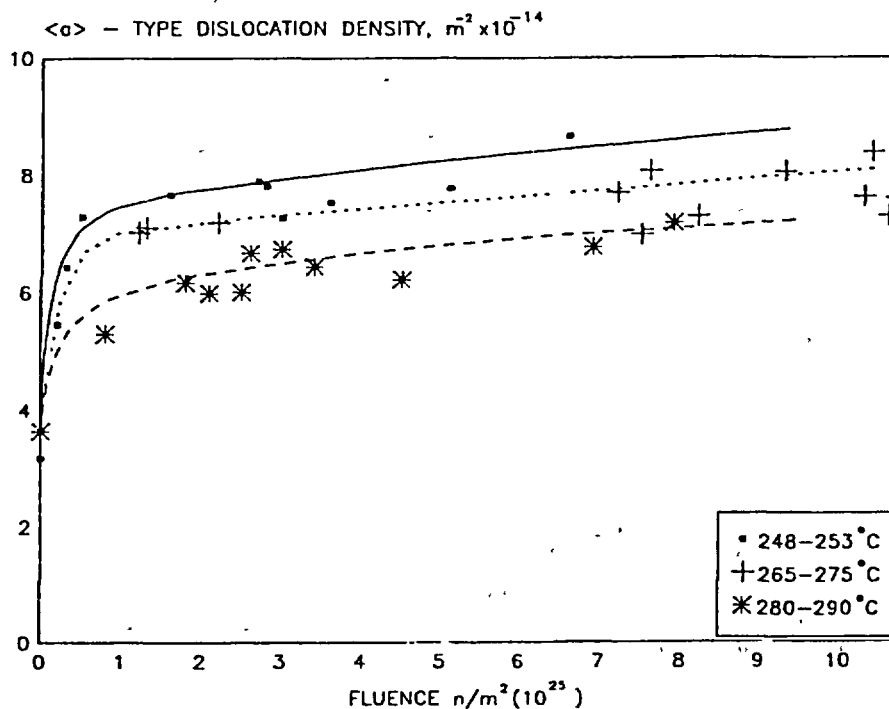


FIG. 18—Variation of dislocation density as a function of fluence for samples of Zr-2.5Nb pressure tubes taken from within 0.5 m of the center line of the reactors.

different crystallographic texture, hence, the effect of yield stress alone cannot be easily isolated. Clearly, the relationship between K_{IH} and yield stress in unirradiated Zr-2.5Nb material needs to be established.

Effect of Irradiation Temperature

It has been shown that the diffusion coefficient in the pure β -phase is about two orders of magnitude above the diffusion coefficient in α -phase [20,21]. In two-phase, cold-worked Zr-2.5Nb material, the presence of the β -phase enhances (up to an order of magnitude) the hydrogen diffusivity, compared with that in the α -phase. Experiments have shown that the crack velocity in Zr-2.5Nb alloy is greater in the material with the continuous β -phase than that in materials with decomposed β -phase [13,21]. These observations can be used in explaining the different crack velocities at the inlet and outlet ends of irradiated pressure tubes. The DHC experiments showed higher crack velocities at inlet ends of irradiated pressure tubes than at the outlet ends, while X-ray diffraction showed a smaller degree of β -phase decomposition at inlet ends than at outlet ends, Figs. 5, 6, 11, and 16. The profile of the crack velocity in an irradiated pressure tube, Figs. 8 and 9, is mainly the result of differences in the β -phase decomposition along the tube, Fig. 16, and to a lesser degree because of decreasing irradiation hardening, Fig. 17.

TABLE 2—Predicted and measured K_{IH} values in unirradiated and irradiated Zr-2.5Nb materials.

Temperature, °C	Predicted K_{IH} , MPa√m	Measured K_{IH} , MPa√m
UNIRRADIATED		
150	4.1	7.5 ± 1.3
250	5.3	7.5 ± 1.3
IRRADIATED		
150	3.7	6.2 ± 0.9
250	4.6	6.2 ± 0.9

Temperature Dependence of DHC Velocity

The temperature dependence in the DHC model derives primarily from the sum of the activation energies for diffusion and solubility contained in the $D_H C_H$ product, which is 70 kJ/mol, Appendix I. A secondary effect comes from the temperature dependence of the yield stress, which reduces the total activation energy for DHC to about 60 kJ/mol, Fig. 19. DHC experiments have shown that the crack velocity follows an Arrhenius type of relationship with temperature, for Zr-2.5Nb alloy

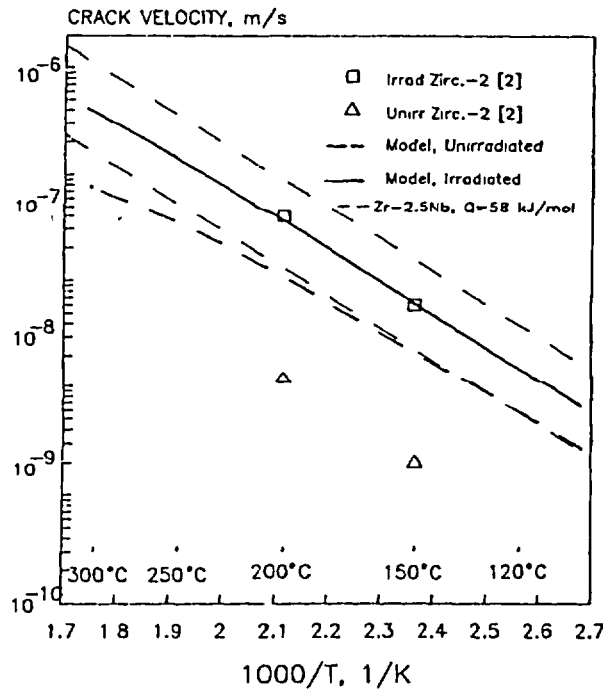


FIG. 19—Comparison between DHC velocities in Zr-2.5Nb and Zircaloy-2.

$$V = A \exp\left(-\frac{Q}{RT}\right) \quad (13)$$

with the coefficients listed in Table 3. All unirradiated materials, but one [7], have temperature dependencies in the range from 58 to 72 kJ/mol, which is reasonably close to the theoretical value. The results in Ref 7 were not obtained using the standard temperature cycling procedure. Most of the unirradiated materials have the β -phase decomposed from homogenization treatment at 400°C for several days after gaseous hydriding, hence, the cracking in both directions is governed mainly by the diffusivity and solubility in the α -phase. In the radial direction, the temperature dependence of cracking of the irradiated material is similar to that of unirradiated material, suggesting that the factors that dominate the temperature dependence, solubility and diffusivity in the α -phase, are not much affected by radiation. Lower temperature dependence of the axial crack velocity in the irradiated material can be explained in terms of the contribution of the β -phase (which is only partially decomposed in the irradiated material) to the diffusion of hydrogen in this direction (the activation energy for diffusion in the β -phase is lower than that in the α -phase [20,21]). These ideas are being explored in our current research programs.

Conclusions

1. Neutron irradiation increases the velocity of DHC in cold-worked Zr 2.5Nb by a factor of 3 to 5 times, and reduces K_{IH} by a small amount, about 20%. The effect of irradiation saturates at a fluence of about $1 \times 10^{25} \text{ n/m}^2$.
2. Temperature dependence of the crack velocity in both the radial and axial directions in the unirradiated material, and in the radial direction in the irradiated material, follows the theoretical predictions based on a diffusional model for the α -phase and the change in yield stress with temperature and irradiation. In the axial direction, the dependence on test temperature does not follow the theory based on diffusion in the α -phase; the theory needs to incorporate a two-phase ($\alpha + \beta$) diffusion model.
3. Crack velocity decreases with irradiation temperature primarily through the change in the configuration of the β -phase and, secondarily, through changes in dislocation density.

TABLE 3—Temperature dependence of DHCV velocity for unirradiated and irradiated Zr-2.5Nb material

Direction	A	Q, kJ/mol	Ref
UNIRRADIATED			
Radial ^a	6.9×10^{-1}	72	[4]
Radial ^a	2.1×10^{-2}	59	this paper
Radial ^b	4.0×10^{-2}	58	this paper
Radial ^a	1.4×10^{-4}	42	[7]
Axial ^a	1.5×10^{-1}	66	[8]
Axial ^a	5.3×10^{-2}	60	this paper
IRRADIATED			
Radial ^a	8.6×10^{-2}	58	this paper
Axial ^a	4.0×10^{-3}	43	this paper

^aHydrogen was added gaseously at 400°C followed by homogenization at 400°C for 72 h.

^bThe material was in the autoclaved condition, that is, it was heated at 400°C for 24 h

^cSome irradiated specimens had hydrogen added electrolytically at 90°C followed by solution treatment at 290°C for 14 days.

Acknowledgments

We would like to thank the following people for assistance with experiments: G. Brady, P. Dhanjal, R. W. Gilbert, J. Kelm, W. G. Newell, D. Sage, J. M. Smeltzer, K. D. Weinsenber, J. E. Winegar, and the staff of the General Chemistry Branch and the Universal Cells at CRL. We enjoyed useful discussions with Drs. M. P. Puls and S. Q. Shi. We thank OHRD for permission to use the TG3R1 material information. The work was funded through Working Party 31 and 33 of the CANDU Owners Group.

APPENDIX I**Parameters used in DHC Model**

- D_0 2.17×10^{-7} is a pre-exponential term in the expression for the diffusion coefficient of hydrogen in zirconium: $D_H = 2.17 \times 10^{-7} \exp(-35\,100/RT)$ m²/s
- C_0 10.2 is a pre-exponential term in the expression for the concentration of hydrogen in solid solution when there is no external stresses: $C_H^s = 10.2 \exp(-35\,000/RT)$ atomic %
- Ω_{Zr} 2.3×10^{-29} m³/atom is the atomic volume of zirconium
- α The thickness to length ratio of the hydride
- a_c^\dagger The distance from the crack tip to the position of the maximum stress = $(0.144 K_I/\sigma_y)^2$
- N_H 6.13×10^{28} atom/m³ is the atomic density of the hydride
- w_H^\dagger $0.577(K_I/\sqrt{r})$ J/mol is the molal interaction energy of the stresses with the hydrogen in solid solution
- Q_D 35 100 J/mol is the activation energy for diffusion of hydrogen in zirconium from the expression for D_H
- $(w_i^{mc})_{L,1}$ 4912 J/mol is the molal elastic strain energy of the matrix and fully constrained δ -hydrides with plate normals parallel to direction [0001]
- $(w_f^\dagger)_L$ $-0.9447(K_I/\sqrt{L})$ J/mol is the interaction energy of matrix δ -hydrides with the applied stress
- $(w_f^\dagger)_T$ $-6\,6563 \sigma_y$ J/mol is the interaction energy of crack-tip δ -hydrides with the applied stress
- x 1.66 is the mole fraction of hydrogen in ZrH_{1.66} hydride
- Q_H 35 kJ/mol is the activation energy of the equilibrium hydrogen concentration given in the expression for C_H^s
- K_I The Mode I stress intensity factor in MPa \sqrt{m}
- ν The Poisson's ratio in zirconium = 0.3
- V_H 16.7×10^{-7} m³/mol is the partial molar volume of hydrogen in zirconium
- V_{hyd} 16.3×10^{-6} m³/mol is the molal volume of hydride with a composition ZrH_{1.66}
- Q^* 25 100 J/mol is the heat of transport of hydrogen in zirconium
- ϵ_y The stress-free strain of the hydride in the y direction = 0.054
- E Young's modulus in the transverse direction = $102.47 - 0.011\,743 T - 8.068\,69 \times 10^{-5} T^2$, where E is in GPa and T is in °C
- σ_f^\dagger The hydride fracture stress = $0\,007\,357 E$

The expressions marked by a dagger (†) are derived in Appendix II.

APPENDIX II

Derivation of formulas marked by a dagger (†) in Appendix I

Position of the Maximum Stress, a_c

The maximum stress, a_c , is assumed to be equal to the position of the maximum stress in the plastic zone that is derived by equating the hydrostatic stress at the crack tip, p_h , to that in the matrix and then solving for r (r is defined in Fig. 20)

$$p_h(r) = -(\sigma_{11} + \sigma_{22} + \sigma_{33})/3 = -2/3 (K_I/\sqrt{2\pi r})(1 + \nu) = -0.346 K_I/\sqrt{r}$$

According to Rice and Johnson [22], the maximum hydrostatic stress is

$$p_h(1) = -2.4 \sigma,$$

hence,

$$2.4 \sigma = 0.346 K_I/\sqrt{r}$$

solving for r

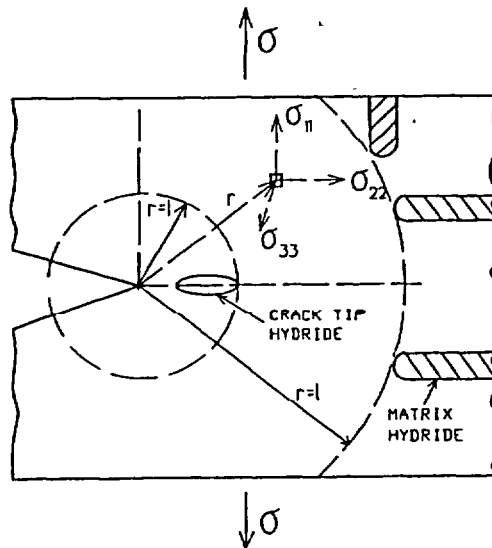


FIG. 20 Crack geometry

$$r(1) = (0.144 K_I/\sigma_r)^2$$

where σ_r is in Mpa and K_I in $\text{MPa}\sqrt{\text{m}}$

Molal Interaction Energy of the Stresses

The molal interaction energy of the stresses with the hydrogen in solid solution is expressed by

$$w_H^s = p_h V_H$$

where $V_H = 16.7 \times 10^{-7} \text{ m}^3/\text{mol}$ and $p_h = (\sigma_{11} + \sigma_{22} + \sigma_{33})/3$ for plane strain conditions

$$\sigma_{11} = \sigma_{22} = K_I/(\sqrt{2\pi L})$$

$$\sigma_{33} = \nu(\sigma_{11} + \sigma_{22}) = 2\nu K_I/\sqrt{2\pi L}$$

At L (matrix)

$$w_H^s = 2/3(K_I/\sqrt{2\pi L})(1 + \nu)V_H = 0.577 K_I/L$$

where K_I is in $\text{MPa}\sqrt{\text{m}}$.

Interaction Energy of Matrix δ -Hydrides with the Applied Stress

At L (matrix)

$$(w_i^s)_L = -V_{\text{hydr}} \Sigma \sigma_y e_y = -V_{\text{hydr}} K_I/\sqrt{2\pi L}(e_{11} + e_{22} + e_{33})$$

for δ -hydrides $e_{11} = 0.72$, $e_{22} = 0.0458$, $e_{33} = 0.0458$

$$(w_i^s)_L = -0.9447 K_I/L$$

where K_I is in $\text{MPa}\sqrt{\text{m}}$ and $V_{\text{hydr}} = 16.3 \times 10^{-6} \text{ m}^3/\text{mol}$.

At l (crack tip)

$$(w_i^s)_l = -V_{\text{hydr}}(3\sigma_y e_{11} + 1.8\sigma_y e_{22} + 2.4\sigma_y e_{33})$$

$$(w_i^s)_l = -6.6563\sigma_y$$

for δ -hydride.

References

- [1] Moan, G. D., Coleman, C. E., Price, E. G., Rodgers, D. K., and Sagat, S., "Leak-Before-Break in the Pressure Tubes of CANDU Reactors," *International Journal of Pressure Vessels & Piping*, Vol 43, 1990, pp. 1-21.
- [2] Huang, F. H. and Mills, W. J., "Delayed Hydride Cracking Behavior for Zircaloy-2 Tubing," *Metallurgical Transactions*, Vol 22A, 1991, pp. 2049-2060.
- [3] Fleck, R. G., Price, E. G., and Cheadle, B. A., "Pressure Tube Development for CANDU Reactors," *Zirconium in the Nuclear Industry: Sixth International Symposium, ASTM STP 824*, D. G. Franklin

- and R. B. Adamson, Eds, American Society for Testing and Materials, Philadelphia, 1984, pp. 88-105.
- [4] Ambler, J. F. R., "Effect of Direction of Approach to Temperature on the Delayed Hydrogen Cracking Behaviour of Cold-Worked Zr-2.5Nb," *Zirconium in the Nuclear Industry, ASTM STP 824*, D. G. Franklin and R. B. Adamson, Eds, American Society for Testing and Materials, Philadelphia, 1984, pp. 653-674.
- [5] Sagat, S., Ambler, J. F. R., and Coleman, C. E., "Application of Acoustic Emission to Hydride Cracking," 29th Acoustic Emission Working Group Meeting, The Royal Military College of Canada, Kingston, Ontario, 1986.
- [6] Simpson, L. A. and Clarke, C. F., "Application of the Potential-Drop Method to Measurement of Hydrogen-Induced Sub-Critical Crack Growth in Zirconium-2.5Nb," AECL Research Report, AECL-5815, Whiteshell Laboratories, Pinawa, Manitoba, 1977.
- [7] Coleman, C. E. and Ambler, J. F. R., "Susceptibility of Zirconium Alloys to Delayed Hydrogen Cracking," *Zirconium in the Nuclear Industry (3rd Conference), ASTM STP 633*, A. L. Lowe, Jr. and G. W. Parry, Eds., American Society for Testing and Materials, Philadelphia, 1977, pp. 589-607.
- [8] Simpson, L. A. and Puls, M. P., "The Effect of Stress, Temperature and Hydrogen Content on Hydride-Induced Crack Growth in Zr-2.5Nb," *Metallurgical Transactions*, Vol. 10A, 1979, pp. 1093-1105.
- [9] Holt, R. A., "Recovery of Cold-Work in Extruded Zr-2.5Nb," *Journal of Nuclear Materials*, Vol. 59, 1976, pp. 234-242.
- [10] Griffiths, M., Winegar, J. E., Mecke, J. F., and Holt, R. A., "Determination of Dislocation Densities in HCP Metals Using X-ray Diffraction and Transmission Electron Microscopy," *Advances in X-ray Analysis*, Vol. 35, 1992, pp. 593-599.
- [11] Chow, C. K., Coleman, C. E., Hosbons, R. R., Davies, P. H., Griffiths, M., and Choubey, R., "Fracture Toughness of Irradiated Zr-2.5Nb Pressure Tubes from CANDU Reactors," *Zirconium in the Nuclear Industry: Ninth International Symposium, ASTM STP 1132*, C. M. Eucken and A. M. Garde, Eds, American Society for Testing and Materials, Philadelphia, 1991, pp. 246-275.
- [12] Shek, G. K. and Graham, D. B., "Effects of Loading and Thermal Manoeuvres on Delayed Hydride Cracking in Zr-2.5Nb Alloys," *Zirconium in the Nuclear Industry: Eighth International Symposium, ASTM STP 1023*, L. F. P. Van Swam and C. M. Eucken, Eds, American Society for Testing and Materials, Philadelphia, 1989.
- [13] Simpson, L. A. and Cann, C. D., "The Effect of Microstructure on Rates of Delayed Hydride Cracking in Zr-2.5Nb Alloy," *Journal of Nuclear Materials*, Vol. 126, 1984, pp. 70-73.
- [14] Dutton, R. and Puls, M. P., "A Theoretical Model for Hydrogen Induced Sub-Critical Crack Growth," *Proceedings, Conference on Effect of Hydrogen on Behavior of Materials*, American Institute of Mining, Metallurgical, and Petroleum Engineers, 7-11 Sept. 1975, pp. 516-525.
- [15] Puls, M. P., "Effect of Crack Tip Stress States and Hydride-Matrix Interaction Stresses on Delayed Hydride Cracking," *Metallurgical Transactions*, Vol. 21A, 1990, pp. 2905-2917.
- [16] Ambler, J. F. R., "The Effect of Thermal Gradients on the Delayed Hydride Cracking Behaviour of Zirconium Alloys—Mathematical Model," AECL Research, unpublished work, Chalk River Laboratories, Chalk River, Ontario, 1985.
- [17] Puls, M. P., Simpson, L. A., and Dutton, R., "Hydride-Induced Crack Growth in Zirconium Alloys," AECL Research Report, AECL-7392, Whiteshell Laboratories, Pinawa, Manitoba, 1982.
- [18] Coleman, C. E., Cheadle, B. A., Causey, A. R., Chow, C. K., Davies, P. H., McManus, M. D., Rodger, D. K., Sagat, S., and van Drunen, G., "Evaluation of Zircaloy-2 Pressure Tubes from NPD," *Zirconium in the Nuclear Industry: Eighth International Symposium, ASTM STP 1023*, L. F. P. Van Swam and C. M. Eucken, Eds, American Society for Testing and Materials, Philadelphia, 1989, pp. 35-49.
- [19] Shi, S. Q. and Puls, M. P., "Criteria of Fracture Initiation at Hydrides in Zirconium," to be published.
- [20] Sawatzky, G. A., Ledoux, R. L., Tough, R. L., and Cann, C. D., "Hydrogen Diffusion in Zirconium-Niobium Alloys," *Metal-Hydrogen Systems, Proceedings*, Miami International Symposium, 1981, Pergamon Press, Oxford, 1982, pp. 109-120.
- [21] Skinner, B. C. and Dutton, R., "Hydrogen Diffusivity in α - β Zirconium Alloys and its Role in Delayed Hydride Cracking," *Hydrogen Effects on Material Behaviour*, N. R. Moody and A. W. Thomson, Eds, The Minerals, Metals & Materials Society, Jackson Lake Lodge, 1989.
- [22] Rice, J. R. and Johnson, M. A. in *Inelastic Behavior of Solids*, M. F. Kanninen, Ed., McGraw-Hill, New York, 1970, p. 641.

DISCUSSION

Brian Cox¹ (written discussion)—One of the questions that D. Franklin hoped to answer in his introduction was whether DHC cracks could be initiated from smooth surfaces, given a high enough stress maintained for a long enough time. Can you comment on whether or not DHC cracks can be initiated at smooth surfaces, and the times and stresses needed to do this.

S. Sagat et al. (authors' closure)—Early experiments by Cheadle and Ells² showed that DHC cracks can be initiated at smooth surfaces. In these experiments, smooth (smooth refers to the original surface quality of the as-received pressure tube) cantilever beam specimens were machined from cold-worked Zr-2.5Nb pressure tubes. Some of the specimens were gaseously hydrided at 400°C to a hydrogen concentration of 40 to 120 ppm, the remainder of specimens were tested with the as-received hydrogen concentration that was between 10 and 15 ppm. The specimens were tested in pure bending. After loading, the specimens were heated to 300°C and then cooled to the test temperature to reorient some of the hydrides under the applied stress. The as-received specimens were tested at 80°C and the hydrided specimens at either 150 or 250°C.

In specimens that contained 10 to 15 ppm hydrogen, cracks initiated at outerfiber stresses >550 MPa, either at surface nicks or angular SiO₂ particles that were embedded to the surface of the tubes by sand blasting operations used to clean the tubes during their fabrication. The range of failure times in these tests was between 53 and 6600 h.

In specimens with hydrogen concentration between 40 and 120 ppm, the crack initiation was not associated with any surface flaws or embedded particles. In these specimens, the cracks initiated at reoriented radial hydrides, near the surface of the specimen, at outerfiber stresses ≥ 413 MPa at a temperature of 150°C, and at stresses ≥ 585 MPa at 250°C. The range of failure times in these tests was between 2 and 1920 h.

In conclusion, crack initiation by DHC at smooth (as-fabricated) surfaces in cold-worked Zr-2.5Nb pressure tubes requires a large tensile stress at a surface asperity or hydrides close to the surface and perpendicular to the stress direction.

C. Lemaignan³ (written discussion)—Is there any tendency for the hydrides to precipitate in α , β phase or at the interface between the two?

S. Sagat et al. (authors' closure)—The microstructure of cold-worked Zr-2.5Nb pressure tubes consists of lath-shaped α -grains (hexagonal close packed) highly elongated in the axial direction. The α -grains (with a thickness of about 0.5 μm) are surrounded by a continuous network of body centered cubic β -phase (about 0.05 μm thick and comprising approximately 7% volume fraction). The original hydrides in this material are oriented parallel to the circumferential-axial plane along the α/β phase boundaries. Very few β -grain boundaries are in the radial direction. The precipitation of hydrides in the hexagonal α -phase is known to occur on habit planes that are very close to the basal planes. The precipitation of hydrides in the β -phase is to my knowledge not very well known. If there is a crack present in the material, the hydride will precipitate at the crack tip that in most cases is the α -phase. No systematic study has been done to see what happens if the β -phase is at the crack tip. However, the DHC crack does not seem to have any problems growing through both, the α and β -phase, as it grows through the pressure tube wall.

¹University of Toronto, Toronto, Ontario, Canada

²Cheadle, B. A., "Crack Initiation in Cold-Worked Zr-2.5Nb by Delayed Hydrogen Cracking," *Proceedings, Second International Congress on Hydrogen in Metals*, Paris, 6-11/VI/1977; also as AECL-5799.

³CEA, Grenoble, France

Suresh K. Yagnik⁴ (written discussion)—What is the typical hydrogen concentration at the crack-tip for DHC mechanism? Is there a threshold value for this?

S. Sagat *et al.* (authors' closure)—The hydrogen concentration at the crack tip that is required for DHC initiation has to be greater than the terminal solid solubility (TSS) limit of hydrogen in zirconium for a given temperature. The Zr-2.5Nb material exhibits hysteresis between the heatup and cooldown TSS. TSS is also affected by the applied stress. To derive the required hydrogen concentration for DHC to occur, one has to choose the appropriate TSS. A theoretical treatment of hydrogen solubility in zirconium alloys can be found in two publications written by Puls.^{5,6}

⁴Electric Power Research Institute, Palo Alto, CA

⁵Puls, M. P., "The Effect of Misfit and External Stress on Terminal Solid Solubility in Hydride-Forming Metals," *Acta Metallurgica*, Vol. 29, 1981, pp. 1961-1968.

⁶Puls, M. P., "On the Consequences of Hydrogen Supersaturation Effects in Zr Alloys to Hydrogen Ingress and Delayed Hydride Cracking," *Journal of Nuclear Materials*, Vol. 165, 1989, pp. 128-141.

Stefan Sagat,¹ Christopher E. Coleman,² Malcolm Griffiths,³ and
Brian J. S. Wilkins⁴

The Effect of Fluence and Irradiation Temperature on Delayed Hydride Cracking in Zr-2.5Nb

REFERENCE: Sagat, S., Coleman, C. E., Griffiths, M., and Wilkins, B. J. S., "The Effect of Fluence and Irradiation Temperature on Delayed Hydride Cracking in Zr-2.5Nb," *Zirconium in the Nuclear Industry: Tenth International Symposium, ASTM STP 1245*, A. M. Garde and E. R. Bradley, Eds., American Society for Testing and Materials, Philadelphia, 1994, pp. 35-61.

ABSTRACT: Zirconium alloys are susceptible to a stable cracking process called delayed hydride cracking (DHC). DHC has two stages: (a) crack initiation that requires a minimum crack driving force (the threshold stress intensity factor, K_{IH}) and (b) stable crack growth that is weakly dependent on K_I . The value of K_{IH} is an important element in determining the tolerance of components to sharp flaws. The rate of cracking is used in estimating the action time for detecting propagating cracks before they become unstable. Hence, it is important for reactor operators to know how these properties change during service in reactors where the components are exposed to neutron irradiation at elevated temperatures. DHC properties were measured on a number of components, made from the two-phase alloy Zr-2.5Nb, irradiated at temperatures in the range of 250 to 290°C in fast neutron fluxes ($E \geq 1$ MeV) between 1.6×10^{17} and 1.8×10^{18} n/m² · s to fluences between 0.01×10^{23} and 9.8×10^{23} n/m². The neutron irradiation reduced K_{IH} by about 20% and increased the velocity of cracking by a factor of about five. The increase in crack velocity was greatest with the lowest irradiation temperature. These changes in the crack velocity by neutron irradiation are explained in terms of the combined effects of irradiation hardening associated with increased <a>-type dislocation density, and β -phase decomposition. While the former process increases crack velocity, the latter process decreases it. The combined contribution is controlled by the irradiation temperature. X-ray diffraction analyses showed that the degree of β -phase decomposition was highest with an irradiation temperature of 290°C while <a>-type dislocation densities were highest with an irradiation temperature of 250°C.

KEY WORDS: delayed hydride cracking, crack velocity, threshold stress intensity factor, irradiation fluence, irradiation temperature, zirconium, zirconium alloys, nuclear materials, nuclear applications, radiation effects

¹Research Metallurgist, AECL Research, Materials and Mechanics Branch, Chalk River Laboratories, Chalk River, Ontario K0J 1J0, Canada.

²Branch manager, AECL Research, Fuel Channel Components Branch, Chalk River Laboratories, Chalk River, Ontario K0J 1J0, Canada.

³Research metallurgist, AECL Research, Reactor Materials Research Branch, Chalk River Laboratories, Chalk River, Ontario K0J 1J0, Canada.

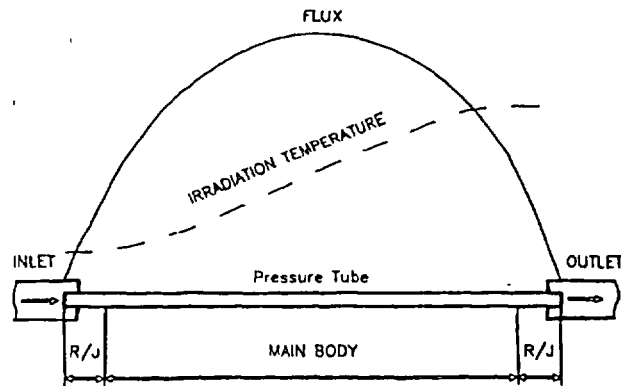
⁴Senior research metallurgist, AECL Research, Materials and Mechanics Branch, Whiteshell Laboratories, Pinawa, Manitoba R0E 1L0, Canada.

Delayed hydride cracking (DHC) is a stable crack growth mechanism in zirconium alloys. Hydrogen accumulates at a stress raiser. If sufficient hydrogen is present, hydrides form and, if the stress is high enough, the hydrides fracture and the crack advances. The process is then repeated until the crack becomes unstable. The two main characteristic parameters of DHC are the crack velocity, V , and the threshold loading below which cracks do not grow; with sharp cracks at moderate loads, linear elastic fracture mechanics is used, and the threshold stress intensity factor is called K_{IH} . Neutron irradiation at some temperatures increases V and reduces K_{IH} [1,2]. At least two methods exist to evaluate the effect of irradiation on DHC: (1) prepare appropriate specimens, then irradiate them in a reactor, or (2) machine specimens from components removed from reactors for surveillance. In this paper, we describe the results of experiments using both methods. Many cold-worked Zr-2.5Nb pressure tubes were removed from CANDU power reactors as part of a planned large-scale retubing program and thus a comprehensive evaluation program was possible. The objectives were to measure the effects of irradiation fluence and irradiation temperature on V and K_{IH} and to relate the results to the microstructural changes produced by irradiation.

Experimental Procedure

Material

Pressure tubes in CANDU reactors are made from Zr-2.5Nb alloy by hot extrusion of hollow billets followed by 25% cold work. The extrusion process results in a crystallographic texture with the following resolved basal pole fractions: 0.32 (radial), 0.61 (transverse), and 0.07 (axial). The pressure tubes are about 6 m long and have an inside diameter of 103 mm and a wall thickness 4.1 mm. They are joined to stainless steel end fittings by internal rolling. The material used in these experiments came from 45 pressure tubes that were removed from power reactors and from offcuts. The offcuts are small pieces of archived material cut off from each end of a pressure tube prior to operation. The tubes were removed from different lattice positions and sampled at different axial positions along the tube to provide a range of irradiation fluences and temperatures. A schematic diagram of a pressure tube and related terminology used throughout this paper are shown in Fig. 1. The rolled joint (R/J) regions are



SCHEMATIC

FIG. 1—A schematic diagram of a fuel channel in CANDU reactor.

defined as the pieces that are within about 200 mm from each end of the tube, and the remainder of the tube is referred as the main body.

Zr-2.5Nb material was also irradiated in a high flux reactor (OSIRIS) at Centre d'Etudes Nucleaires de Saclay. The purpose of this irradiation was to achieve end-of-life fluences substantially ahead of the life of the tubes in the reactors. Two materials were used for this irradiation: standard, cold-worked Zr-2.5Nb (tube H737) and Zr-2.5Nb material produced by a modified route, TG3R1 (Task Group 3 Route 1 material developed at Ontario Hydro). The TG3R1 pressure tubes were produced using a lower extrusion ratio and higher percent cold-work than standard pressure tubes, and had an extra stress relieve at 500°C for 6 h after cold drawing. Details about production routes for the fabrication of cold-worked Zr-2.5Nb tubes are given in Ref 3. About 1 atomic percent of hydrogen was added gaseously to these materials prior to irradiation. To achieve a uniform distribution of hydrogen, the materials were homogenized at 400°C for 72 h. The irradiation of H737 material was called ERABLE and the irradiation of TG3R1 material was called TRILLIUM. Both irradiations have been carried out at a temperature of 250°C.

Specimens

Two types of specimens were prepared from the tubes: (1) cantilever beam (CB) and (2) curved compact toughness (CCT) specimens, Fig. 2. The CB specimens were used for measuring

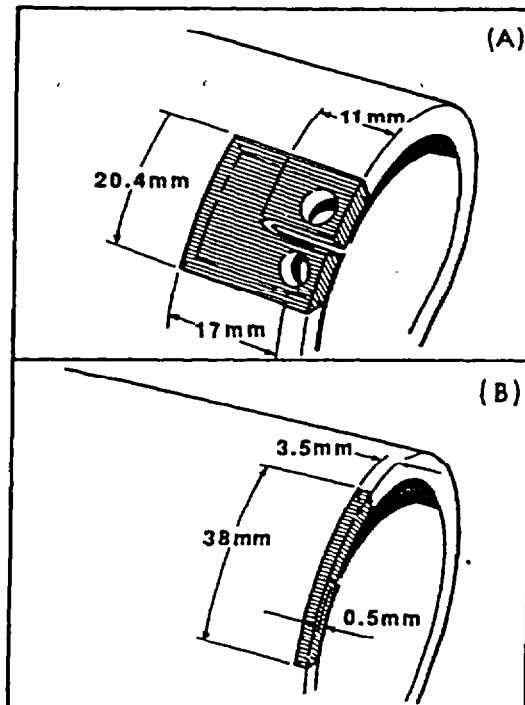


FIG. 2—Curved compact toughness (A) and cantilever beam (B) specimens used in DHC tests.

V and K_{IH} in the radial direction, and the CCT specimens for measuring V in the axial direction. Cracks were started in CB specimens from 0.5-mm-deep notches machined on the inside surface. The CCT specimens were fatigue pre-cracked. Because the initial hydrogen concentration in the specimens was low, hydrogen was added to some specimens electrolytically to allow testing up to 290°C. In this technique a layer of solid zirconium hydride is deposited on the surface of the specimen. The specimen is then homogenized at a solvus temperature corresponding to the required hydrogen concentration. This treatment results in uniform distribution of fine hydrides through the bulk of the specimen.

Experimental Techniques

Crack velocity of DHC is sensitive to the temperature history; the maximum value of V is attained by cooling (without undercooling) to the test temperature from above the solvus temperature of hydrogen in zirconium [4]. Thus, a standard procedure for measuring V was developed as shown in Fig. 3. To minimize annealing of irradiation damage, the maximum peak test temperature in irradiated material should not be greater than the irradiation temperature plus 10°C. The load can be applied either at the end of the high temperature soak, or after attaining the test temperature. The latter avoids premature cracking during cooling and allows an accurate evaluation of the time to crack initiation. The loads applied should be within ASTM criteria for linear elastic fracture mechanics, that is, ASTM Test Method for Plane-Strain Fracture Toughness of Metallic Materials (E 399-90). CB specimens were loaded in

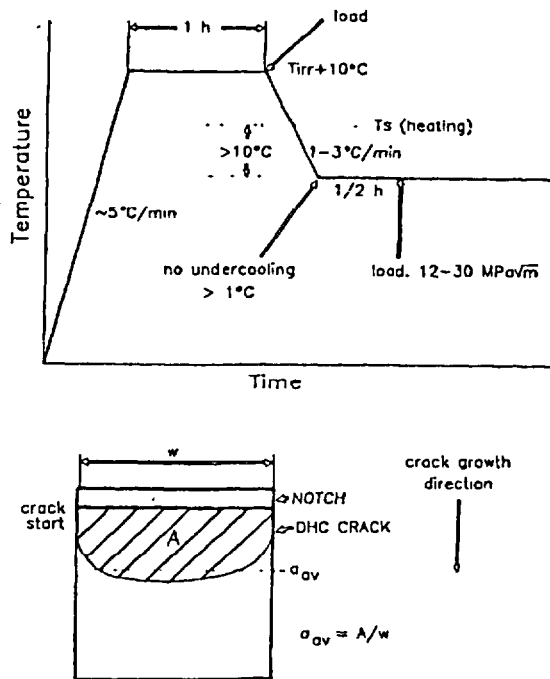


FIG. 3—Standard temperature and loading history for DHC testing.

bending and cracking was detected by acoustic emission [5]. CCT specimens were dead weight loaded in tension in a creep frame and cracking was monitored by a d-c potential drop method [6]. The cracks were grown from about 0.5 to 2.0 mm. Crack velocity was derived from the average crack depth divided by the time over which steady cracking occurred. Crack depth was defined as the area of DHC, delineated by heat-tinting, divided by the specimen thickness

In the literature, two methods of determining K_{IH} have been described as follows:

1. A number of specimens are loaded to different K_I and incubation times for cracking are measured; K_{IH} is estimated by a projection to infinite time [7]. Measuring K_{IH} using this technique takes several years, but provides realistic values.
2. One specimen only is used and K_{IH} is measured over a relatively short period of time by either increasing the load until cracking starts or decreasing the load until cracking ceases [5,8].

The method we have standardized on for quick comparisons is based on decreasing the load. After the standard temperature cycle, the specimen is loaded to $17 \text{ MPa}\sqrt{\text{m}}$. Once cracking is initiated, the K_I is reduced 2% per $5 \mu\text{m}$ of crack growth, derived from the calibration of the acoustic emission through an automatic feedback system [5]. The load is reduced until acoustic emission stopped and no further indications are obtained for at least 24 h. K_{IH} is derived from this final load and the average crack depth.

Experimental Errors

The main sources of errors in the measurement of DHC velocity are:

1. uncertainty in the determination of the time for steady cracking, and
2. uncertainty in the determination of the crack depth.

It takes a certain amount of time, called incubation time, before cracking starts. Before steady crack growth is attained, the cracking may go through a transient period, during which the cracking may be erratic or intermittent. Neither the incubation time nor the transient time should be included in the crack velocity calculation. The uncertainty in determining the time of steady cracking depends on the sensitivity of the acoustic emission or potential drop techniques and on estimating the onset of steady cracking, which is not always clear-cut.

Crack propagation is not always uniform across the specimen section; hence, the average crack depth, derived by dividing the cracked area by the specimen thickness, is sensitive to the crack shape. Crack velocity in nonuniform cracks and cracks that tunnel excessively, may be different from those in uniform cracks, even if crack areas are the same.

The errors arising from temperature and load measurements are small in comparison with the errors in determining crack depth and time of cracking.

Based on data, we estimate that the error in measurement of DHC velocity is $\pm 25\%$ and $\pm 50\%$ from the mean, in unirradiated and irradiated material, respectively.

The error in the measurement of K_{IH} , using the standard load reducing method, depends on the following:

1. uniformity of DHC crack,
2. accuracy of acoustic emission equipment,
3. accuracy of load measurement, and
4. the required "wait time" of no cracking.

As far as the crack shape is concerned, similar arguments apply to K_{IH} tests as those discussed for crack velocity tests. In a K_{IH} test, it is absolutely mandatory that the acoustic emission equipment is not noisy, because each time false counts are recorded, the load is reduced and this leads to underestimating K_{IH} .

An accurate load measurement is important because the loads are very small when K_{IH} is approached.

We estimate the error in measuring K_{IH} , using the load reducing method, to be ± 1 MPa \sqrt{m} ($\pm 15\%$).

Microstructural Examinations

The microstructure of cold-worked Zr-2.5Nb consists of flat, α -zirconium grains surrounded by thin layers of continuous β -zirconium, Fig. 4. To study the evolution of the microstructure, notably the decomposition of the β -phase during the irradiation, and the evolution of the dislocation substructure, X-ray diffraction (XRD) was used; transmission electron microscopy was not able to resolve the changes occurring in the β -phase or evaluate the dislocation substructure quantitatively. Specimens for analysis by XRD were prepared by cutting thin slices from the tube perpendicular to each of the three principal tube axes, that is, longitudinal normal (LN), transverse normal (TN), radial normal (RN). The LN(10 $\bar{1}$ 0) α , TN(0002) α , LN(110) β , and RN(200) β diffraction lines were measured using a Rigaku rotating anode diffractometer, with CuK α radiation. The RN(11 $\bar{2}$ 0) α diffraction lines were measured using a Siemens diffractometer also operating with CuK α radiation. The line shapes of the X-ray profiles for the α -phase were analyzed using the Fourier method and these were interpreted in terms of dislocation density for $\langle a \rangle$ -type and $\langle c \rangle$ -component dislocations [9,10].

Results

The factors that affect DHC were expected to be irradiation fluence, irradiation temperature, test temperature, and direction of testing on the plane normal to the transverse direction.

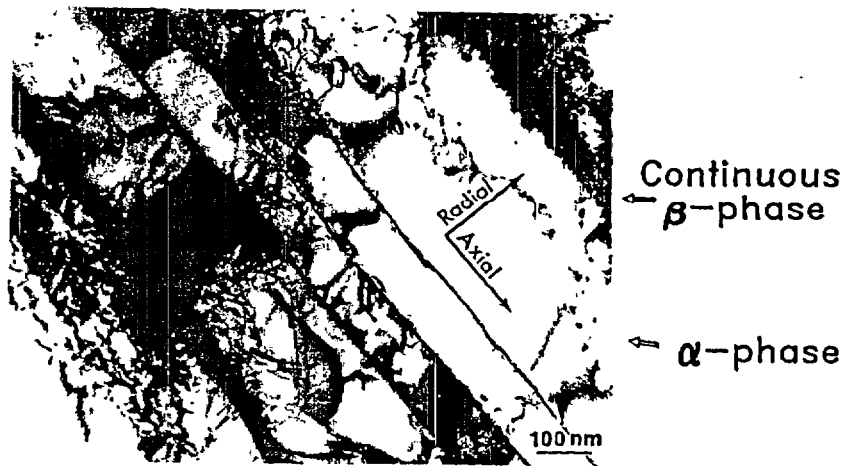


FIG. 4—Microstructure of cold-worked Zr-2.5Nb pressure tube.

Effect of Irradiation Fluence

The effect of irradiation fluence was studied on specimens prepared from the R/J and main body regions of pressure tubes removed from power reactors, and on specimens from the end-of-life irradiations in France. DHC velocities in both the radial and axial directions were determined as a function of fluence. Tensile properties in the transverse direction were determined as a function of fluence.

In the R/J region, the crack velocity increased rapidly with fluence, Figs. 5 and 6. The results from the end-of-life irradiations (TRILLIUM and ERABLE) showed a weak dependence of the crack velocity on fluence, Fig. 6. In specimens from the main bodies of pressure tubes, the crack velocity was three to five times higher than that of unirradiated material and was found to be independent of fluence, Figs. 5 and 6. These observations suggest that the effect of irradiation saturates at about 1×10^{25} n/m². The yield stress follows a similar behavior, Fig. 7 [11], it saturates at about 0.3×10^{31} n/m².

Effect of Irradiation Temperature

In CANDU reactors, the temperature along the channel increases from about 250°C at the inlet end to about 290 to 300°C at the outlet end. As shown in Figs. 5 and 6, the crack velocities are higher at the inlet end than at the outlet end. Figures 8 and 9 show the crack velocity as a function of position along the fuel channel. The velocity drops off sharply towards the R/Js and decreases gently from the inlet end towards the outlet end. These results are obtained on 45 pressure tubes and the scatter includes tube-to-tube variability.

Direction of Testing

Shapes of cracks in early Pickering and Bruce reactors indicated that the rate of crack growth in the axial direction of the tube is about twice that in the radial direction. This

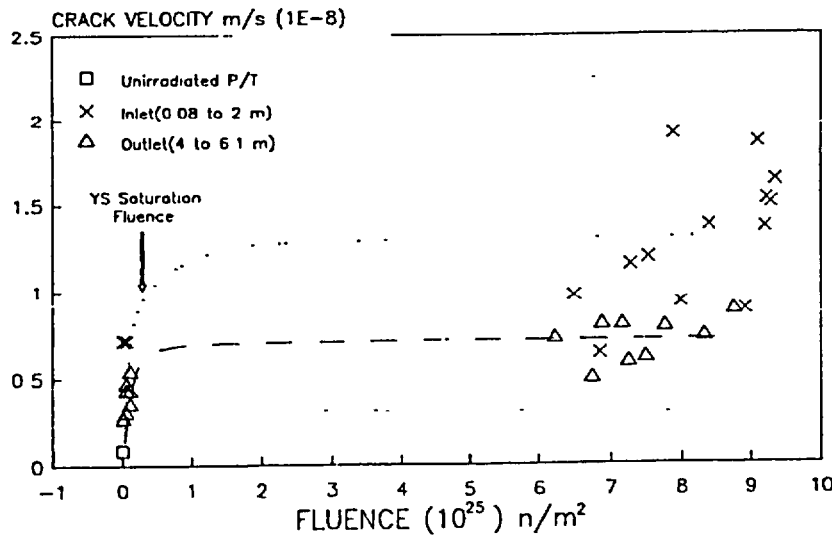


FIG. 5—Dependence of axial DHC velocity on irradiation fluence (test temperature 130°C)

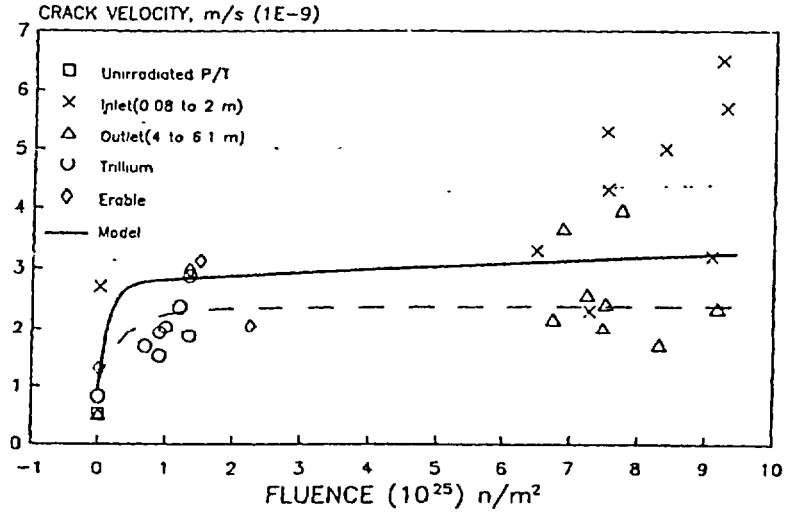


FIG. 6—Dependence of radial DHC velocity on irradiation fluence (test temperature: 130°C).

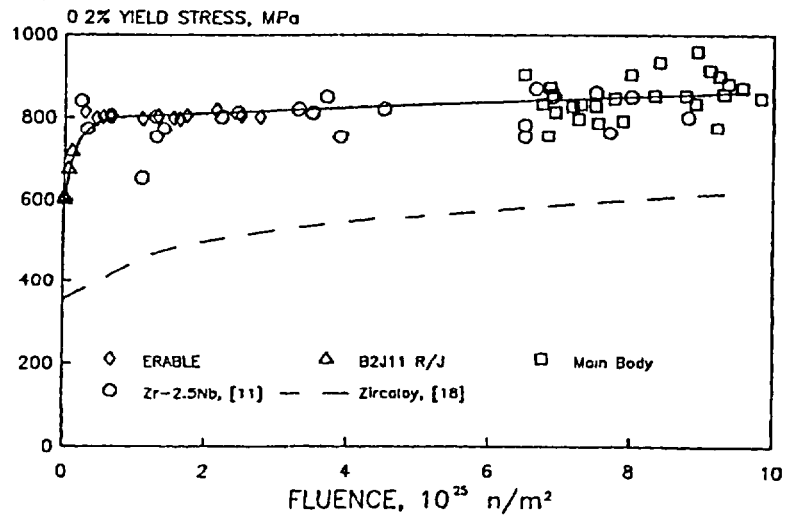


FIG. 7—Dependence of yield stress on irradiation fluence (test temperature: 250°C).

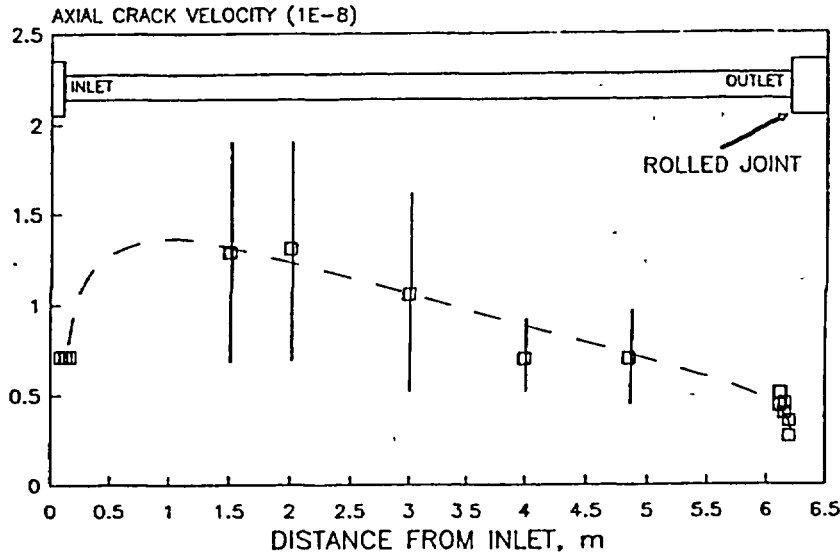


FIG. 8—Variation of axial DHC velocity along pressure tube (test temperature: 130°C).

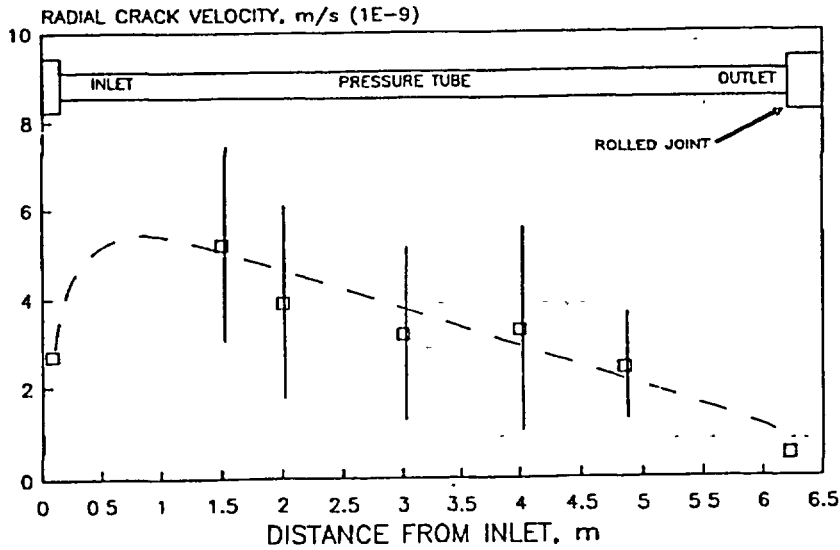


FIG. 9—Variation of radial DHC velocity along pressure tube (test temperature: 130°C)

observation was confirmed in a round-robin test performed at Chalk River Laboratories (CRL), Whiteshell Laboratories (WL), and Ontario Hydro Research Division (OHRD). Standard, unirradiated Zr-2.5Nb pressure tube material with two hydrogen concentrations, 0.36 and 0.50 atomic percent, was used in this round robin. WL and OHR used CCT specimens and measured crack velocity in the axial direction of the pressure tube, and CRL used CB specimens and measured crack velocity in both the radial and axial directions. The objective of this round robin was to determine the variability in crack velocity between CCT and CB specimens and to determine the effect of crack growth direction on DHC velocity. In general, there was good agreement between all three laboratories in the axial crack velocity measurements, which confirmed that the specimen type was not a factor in crack velocity determination. The experimental uncertainty in the results from all three laboratories was less than 25% of the mean at a given hydrogen concentration and crack growth direction. The crack velocity in the axial direction was found to be 1.7 to 1.9 times higher than that in the radial direction, Table 1.

Crack velocities were also measured, in both the radial and axial directions, on the 45 pressure tubes removed from different lattice positions in four power reactors. The majority of the tubes from the power reactors had low hydrogen isotope concentrations (0.05 to 0.1 atomic percent) and had to be tested at temperatures between 120 and 140°C. Some tubes had high hydrogen isotope concentrations at the outlet end, and some specimens were hydrided electrolytically to allow testing up to 300°C.

To measure the radial velocity, cantilever beam specimens were prepared from different axial positions of these tubes. The temperature dependence of the crack velocity followed an Arrhenius relationship as shown in Fig. 10. A least-squares regression produced the following expression for V in m/s

$$V_r = 0.0863 \exp(-58/RT) \quad (1)$$

where

$$R = 8.314 \times 10^{-3} \text{ kJ/mol,}$$

T = the absolute temperature, and 95% confidence limits are a factor of ± 2.6 from the mean.

Crack velocities, measured on the offcut material from two tubes, are grouped around the lower bound line of the irradiated material, Fig. 10. In these tests, many specimens were prepared from sections near the inlet and outlet ends of pressure tubes. Comparing crack velocities in these sections, it was observed that those coming from the inlet sections had consistently higher crack velocities than those from the outlet sections, as shown in Fig. 11. The average crack velocity at the inlet end is about twice that at the outlet end. The least-square regression analysis gave the following expression for the mean V , in m/s, for inlet and outlet, respectively

TABLE 1—Comparison of axial (V_a) and Radial (V_r) velocities determined at CRL

H concentration, atomic %	Test Temperature, °C	Axial V , m/s	Radial V , m/s	V_a/V_r
0.5	250	$11.8 \times 10^{-4} \pm 3.1$	$6.1 \times 10^{-4} \pm 1.3$	1.9
0.5	200	$2.3 \times 10^{-4} \pm 0.15$	$1.2 \times 10^{-4} \pm 0.16$	1.9
0.36	250	$5.9 \times 10^{-4} \pm 0.87$	$3.5 \times 10^{-4} \pm 0.46$	1.7
0.36	200	$2.2 \times 10^{-4} \pm 0.23$	$1.3 \times 10^{-4} \pm 0.17$	1.7

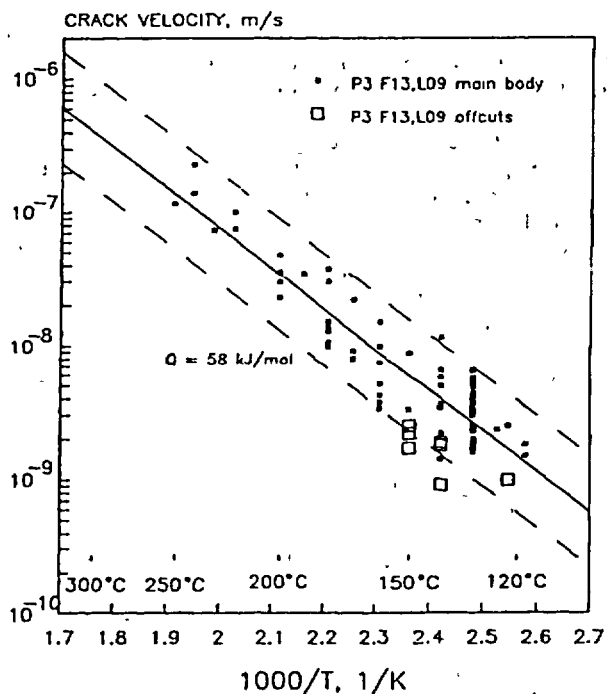


FIG. 10—Temperature dependency of radial DHC velocity

$$V_{rad} = 0.169 \exp(-59/RT) \tag{2}$$

with 95% confidence limits equal to a factor of ± 1.7 from the mean, and

$$V_{rot} = 0.068 \exp(-58/RT) \tag{3}$$

with 95% confidence limits equal to a factor of ± 2.1 from the mean.

Figure 12 shows the temperature dependence of the axial crack velocity. The least-square analysis gave the following expression for the mean V_A in m/s

$$V_A = 4.02 \times 10^{-3} \exp(-43/RT) \tag{4}$$

with 95% confidence limits equal to a factor of ± 2.3 from the mean.

These results show that the temperature dependency of V in the axial direction is smaller than that in the radial direction, Fig. 13. At low temperature, $V_A > V_R$, but at 300°C, both velocities have about the same value.

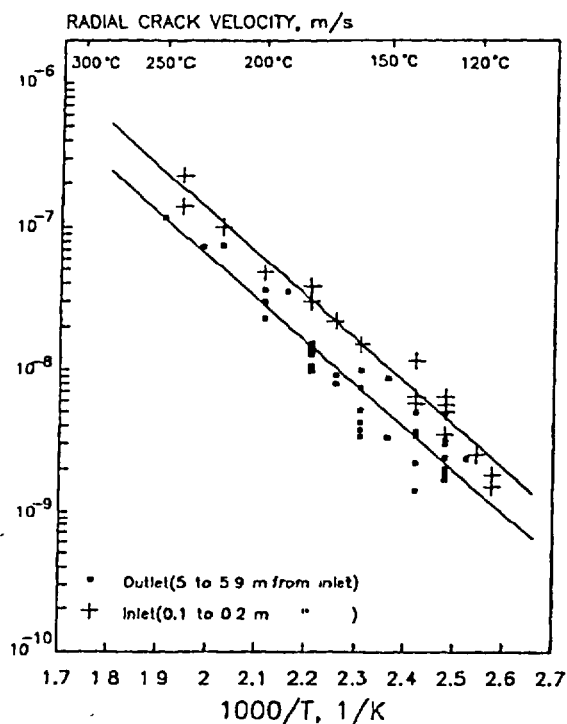


FIG. 11—Difference between radial DHC velocity at the outlet and inlet ends of pressure tube.

Threshold Stress Intensity Factor

The threshold stress intensity factor, K_{IH} , was measured using the load-reducing method on several tubes removed from reactors and on their offcuts. The results showed a small decrease in K_{IH} as the fluence increased to about 1×10^{23} n/m², but no decrease in K_{IH} was observed with further increase in fluence, Fig. 14. The average K_{IH} in the offcuts was 7.5 ± 1.3 MPa \sqrt{m} and, in the irradiated material, it was 6.2 ± 0.9 MPa \sqrt{m} at the 95% confidence level. Within the temperature range of 140 to 250°C, K_{IH} remained constant, Fig. 15.

Microstructural Examinations

XRD analysis shows that enrichment of the β -phase by niobium occurs during service and increases significantly from the inlet toward the outlet, Fig. 16. The enrichment is the result of a gradual decomposition of metastable 20 to 40 atomic percent niobium-enriched β -Zr towards a stable β -Nb phase about 88 atomic percent niobium at 300°C. X-ray diffraction indicates a variation in $\langle a \rangle$ -type dislocation density along the length of the tubes, being highest at the inlet end and decreasing by about 20% toward the outlet end, Fig. 17. The data from samples taken from within 0.5 m of the centers of the tubes show that the $\langle a \rangle$ -type dislocation density has saturated by fluences of about 2×10^{23} n/m², Fig. 18.

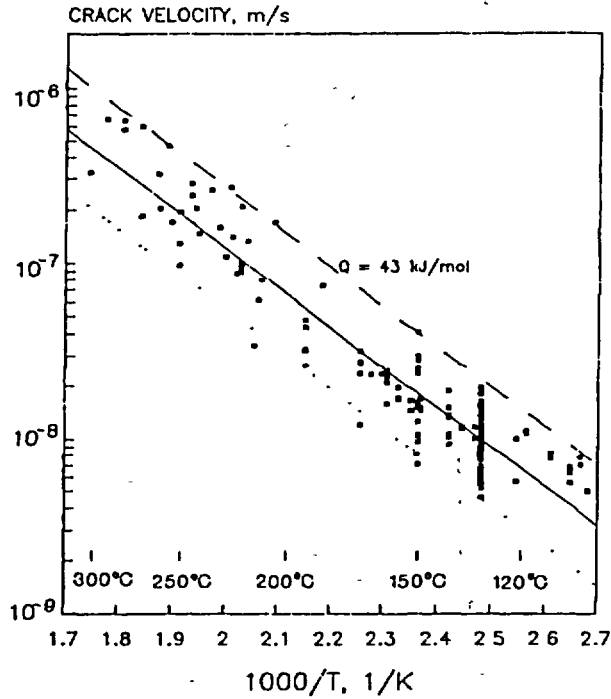


FIG. 12—Temperature dependency of axial DHC velocity

Discussion

The results are summarized as follows. The crack velocity, V , of DHC in cold-worked Zr-2.5Nb is increased by a factor of up to five times, and K_{IH} is slightly reduced by neutron irradiation. The effects saturate after about $1 \times 10^{25} \text{ n/m}^2$. V decreases with increase in irradiation temperature. In unirradiated material, V in the axial direction is twice that in the radial direction, but in irradiated material, the dependence of V on direction changes with testing temperature. Neutron irradiation produces damage in the crystal lattice of Zr-2.5Nb in the form of predominantly type- $\langle a \rangle$ dislocation loops that harden the material. The irradiation hardening saturates at a fluence of about $2 \times 10^{25} \text{ n/m}^2$ and so does the yield stress. The β -phase decomposition is controlled by the irradiation temperature—the higher the temperature, the greater is the decomposition. Both the yield stress and the state of the β -phase decomposition have been shown to affect DHC velocity [12,13]. The results will be discussed in the context of these observations.

Effect of Irradiation Fluence

The effect of irradiation fluence on DHC can be explained by the theory of delayed hydride cracking developed by Dutton and Puls [14], and later improved by Puls [8,15] and Ambler [16]. According to this theory, when there is a hydride present at the crack tip, its rate of growth is determined by the rate of diffusion of hydrogen into the crack-tip region. The driving

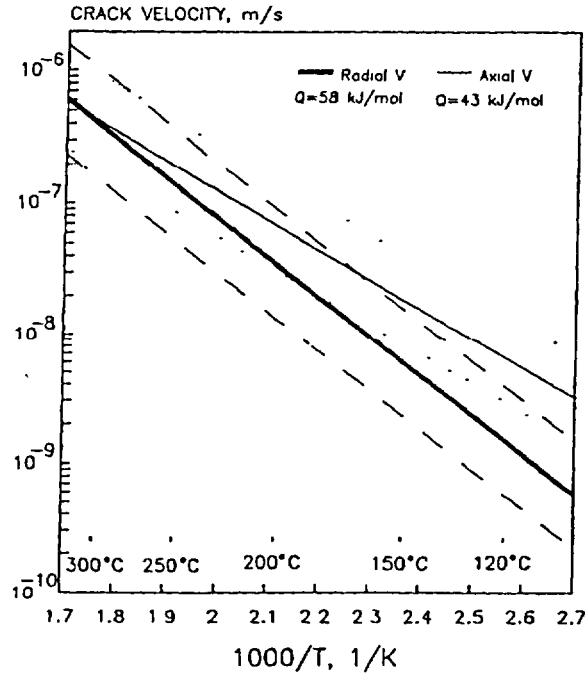


FIG. 13—Comparison between radial and axial DHC velocity.

forces for diffusion are: hydrogen concentration gradient, stress gradient, and thermal gradient. The theory assumes that the crack velocity is equal to the rate of growth of the hydride at the crack tip. The rate of diffusion of hydrogen atoms, dN/dt , into the cylinder of unit length and radius, r , is

$$\frac{dN}{dt} = -2\pi r J_H \tag{5}$$

where J_H is the hydrogen flux ($\text{atoms} \cdot \text{m}^{-2} \cdot \text{s}^{-1}$).

Assuming that the crack velocity is equal to the rate of growth of the hydride at the crack tip, the crack velocity, da/dt , can be written as

$$\frac{da}{dt} = \frac{-2\pi r J_H}{\alpha \alpha_r N_H} \tag{6}$$

where

- α = the thickness to length ratio of the hydride,
- $\alpha \alpha_r$ = the thickness of the hydride at fracture, and
- N_H = the atomic density of the hydride

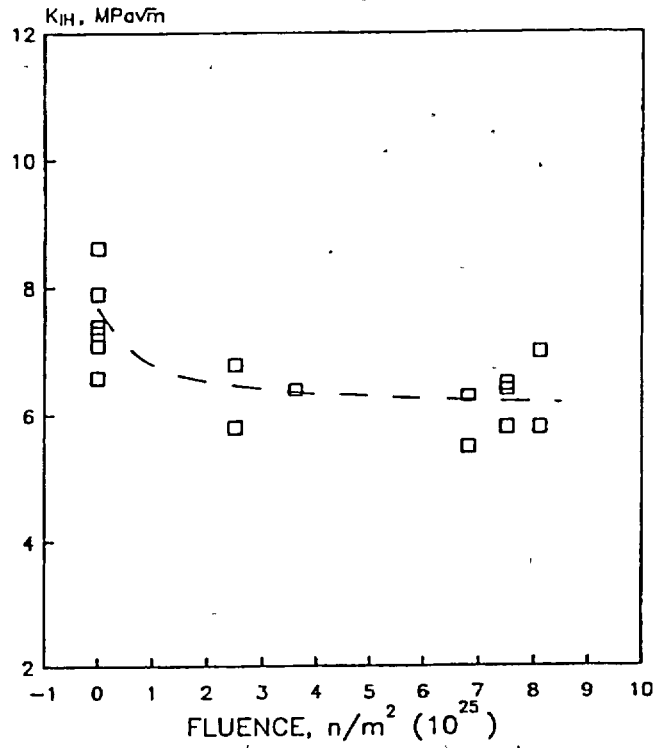


FIG. 14—Dependence of K_{IH} on irradiation fluence.

Substituting for hydrogen flux

$$J_H = \frac{D_0 C_0}{r \Omega_Z \phi} (E_L - E_I) \tag{7}$$

the crack velocity, da/dt , can be written as

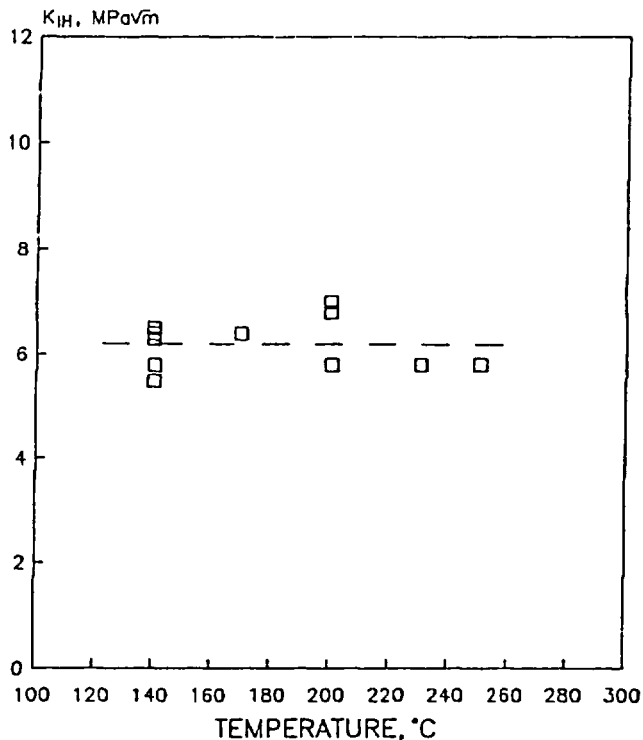
$$\frac{da}{dt} = \frac{2\pi D_0 C_0}{\Omega_Z \alpha \alpha_c N_H \phi} (E_L - E_I) \tag{8}$$

where

$$E_{L,I} = \exp\left\{\frac{(w_r^{nc})_{L,I} + (w_r^c)_{L,I}}{xR(T)_{L,I}}\right\} \tag{9}$$

$$\phi = \int_1^t \frac{1}{r} \exp\left\{\frac{(F - w_H^c + Q_D)}{RT}\right\} dr \tag{10}$$

The remaining parameters in Eqs 5 to 10 are given in Appendix I.

FIG. 15—Temperature dependency of K_{IH} .

In this model, the effect of irradiation fluence can be accounted for through the value of the yield stress of the material as shown by Puls [15]. There are two terms that are sensitive to yield stress: the position of the maximum stress, a_c , and the interaction energy of the crack-tip hydride with the locally applied stress, $(w_f)_c$. a_c is related to the plastic zone size at the crack tip that depends on the yield stress. $(w_f)_c = -6.66\sigma_y$ for δ -hydrides. Using the average yield stress from Fig. 7, the model predicts an increase in the mean DHC velocity due to the irradiation hardening to be a factor of about 3, Fig. 19. The current model does not account for either the direction of the crack growth or for the decomposition of the β -phase. However, as diffusion data become available for the anisotropic microstructures of pressure tubes, the model can be expanded to include the crack growth in two-phase material in both the radial and axial directions.

Crack velocity in unirradiated cold-worked Zircaloy-2 is much lower than that in Zr-2.5Nb [2,17]. Results of experiments show that irradiation to a fluence of 7.7×10^{24} n/m² increases the crack velocity in Zircaloy-2 by a factor of 50, making it similar to that of irradiated Zr-2.5Nb, Fig. 19 (for Harvey tubes in Ref 2 that had a similar texture to that of standard Zr-2.5Nb pressure tubes). Using an increase in yield stress from 350 to 600 MPa from irradiation [18], and the diffusion coefficient for α -Zr, the preceding model predicts an increase in the crack velocity, but only by an order of magnitude. Clearly, the increase in yield stress alone cannot fully account for the observed behavior in Zircaloy-2.

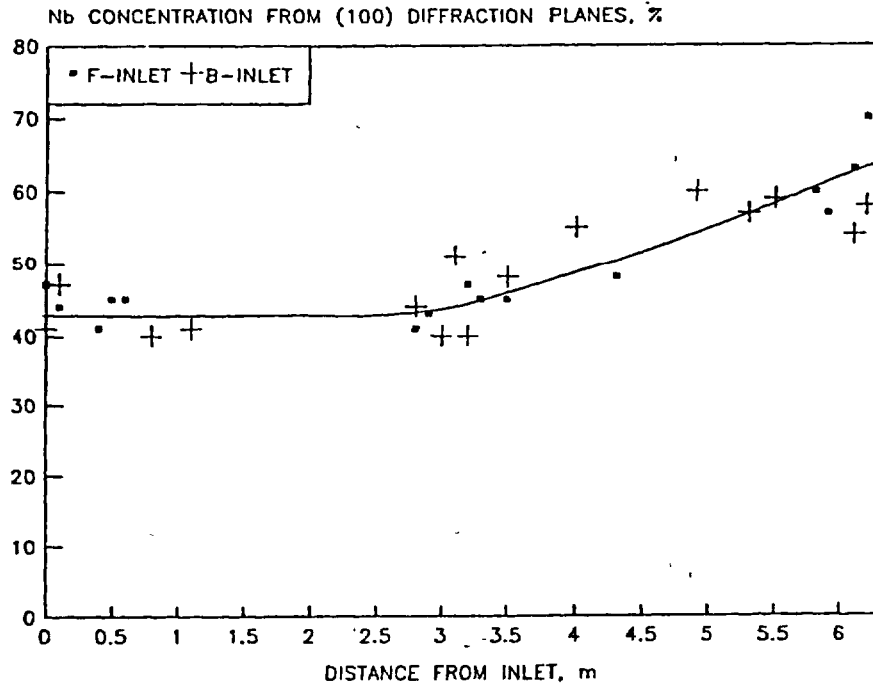


FIG. 16—Percentage of niobium in the β -phase of Zr-2.5Nb pressure tubes as a function of position relative to the inlet, for back (B) and front (F) ends relative to the extrusion process.

A conceptual model for K_{IH} was recently developed [19]. The theoretical expression for K_{IH} is given in terms of the elastic constants, the yield stress of the material, the hydride fracture stress (σ_f^h), and the thickness of the crack-tip hydride (t) as follows

$$(K_{IH})^2 = \frac{E \cdot t}{1 - \nu^2} \left\{ \frac{0.043E \cdot \epsilon_w}{(1 - \nu^2) \left[\frac{1}{1 - 2\nu} - \frac{\sigma_f^h}{\sigma_y} \right]} - \gamma \cdot \sigma_y \right\} \quad (11)$$

where

σ_y = the yield stress of the material, and
 γ = a constant (~ 0.025).

Other parameters in this equation are defined in Appendix I. The values of K_{IH} calculated by this model are smaller than those measured experimentally, Table 2. The model assumes that the crack-tip hydride covers the entire fracture surface. The higher values measured in experi-

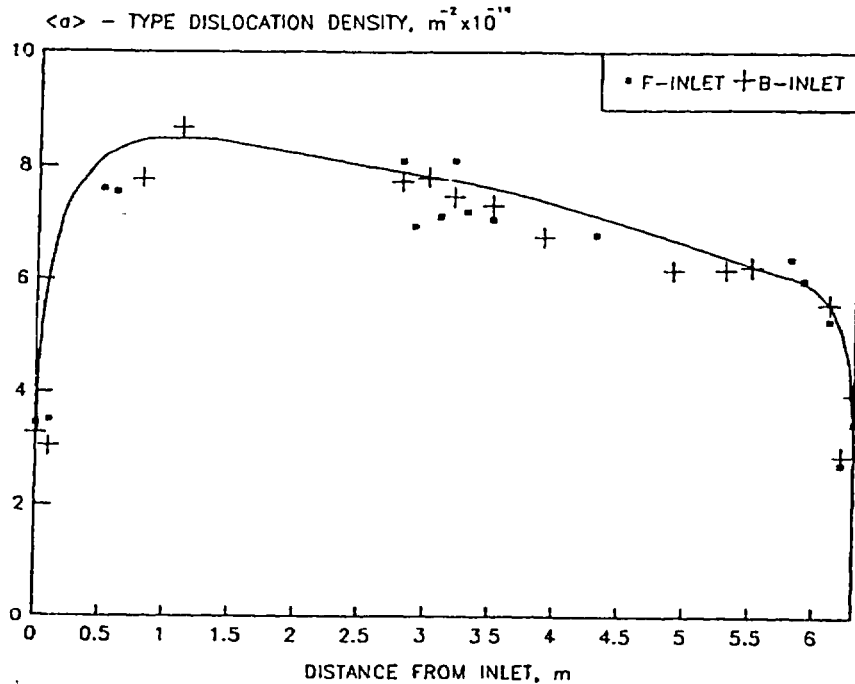


FIG. 17— $\langle a \rangle$ -type dislocation density in Zr-2.5Nb pressure tubes as a junction of position relative to the inlet, for back (B) and front (F) ends relative to the extrusion process.

ments were assumed to be caused by the fact that the hydrides may not cover the whole front of the crack and the experimental K_{IH}^{exp} was related to the theoretical K_{IH} as follows

$$K_{IH}^{exp} = fK_{IH} + (1 - f)K_i \quad (12)$$

where

f = the fraction of hydride coverage at the crack tip, and
 K_i = the initiation fracture toughness of the matrix (zirconium alloy) material.

Substituting $K_{IH} = 3.7 \text{ MPa}\sqrt{\text{m}}$, $K_{IH}^{exp} = 6.2 \text{ MPa}\sqrt{\text{m}}$, and $K_i = 30 \text{ MPa}\sqrt{\text{m}}$ into Eq 12, f is 0.9, that is, hydrides should cover nearly all of the area ahead of the crack tip. Our preliminary results based on metallographic examinations of hydrides at crack tips show that, at low values of K_I (near K_{IH}), the hydrides are well developed and continuous. However, further examinations need to be done to quantify the state of the crack-tip hydrides more accurately.

The model predicts a slight reduction in K_{IH} with irradiation that agrees with experimental results. This reduction is mainly due to an increased yield stress by neutron irradiation in the irradiated material. Our preliminary results on unirradiated Zr-2.5Nb indicate that a material with a lower yield stress has a higher value of K_{IH} , but most of such material also has a

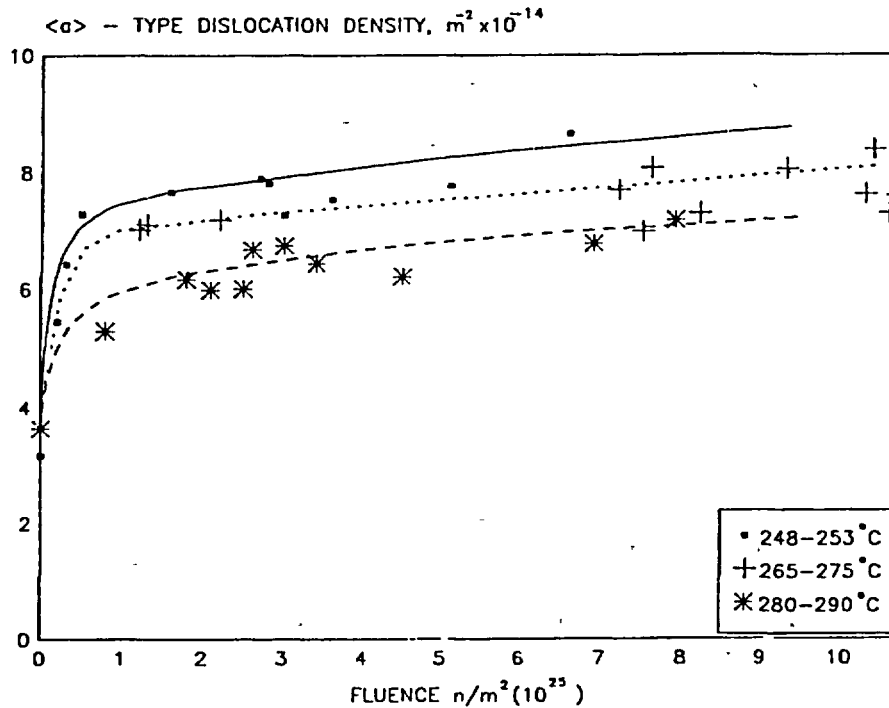


FIG. 18—Variation of dislocation density as a function of fluence for samples of Zr-2.5Nb pressure tubes taken from within 0.5 m of the center line of the reactors.

different crystallographic texture, hence, the effect of yield stress alone cannot be easily isolated. Clearly, the relationship between K_{IH} and yield stress in unirradiated Zr-2.5Nb material needs to be established.

Effect of Irradiation Temperature

It has been shown that the diffusion coefficient in the pure β -phase is about two orders of magnitude above the diffusion coefficient in α -phase [20,21]. In two-phase, cold-worked Zr-2.5Nb material, the presence of the β -phase enhances (up to an order of magnitude) the hydrogen diffusivity, compared with that in the α -phase. Experiments have shown that the crack velocity in Zr-2.5Nb alloy is greater in the material with the continuous β -phase than that in materials with decomposed β -phase [13,21]. These observations can be used in explaining the different crack velocities at the inlet and outlet ends of irradiated pressure tubes. The DHC experiments showed higher crack velocities at inlet ends of irradiated pressure tubes than at the outlet ends, while X-ray diffraction showed a smaller degree of β -phase decomposition at inlet ends than at outlet ends, Figs. 5, 6, 11, and 16. The profile of the crack velocity in an irradiated pressure tube, Figs. 8 and 9, is mainly the result of differences in the β -phase decomposition along the tube, Fig. 16, and to a lesser degree because of decreasing irradiation hardening, Fig. 17.

TABLE 2—Predicted and measured K_{IH} values in unirradiated and irradiated Zr-2.5Nb materials

Temperature, °C	Predicted K_{IH} , MPa√m	Measured K_{IH} , MPa√m
UNIRRADIATED		
150	4.1	7.5 ± 1.3
250	5.3	7.5 ± 1.3
IRRADIATED		
150	3.7	6.2 ± 0.9
250	4.6	6.2 ± 0.9

Temperature Dependence of DHC Velocity

The temperature dependence in the DHC model derives primarily from the sum of the activation energies for diffusion and solubility contained in the $D_H C_H$ product, which is 70 kJ/mol, Appendix I. A secondary effect comes from the temperature dependence of the yield stress, which reduces the total activation energy for DHC to about 60 kJ/mol, Fig. 19. DHC experiments have shown that the crack velocity follows an Arrhenius type of relationship with temperature, for Zr-2.5Nb alloy

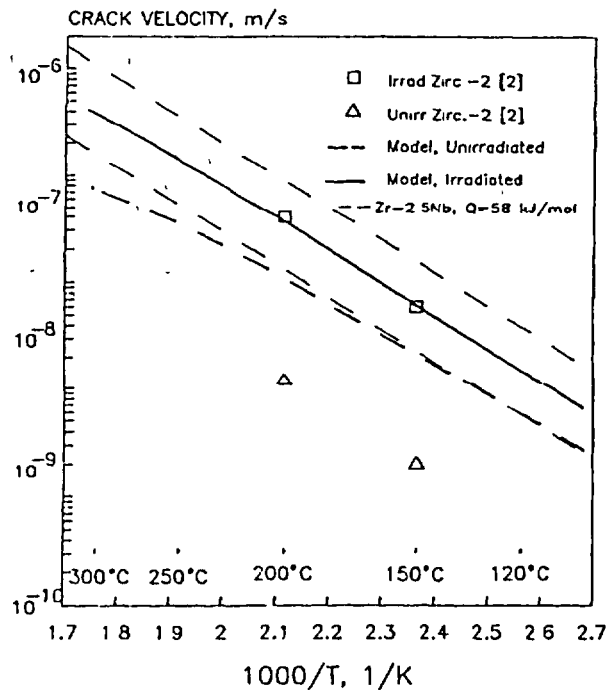


FIG. 19—Comparison between DHC velocities in Zr-2.5Nb and Zircaloy-2.

$$V = A \exp\left(-\frac{Q}{RT}\right) \quad (13)$$

with the coefficients listed in Table 3. All unirradiated materials, but one [7], have temperature dependencies in the range from 58 to 72 kJ/mol, which is reasonably close to the theoretical value. The results in Ref 7 were not obtained using the standard temperature cycling procedure. Most of the unirradiated materials have the β -phase decomposed from homogenization treatment at 400°C for several days after gaseous hydriding, hence, the cracking in both directions is governed mainly by the diffusivity and solubility in the α -phase. In the radial direction, the temperature dependence of cracking of the irradiated material is similar to that of unirradiated material, suggesting that the factors that dominate the temperature dependence, solubility and diffusivity in the α -phase, are not much affected by radiation. Lower temperature dependence of the axial crack velocity in the irradiated material can be explained in terms of the contribution of the β -phase (which is only partially decomposed in the irradiated material) to the diffusion of hydrogen in this direction (the activation energy for diffusion in the β -phase is lower than that in the α -phase [20,21]). These ideas are being explored in our current research programs.

Conclusions

1. Neutron irradiation increases the velocity of DHC in cold worked Zr 2.5Nb by a factor of 3 to 5 times, and reduces K_{IH} by a small amount, about 20%. The effect of irradiation saturates at a fluence of about $1 \times 10^{25} \text{ n/m}^2$.
2. Temperature dependence of the crack velocity in both the radial and axial directions in the unirradiated material, and in the radial direction in the irradiated material, follows the theoretical predictions based on a diffusional model for the α -phase and the change in yield stress with temperature and irradiation. In the axial direction, the dependence on test temperature does not follow the theory based on diffusion in the α -phase; the theory needs to incorporate a two-phase ($\alpha + \beta$) diffusion model.
3. Crack velocity decreases with irradiation temperature primarily through the change in the configuration of the β -phase and, secondarily, through changes in dislocation density.

TABLE 3—Temperature dependence of DHCV velocity for unirradiated and irradiated Zr-2.5Nb material

Direction	A	Q, kJ/mol	Ref
UNIRRADIATED			
Radial ^a	6.9×10^{-1}	72	[4]
Radial ^a	2.1×10^{-2}	59	this paper
Radial ^b	4.0×10^{-2}	58	this paper
Radial ^a	1.4×10^{-4}	42	[7]
Axial ^a	1.5×10^{-1}	66	[8]
Axial ^a	5.3×10^{-2}	60	this paper
IRRADIATED			
Radial ^a	8.6×10^{-2}	58	this paper
Axial ^c	4.0×10^{-3}	43	this paper

^aHydrogen was added gaseously at 400°C followed by homogenization at 400°C for 72 h

^bThe material was in the autoclaved condition, that is, it was heated at 400°C for 24 h.

^cSome irradiated specimens had hydrogen added electrolytically at 90°C followed by solution treatment at 290°C for 14 days.

Acknowledgments

We would like to thank the following people for assistance with experiments: G. Brady, P. Dhanjal, R. W. Gilbert, J. Kelm, W. G. Newell; D. Sage, J. M. Smeltzer, K. D. Weinsberg, J. E. Winegar, and the staff of the General Chemistry Branch and the Universal Cells at CRL. We enjoyed useful discussions with Drs. M. P. Puls and S. Q. Shi. We thank OHRD for permission to use the TG3R1 material information. The work was funded through Working Party 31 and 33 of the CANDU Owners Group.

APPENDIX I**Parameters used in DHC Model**

- D_0 2.17×10^{-7} is a pre-exponential term in the expression for the diffusion coefficient of hydrogen in zirconium: $D_H = 2.17 \times 10^{-7} \exp(-35\,100/RT)$ m²/s
- C_0 10.2 is a pre-exponential term in the expression for the concentration of hydrogen in solid solution when there is no external stresses: $C_H^0 = 10.2 \exp(-35\,000/RT)$ atomic %
- Ω_{Zr} 2.3×10^{-29} m³/atom is the atomic volume of zirconium
- α The thickness to length ratio of the hydride
- a_c^\dagger The distance from the crack tip to the position of the maximum stress = $(0.144 K_I/\sigma)^2$
- N_H 6.13×10^{28} atom/m³ is the atomic density of the hydride
- w_H^\dagger $0.577(K_I/\sqrt{r})$ J/mol is the molal interaction energy of the stresses with the hydrogen in solid solution
- Q_D 35 100 J/mol is the activation energy for diffusion of hydrogen in zirconium from the expression for D_H
- $(w_i^{inc})_{L,1}$ 4912 J/mol is the molal elastic strain energy of the matrix and fully constrained δ -hydrides with plate normals parallel to direction [0001]
- $(w_f)^\dagger$ $-0.9447(K_I/\sqrt{L})$ J/mol is the interaction energy of matrix δ -hydrides with the applied stress
- $(w_f)^\dagger$ $-6\,6563 \sigma$, J/mol is the interaction energy of crack-tip δ -hydrides with the applied stress
- x 1.66 is the mole fraction of hydrogen in ZrH_{1.66} hydride
- Q_H 35 kJ/mol is the activation energy of the equilibrium hydrogen concentration given in the expression for C_H^0
- K_I The Mode I stress intensity factor in MPa \sqrt{m}
- ν The Poisson's ratio in zirconium = 0.3
- V_H 16.7×10^{-7} m³/mol is the partial molar volume of hydrogen in zirconium
- V_{hyd} 16.3×10^{-6} m³/mol is the molal volume of hydride with a composition ZrH_{1.66}
- Q^* 25 100 J/mol is the heat of transport of hydrogen in zirconium
- ϵ_y The stress-free strain of the hydride in the y direction = 0.054
- E Young's modulus in the transverse direction = $102\,47 - 0.011\,743 T - 8.068\,69 \times 10^{-3} T^2$, where E is in GPa and T is in °C
- σ_f^\dagger The hydride fracture stress = $0.007\,357 E$

The expressions marked by a dagger (†) are derived in Appendix II.

APPENDIX II

Derivation of formulas marked by a dagger (†) in Appendix I.

Position of the Maximum Stress, a .

The maximum stress, a , is assumed to be equal to the position of the maximum stress in the plastic zone that is derived by equating the hydrostatic stress at the crack tip, p_h , to that in the matrix and then solving for r (r is defined in Fig. 20)

$$p_h(r) = -(\sigma_{11} + \sigma_{22} + \sigma_{33})/3 = -1/3 (K_I/\sqrt{2\pi r})(1 + \nu) = -0.346 K_I/\sqrt{r}$$

According to Rice and Johnson [22], the maximum hydrostatic stress is

$$p_h(1) = -2.4 \sigma_y$$

hence,

$$2.4 \sigma_y = 0.346 K_I/\sqrt{r}$$

solving for r

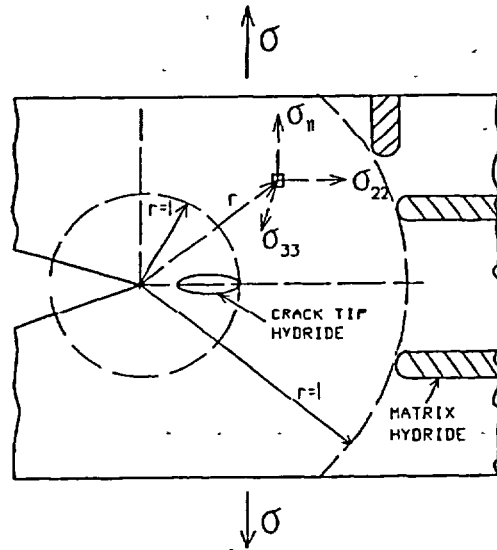


FIG. 20 Crack geometry.

$$r(1) = (0.144 K_I/\sigma_y)^2$$

where σ_y is in Mpa and K_I in $\text{MPa}\sqrt{\text{m}}$

Molal Interaction Energy of the Stresses

The molal interaction energy of the stresses with the hydrogen in solid solution is expressed by

$$w_H^s = p_h V_H$$

where $V_H = 16.7 \times 10^{-7} \text{ m}^3/\text{mol}$ and $p_h = (\sigma_{11} + \sigma_{22} + \sigma_{33})/3$ for plane strain conditions

$$\sigma_{11} = \sigma_{22} = K_I/\sqrt{2\pi L}$$

$$\sigma_{33} = \nu(\sigma_{11} + \sigma_{22}) = 2\nu K_I/\sqrt{2\pi L}$$

At L (matrix)

$$w_H^s = 2/3(K_I/\sqrt{2\pi L})(1 + \nu)V_H = 0.577 K_I\sqrt{L}$$

where K_I is in $\text{MPa}\sqrt{\text{m}}$.

Interaction Energy of Matrix δ -Hydrides with the Applied Stress

At L (matrix)

$$(w_f^s)_L = -V_{\text{hydr}} \sum \sigma_y e_y = -V_{\text{hydr}} K_I/\sqrt{2\pi L}(e_{11} + e_{22} + e_{33})$$

for δ -hydrides $e_{11} = 0.72$, $e_{22} = 0.0458$, $e_{33} = 0.0458$

$$(w_f^s)_L = -0.9447 K_I\sqrt{L}$$

where K_I is in $\text{MPa}\sqrt{\text{m}}$ and $V_{\text{hydr}} = 16.3 \times 10^{-6} \text{ m}^3/\text{mol}$.

At l (crack tip)

$$(w_f^s)_l = -V_{\text{hydr}}(3\sigma_y e_{11} + 1.8\sigma_y e_{22} + 2.4\sigma_y e_{33})$$

$$(w_f^s)_l = -6.6563\sigma_y$$

for δ -hydride.

References

- [1] Moan, G. D., Coleman, C. E., Price, E. G., Rodgers, D. K., and Sagat, S., "Leak-Before-Break in the Pressure Tubes of CANDU Reactors," *International Journal of Pressure Vessels & Piping*, Vol. 43, 1990, pp. 1-21.
- [2] Huang, F. H. and Mills, W. J., "Delayed Hydride Cracking Behavior for Zircaloy-2 Tubing," *Metallurgical Transactions*, Vol. 22A, 1991, pp. 2049-2060.
- [3] Fleck, R. G., Price, E. G., and Cheadle, B. A., "Pressure Tube Development for CANDU Reactors," *Zirconium in the Nuclear Industry: Sixth International Symposium*, ASTM STP 824, D. G. Franklin

- and R. B. Adamson, Eds., American Society for Testing and Materials, Philadelphia, 1984, pp. 88-105.
- [4] Ambler, J. F. R., "Effect of Direction of Approach to Temperature on the Delayed Hydrogen Cracking Behaviour of Cold-Worked Zr-2.5Nb," *Zirconium in the Nuclear Industry, ASTM STP 824*, D. G. Franklin and R. B. Adamson, Eds., American Society for Testing and Materials, Philadelphia, 1984, pp. 653-674.
 - [5] Sagat, S., Ambler, J. F. R., and Coleman, C. E., "Application of Acoustic Emission to Hydride Cracking," 29th Acoustic Emission Working Group Meeting, The Royal Military College of Canada, Kingston, Ontario, 1986.
 - [6] Simpson, L. A. and Clarke, C. F., "Application of the Potential-Drop Method to Measurement of Hydrogen-Induced Sub-Critical Crack Growth in Zirconium-2.5Nb," AECL Research Report, AECL-5815, Whiteshell Laboratories, Pinawa, Manitoba, 1977.
 - [7] Coleman, C. E. and Ambler, J. F. R., "Susceptibility of Zirconium Alloys to Delayed Hydrogen Cracking," *Zirconium in the Nuclear Industry (3rd Conference), ASTM STP 633*, A. L. Lowe, Jr. and G. W. Parry, Eds., American Society for Testing and Materials, Philadelphia, 1977, pp. 589-607.
 - [8] Simpson, L. A. and Puls, M. P., "The Effect of Stress, Temperature and Hydrogen Content on Hydride-Induced Crack Growth in Zr-2.5Nb," *Metallurgical Transactions*, Vol. 10A, 1979, pp. 1093-1105.
 - [9] Holt, R. A., "Recovery of Cold-Work in Extruded Zr-2.5Nb," *Journal of Nuclear Materials*, Vol. 59, 1976, pp. 234-242.
 - [10] Griffiths, M., Winegar, J. E., Mecke, J. F., and Holt, R. A., "Determination of Dislocation Densities in HCP Metals Using X-ray Diffraction and Transmission Electron Microscopy," *Advances in X-ray Analysis*, Vol. 35, 1992, pp. 593-599.
 - [11] Chow, C. K., Coleman, C. E., Hosbons, R. R., Davies, P. H., Griffiths, M., and Choubey, R., "Fracture Toughness of Irradiated Zr-2.5Nb Pressure Tubes from CANDU Reactors," *Zirconium in the Nuclear Industry: Ninth International Symposium, ASTM STP 1132*, C. M. Eucken and A. M. Garde, Eds., American Society for Testing and Materials, Philadelphia, 1991, pp. 246-275.
 - [12] Shek, G. K. and Graham, D. B., "Effects of Loading and Thermal Manoeuvres on Delayed Hydride Cracking in Zr-2.5Nb Alloys," *Zirconium in the Nuclear Industry. Eighth International Symposium, ASTM STP 1023*, L. F. P. Van Swam and C. M. Eucken, Eds., American Society for Testing and Materials, Philadelphia, 1989.
 - [13] Simpson, L. A. and Cann, C. D., "The Effect of Microstructure on Rates of Delayed Hydride Cracking in Zr-2.5Nb Alloy," *Journal of Nuclear Materials*, Vol. 126, 1984, pp. 70-73.
 - [14] Dutton, R. and Puls, M. P., "A Theoretical Model for Hydrogen Induced Sub-Critical Crack Growth," *Proceedings, Conference on Effect of Hydrogen on Behavior of Materials*, American Institute of Mining, Metallurgical, and Petroleum Engineers, 7-11 Sept. 1975, pp. 516-525.
 - [15] Puls, M. P., "Effect of Crack Tip Stress States and Hydride-Matrix Interaction Stresses on Delayed Hydride Cracking," *Metallurgical Transactions*, Vol. 21A, 1990, pp. 2905-2917.
 - [16] Ambler, J. F. R., "The Effect of Thermal Gradients on the Delayed Hydride Cracking Behaviour of Zirconium Alloys—Mathematical Model," AECL Research, unpublished work, Chalk River Laboratories, Chalk River, Ontario, 1985.
 - [17] Puls, M. P., Simpson, L. A., and Dutton, R., "Hydride-Induced Crack Growth in Zirconium Alloys," AECL Research Report, AECL-7392, Whiteshell Laboratories, Pinawa, Manitoba, 1982.
 - [18] Coleman, C. E., Cheadle, B. A., Causey, A. R., Chow, C. K., Davies, P. H., McManus, M. D., Rodger, D. K., Sagat, S., and van Drunen, G., "Evaluation of Zircaloy-2 Pressure Tubes from NPD," *Zirconium in the Nuclear Industry. Eighth International Symposium, ASTM STP 1023*, L. F. P. Van Swam and C. M. Eucken, Eds., American Society for Testing and Materials, Philadelphia, 1989, pp. 35-49.
 - [19] Shi, S. Q. and Puls, M. P., "Criteria of Fracture Initiation at Hydrides in Zirconium," to be published.
 - [20] Sawatzky, G. A., Ledoux, R. L., Tough, R. L., and Cann, C. D., "Hydrogen Diffusion in Zirconium-Niobium Alloys," *Metal-Hydrogen Systems, Proceedings*, Miami International Symposium, 1981, Pergamon Press, Oxford, 1982, pp. 109-120.
 - [21] Skinner, B. C. and Dutton, R., "Hydrogen Diffusivity in α - β Zirconium Alloys and its Role in Delayed Hydride Cracking," *Hydrogen Effects on Material Behaviour*, N. R. Moody and A. W. Thomson, Eds., The Minerals, Metals & Materials Society, Jackson Lake Lodge, 1989.
 - [22] Rice, J. R. and Johnson, M. A. in *Inelastic Behavior of Solids*, M. F. Kanninen, Ed., McGraw-Hill, New York, 1970, p. 641.

DISCUSSION

Brian Cox¹ (written discussion)—One of the questions that D. Franklin hoped to answer in his introduction was whether DHC cracks could be initiated from smooth surfaces, given a high enough stress maintained for a long enough time. Can you comment on whether or not DHC cracks can be initiated at smooth surfaces, and the times and stresses needed to do this?

S. Sagat et al. (authors' closure)—Early experiments by Cheadle and Ells² showed that DHC cracks can be initiated at smooth surfaces. In these experiments, smooth (smooth refers to the original surface quality of the as-received pressure tube) cantilever beam specimens were machined from cold-worked Zr-2.5Nb pressure tubes. Some of the specimens were gaseously hydrided at 400°C to a hydrogen concentration of 40 to 120 ppm, the remainder of specimens were tested with the as-received hydrogen concentration that was between 10 and 15 ppm. The specimens were tested in pure bending. After loading, the specimens were heated to 300°C and then cooled to the test temperature to reorient some of the hydrides under the applied stress. The as-received specimens were tested at 80°C and the hydrided specimens at either 150 or 250°C.

In specimens that contained 10 to 15 ppm hydrogen, cracks initiated at outerfibre stresses >550 MPa, either at surface nicks or angular SiO₂ particles that were embedded to the surface of the tubes by sand blasting operations used to clean the tubes during their fabrication. The range of failure times in these tests was between 53 and 6600 h.

In specimens with hydrogen concentration between 40 and 120 ppm, the crack initiation was not associated with any surface flaws or embedded particles. In these specimens, the cracks initiated at reoriented radial hydrides, near the surface of the specimen, at outerfibre stresses ≥ 413 MPa at a temperature of 150°C, and at stresses ≥ 585 MPa at 250°C. The range of failure times in these tests was between 2 and 1920 h.

In conclusion, crack initiation by DHC at smooth (as-fabricated) surfaces in cold-worked Zr-2.5Nb pressure tubes requires a large tensile stress at a surface asperity or hydrides close to the surface and perpendicular to the stress direction.

C. Lemaignan³ (written discussion)—Is there any tendency for the hydrides to precipitate in α , β phase or at the interface between the two?

S. Sagat et al. (authors' closure)—The microstructure of cold-worked Zr-2.5Nb pressure tubes consists of lath-shaped α -grains (hexagonal close packed) highly elongated in the axial direction. The α -grains (with a thickness of about 0.5 μm) are surrounded by a continuous network of body centered cubic β -phase (about 0.05 μm thick and comprising approximately 7% volume fraction). The original hydrides in this material are oriented parallel to the circumferential-axial plane along the α/β phase boundaries. Very few β -grain boundaries are in the radial direction. The precipitation of hydrides in the hexagonal α -phase is known to occur on habit planes that are very close to the basal planes. The precipitation of hydrides in the β -phase is to my knowledge not very well known. If there is a crack present in the material, the hydride will precipitate at the crack tip that in most cases is the α -phase. No systematic study has been done to see what happens if the β -phase is at the crack tip. However, the DHC crack does not seem to have any problems growing through both, the α and β -phase, as it grows through the pressure tube wall.

¹University of Toronto, Toronto, Ontario, Canada.

²Cheadle, B. A., "Crack Initiation in Cold-Worked Zr-2.5Nb by Delayed Hydrogen Cracking," *Proceedings, Second International Congress on Hydrogen in Metals*, Paris, 6-11/VII/1977; also as AECL-5799.

³CEA, Grenoble, France

Suresh K. Yagnik⁴ (written discussion)—What is the typical hydrogen concentration at the crack-tip for DHC mechanism? Is there a threshold value for this?

S. Sagat et al. (authors' closure)—The hydrogen concentration at the crack tip that is required for DHC initiation has to be greater than the terminal solid solubility (TSS) limit of hydrogen in zirconium for a given temperature. The Zr-2.5Nb material exhibits hysteresis between the heatup and cooldown TSS. TSS is also affected by the applied stress. To derive the required hydrogen concentration for DHC to occur, one has to choose the appropriate TSS. A theoretical treatment of hydrogen solubility in zirconium alloys can be found in two publications written by Puls.^{5,6}

⁴Electric Power Research Institute, Palo Alto, CA

⁵Puls, M. P., "The Effect of Misfit and External Stress on Terminal Solid Solubility in Hydride-Forming Metals," *Acta Metallurgica*, Vol. 29, 1981, pp 1961-1968.

⁶Puls, M. P., "On the Consequences of Hydrogen Supersaturation Effects in Zr Alloys to Hydrogen Ingress and Delayed Hydride Cracking," *Journal of Nuclear Materials*, Vol. 165, 1989, pp 128-141.